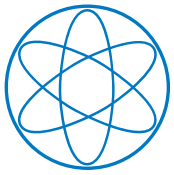

Technische Universität München

Physik Department E21 (Lehrstuhl für Experimentalphysik III)

Neutron μstiX

Micrometer Structure Investigation with Real Space and Reciprocal Space Crossover using Neutron Imaging Detectors

Dipl.-Phys. (Univ.) Martin Johann Mühlbauer

Vollständiger Abdruck der von der Fakultät für Physik der Technischen Universität München zur Erlangung des akademischen Grades eines

Doktors der Naturwissenschaften (Dr. rer. nat.)

genehmigten Dissertation.

Vorsitzender:	Univ.-Prof. Dr. Martin Zacharias
Prüfer der Dissertation:	1. Univ.-Prof. Dr. Peter Böni
	2. Univ.-Prof. Dr. Winfried Petry

Die Dissertation wurde am 26.04.2013 an der Technischen Universität München eingereicht und durch die Fakultät für Physik am 19.07.2013 angenommen.

Abstract:

This work is concerned with the investigation of inhomogeneities in materials with length scales of the order of micrometers by means of neutrons. In real space this is done by neutron imaging methods measuring the transmitted signal while for Ultra Small Angle Neutron Scattering (USANS) the signal of the scattered neutrons is assigned to a spatial frequency distribution in reciprocal space. The part about neutron imaging is focused on time-resolved neutron radiography on an injection nozzle similar to the ones used for modern diesel truck engines. The associated experiments have been carried out at the neutron imaging facility ANTARES at the Forschungs-Neutronenquelle Heinz Maier-Leibnitz (FRM II) of the Technische Universität München in Garching near Munich. Especially the demands on the detector system were high. Therefore different detection methods and detector configurations have been tested. On the one hand the detector should allow for a time resolution high enough to record the injection process lasting about 900 μs. On the other hand it needed to offer a spatial resolution sufficient to resolve the test oil inside the spray hole of a maximum diameter of less than 200 μm. An advanced aim of this work is the visualization of cavitation phenomena which may occur during the injection process inside of the spray hole. In order to operate the injector at conditions as close to reality as possible a high pressure pump supplying the injector with test oil at a pressure of 1600 bar was needed in addition to the specially developed control electronics, the recuperation tank and the exhaust gas equipment for the escaping atomized spray. A second part of the work describes USANS experiments based on the idea of Dr. Roland Gähler and carried out at the instrument D11 at the Institut Laue-Langevin in Grenoble. For this purpose a specific multi-beam geometry was applied, where a multi-slit aperture replaced the standard source aperture and the sample aperture was exchanged for an array of cylindrical shaped neutron lenses. The measurements conducted with this temporary setup gave a first impression of the interaction of the multi-beam geometry and the employed neutron lenses. The Q-range accessible with such a setup at a standard SANS instrument was determined by means of calibration samples. Within this work especially the formation of the primary beam profile plays a significant role because of its substantial influence on the achievable resolution and data evaluation. Within this scope similarities and differences of the basic layout for neutron imaging and SANS or USANS are highlighted.

Zusammenfassung:

Die vorliegende Arbeit befasst sich mit der Untersuchung von Inhomogenitäten in Materialien mit einer Größe im Bereich von Mikrometern unter Zuhilfenahme von Neutronen. Im realen Ortsraum geschieht dies mit bildgebenden Verfahren der Neutronenradiographie durch Messung des Transmissionssignals, wohingegen bei der Ultra-Kleinwinkel Neutronenstreuung das Signal der gestreuten Neutronen einer Intensitätsverteilung im reziproken Impulsraum zugeordnet wird. Der Teil über zeitaufgelöste Neutronenradiographie konzentriert sich auf Messungen an einer Einspritzdüse, wie sie zum Beispiel in aktuellen LKW-Motoren Verwendung finden. Die zugehörigen Experimente wurden an der Anlage ANTARES an der Forschnungs-Neutronenquelle Heinz Maier-Leibnitz (FRM II) der Technischen Universität München in Garching bei München durchgeführt. Hierbei wurden vor allem an den Detektor besondere Anforderungen gestellt, weshalb unterschiedliche Detektionsverfahren und Dektektorkonfigurationen getestet wurden. Zum einen sollte es der Detektor ermöglichen den etwa 900 μs andauerenden Einspritzvorgang mit ausreichender Zeitauflösung festzuhalten, zum anderen musste er gleichzeitig eine Ortsauflösung besitzen, die es erlaubte das für die Messungen verwendete Prüföl auch im Inneren des Spritzlochs der Düse darzustellen, welches einen Maximaldurchmesser von weniger als 200 μm besitzt. Ein weiterführendes Ziel dieser Arbeiten liegt in der Visualisierung von Kavitationseffekten, wie sie während des Einspritzvorgangs innerhalb des Spritzlochs auftreten können. Zum Betrieb der Einspritzdüse unter möglichst realistischen Bedingungen wurde neben der eigens entwickelten Ansteuerelektronik und einer Auffang- und Absaugeinrichtung für den austretenden Sprühnebel auch eine Hochdruckpumpe am Instrument benötigt, die den Injektor mit Prüföl unter einem Druck von 1600 bar versorgte. Ein weiterer Teil der Arbeit beschreibt Experimente zur Ultra-Kleinwinkel Neutronenstreuung, die auf Überlegungen von Dr. Roland Gähler basieren und am Instrument D11 am Institut Laue-Langevin in Grenoble durchgeführt wurden. Hierfür wurde eine spezielle Vielstrahlgeometrie verwendet, wobei eine Multischlitzblende die Standardquellblende ersetzte und die Probenblende gegen ein Array aus Zylinderlinsen für Neutronen ausgetauscht wurde. Die mit diesem vorübergehenden Aufbau durchgeführten Messungen liefern einen ersten Eindruck über das Zusammenspiel der Vielstrahlgeometrie mit den verwendeten Neutronenlinsen. Anhand von Kalibrierproben wurde der durch einen derartigen Aufbau an einer normalen Kleinwinkelanlage zugängliche Q-Bereich ermittelt. Innerhalb dieser Arbeit nimmt vor allem die Ausbildung des primären Strahlprofils einen hohen Stellenwert ein, da es einen wesentlichen Einfluss auf die erreichbare Auflösung und die Datenauswertung hat. Hierbei werden auch Parallelen und Unterschiede zwischen den grundsätzlichen Aufbauten für Neutronenradiographie und Kleinwinkelstreuung bzw. Ultra-Kleinwinkelstreuung aufgezeigt.

Contents

List of Abbreviations

Advanced Neutron Tomography and Radiography Experimental Setup (ANTARES)

ANTARES is the name of the neutron radiography and tomography facility using thermal neutrons at the Forschungs-Neutronenquelle Heinz Maier-Leibnitz. 1, 52, 57, 58

Charge-coupled Device (CCD)

A charge-coupled device is a device for the movement of electrical charge, usually from within the device to an area where the charge can be manipulated, for example conversion into a digital value. 20, 55, 58, 61, 66, 74, 115, 117

Complementary Metal Oxid Semiconductor (CMOS)

This technology for the production of integrated circuits is also used for imaging sensors. 27, 42, 51, 55, 74

small angle neutron scattering instrument D11 (D11)

One of the small angle neutron scattering instruments at the Institut Laue-Langevin. 1, 79, 80

Detection Quantum Efficiency (DQE)

Using the detection quantum efficiency it is possible to describe the efficiency of information or signal transfer from the first stage of a multi stage detection system to the last one. Calculations and simulations of the DQE allow for a determination of the detector stage limiting spatial resolution or/and detector statistics. 1, 29–33, 38, 41, 46, 47, 49, 63, 74

field of view (FOV)

The area of the neutron beam the detector is capable to image. 30, 33, 38, 47, 49, 55, 58, 61, 72, 74, 115, 125, 144

Forschungs-Neutronenquelle Heinz Maier-Leibnitz (FRM II)

The Forschungs-Neutronenquelle Heinz Maier-Leibnitz is a high flux reactor powered neutron source operated by the Technische Universität München. 15, 52, 115

intensified Charge-coupled Device (iCCD)

An intensified Charge-coupled Device is a detector system where an image intensifier is directly coupled to a charge-coupled device (see CCD) via an fiber optical taper. The image intensifier allows to operate the detector in combination with weak light sources, or it may be used as an fast optical shutter [1]. 55, 57, 58

Institut Laue-Langevin (ILL)

The Institut Laue-Langevin is an international research centre based in Grenoble, France. 1, 15, 79, 80, 84

Lehrstuhl Verbrennungskraftmaschinen (LVK)

It is the Institute of Combustion Engines at the Faculty of Mechanical Engineering of the Technical University of Munich. 57

multi channel plate (MCP)

27, 28, 42, 44–49, 51, 55, 57, 58, 61, 72, 74, 113

modulation transfer function (MTF)

modulation transfer function 38, 46

quantum accounting diagram (QAD)

A quantum accounting diagram is a plot showing the evolution of the number of quanta carrying information for a cascaded system. It is normalized to 1 incident quantum. 1, 29, 33, 63

region of interest (ROI)

An area inside a radiograph or image the interest of a certain evaluation is focused to. 74

Small Angle Neutron Scattering (SANS)

Small Angle Neutron Scattering is a well known neutron scattering technique. 1, 3, 13–17, 20, 23, 26, 79, 89, 91, 98, 100, 103, 106, 110, 113, 125, 138, 141

Signal to Noise Ratio (SNR)

It gives the ratio between the evaluated signal and the deviation of this signal from the mean value. 30, 31, 63

Technische Universität München (TUM)

Technische Universität München 57

Ultra Small Angle Neutron Scattering (USANS)

Ultra Small Angle Neutron Scattering is a technique, which expands Q-range of Small Angle Neutron Scattering to Q-values even larger than the ones accessible by VSANS making it possible to investigate structures or particle sizes of several micrometers. 1, 13, 20, 23, 25, 26, 28, 79, 80, 84–86, 91, 92, 96, 98, 100, 103, 106, 110, 113, 125, 136, 138, 141, 142, 144

Very Small Angle Neutron Scattering (VSANS)

Very Small Angle Neutron Scattering is a technique to expand the range of measurable Q-values of Small Angle Neutron Scattering to larger Q-values. 1

Chapter 1

Introduction

In 1932 James Chadwick proposed the "Possible Existence of a Neutron" [2]. He did so to allow for an explanation of observations made by Walther Bothe et al., Irène Curie-Joliot and Frédéric Joliot. When beryllium is hit by α-particles, radiation of a characteristic unknown at that time is emitted. Especially its transfer of energy and momentum to protons, could only be explained "if the radiation consists of particles of mass 1 and charge 0, or neutrons" [2], while the principles of conservation of energy and momentum still hold. These measurements were in fact some of the first neutron transmission and neutron scattering experiments. At that time the aim was to investigate the properties of the neutron itself. Nowadays the characteristic properties of the neutron make it a unique tool for scientific investigations. Sophisticated instrumentations make use of the transmitted or scattered neutron intensities in order to gain information on samples from an atomic to a macroscopic length scale. While neutron radiography determines the neutron transmission behaviour of an object in real space using two-dimensional position-sensitive imaging detectors, neutron diffraction results in data represented in coordinates in reciprocal space, which are linked to dimensions in real space after data evaluation. Neutron radiography investigations and Ultra Small Angle Neutron Scattering (USANS) measurements carried out at the lower limit of the achievable detector resolution start to overlap with respect to the investigated particle size in the micrometer range. One is heading towards a micrometer resolution starting from larger structures for neutron imaging application, while an extension of the accessible Q-range towards $10^{-5}\,\text{Å}^{-1}$ for the USANS applications is equivalent to lateral coherence lengths of $63\,\mu$m. This somehow connects the worlds of both neutron techniques, neutron imaging and neutron diffraction, as the crossover from real space to reciprocal space allows for an investigation on the same length scale using two different neutron techniques. The two main parts of this work cover time resolved neutron imaging of a diesel injection process focusing on the test oil inside the injection nozzle and USANS measurements using a multiple neutron beam geometry and applying neutron lens arrays instead of standard apertures in order to reach a higher neutron flux at the sample.

Investigations of the diesel injection process by means of neutrons are motivated by the fact that neutrons show higher attenuation for diesel fuel or the flame retardant test oil used instead, while they can easily penetrate the steel body of the nozzle. Thus neutrons yield better contrast for the test oil than X-rays and they allow for an operation of the injector under real operating conditions, e.g. pressure, temperature. An improved knowledge about cavitation phenomena taking place inside the spray hole is of interest, because they affect the break up of the injection spray and therefore the effectiveness of the combustion process in terms of fuel consumption and production of harmful exhaust gases. On the other hand cavitation occurring inside the spray hole may cause undesirable erosion and yield a much faster degeneration of the nozzle itself.

The general aim of USANS is to extend the Q-range of standard Small Angle Neutron Scattering (SANS) or Very Small Angle Neutron Scattering (VSANS) in order to get access to neutron intensities scattered at even smaller scattering angles. The use of a neutron imaging detector instead of a standard detector not only improves the detector resolution but it also allows to work without a beam stop when the signal scattered by the sample is acquired. That way the minimum scattering

angle or Q-value which is accessible is not limited by the size of the beam stop but rather by the spatial resolution of the detector. Of course the beam divergence of the primary beam has to be reduced drastically to meet the improved detector resolution. A straight forward approach to do so is to reduce the size of the source and sample aperture of the collimation defining the divergence of the beam. This would result in a huge loss of neutron flux at the sample position though. The multiple beam approach described in here compensates for this loss by a combination of a multi source aperture array and a neutron lens array used as sample aperture. That way the effective transmission area of the source and sample aperture arrays get equivalent to standard SANS apertures, which in turn allows to yield a similar neutron flux at the sample. It is necessary though to fulfill some geometrical constraints and the imaging condition of the lenses to yield the intended superposition of a multiplicity of the resulting multiple peak pattern of the primary beam profile on the detector. An introduction to this multiple beam along with a basic introduction to neutron imaging and SANS / USANS is given in chapter 2.
The characteristics of the detector, like its spatial resolution and the achievable signal statistics influenced by its neutron detection efficiency, are important for neutron imaging and ultra small angle neutron scattering (USANS). Hence an excursus to the signal statistics of imaging detectors with cascaded conversion stages is added in chapter 3. Therein the concept of Detection Quantum Efficiency (DQE) as a measure to describe the statistical behaviour of these systems will be explained together with the quantum accounting diagram (QAD) as a way to illustrate the propagation of information from the input, starting with the detection of a neutron, to the output of the detector. Chapter 4 about time resolved neutron radiography at Advanced Neutron Tomography and Radiography Experimental Setup (ANTARES) starts with a detailed description of the neutron radiography setup. Special emphasis is put on the sample environment to operate the investigated injection nozzle and the different detection systems. It explains different approaches for data evaluation and ends with a short summary. The experimental layout for USANS at the small angle neutron scattering instrument D11 (D11) at Institut Laue-Langevin (ILL) in Grenoble and the corresponding measurements are described at the beginning of chapter 5. Two different techniques are applied to evaluate the data acquired with the multiple beam USANS geometry. Again a short summary is found at the end of the chapter. Finally chapter 6 summarizes the results and gives an outlook to further improvements for time resolved neutron radiography and the use of imaging techniques in neutron scattering. Additional information may be found in the appendix, e.g. extensive calculations or drawings of parts of the mechanical layout.

Chapter 2

Neutron Radiography and Small Angle Neutron Scattering

Up to a certain level the theory of small angle neutron scattering (SANS) and neutron radiography are described by the same formalism. For example the shape of the primary beam profile at the detector position is determined by the same formula, but the parameters for the beam collimation are optimized according to the demands of each method. The idealized primary beam profile for neutron radiography is a uniform intensity across the whole sample and detector area. For SANS measurements the perfect beam profile at the detector position would be a delta peak (Sec. 2.1.2 and Sec. 2.2.2). Both methods suffer from background caused by incoherent scattering of neutrons. The main difference of the description of the measured intensity at the detector plane arises from two assumptions:
(i) For neutron radiography scattered neutrons do not reach the detector in a first approximation. The measured intensity at the detector is attributed to transmitted neutrons only.
(ii) For SANS the transmission of the sample is considered to be constant for the whole sample area. Thus the sample is expected to be homogeneous.

2.1 Neutron Radiography - Measuring Neutron Transmission

All radiographic techniques are based on the same principle independent of the type of radiation applied: The measurement of the attenuation of radiation while penetrating an object. For radiographic imaging the transmitted intensity is recorded by a position sensitive detection system. According to Harms and Wyman [3] there are three essential components for neutron radiography:
≫
i) a suitable neutron beam
ii) an object of radiographic interest
iii) a device to record - promptly or latently - the radiation information associated with the neutron beam transmitted through the object.
≪
The statement "a suitable neutron beam" already includes that the neutron beam for radiography does not have to be perfect or optimized. In fact radiographies may be acquired using a neutron beam with inhomogeneities of the neutron flux density or the neutron energy spectrum along the x and y direction (Fig. 2.1) at the sample position or the detector position, respectively. The use of digital detectors allows to correct for variations of the neutron flux density or the detection efficiency across the detector area. Of course best results will be achieved by a perfect neutron beam of zero divergence, uniform intensity and a high flux density with a narrow energy spread.
"An object of radiographic interest" is a sample where neutrons are likely to yield an (attenuation) contrast, while other types of radiation do not yield contrast or can not penetrate the sample.
And the "device to record the radiation information" is a position sensitive neutron detector (Chap. 3).

2.1.1 Neutron Radiography Instrumentation

The main components of a neutron radiography setup are shown in figure 2.1. And their function is described by a short paragraph below.

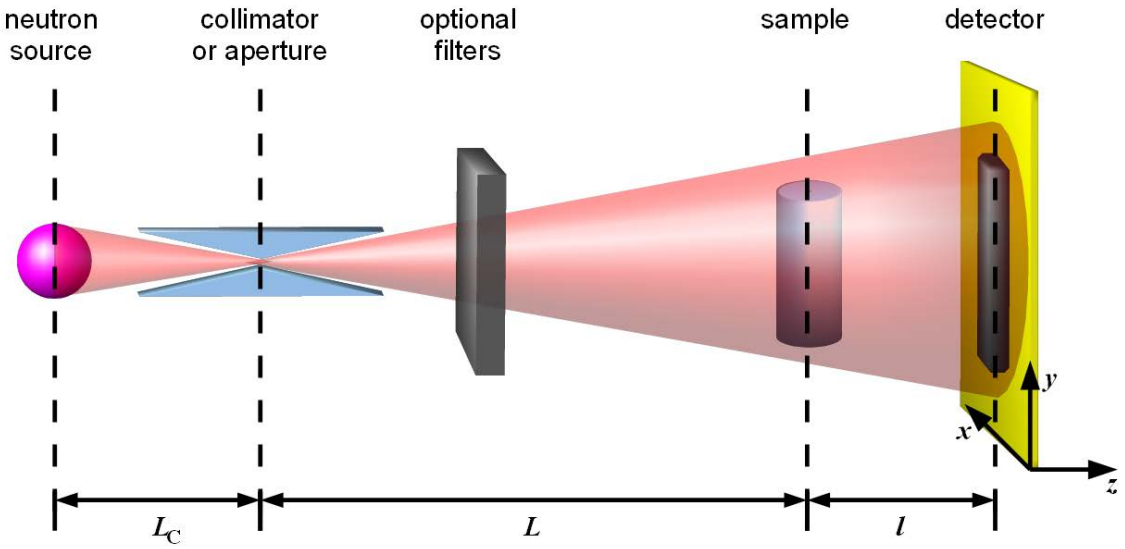

Fig. 2.1: A principle setup for neutron radiography consists of a neutron source, a collimator or aperture, a sample and a detector. An evacuated flight tube (not shown) enclosing the neutron flight path reduces the attenuation caused by air and the background caused by scattered neutrons.

Neutron Source Independent of the way of neutron generation the neutron source is defined by a volume of moderator material.[1] If this volume is sufficiently large, the neutron flux density at the interface of this volume and the entrance window of the beam tube can be assumed to be homogeneous. The effective size of this interface, the source area, is normally determined by the geometry of structure material. A continuous source, e.g. fission based, is of advantage for steady state radiography and tomography. While a pulsed source, e.g. a spallation source, is beneficial for energy dependent radiography or time resolved imaging in case it is possible to synchronize the investigated process to the pulses of the source.

Collimator or Aperture It defines a minimum lateral dimension of the neutron beam on its path from the source to the sample. Whether it is called collimator or aperture depends on the ratio of the minimum diameter and its length or thickness in beam direction. If the total length in beam direction is much larger than the minimum diameter, one will call it collimator. If their length scale is comparable, it is rather called an aperture. Usually material offering high attenuation for neutrons and gamma radiation is chosen for the collimator, as gamma radiation is commonly emitted by neutron sources, too. A more detailed description of the design and optimization of a neutron collimator is given in [4]. In the following an idealized aperture[2] at a distance L_C from the source with a diameter D equal to the minimum diameter of the collimator simplifies the determination of the beam geometry. In practice the collimator extends from this aperture position towards the neutron source as well as towards the sample position. Its total length may be up to one meter or more. The additional material enables to restrict the size of the visible source area and to cut away the penumbra region surrounding the fully illuminated part of the neutron beam (Fig. 2.2). This and the increased effectiveness of blocking high energy radiation are reasons why longer collimators are preferred in order to reduce the radiation background at the sample and detector position. The aperture or collimator is an important part of a neutron radiography

[1] There is an exception for fast neutron sources, as they are not moderated usually.

[2] An idealized aperture is infinitely thin and the material it is made of is totally opaque for any kind of radiation.

facility. It not only defines the neutron flux density and the fully illuminated area A_f at the sample position, but it also restricts the divergence of the neutron beam. Neutrons are assumed to be emitted isotropically from the source, which is valid for a big enough moderator volume. Thus the neutron flux density passed to the instrument is limited by the solid angle covered by the aperture

$$\Delta\Omega = 2\pi \cdot \left(1 - \cos\left(\frac{\delta}{2}\right)\right) . \tag{2.1}$$

Here δ is a numerical value for the global divergence[3] of the neutron beam (Fig. 2.2). If

$$L_C \gg D\,, \tag{2.2}$$

which is true for most radiography setups, the global divergence δ is constant for any position inside the beam and it is approximated by

$$\delta = \arctan\left(\frac{D}{L_C}\right). \tag{2.3}$$

Figure 2.2 illustrates how the size of the neutron source D_S in combination with the global divergence influence the size of the neutron beam at the detector position. A larger global divergence

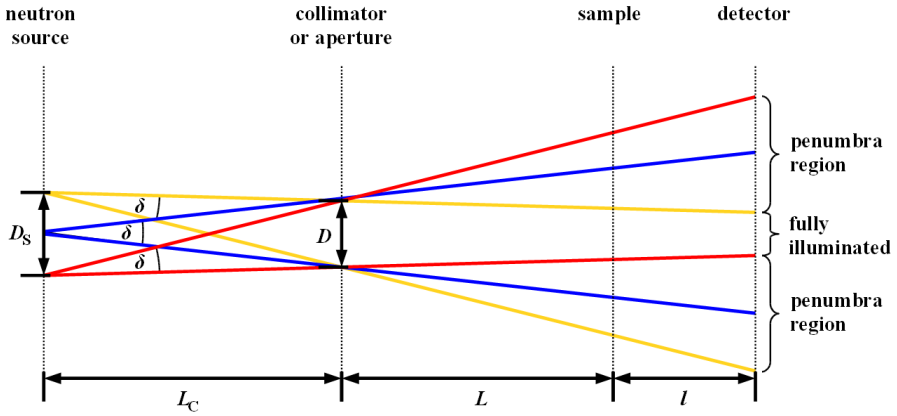

Fig. 2.2: The global divergence δ of the neutron beam is defined by the diameter D of the aperture and the distance L_C from the neutron source to the aperture. Note that it is independent of the sample or detector position. The marginal rays drawn above are one option for a geometrical construction of the so-called fully illuminated part and the penumbra region of the neutron beam [4].

leads to an increased neutron flux density[4] (according to equation (2.1)) and a larger fully illuminated area A_f[5], which is the part of the neutron beam with uniform flux density. Up to here simply increasing the aperture diameter D would improve the parameters of the radiography setup. But linked with this diameter is also the local divergence φ[6] (Fig. 2.3).

$$\varphi = \arctan\left(\frac{D}{L}\right) \tag{2.4}$$

A more common numerical value in neutron radiography to describe the local divergence is the so-called L over D ratio (L/D ratio). Other than the global divergence the local divergence or L/D ratio depends on the sample position. As long as

$$L > L_C \quad \text{and} \quad L \gg l \tag{2.5}$$

the geometrical blurring is determined by the local divergence or L/D and the distance l from the sample to the detector. This is illustrated by figure 2.3. The geometrical blurring d is given by

[3] This is the divergence looking from the source towards the detector.
[4] This is true as long as the projection of the aperture onto the source plane is smaller than the source area.
[5] Here the projection of the aperture onto the source plane is larger than the source area.
[6] It is the divergence looking from the sample towards the source.

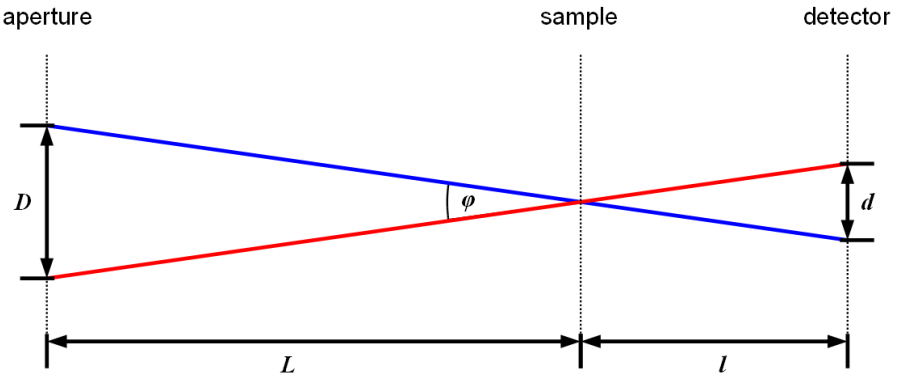

Fig. 2.3: The local divergence φ is defined by the diameter D of the aperture and the distance L from the aperture towards the sample. Due to the local divergence the projection of a point at the sample position is imaged to a circle of diameter d on the detector.

$$d = l \cdot \frac{D}{L} \qquad (\text{or} \quad d = l \cdot \tan(\varphi)) \ . \tag{2.6}$$

To achieve a minimum blur the detector has to be positioned as close as possible to the sample.[7] While the L/D ratio is a standard parameter to compare the beam collimation of different neutron imaging facilities, the beam divergence at neutron scattering instruments is usually specified in degrees. The following table gives a quick comparison of some L/D ratios and the corresponding divergences in degrees.

L/D ratio	divergence $\Delta\delta$
60	1.00 °
120	0.50 °
240	0.25 °
600	0.10 °
1200	0.05 °
2400	0.025 °

The beam divergence $\Delta\delta$ expressed in degrees can be calculated for any L/D ratio by using

$$\tan(\frac{\Delta\delta}{2}) = \frac{D}{2\,L} \implies \Delta\delta \approx \frac{180\,^\circ}{\pi} \cdot \frac{1}{\mathrm{L/D}} \approx \frac{60\,^\circ}{\mathrm{L/D}} \tag{2.7}$$

as a rule of thumb. The global divergence as well as the local divergence might be limited by the divergence of the source, in case the later is lower than the divergence that is passed through the collimator.

Filters Additional filters allow for a reduction of the gamma background, a change of the neutron energy spectrum or a polarization of the neutron beam. Bismuth, lead or other materials of high transmission for neutrons but efficiently attenuating gamma radiation improve the neutron to gamma ratio if the neutron beam contains a significant amount of gamma radiation. Transmission filters, like beryllium or sapphire, modify the neutron energy spectrum due to an energy dependent transmission [5]. A small bandwidth of neutron wavelengths may be selected by a neutron velocity selector [6] or a double crystal monochromator [7]. A polarization of the neutron beam can be achieved by means of polarizing benders or guides or ^{3}He-spin-filters [7].

Sample The neutron beam interacts with the sample via neutron absorption, coherent and incoherent scattering. This leads to an attenuation of the neutron beam. The transmitted neutron beam carries information about the sample composition (Sec. 2.1.2).

[7] When neutrons are detected by film or imaging plates, they are often even put in direct contact with the sample.

Detector For neutron radiography a two dimensional, position sensitive detector, an imaging detector, records the intensity distribution of neutrons at the detector plane. It is possible to apply counting or integrating detectors. But due to the high neutron flux density[8] at state of the art radiography facilities it is likely for counting detectors to reach their maximum count rates even if the neutron beam is attenuated by the sample. Therefore, the majority of neutron radiography detectors are integrating detectors. For a more detailed description of the neutron imaging detectors applied here see chapter 3.

2.1.2 Neutron Radiography Formalism

This section covers three topics: the formation of the primary beam intensity at the detector position[9] related to the geometry of the neutron source and the aperture, the composition of the measured intensity at the detector resulting from interaction of the neutron beam with a sample and the correction of measured raw data to yield the neutron transmission signal. In the following a time dependency of signals or intensities is denoted by the variable t. Throughout the formalism of neutron radiography the time t may correspond to a certain point in time, when a continuous process is observed, or to the position of a time frame equivalent to a delay, when periodic processes are involved. A trigger signal applied to the detector resets the timing to zero here.[10] The energy dependency of neutron absorption is often neglected to ease the description of the formalism of neutron radiography. This is equivalent to neutron radiography using a monochromatic beam.

Primary Beam Profile Assuming the source area and the aperture to be centered and symmetric with respect to the beam axis, here the z-axis, enables a simplified illustration of the primary beam profile. The marginal rays for three regions at the detector plane are shown in figure 2.4. As long as the source is visible from position (x,y) at the detector plane when looking through the aperture towards the source, neutrons reach the detector plane. The intensity is proportional to the "visible" area of the source. A position at the detector plane is called fully illuminated if the marginal rays for this position are all inside the source area. This describes the standard case of a neutron radiography setup, where the projection of the aperture onto the source plane is smaller than the source area. In case the projection of the aperture onto the source plane is larger than the source area, the fully illuminated area consists of all points at the detector plane from which it is possible to see the whole source area. The intensity profile $\hat{I}_0(x, y)$ at the detector position can be described by a correlation of the source area and the aperture, i.e. the minimum diameter of the collimator. Therefore the opening functions of the source $A_\mathrm{S}(x_\mathrm{S}, y_\mathrm{S})$ and the aperture $A_\mathrm{A}(x_\mathrm{A}, y_\mathrm{A})$ have to be scaled according to the distances L_C and L_D to yield the correct size of the intensity profile at the detector plane. These opening functions[11] are defined by

$$A_\mathrm{S}(x_\mathrm{S}, y_\mathrm{S}) = \left\{ \begin{array}{ll} 1 & (x_\mathrm{S}, y_\mathrm{S}) \in \text{ source area} \\ 0 & (x_\mathrm{S}, y_\mathrm{S}) \notin \text{ source area} \end{array} \right\} \text{for a homogeneous source} \tag{2.8}$$

$$A_\mathrm{A}(x_\mathrm{A}, y_\mathrm{A}) = \left\{ \begin{array}{ll} 1 & (x_\mathrm{A}, y_\mathrm{A}) \in \text{ aperture area} \\ 0 & (x_\mathrm{A}, y_\mathrm{A}) \notin \text{ aperture area} \end{array} \right. \tag{2.9}$$

using coordinates at the source plane and the aperture plane, respectively. Here a homogeneous source is assumed. The appropriate scaling is applied by replacing the coordinates x_S, y_S, x_A and

[8] Neutron flux densities of typically $10^7 \frac{\mathrm{n}}{\mathrm{cm}^2\,\mathrm{s}}$ to $10^9 \frac{\mathrm{n}}{\mathrm{cm}^2\,\mathrm{s}}$ or even higher are available nowadays.

[9] For neutron radiography the shape of the neutron beam at the sample position is very similar to the one at the detector position, as the sample is usually close to the detector.

[10] In the same way periodic changes of the primary intensity, e.g. at a pulsed neutron source, can be covered.

[11] This representation of the opening function does not include any inhomogeneities at the surface of the neutron source. To include inhomogeneities an emission rate function could be multiplied with the opening function of the source.

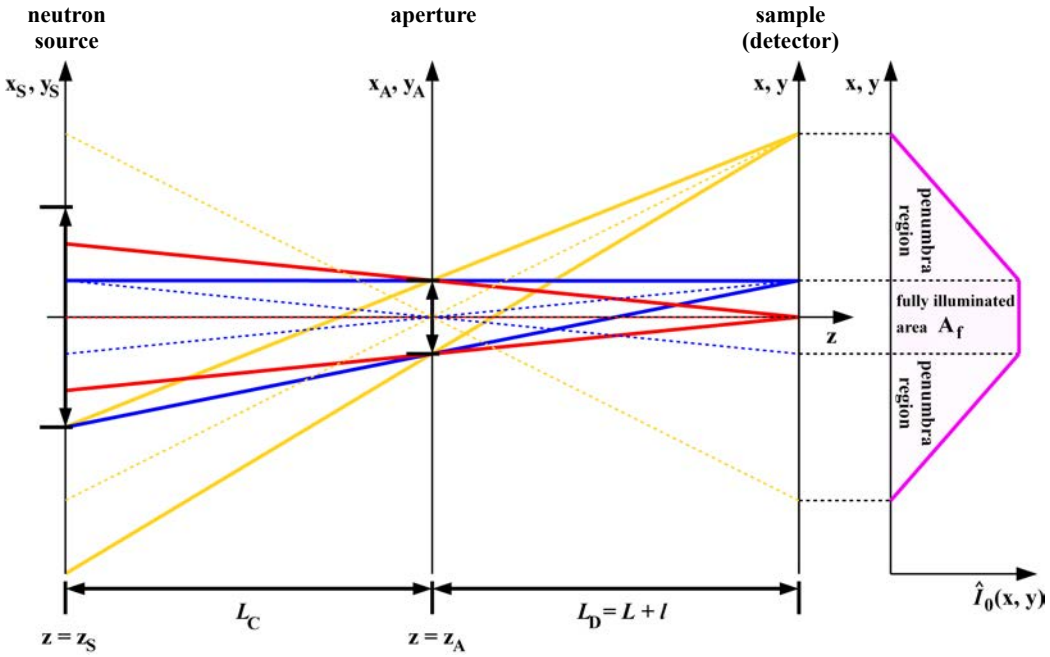

Fig. 2.4: The primary beam intensity at a certain point on the detector plane results from the source area, which is seen from this point, when looking through the aperture towards the source. To simplify the representation, the neutron source and the aperture are drawn as one-dimensional slits. Note that the size of the fully illuminated area A_f changes with the detector position.

y_A using the following mapping

$$x_S = -\frac{L_C}{L_D} x = \alpha x \tag{2.10}$$

$$y_S = -\frac{L_C}{L_D} y = \alpha y \tag{2.11}$$

$$x_A = -\frac{L_C}{L_D + L_C} x = \beta x \tag{2.12}$$

$$y_A = -\frac{L_C}{L_D + L_C} y = \beta y\,. \tag{2.13}$$

$\hat{I}_0(x, y)$ is normalized to the area of the source and reaches a maximum of 1 only if the full area of the source contributes to the intensity at the position (x, y) of the detector plane.

$$\hat{I}_0(x, y) = \frac{\int\int A_S\,(\alpha \cdot u, \alpha \cdot v)\; A_A\,(\beta \cdot (u + x), \beta \cdot (v + y))\; \mathrm{d}u\,\mathrm{d}v}{\int\int A_S(\alpha \cdot u, \alpha \cdot v)\,\mathrm{d}u\,\mathrm{d}v} \tag{2.14}$$

This formalism holds for any shape of the source or aperture (App. A.7).

Neutron Interaction with the Sample The probability of neutrons interacting with an atom, either by absorption or scattering, is proportional to the microscopic cross sections for absorption σ_a, coherent scattering σ_{coh} and incoherent scattering σ_{inc}. The energy dependency of these cross sections is not taken into account here. In a first approximation there is no distinction between coherent and incoherent scattering. Only their contribution to the attenuation of the neutron beam is considered. Thus coherent and incoherent scattering cross sections are summed up to a total scattering cross section σ_s. All scattering processes are assumed to be isotropic for this simple model of attenuation contrast. There are effects though like neutron reflection at the surface of the sample, neutron refraction due to the sample geometry or Bragg scattering that alter the intensity profile at the detector due to coherent neutron scattering. These effects are not taken into account for

standard neutron radiography applications.[12] Inside an infinitesimally small volume $\Delta V(x,y,z)$ at position (x,y,z) the material composition and the density of the sample are assumed to be homogeneous. Then the macroscopic cross sections for absorption and scattering are

$$\Sigma_{\mathrm{a}}(x,y,z,t) = \sum_{\mathrm{i}} \eta_{\mathrm{i}}(x,y,z,t)\,\sigma_{\mathrm{a,i}}(x,y,z) \quad \text{and} \tag{2.15}$$

$$\Sigma_{\mathrm{s}}(x,y,z,t) = \sum_{\mathrm{i}} \eta_{\mathrm{i}}(x,y,z,t)\,\sigma_{\mathrm{s,i}}(x,y,z)\,. \tag{2.16}$$

Where the index i denotes the contribution of a single isotope of the material composition with its corresponding particle density $\eta_{\mathrm{i}}(x,y,z,t)$ at position (x,y,z) and time t. The total macroscopic cross section

$$\Sigma_{\mathrm{t}}(x,y,z,t) = \Sigma_{\mathrm{a}}(x,y,z,t) + \Sigma_{\mathrm{s}}(x,y,z,t) \tag{2.17}$$

combines interaction due to absorption and scattering [3, p. 13f]. The probability for a neutron interacting while crossing volume ΔV on path $\mathrm{d}s$ is

$$\Sigma_{\mathrm{t}}(x,y,z,t)\,\mathrm{d}s \tag{2.18}$$

according to the law of linear attenuation. The intensity at the detector position including attenuation and scattering inside the sample and a background signal is

$$I(x,y,t) = T(x,y,t) + S(x,y,t) + B(x,y,t)\,. \tag{2.19}$$

The transmitted signal is given by

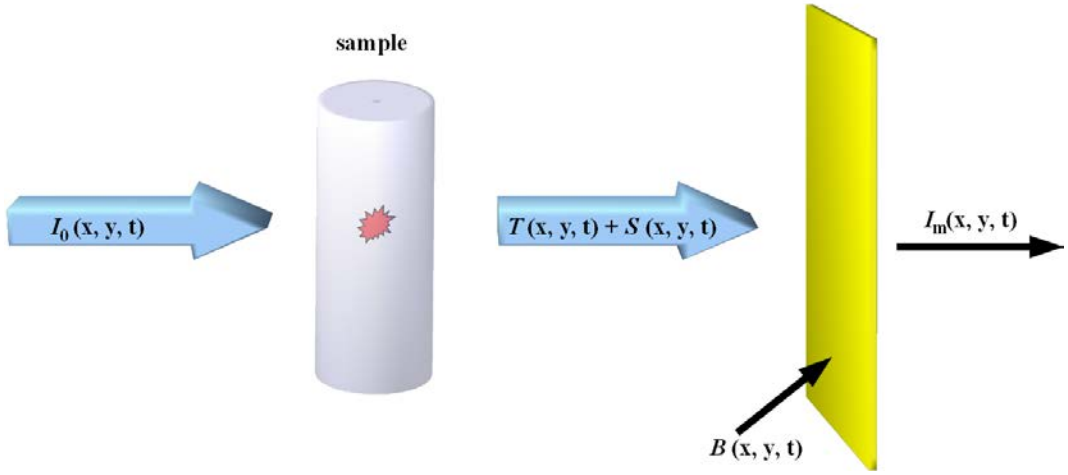

Fig. 2.5: The measured intensity $I_{\mathrm{m}}(x,y,t)$ at the detector output is composed of signals due to transmitted neutrons $T(x,y,t)$, scattered neutrons $S(x,y,t)$ and background $B(x,y,t)$.

$$T(x,y,t) = I_0(x,y,t)\,\exp\left(-\int_{C_{\mathrm{S}}} \Sigma_{\mathrm{t}}(x,y,s,t)\,\mathrm{d}s\right) = I_0(x,y,t)\,\hat{T}(x,y,t) \tag{2.20}$$

where C_{S} is a path along the z-direction through the sample and $I_0(x,y,t)$ is the primary intensity. $\hat{T}(x,y,t)$ is the space and time resolved transmission of the sample.
The scattered intensity reaching the detector plane at position z may be approximated by

$$S(x,y,t) = \int_{V_{\mathrm{S}}} \frac{I_0(u,v,t)\,\mathrm{e}^{\left(-\int_{w_0(u,v)}^{w} \Sigma_{\mathrm{t}}(u,v,s,t)\,\mathrm{d}s\right)}\,\Sigma_{\mathrm{s}}(u,v,w,t)\,\mathrm{e}^{\left(-\int_{C_s} \Sigma_{\mathrm{t}}(\mathbf{s},t)\,\mathrm{d}\mathbf{s}\right)}}{4\pi\left[(x-u)^2+(y-v)^2+(z-w)^2\right]}\,\mathrm{d}u\,\mathrm{d}v\,\mathrm{d}w\,. \tag{2.21}$$

[12] Neutron phase contrast imaging makes use of these effects to enhance edges [5], [6]. Specialized setups for polarized neutron beams enable to evaluate neutron depolarization due to spin dependent neutron scattering or magnetic fields inside and outside a sample [7].

The first integral is evaluated for the whole sample volume V_S. The expression inside the integral describes the fraction of neutrons that reach the detector at point (x, y, z) if they are scattered inside an infinitesimal volume element $\mathrm{d}u\,\mathrm{d}v\,\mathrm{d}w$ at position (u, v, w). $w_0(u, v)$ is the coordinate of the sample surface in z-direction where the neutron beam enters the sample when evaluating a scattering interaction at the coordinates u and v in x and y direction.
The incident intensity of the neutron beam is given by $I_0(u, v, t)$. The factor $\mathrm{e}^{\left(-\int_{w_0(u,v)}^{w} \Sigma_\mathrm{t}(u,v,s,t)\,\mathrm{d}s\right)}$ corresponds to the attenuation of the neutron beam until it reaches the evaluated volume element. At the position (u, v, w) the probability of a scattering event is given by the total macroscopic scattering cross section $\Sigma_\mathrm{s}(u, v, w, t)$. In this approximation the distribution of the scattered neutrons is isotropic and the scattered intensity at the detector position follows a $\frac{1}{r^2}$ law [3, p. 119]. It gives rise to the denominator $4\pi\left[(x-u)^2+(y-v)^2+(z-w)^2\right]$, which describes the isotropic scattering intensity. To take into account the attenuation of the scattered neutrons when leaving the sample, the expression $\mathrm{e}^{\left(-\int_{C_s} \Sigma_\mathrm{t}(\mathbf{s},t)\,\mathrm{d}\mathbf{s}\right)}$ represents the corresponding attenuation factor. Here the integration is carried out along a straight path C_s of the neutrons from the evaluated volume element at (u, v, w) to the position (x, y, z) at the detector. The background signal $B(x, y, t)$ is a sum of inherent background or offset of the detector, intensity due to direct detection of gamma radiation and signal induced by neutrons other than neutrons transmitted through the sample or scattered by the sample.

Data Correction, Normalization The aim of neutron radiography is to extract the space and time resolved transmission $\hat{T}(x, y, t)$ of the sample from measured intensities at the detector. These measured signals deviate from the ones of equation (2.19), because they include effects due to an energy dependent attenuation of neutrons (Sec. 2.1.3), the detection efficiency of the neutron detector or a scattering characteristics of neutrons that differs from the one approximated by equation (2.21). All measured signals are marked by an index "m". In analogy to equation (2.19) the measured intensity at the detector becomes

$$I_\mathrm{m}(x, y, t) = T_\mathrm{m}(x, y, t) + S_\mathrm{m}(x, y, t) + B_\mathrm{m}(x, y, t)\,.$$

This equation has to be solved for the signal of transmitted neutrons $T_\mathrm{m}(x, y, t)$ by subtracting the measured background $B_\mathrm{m}(x, y, t)$ and scattered intensity $S_\mathrm{m}(x, y, t)$ from $I_\mathrm{m}(x, y, t)$.

$$T_\mathrm{m}(x, y, t) = I_\mathrm{m}(x, y, t) - S_\mathrm{m}(x, y, t) - B_\mathrm{m}(x, y, t)\,. \tag{2.22}$$

It is not possible to measure the scattered signal separated from the transmission signal with a standard neutron radiography setup. And it is hard to estimate the scattered intensity without prior knowledge of the sample. The scattered intensity is often negligible compared to the transmitted intensity. Therefore a scattering correction is omitted most of the times assuming $S_\mathrm{m}(x, y, t)$ is zero. This obviously changes the transmission signal $T_\mathrm{m}(x, y, t)$. In cases, where attenuation is mainly due to scattering and the detector is close to the sample, a scattering correction should be considered to minimize this error [8]. Another way to reduce the contribution of scattered neutrons is the application of collimators to hinder scattered neutrons to reach the detector [9]. The background signal $B_\mathrm{m}(x, y, t)$ may be acquired while the shutter for the neutron beam is opened or closed and the sample is placed in front of the detector or not. In case the neutron beam is not active not all sources of background considered above contribute to the recorded signal. But in any case the background signal $B_\mathrm{m}(x, y, t)$ contains the detector offset, which is the most prominent background signal for integrating detectors based on imaging sensors. In analogy to equation 2.20 the measured space and time resolved transmission is

$$\hat{T}_\mathrm{m}(x, y, t) = \frac{T_\mathrm{m}(x, y, t)}{I_{0,\mathrm{m}}(x, y, t)} = \frac{I_{0,\mathrm{m}}(x, y, t)\,\exp\left(-\int_{C_\mathrm{S}} \Sigma_{\mathrm{t,m}}(x, y, s, t)\,\mathrm{d}s\right)}{I_{0,\mathrm{m}}(x, y, t)}\,. \tag{2.23}$$

In order to get $I_{0,\mathrm{m}}(x,y,t)$ a radiograph of the primary intensity of the neutron beam is taken without the sample. It is called open beam or flat field image. By this image an intensity of

$$O_{\mathrm{m}}(x,y,t) = I_{0,\mathrm{m}}(x,y,t) + B_{\mathrm{m}}(x,y,t) \tag{2.24}$$

is measured. Here again the background $B_{\mathrm{m}}(x,y,t)$ has to be subtracted from the measured open beam intensity $O_{\mathrm{m}}(x,y,t)$ to yield $I_{0,\mathrm{m}}(x,y,t)$. This measured intensity distribution does not only contain the intensity profile determined by the beam geometry, but it also includes inhomogeneities of the detector, e.g. different detection efficiencies of the detector pixels. The sample transmission is now obtained dividing the measured transmission signal (2.22) by the measured primary intensity.

$$\begin{aligned}
\hat{T}_{\mathrm{m}}(x,y,t) &= \frac{T_{\mathrm{m}}(x,y,t)}{I_{0,\mathrm{m}}(x,y,t)} = \underbrace{\frac{I_{\mathrm{m}}(x,y,t) - S_{\mathrm{m}}(x,y,t) - B_{\mathrm{m}}(x,y,t)}{O_{\mathrm{m}}(x,y,t) - B_{\mathrm{m}}(x,y,t)}}_{\text{with scattering correction}} \\
&\approx \underbrace{\frac{I_{\mathrm{m}}(x,y,t) - B_{\mathrm{m}}(x,y,t)}{O_{\mathrm{m}}(x,y,t) - B_{\mathrm{m}}(x,y,t)}}_{\text{without scattering correction}} \\
&= \frac{I_{0,\mathrm{m}}(x,y,t) \cdot \exp\left(-\int_{C_{\mathrm{S}}} \Sigma_{\mathrm{t,m}}(x,y,s,t)\,\mathrm{d}s\right)}{I_{0,\mathrm{m}}(x,y,t)} \\
&= \exp\left(-\int_{C_{\mathrm{S}}} \Sigma_{\mathrm{t,m}}(x,y,s,t)\,\mathrm{d}s\right)
\end{aligned} \tag{2.25}$$

Equation (2.25) is the result of the basic evaluation step of neutron radiography called normalization. After the normalization the spatial and time resolved transmission $\hat{T}_{\mathrm{m}}(x,y,t)$ is corrected for the primary intensity and inhomogeneities of the detector.[13] Further processing and evaluation of $\hat{T}_{\mathrm{m}}(x,y,t)$ is now independent of the instrumentation.

2.1.3 Beam Hardening Effects

Neutrons of a broad energy spectrum undergo different attenuation depending on their energy, when they pass a sample. On the one hand the probability of neutron absorption of most isotopes obeys a $\frac{1}{v}$ law for cold and thermal neutrons; v being the neutron velocity. On the other hand there is a wavelength dependency of coherent neutron scattering, too, because for long wavelengths the Bragg condition can not be fulfilled anymore. Therefore there is a step like increase of neutron transmission with increasing wavelength, a so-called Bragg edge. For most samples there is a prominent effect of larger attenuation for longer neutron wavelengths due to the larger absorption cross sections. Thus the average energy of a neutron beam is shifted towards higher energies after the neutron beam passed the sample. This is known as beam hardening. The shift of the average energy is larger for materials of higher absorption cross sections and for longer path lengths through the sample. It is not possible to compensate the effect of energy dependent absorption by assuming an effective wavelength, e.g. the mean wavelength of the neutron energy spectrum, during data evaluation, because the effective wavelength is different for each position at the detector plane. The energy dependent detection efficiency of the detector has a further influence on this effect. The detected signal is proportional to the number of neutrons absorbed by the detector. Here again neutron absorption is higher for neutrons of lower energy. Regions of the sample with low neutron transmission reveal a larger beam hardening effect and therefore a larger shift of the average neutron energy, the detection efficiency for that regions is lower than for the initial neutron energy spectrum. For large transmission values the reduction of the primary intensity is due to the attenuation of neutrons from the full energy spectrum. Especially the loss of neutrons of lower energy cause the

[13] A scattering correction may be included here.

measured transmitted intensity to drop. Thus the sample attenuation is assumed to be too high and the sample transmission is underestimated. The situation is different for low transmission values. As the low energy part of the neutron beam is nearly blocked completely by the sample, the measured transmission is based on a neutron spectrum of higher average neutron energy. Thus the sample transmission is overestimated compared to the transmission value expected for the average energy of the incident neutron beam. The detected intensity due to neutrons scattered by the sample will alter the measured transmission, too. A similar effect like the beam hardening described above is caused by this additional intensity. Especially for the center regions of the sample the transmission will be overestimated. This effect is most obvious if the attenuation is mainly caused by scattering and the transmission signal is comparable to the signal caused by scattered neutrons. For a single neutron wavelength the transmission is described as given by equation (2.20). Introducing a wavelength dependency of the total macroscopic cross section $\Sigma_\mathrm{t}(x, y, s, t, \lambda_0)$.

$$\hat{T}(x, y, t, \lambda_0) = \exp\left(-\int_{C_\mathrm{S}} \Sigma_\mathrm{t}(x, y, s, t, \lambda_0)\,\mathrm{d}s\right) \tag{2.26}$$

The transmission resulting from a full neutron spectrum is given by

$$\begin{aligned}\hat{T}(x, y, t) &= \frac{\int \left(\frac{\mathrm{d}I_0(x,y,t)}{\mathrm{d}\lambda}\right)(\lambda)\,\hat{T}(x, y, t, \lambda)\,\mathrm{d}\lambda}{\int \left(\frac{\mathrm{d}I_0(x,y,t)}{\mathrm{d}\lambda}\right)(\lambda)\,\mathrm{d}\lambda} \\ &= \frac{\int \left(\frac{\mathrm{d}I_0(x,y,t)}{\mathrm{d}\lambda}\right)(\lambda)\,\exp\left(-\int_{C_\mathrm{S}} \Sigma_\mathrm{t}(x, y, s, t, \lambda)\,\mathrm{d}s\right)\mathrm{d}\lambda}{\int \left(\frac{\mathrm{d}I_0(x,y,t)}{\mathrm{d}\lambda}\right)(\lambda)\,\mathrm{d}\lambda}\,.\end{aligned} \tag{2.27}$$

Still there is a difference for the measured transmission $\hat{T}_\mathrm{m}(x, y, t)$, as the efficiency of the detector is not yet included. Let the detector efficiency be $\epsilon(x, y, \lambda)$ including a spatial dependency to take into account possible inhomogeneities of the detector. Then

$$\hat{T}_\mathrm{m}(x, y, t) = \frac{\int \left(\frac{\mathrm{d}I_0(x,y,t)}{\mathrm{d}\lambda}\right)(\lambda)\,\exp\left(-\int_{C_\mathrm{S}} \Sigma_\mathrm{t}(x, y, s, t, \lambda)\,\mathrm{d}s\right)\epsilon(x, y, \lambda)\,\mathrm{d}\lambda}{\int \left(\frac{\mathrm{d}I_0(x,y,t)}{\mathrm{d}\lambda}\right)(\lambda)\,\epsilon(x, y, \lambda)\,\mathrm{d}\lambda} \tag{2.28}$$

is the measured transmission. The detector efficiency is already included in the measured primary beam intensity $I_{0,\mathrm{m}}(x, y, t)$ defined by

$$I_{0,\mathrm{m}}(x, y, t) = \int \left(\frac{\mathrm{d}I_{0,\mathrm{m}}(x, y, t)}{\mathrm{d}\lambda}\right)(\lambda)\,\mathrm{d}\lambda = \int \left(\frac{\mathrm{d}I_0(x, y, t)}{\mathrm{d}\lambda}\right)(\lambda)\,\epsilon(x, y, \lambda)\,\mathrm{d}\lambda\,. \tag{2.29}$$

This is in fact the primary beam intensity measured by the detector. Equation (2.28) is just another way to write the measured sample transmission, which can be seen by a comparison with equation (2.25).
For a simulation or calculation of a radiograph one should be aware that still the background signal $B_\mathrm{m}(x, y, t)$ and of course the signal arising from scattered neutrons $S_\mathrm{m}(x, y, t)$[14] have to be taken into account.

[14]The intensity $S_\mathrm{m}(x, y, t)$ measured due to scattered neutrons may cause a similar effect like beam hardening, especially for tomographic reconstructions and very low sample transmission.

2.2 Small Angle Neutron Scattering - SANS

While neutron imaging gives information on the inner structure of samples on a length scale of several micrometers, standard neutron diffraction reveals the sample composition on an atomic length scale. Small Angle Neutron Scattering (SANS) and Ultra Small Angle Neutron Scattering (USANS) fill the gap between these two regions. SANS is sensitive to changes of the neutron scattering length density of elementary sample volumes on a length scale of 10 Å to 1000 Å [10, p. 2.1-1]. USANS extends this range up to some 10000 Å, which is large enough to reach an overlap with neutron imaging techniques. The basic equation for neutron diffraction is Bragg's law. It gives a well known relation between the order of the observed reflection n, the neutron wavelength λ, the lattice parameter d and the scattering angle θ

$$n\,\lambda = 2\,d\,\sin\theta\,. \tag{2.30}$$

Simplified for first order reflexes ($n = 1$) one gets

$$\lambda = 2\,d\,\sin\theta \quad \text{or} \quad \sin\theta = \frac{\lambda}{2\,d}\,. \tag{2.31}$$

Given a fixed neutron wavelength large values of the observed length scale d induce small scattering angles. For SANS the scattering angle θ is given by the distance from the sample to the detector l and the distance r_D of the evaluated detector position with respect to the center of the incident neutron beam (Fig. 2.6). As the sample is placed next to the sample aperture ($L \ll l$), the distance l may be approximated by L_D from the sample aperture to the detector. Thus the scattering angle θ is given by

$$\tan(2\,\theta) = \frac{r_\mathrm{D}}{l} \approx \frac{r_\mathrm{D}}{L_\mathrm{D}} \quad \Longrightarrow \quad \tan\theta \approx \frac{r_\mathrm{D}}{2\,L_\mathrm{D}} \quad \Longrightarrow \quad \sin(\theta) \approx \frac{r_\mathrm{D}}{2\,L_\mathrm{D}}\,. \tag{2.32}$$

Usually the scattered intensities are not plotted versus the scattering angle θ but with respect to the

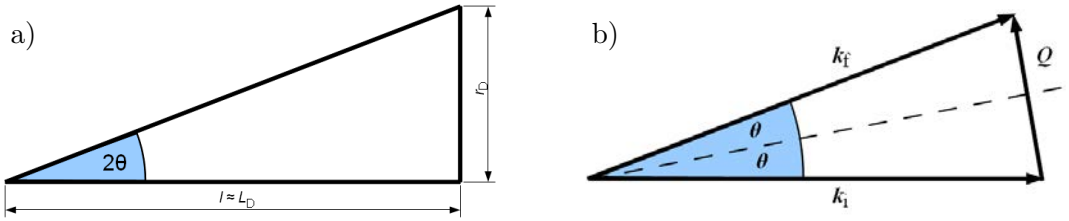

Fig. 2.6: a) The scattering angle θ is defined by the distances l and r_D. b) The momentum transfer $\mathbf{Q}$ corresponds to the change of the neutron wave vector.

scattering vector $\mathbf{Q}$, because this makes the representation independent of the neutron wavelength used for the measurement. It is defined as

$$\mathbf{Q} = \mathbf{k}_\mathrm{f} - \mathbf{k}_\mathrm{i} \tag{2.33}$$

and corresponds to a momentum transfer. $\mathbf{k}_\mathrm{i}$ and $\mathbf{k}_\mathrm{f}$ are the initial and final wave vectors of the incident and outgoing neutron wave. For elastic scattering, $|\mathbf{k}_\mathrm{i}| = |\mathbf{k}_\mathrm{f}|$, the correlation of the scattering angle θ and the scattering vector $\mathbf{Q}$ is given by

$$|\mathbf{Q}| = Q = 2\,|\mathbf{k}_\mathrm{i}|\,\sin\theta = 2\,k_\mathrm{i}\,\sin\theta\,. \tag{2.34}$$

With help of equation (2.32) every position on the detector can be mapped to the corresponding Q-value:

$$Q = 2\,k_\mathrm{i}\,\sin\theta = 2\,k_\mathrm{i}\,\frac{r_\mathrm{D}}{2\,L_\mathrm{D}} = \frac{2\,\pi\,r_\mathrm{D}}{\lambda\,L_\mathrm{D}}\,. \tag{2.35}$$

As the resolution of the detector and therefore the resolution in r_D is fixed, one may vary the wavelength and the distance L_D in order to change the resolution and range in Q. Using the definition of the neutron wave vector $k_\mathrm{i} = \frac{2\pi}{\lambda}$ and equation (2.31) in equation (2.34) one gets

$$Q = 2\,k_\mathrm{i}\,\sin\theta = 2\,\frac{2\,\pi}{\lambda}\,\frac{\lambda}{2\,d} = \frac{2\,\pi}{d}\,. \tag{2.36}$$

In other words the Q-values determined from the scattering angle θ correspond to a structure size of

$$d = \frac{2\,\pi}{Q} \tag{2.37}$$

in real space. The representation of the scattered intensity versus Q rather than the scattering angle θ makes the correlation of the scattering function and the corresponding structure size of the sample independent of the neutron wavelength used to measure it.[15]

2.2.1 SANS Instrumentation

All basic parts of a standard pinhole instrumentation for SANS are shown in figure 2.7. Their function is explained in the following paragraphs.

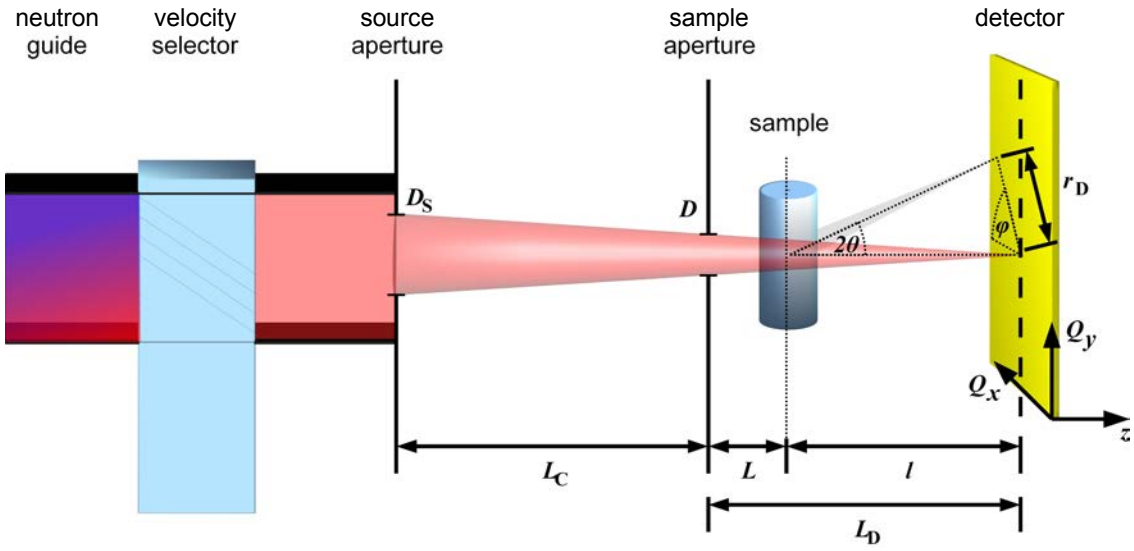

Fig. 2.7: A standard pinhole SANS instrumentation consists of a neutron guide to transport neutrons from a neutron source to the instrument, a velocity selector to select a neutron wavelength band, a source aperture and a sample aperture to define the divergence or collimation of the neutron beam, the sample and a position sensitive detector. The nomenclature is chosen in analogy to the one of the neutron radiography setup (Fig. 2.1).

Velocity Selector If the neutrons originate from a continuous neutron source, a neutron velocity selector is most common to define the wavelength of the incident neutrons. At pulsed neutron sources a chopper system is used to select the neutron wavelength by time of flight. The wavelength spread $\frac{\Delta\lambda}{\lambda}$ is about 10 % for SANS measurements.[16]

[15] It may be necessary though to use different wavelengths to adapt the accessible Q-range of the instrument to the particle sizes of the investigated samples.

[16] `http://www.ill.eu/instruments-support/instruments-groups/instruments/d11/characteristics/` `http://www.fz-juelich.de/jcns/DE/Leistungen/Instruments2/Structures/KWS1/_node.html`

Source Aperture The source aperture defines the size of the source area A_S, or in other words the opening function $A_\mathrm{S}(Q_x, Q_y)$. It is one of the main parameters responsible for the flux at the sample position (section 5.1). In combination with the sample aperture and the distance L_C it forms a collimation for the neutron beam. Assuming a circular aperture it is described by its diameter D_S.

Sample Aperture This aperture restricts the size of the neutron beam at the sample position. The neutron beam should not be larger than the sample. In analogy to neutron radiography a global divergence δ is defined by the diameter D of the sample aperture and the distance L_C between the sample aperture and the source aperture (Fig. 2.7)

$$\delta = \frac{D}{L_\mathrm{C}} \,. \tag{2.38}$$

Depending on the size of the sample aperture the global divergence may be limited not by the sample aperture but by the divergence of the neutron beam at the exit of the neutron guide (Sec. 5.4.1). In this case the sample aperture is not fully illuminated by the neutron beam. The diameter D of the sample aperture should be chosen to get an optimized peak shape at the detector position. It is therefore correlated to the size of the source aperture D_S and the distances L_C and L_D. A well defined peak shape of the intensity profile is obtained if

$$D = D_\mathrm{S} \frac{L_\mathrm{D}}{L_\mathrm{D} + L_\mathrm{C}} \,. \tag{2.39}$$

The intensity profile of the primary beam at the detector plane is derived in section 2.2.2.

Sample The sample should be homogeneous and of constant thickness over the whole beam cross section. If the sample is at least as large as the neutron beam at the sample position, the scattered intensity is described by a convolution of the primary intensity and the scattering function (sec. 2.2.2). Therefore the peak shape is conserved for neutrons scattered at the same angle. To reach an optimum scattering signal the sample thickness has to be large enough to get a sufficient number of scattering events, but at the same time it has to allow for a high transmission of scattered neutrons, which results in an optimized sample thickness depending on its scattering characteristics.

Detector At state of the art SANS instruments position sensitive detectors of active areas up to more than $1\,\mathrm{x}\,1\,\mathrm{m}^2$ and a spatial resolution of several millimeters are applied.[17] For high resolution measurements detectors have an active area of about 10 x $10\,\mathrm{cm}^2$ and a spatial resolution below 1 mm.[18] This is comparable to the active area of neutron imaging detectors, which often offer even higher spatial resolution.

2.2.2 SANS Formalism

Primary Intensity Profile The primary intensity profile $\hat{I}_0(Q_\mathrm{x}, Q_\mathrm{y})$ at the detector plane (Fig. 2.8) is derived in analogy to the primary beam profile for neutron radiography given by equation (2.14).

$$\hat{I}_0(Q_\mathrm{x}, Q_\mathrm{y}) = \frac{\int\int A_\mathrm{S}(\alpha \cdot u, \alpha \cdot v)\, A_\mathrm{A}(\beta \cdot (u + Q_\mathrm{x}), \beta \cdot (v + Q_\mathrm{y}))\, \mathrm{d}u\, \mathrm{d}v}{\int\int A_\mathrm{S}(\alpha \cdot u, \alpha \cdot v)\, \mathrm{d}u\, \mathrm{d}v} \tag{2.40}$$

Again this is a correlation of the opening functions $A_\mathrm{S}(Q_\mathrm{S,x}, Q_\mathrm{S,y})$ of the source and $A_\mathrm{A}(Q_\mathrm{A,x}, Q_\mathrm{A,y})$ of the sample aperture normalized to the area of the source. Both apertures are scaled using the

[17] D11 at ILL `http://www.ill.eu/instruments-support/instruments-groups/instruments/d11/`
[18] KWS-2 at Forschungs-Neutronenquelle Heinz Maier-Leibnitz (FRM II) `http://www.jcns.info/jcns_kws2/`

factors α and β

$$\alpha = -\frac{L_C}{L_D} \tag{2.41}$$

$$\beta = -\frac{L_C}{L_C + L_D} \tag{2.42}$$

to yield the intensity $\hat{I}_0$ in coordinates Q_x and Q_y at the detector plane. The opening functions of

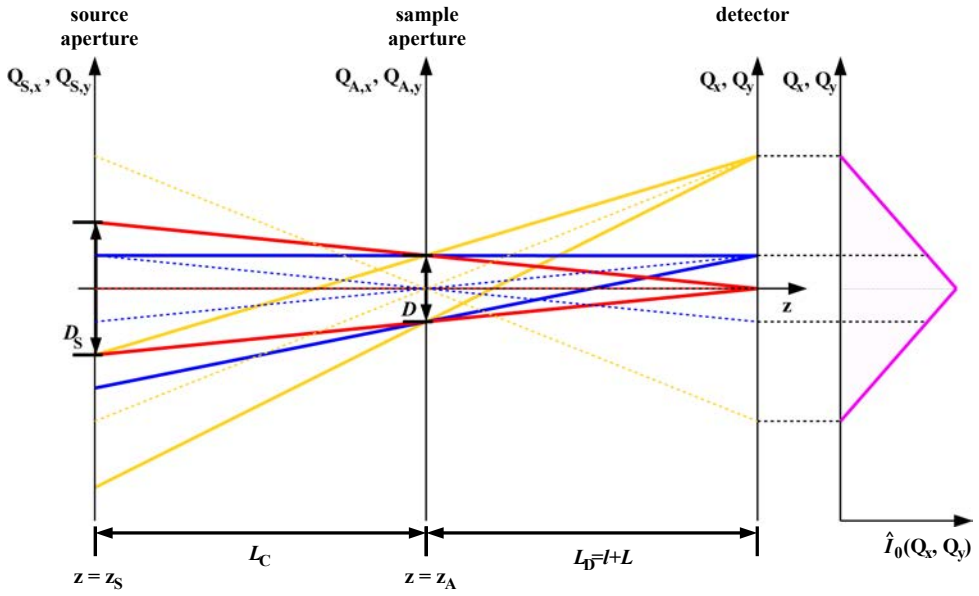

Fig. 2.8: The primary beam profile is defined by the geometry of the source aperture and the sample aperture and their distances to the detector. The intensity profile at the detector plane for slit shaped apertures is shown on the right.

the apertures are defined by

$$A_S(Q_{S,x}, Q_{S,y}) = \begin{cases} 1 & (Q_{S,x}, Q_{S,y}) \in \text{source area} \\ 0 & (Q_{S,x}, Q_{S,y}) \notin \text{source area} \end{cases} \tag{2.43}$$

$$A_A(Q_{A,x}, Q_{A,y}) = \begin{cases} 1 & (Q_{A,x}, Q_{A,y}) \in \text{aperture area} \\ 0 & (Q_{A,x}, Q_{A,y}) \notin \text{aperture area} \end{cases} \tag{2.44}$$

Although the apertures may be of any shape for the formalism above, circular apertures or slits are used on standard pinhole SANS instruments. Circular apertures induce a primary intensity of radial symmetry at the detector plane and offer a uniform Q-resolution in all directions. Slit shaped apertures only allow for an evaluation of the scattered intensities in one dimension perpendicular to the slits. But they offer an increased neutron flux at the sample due to a larger transmission area.

Other than for neutron radiography the geometry of the apertures is optimized to yield a narrow peak shape of the primary intensity profile instead of a large fully illuminated area of uniform intensity. The shape of the primary intensity profile has a major influence on the instrument resolution. A narrow peak shape (Fig. 2.9a) is obtained if the diameters D_S and D of the source aperture and the sample aperture fulfill the following equation

$$\frac{D_S}{D} = \frac{L_C + L + l}{L + l} = \frac{L_C + L_D}{L_D}\,. \tag{2.45}$$

It is obvious that the peak profile at the detector is narrower for reduced diameters of both apertures. But at the same time the neutron flux at the sample position is less by the same factor to the power

of four, as the flux at the sample position is proportional to the area of the source aperture and the area of the sample aperture.[19] If there is a mismatch of the diameters of the source aperture and the sample aperture the primary intensity profile $\hat{I}_0$ has a flat center region, like it is illustrated in figure 2.9. If the sample aperture is larger than suggested by equation (2.45), the maximum intensity is equal to the one of the matched case, but the intensity profile at the detector shows a plateau and its width is increased (Fig. 2.9b). For a sample aperture that is smaller than the size calculated from equation (2.45) the primary beam profile is similar to the profile of a neutron radiography facility (sec. 2.1.2). A fully illuminated area of uniform intensity is formed at the center. Due to the smaller size of the sample aperture the maximum intensity of the profile is reduced (Fig. 2.9c). For small sample apertures the FWHM of the beam profile is primarily determined by the width of the source aperture scaled to the detector plane. For slit shaped apertures the FWHM of the peak profile perpendicular to the slits does not change as long as the sample aperture is not larger than suggested by equation (2.45). If the width of the sample aperture gets larger than the width given by equation (2.45), the FWHM of the beam profile at the detector is no longer determined by the width of the source aperture but by the width of the sample aperture. For slit shaped apertures this can be shown quite easily, as there is a linear increase of the intensity at the detector as soon as the projection of the sample aperture onto the source plane starts to overlap with the source aperture. This correlation/relation is more complicated for circular apertures, because their circular shape will introduce a non linear increase of the intensity from zero to the maximum intensity of the profile. Thus there will be a slight change of the FWHM even if the sample aperture is smaller than the value given by equation (2.45). This behaviour can be explained by plotting the area of the intersection of two circles for different distances of their centers (App. A.10).

Signal at the Detector For SANS the intensity at the detector position is composed of a signal due to transmitted neutrons $T(Q_\mathrm{x}, Q_\mathrm{y})$, a signal due to coherent scattering $S(Q_\mathrm{x}, Q_\mathrm{y})$ and a background $B(Q_\mathrm{x}, Q_\mathrm{y})$. This is in analogy to neutron radiography (eqn. (2.19))

$$I(Q_\mathrm{x}, Q_\mathrm{y}) = T(Q_\mathrm{x}, Q_\mathrm{y}) + S(Q_\mathrm{x}, Q_\mathrm{y}) + B(Q_\mathrm{x}, Q_\mathrm{y})\,. \tag{2.46}$$

The transmission signal is

$$T(Q_\mathrm{x}, Q_\mathrm{y}) = I_0(Q_\mathrm{x}, Q_\mathrm{y})\, \exp\left(-\int_{C_\mathrm{S}} \Sigma_\mathrm{t}(Q_\mathrm{x}, Q_\mathrm{y}, s)\,\mathrm{d}s\right) = I_0(Q_\mathrm{x}, Q_\mathrm{y})\, \hat{T}(Q_\mathrm{x}, Q_\mathrm{y}) \tag{2.47}$$

and equivalent to the transmission signal of neutron radiography (eqn. 2.20). As it is assumed that the sample is homogeneous and it has a defined thickness, the sample transmission $\hat{T}(Q_\mathrm{x}, Q_\mathrm{y})$ is identical for the whole sample. If it is further assumed that the incident neutron beam is not larger than the sample, the sample transmission may be simplified to

$$\hat{T}(Q_\mathrm{x}, Q_\mathrm{y}) = \hat{T}(0,0) = \hat{T}_0\,. \tag{2.48}$$

The transmitted signal is proportional to the primary intensity then

$$T(Q_\mathrm{x}, Q_\mathrm{y}) = I_0(Q_\mathrm{x}, Q_\mathrm{y}) \cdot \hat{T}_0\,. \tag{2.49}$$

Neutrons are scattered due to coherent and incoherent scattering. The incoherent scattering signal does not contain structure information [11]. It is therefore part of the background signal $B(Q_\mathrm{x}, Q_\mathrm{y})$. Signals due to a hall background or effects related to the detector are also part of $B(Q_\mathrm{x}, Q_\mathrm{y})$.
$S(Q_\mathrm{x}, Q_\mathrm{y})$ is the intensity distribution of the coherent scattering. For static problems the intensity scattered due to the coherent scattering length density $\rho(\mathbf{r})$ per unit volume V of the sample is given by the Fourier transformation [11, p. 50]

$$\tilde{S}(Q_\mathrm{x}, Q_\mathrm{y}) = \tilde{S}(Q_\mathrm{x}, Q_\mathrm{y}, 0) = \tilde{S}(\mathbf{Q}) = \frac{1}{V} \int_V \int_V \rho(\mathbf{r}')\, \rho(\mathbf{r})\, \mathrm{e}^{-\mathrm{i}\,\mathbf{Q}\cdot(\mathbf{r}-\mathbf{r}')}\,\mathrm{d}\mathbf{r}\,\mathrm{d}\mathbf{r}'\,. \tag{2.50}$$

[19] e.g. for circular apertures and a two-dimensional Q-resolution

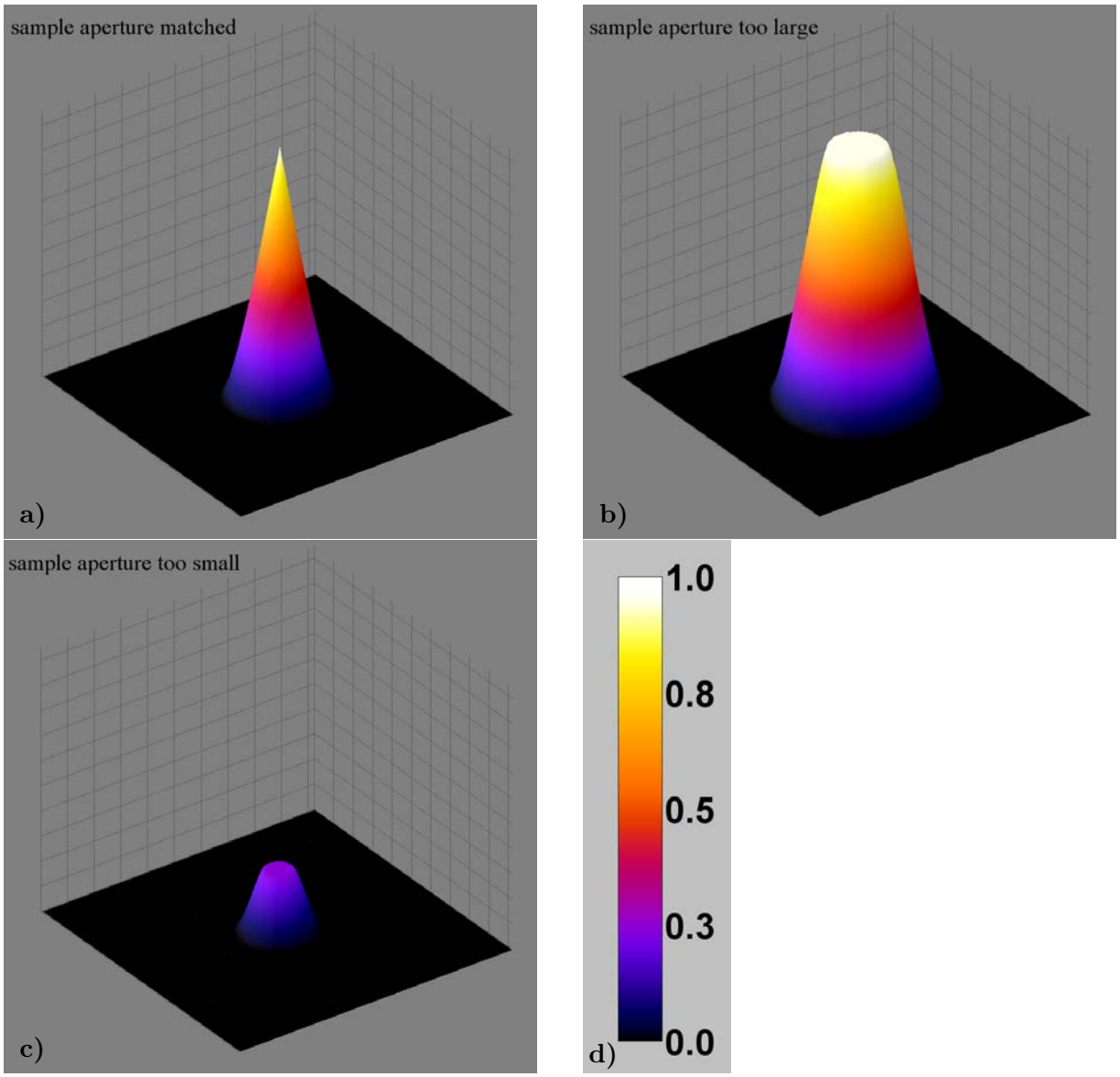

Fig. 2.9: Surface plots of calculated intensity profiles a) corresponding to two circular apertures, whose diameters and distances to the detector plane are matched, b) in case the diameter of the sample aperture is twice as large as in the matched case and c) in case the diameter of the sample aperture is half of the ideal diameter. d) The calibration bar shows the applied color scheme for the intensities normalized to the source aperture.

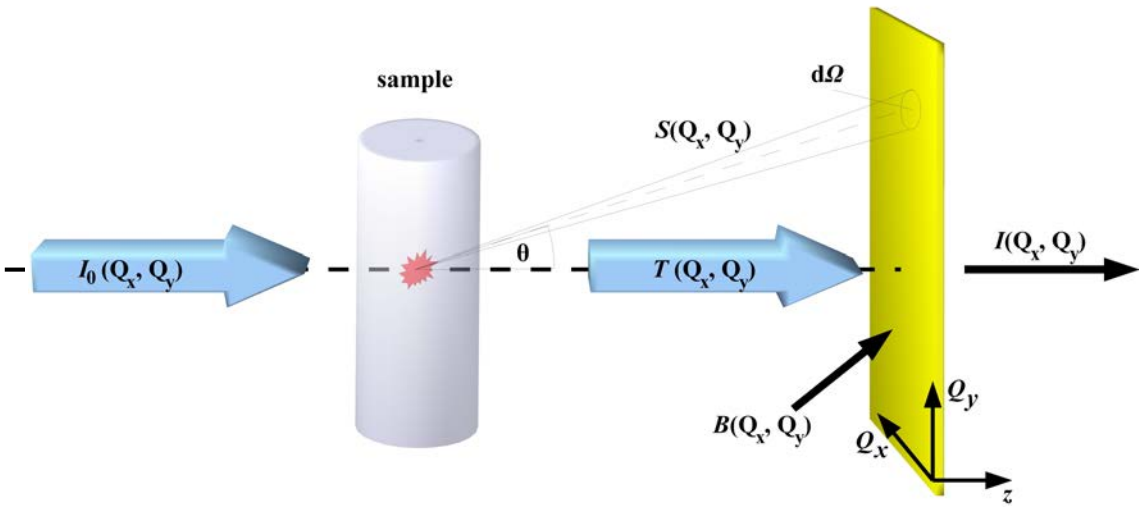

Fig. 2.10: The intensity at the detector is composed of transmitted neutrons $T(Q_\mathrm{x}, Q_\mathrm{y})$, scattered neutrons $S(Q_\mathrm{x}, Q_\mathrm{y})$ and background $B(Q_\mathrm{x}, Q_\mathrm{y})$.

Here only two dimensions of $\mathbf{Q}$ can be resolved by the detector, namely Q_x and Q_y. Therefore

$$\mathbf{Q} \approx (Q_\mathrm{x}, Q_\mathrm{y}, 0) \,. \tag{2.51}$$

Thus the scattered intensity distribution does not contain information about changes of the scattering length density in beam direction z.
Introducing the pair correlation function $\gamma(\mathbf{r})$ [11, p. 50]

$$\gamma(\mathbf{r}) = \frac{1}{V} \int_V \rho(\mathbf{r}') \, \rho(\mathbf{r} + \mathbf{r}') \, \mathrm{d}\mathbf{r} \tag{2.52}$$

equation (2.50) can be rewritten to [11, p. 51]

$$\tilde{S}(\mathbf{Q}) = \int_V \gamma(\mathbf{r}) \, \mathrm{e}^{-\mathrm{i}\,\mathbf{Q}\cdot\mathbf{r}} \, \mathrm{d}\mathbf{r} \tag{2.53}$$

which is the Fourier transform of the spatial correlation of the coherent scattering length density. With help of the local fluctuation $\Gamma(\mathbf{r})$ of the scattering length density $\rho(\mathbf{r})$ given by [11, p. 51]

$$\Gamma(\mathbf{r}) = \rho(\mathbf{r}) - \langle \rho \rangle \tag{2.54}$$

and [11, p. 51]

$$\langle \Gamma^2 \rangle = \langle \rho^2 \rangle - \langle \rho \rangle^2 \tag{2.55}$$

it is possible to define a dimensionless correlation function $\gamma_0(\mathbf{r})$ [11, p. 51]

$$\langle \Gamma^2 \rangle \, \gamma_0(\mathbf{r}) = \frac{1}{V} \int_V \Gamma(\mathbf{r}') \, \Gamma(\mathbf{r} + \mathbf{r}') \, \mathrm{d}\mathbf{r}' \,. \tag{2.56}$$

Thus $\gamma(\mathbf{r})$ can be expressed by [11, p. 51]

$$\gamma(\mathbf{r}) = \langle \Gamma^2 \rangle \, \gamma_0(\mathbf{r}) + \langle \rho \rangle^2 \,. \tag{2.57}$$

Inserting this into equation (2.53) yields the scattered intensity

$$\tilde{S}(\mathbf{Q}) = \langle \Gamma^2 \rangle \int \gamma_0(\mathbf{r}) \, \mathrm{e}^{-\mathrm{i}\,\mathbf{Q}\cdot\mathbf{r}} \, \mathrm{d}\mathbf{r} + \langle \rho \rangle^2 \, \delta(\mathbf{Q}) \,. \tag{2.58}$$

The term $\langle\rho\rangle^2\,\delta(\mathbf{Q})$ corresponds to forward scattering at $\mathbf{Q} = \mathbf{0}$ proportional to the square of the average coherent scattering length density and does not contain information about the structure of the sample.[20] The resulting signal at the detector is included in the transmitted intensity $T(Q_\mathrm{x}, Q_\mathrm{y})$.[21] The remaining part of $\tilde{S}(\mathbf{Q})$ contains information about the structure of the sample [11, p. 51]. A multiplication with the sample volume V_s the neutrons pass through results in the scattering function

$$\hat{S}_\mathrm{coh}(Q_\mathrm{x}, Q_\mathrm{y}) = \hat{S}_\mathrm{coh}(Q_\mathrm{x}, Q_\mathrm{y}, 0) = \hat{S}_\mathrm{coh}(\mathbf{Q}) = V_\mathrm{s}\,\langle\Gamma^2\rangle \int \gamma_0(\mathbf{r})\,\mathrm{e}^{-\mathrm{i}\,\mathbf{Q}\cdot\mathbf{r}}\,\mathrm{d}\mathbf{r}\,. \tag{2.59}$$

The scattered signal $S(Q_\mathrm{x}, Q_\mathrm{y})$ is then given by a convolution of the incident neutron intensity $I_0(Q_\mathrm{x}, Q_\mathrm{y})$ and the scattering function $\hat{S}_\mathrm{coh}(Q_\mathrm{x}, Q_\mathrm{y})$ including a correction for the sample transmission.

$$S(Q_\mathrm{x}, Q_\mathrm{y}) = \int\int I_0(Q_\mathrm{x} - U, Q_\mathrm{y} - V) \cdot \exp\left(-\int_{C_\mathrm{S}} \Sigma_\mathrm{t}(Q_\mathrm{x}, Q_\mathrm{y}, s)\,\mathrm{d}s\right) \cdot \hat{S}_\mathrm{coh}(U, V)\,\mathrm{d}U\,\mathrm{d}V \tag{2.60}$$

This is simplified using equations (2.47) and (2.49)

$$S(Q_\mathrm{x}, Q_\mathrm{y}) = \hat{T}_0 \int\int I_0(Q_\mathrm{x} - U, Q_\mathrm{y} - V)\,\hat{S}_\mathrm{coh}(U, V)\,\mathrm{d}U\mathrm{d}V\,. \tag{2.61}$$

Data Evaluation When using a multiple beam SANS or USANS geometry, the data evaluation is not straight forward just using standard evaluation software. On the one hand a multiple number of scattering patterns have to be evaluated at the same time or summed up to get a single pattern for evaluation. On the other hand the transmitted primary beam is measured in parallel to the scattered signal, because no beam stop is used.[22] This offers a possibility to evaluate a even larger Q-range, as the scattered signal is recorded down to $\mathbf{Q} = \mathbf{0}$. Thus the Q-range is limited rather by the resolution of the detector than the size of the beam stop. In the following two different ways to evaluate the acquired data are explained. One of them is in analogy to a standard pinhole SANS evaluation like the one given in [11, p. 29]. This kind of data reduction is used to extract information from regions where the scattered signal has no overlap with the transmitted primary beam. This is due to the reason that forward scattering is not taken into account. Coherent scattering at $\mathbf{Q} = \mathbf{0}$ is treated to be zero, as the measured intensity at $\mathbf{Q} = \mathbf{0}$ is used to determine the transmission of the sample [11, p. 29]. All profiles of the multiple scattering patterns are summed up and standard processing routines are used for further evaluation (App. A.12.1). Another way to evaluate the data is based on the Guinier or Zimm approximation[23] and a convolution of the primary beam profile and the scattering function $\hat{S}(Q_\mathrm{x}, Q_\mathrm{y})$. Here functions corresponding to the multiple beam geometry are fitted to the primary intensity profile and the intensity profile measured with the sample. No prior corrections are applied to the data. This evaluation enables to evaluate data close to $\mathbf{Q} = \mathbf{0}$ even if there is an overlap of the scattered intensity and the transmitted primary beam (Sec. 5.4). In that case information about the particle size of the sample is extracted by determination of the radius of gyration [12, p. 10].

i) Standard Data Evaluation

The terminology of the standard data reduction is kept close to the one given in [11, p. 23ff]. It is slightly adapted to handle the special geometry of the multi aperture setup and differences of the data taken by an integrating imaging detector instead of an position sensitive neutron counting

[20] It does not show an angular dependency.

[21] Due to this forward scattering the attenuation caused by the sample is underestimated.

[22] The integrating Charge-coupled Device (CCD) detector is able to record the transmitted primary beam without the need to use any attenuators.

[23] When $Q\,R \leq 1$, R being the radius of gyration of the investigated particles, the Guinier approximation or the Zimm approximation is often applied for the scattering function. Both approximations have their maximum at $Q = 0$, as they are given by a Gaussian or a Lorenz curve centered at $Q = 0$ [12, p. 11].

notation Lindner et al.[11]	description
$I^{\mathrm{m}}_{\mathrm{SB}}$	measured intensity from sample container
I_{SB}	scattered intensity from sample container
$\hat{T}_{\mathrm{SB}}$	transmission of sample container
I_{Cd}	hall background
$I^{\mathrm{m}}_{\mathrm{S+SB}}$	measured intensity of sample and sample container
I_{S}	scattered intensity from sample
$\hat{T}_{\mathrm{S}}$	transmission of sample
I_0	intensity of incident neutron beam

Table 2.1: The terminology of the parameters to describe the measured intensity at the detector. It is kept as close as possible to [11, p. 23ff].

detector. An explicit dependency of the intensities on Q_{x} and Q_{y} is omitted here to simplify the formula. An index m is used to mark measured values. A definition of the single terms is given in table 2.1. For real samples often the scattering caused by the sample container has to be taken into account. It is described by the scattering signal I_{SB} of the sample background. The measured intensity with only a sample container or a solvent in the neutron beam is given by

$$I^{\mathrm{m}}_{\mathrm{SB}} = \underbrace{\hat{T}_{\mathrm{SB}} \cdot I_{\mathrm{SB}}}_{S_{\mathrm{SB}}(Q_{\mathrm{x}},Q_{\mathrm{y}})} + \underbrace{I_{\mathrm{Cd}}}_{B(Q_{\mathrm{x}},Q_{\mathrm{y}})} + \underbrace{\hat{T}_{\mathrm{SB}} \cdot I_0}_{T_{\mathrm{SB}}(Q_{\mathrm{x}},Q_{\mathrm{y}})} \,. \tag{2.62}$$

It is measured using an empty sample container or sample container filled with solvent. The measured intensity $I^{\mathrm{m}}_{\mathrm{S+SB}}$ is a combination of the signal due to the sample and due to the sample container.

$$I^{\mathrm{m}}_{\mathrm{S+SB}} = \underbrace{\hat{T}_{\mathrm{S}} \cdot \hat{T}_{\mathrm{SB}} \cdot I_{\mathrm{S}} + \hat{T}_{\mathrm{S}} \cdot \hat{T}_{\mathrm{SB}} \cdot I_{\mathrm{SB}}}_{S_{\mathrm{S+SB}}(Q_{\mathrm{x}},Q_{\mathrm{y}})} + \underbrace{I_{\mathrm{Cd}}}_{B(Q_{\mathrm{x}},Q_{\mathrm{y}})} + \underbrace{\hat{T}_{\mathrm{S}} \cdot \hat{T}_{\mathrm{SB}} \cdot I_0}_{T_{\mathrm{S+SB}}(Q_{\mathrm{x}},Q_{\mathrm{y}})} \tag{2.63}$$

The transmission of the sample container is calculated from intensity values for $\mathbf{Q}$=0 using equation (2.62)

$$\hat{T}_{\mathrm{SB}} = \frac{I^{\mathrm{m}}_{\mathrm{SB}}(\mathbf{Q}=0) - I^{\mathrm{m}}_{\mathrm{Cd}}(\mathbf{Q}=0)}{I^{\mathrm{m}}_{0}(\mathbf{Q}=0) - I^{\mathrm{m}}_{\mathrm{Cd}}(\mathbf{Q}=0)} \,. \tag{2.64}$$

This is possible, as it is assumed that there is no scattering signal for $\mathbf{Q} = 0$ [11, p. 29], which is not valid for all samples. It only holds if forward scattering can be assumed to be negligible compared to the transmitted intensity.[24] In analogy the transmission through the sample and the sample container follows from equation (2.63)

$$\hat{T}_{\mathrm{S}} \cdot \hat{T}_{\mathrm{SB}} = \frac{I^{\mathrm{m}}_{\mathrm{S+SB}}(\mathbf{Q}=0) - I^{\mathrm{m}}_{\mathrm{Cd}}(\mathbf{Q}=0)}{I^{\mathrm{m}}_{0}(\mathbf{Q}=0) - I^{\mathrm{m}}_{\mathrm{Cd}}(\mathbf{Q}=0)} \tag{2.65}$$

The intensity scattered by the sample I_{S}, equal to $S_{\mathrm{S}}(Q_{\mathrm{x}}, Q_{\mathrm{y}})$, is then given by (App. A.12.2)

$$S_{\mathrm{S}}(Q_{\mathrm{x}}, Q_{\mathrm{y}}) = I_{\mathrm{S}} = \frac{I^{\mathrm{m}}_{\mathrm{S+SB}} - I_{\mathrm{Cd}}}{\hat{T}_{\mathrm{S}}\, \hat{T}_{\mathrm{SB}}} - \frac{I^{\mathrm{m}}_{\mathrm{SB}} - I_{\mathrm{Cd}}}{\hat{T}_{\mathrm{SB}}} \,. \tag{2.66}$$

Including the transmission values $\hat{T}_{\mathrm{S}}$ and $\hat{T}_{\mathrm{SB}}$ from equations (2.65) and (2.64) $S_{\mathrm{S}}(\mathbf{Q})$ is given by

$$S_{\mathrm{S}}(\mathbf{Q}) = \left(I^{\mathrm{m}}_{\mathrm{S+SB}} - I^{\mathrm{m}}_{\mathrm{Cd}}\right) \cdot \frac{I^{\mathrm{m}}_{0}(\mathbf{Q}=0) - I^{\mathrm{m}}_{\mathrm{Cd}}(\mathbf{Q}=0)}{I^{\mathrm{m}}_{\mathrm{S+SB}}(\mathbf{Q}=0) - I^{\mathrm{m}}_{\mathrm{Cd}}(\mathbf{Q}=0)} - \left(I^{\mathrm{m}}_{\mathrm{SB}} - I^{\mathrm{m}}_{\mathrm{Cd}}\right) \cdot \frac{I^{\mathrm{m}}_{0}(\mathbf{Q}=0) - I^{\mathrm{m}}_{\mathrm{Cd}}(\mathbf{Q}=0)}{I^{\mathrm{m}}_{\mathrm{SB}}(\mathbf{Q}=0) - I^{\mathrm{m}}_{\mathrm{Cd}}(\mathbf{Q}=0)} \,.$$

[24] This is in analogy to neutron radiography, where scattering corrections are omitted most of the time assuming that the scattered intensity reaching the detector is much less than the transmitted intensity.

(2.67)

The scattered intensity distribution $S_{\mathrm{S}}(\mathbf{Q})$ of the sample is now derived from measured quantities only.

ii) Data Evaluation using the Guinier Approximation

For compact particles approximated by spheres or cylinders with large radii it is possible to describe the scattering function by a Gaussian [12, p. 11]

$$\hat{S}_{\mathrm{coh}}(Q_{\mathrm{x}}, Q_{\mathrm{y}}) \propto \mathrm{e}^{\left(-\frac{\left(Q_{\mathrm{x}}^2+Q_{\mathrm{y}}^2\right) R_{\mathrm{G}}^2}{3}\right)} . \tag{2.68}$$

It is possible to do so inside the so-called Guinier range where $Q\,R_{\mathrm{G}} \leq 1$ is fulfilled with R_{G} being the radius of gyration given by

$$R_{\mathrm{G}}^2 = \frac{1}{\mathrm{N}} \sum_{\mathrm{i}=1}^{\mathrm{N}} \langle \mathbf{r}_{\mathrm{i}}^2 \rangle \,; \quad \sum_{\mathrm{i}} \mathbf{r}_{\mathrm{i}} = 0 \,. \tag{2.69}$$

According to equation (2.61) the scattered signal at the detector is a convolution of the primary intensity $I_0(Q_{\mathrm{x}}, Q_{\mathrm{y}})$ and the scattering function $\hat{S}_{\mathrm{coh}}(Q_{\mathrm{x}}, Q_{\mathrm{y}})$. If the intensity profile of the incident neutron beam is now described by a Gaussian[25], too, the scattered signal $S(Q_{\mathrm{x}}, Q_{\mathrm{y}})$ at the detector is again a Gaussian

$$\begin{aligned}
S(Q_{\mathrm{x}}, Q_{\mathrm{y}}) &= \hat{T}_0 \int\int I_0(Q_{\mathrm{x}} - U, Q_{\mathrm{y}} - V)\, \hat{S}_{\mathrm{coh}}(U, V)\, \mathrm{d}U \mathrm{d}V && (2.70)\\
&= \hat{T}_0 \int\int A_1\, \mathrm{e}^{\left(-\frac{(Q_{\mathrm{x}}-U)^2}{2\,\sigma_{\mathrm{x}}^2}\right)} \mathrm{e}^{\left(-\frac{(Q_{\mathrm{y}}-V)^2}{2\,\sigma_{\mathrm{y}}^2}\right)} A_2\, \mathrm{e}^{\left(-\frac{\left(U^2+V^2\right) R_{\mathrm{G}}^2}{3}\right)} \mathrm{d}U \mathrm{d}V && (2.71)\\
&= \hat{T}_0\, A_1\, A_2\, \mathrm{e}^{\left(-\frac{Q_{\mathrm{x}}^2}{2\,(\sigma_{\mathrm{x}}^2+\frac{3}{2\,R_{\mathrm{G}}^2})}\right)} \mathrm{e}^{\left(-\frac{Q_{\mathrm{y}}^2}{2\,(\sigma_{\mathrm{y}}^2+\frac{3}{2\,R_{\mathrm{G}}^2})}\right)} && (2.72)\\
&= \hat{T}_0\, A_{\mathrm{tot}}\, \mathrm{e}^{\left(-\frac{Q_{\mathrm{x}}^2}{2\,\sigma_{\mathrm{tot,x}}^2}\right)} \mathrm{e}^{\left(-\frac{Q_{\mathrm{y}}^2}{2\,\sigma_{\mathrm{tot,y}}^2}\right)} . && (2.73)
\end{aligned}$$

The neutrons transmitted through the sample and the neutrons scattered by the sample now generate a signal at the detector that is described by the sum of two Gaussians

$$I(Q) = \hat{T}_0\, I_0(Q) + S(Q) = \hat{T}_0\, A_1\, \mathrm{e}^{\left(-\frac{Q_{\mathrm{x}}^2}{2\,\sigma_{\mathrm{x}}^2}\right)} \mathrm{e}^{\left(-\frac{Q_{\mathrm{y}}^2}{2\,\sigma_{\mathrm{y}}^2}\right)} + \hat{T}_0\, A_{\mathrm{tot}}\, \mathrm{e}^{\left(-\frac{Q_{\mathrm{x}}^2}{2\,\sigma_{\mathrm{tot,x}}^2}\right)} \mathrm{e}^{\left(-\frac{Q_{\mathrm{y}}^2}{2\,\sigma_{\mathrm{tot,y}}^2}\right)} . \tag{2.74}$$

The parameters A_1, σ_x and σ_y are determined by fitting $I_0(Q_{\mathrm{x}}, Q_{\mathrm{y}})$ to the intensity profile of the incident neutron beam. Thus only the parameters $\hat{T}_0$, A_{tot}, $\sigma_{\mathrm{tot,x}}$ and $\sigma_{\mathrm{tot,y}}$ are to be fitted when evaluating the signal measured with a sample inside the neutron beam. The radius of gyration R_{G} can then be extracted from the fitted parameters. From equations (2.72) and (2.73) one gets the identities

$$\begin{aligned}
\sigma_{\mathrm{tot,x}}^2 &= \sigma_{\mathrm{x}}^2 + \frac{3}{2\,R_{\mathrm{G}}^2} && (2.75)\\
\sigma_{\mathrm{tot,y}}^2 &= \sigma_{\mathrm{y}}^2 + \frac{3}{2\,R_{\mathrm{G}}^2} \,. && (2.76)
\end{aligned}$$

[25] The primary intensity may also be described by a Gaussian, especially in case the sample aperture is replaced by a lens of lens array (section 5.4.2).

geometrical shape	radius of gyration R_G
sphere (radius R)	$\frac{3}{5}R$
hollow sphere (radii R_1 and R_2)	$\frac{3}{5}\frac{R_2^5-R_1^5}{R_2^3-R_1^3}$
ellipsoid (semi-axes a, b, c)	$\frac{a^2+b^2+c^2}{5}$
parallelepiped (edge lengths A, B, C)	$\frac{A^2+B^2+C^2}{12}$
elliptic cylinder (semi-axes a, b; height h)	$\frac{a^2+b^2}{4}+\frac{h^2}{12}$
hollow cylinder (radii R_1 and R_2)	$\frac{R_2^2+R_1^2}{2}+\frac{h^2}{12}$

Table 2.2: Some geometric models used to approximate particle shapes and the resulting radius of gyration [10, p. 2.1-5].

This is solved for the radius of gyration to get

$$R_\mathrm{G} = \sqrt{\frac{3}{2\left(\sigma_{\mathrm{tot,x}}^2-\sigma_\mathrm{x}^2\right)}} \tag{2.77}$$

or

$$R_\mathrm{G} = \sqrt{\frac{3}{2\left(\sigma_{\mathrm{tot,y}}^2-\sigma_\mathrm{y}^2\right)}}\,. \tag{2.78}$$

Without any preferred orientation equations (2.77) and (2.78) should give the same value for the radius of gyration R. Depending on the shape of the investigated particles the radius of gyration is a known function of their dimensions. Some examples taken form [10, p. 2.1-5] are listed in table 2.2.

2.2.3 Multiple Beam Small Angle Neutron Scattering

Extending the Q-range of an SANS instrument to smaller Q-values is equivalent to measuring smaller scattering angles. Investigations of Q-values in the range of $10^{-4}\,\text{Å}^{-1}$ to $10^{-6}\,\text{Å}^{-1}$ is called Ultra Small Angle Neutron Scattering (USANS). To reach this Q-range at a standard pinhole SANS instrument without an overlap of the primary beam and the scattered intensity the instrument resolution has to be improved. This means either to increase the distance between the sample and the detector or to use a higher collimation of the primary beam by reducing the size of the source and the sample aperture. Both measures diminish the count rate at the detector due to the reduced neutron flux at the sample position or the detector. If a tighter collimation is chosen, the spatial resolution of the detector has to be increased at the same time. A further increase of the sample to detector distance is often not possible or practicable, as standard SANS instruments already extend to a length of 60 m to 80 m including the collimation [13]. In order to reach the Q-range for USANS by an improved collimation keeping the standard configuration of single circular apertures would afford to reduce the diameter of the source aperture by at least a factor of 10 [14]. According to equation (2.45) the sample aperture has to be reduced by the same factor to maintain an optimum peak shape at the detector plain. Without this optimum peak shape it is not possible to increase the instrument resolution. But reducing both, the source and the sample aperture, at the same time would cause the neutron flux to drop by a factor of 10000. This would of course result in incredible long acquisition times. A "simple" way to overcome this is to use a multiplicity of small source and sample apertures, which in turn give a large number of primary beams and their corresponding scattered intensity profiles [15], [16]. The basic principle of such a configuration is explained in the upcoming paragraphs. Here the option to use neutron lenses as sample aperture and a limitation of the maximum Q-value are covered as well.

Multiple Beam Geometry The use of a multiple beam SANS setup in order to compensate for the lower primary intensity was proposed by Roland Gähler. It offers many small neutron beams

of low divergence at the sample position. Those small neutron beams result from a multiple source aperture array and a multi sample aperture array. The beam geometry of a one-dimensional multi aperture layout is show in figure 2.11. The primary intensity distribution at the detector is again given by the correlation of the opening functions of the source array and the sample array. The size

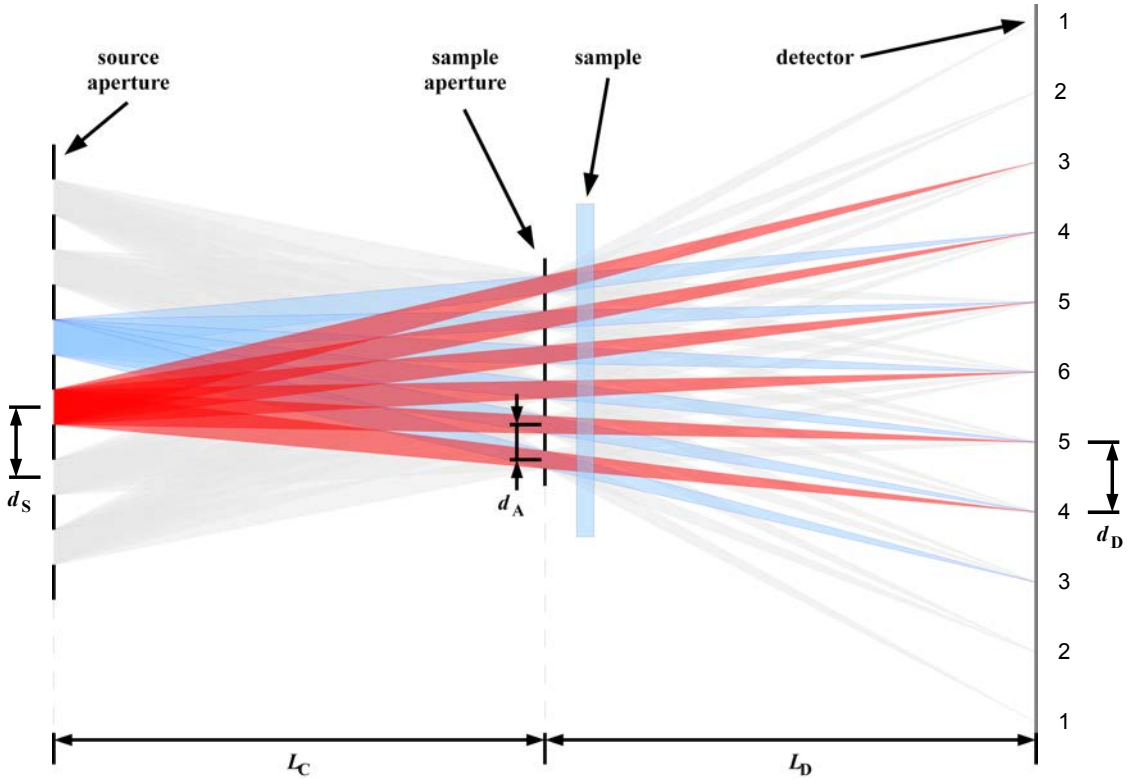

Fig. 2.11: The beam geometry of a multiple beam SANS instrument is defined by the center to center distances of the source apertures d_S and the sample apertures d_A, the length of the collimation setup L_C and the distance L_D from the sample aperture to the detector. The number of single beams that contribute to each peak at the detector for the illustrated one-dimensional case is denoted by the numbers on the right.

of the apertures is chosen to meet equation (2.45). That way each single neutron beam results in an optimized peak shape at the detector plane. A superposition of the single peaks at the detector plane is obtained if the center to center distances d_S and d_A of the source and the sample apertures fulfill the condition for a centric elongation

$$\frac{d_A}{d_S} = \frac{L_D}{L_D + L_C} \text{ [15].} \tag{2.79}$$

The number of peaks that are superimposed at the detector that way is assigned by a number on the right hand side of figure 2.11. The spacing d_D of the peaks at the detector is again given by a centric elongation

$$d_D = d_A \frac{L_C + L_D}{L_C} . \tag{2.80}$$

The total number of neutron beams for a source aperture array with m holes and a sample aperture array with n holes is $m \cdot n$. To compensate a loss of the neutron flux by a factor of 10000 due to the smaller diameter[26] of the single apertures the source aperture array and the sample aperture array must have 100 holes each. As a certain center to center distance of the resulting primary beams on the detector (eqn. (2.80))is needed to separated the primary beam from the scattered intensity and to avoid an overlap of the scattered intensities resulting from two different primary beams. This restricts the transmission area of the source and the sample aperture array if they must not be larger than standard apertures.

[26]The diameter is reduced ba a factor of 10.

Lens Array as Sample Aperture In order to further increase the intensity at the sample position Roland Gähler suggested to replace the sample aperture array by an array of neutron lenses. Lenses offer a larger transmission area than small apertures. If the neutron lenses fulfill the imaging equation (A.28)

$$\frac{1}{f} = \frac{1}{L_\mathrm{C}} + \frac{1}{L_\mathrm{D}} \tag{2.81}$$

and map the source aperture array to the detector, they act like nearly perfect pinhole apertures on the one hand. On the other hand the transfered intensity through a lens is comparable to the intensity, which is transmitted by a standard aperture whose diameter is equal to the diameter of the lens (Fig. 2.12). There is only a small loss of intensity owing to the reduced neutron transmission

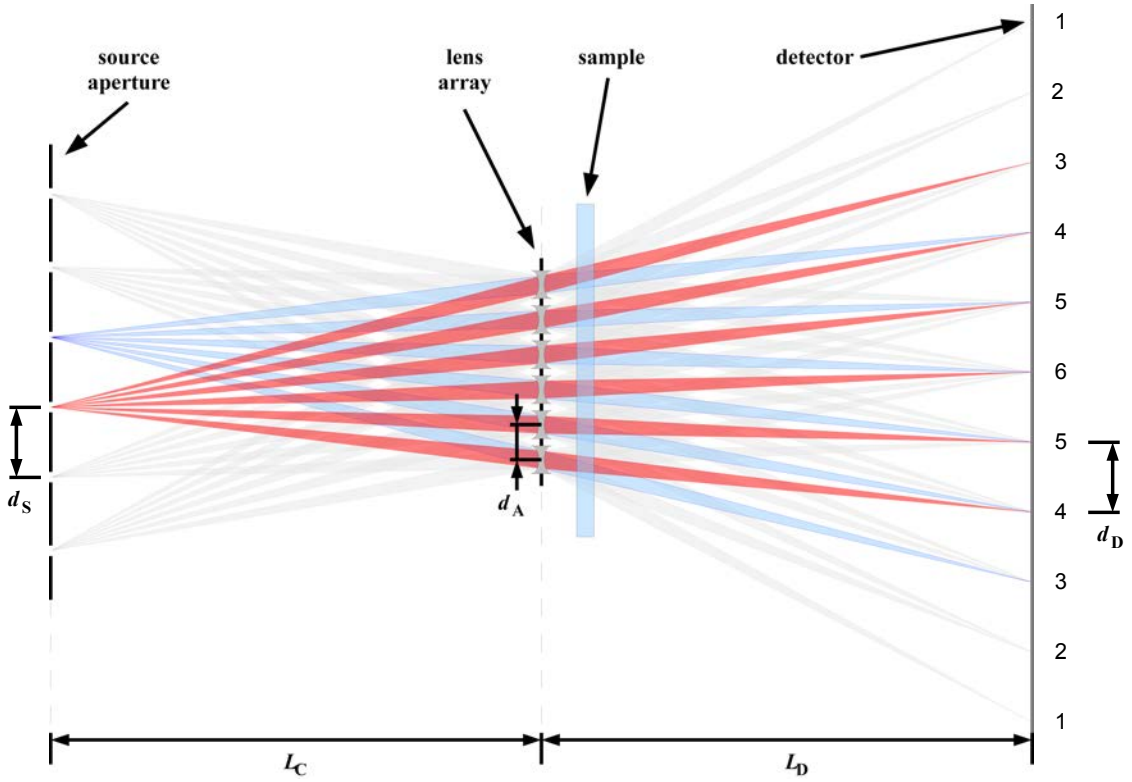

Fig. 2.12: The beam geometry of for USANS measurements employing a lens array as sample aperture is similar to the one for an array of normal apertures (Fig. 2.11). The diameter of the lenses defines the transmission area of the lens array, while the refraction of neutrons due to the curvature of the lenses lets them act like nearly perfect pinholes.

through the lens material.[27] A chromatic aberration has to be taken into account due to the wavelength spread of $\frac{\Delta\lambda}{\lambda}$. Thus the peak size w_p at the detector of each of the multiple neutron beams is the size of the source aperture w scaled to the the detector plane plus a blurring Δw caused by the chromatic aberration (App. A.9). Thus the peak size w_p of a single peak at the detector is given by

$$w_\mathrm{p} = \sqrt{(\alpha\, w)^2 + (\Delta w)^2}\ [15]. \tag{2.82}$$

Here α is the appropriate scaling factor that takes into account the imaging of the source aperture onto the detector plane by the lens array at the sample position. The focal length f of a thin, spherical lens is given by

$$\frac{1}{f} = (n_\mathrm{l} - 1)\left(\frac{1}{R_1} - \frac{1}{R_2}\right). \tag{2.83}$$

[27] Depending on the material used for the neutron lenses they may cause an additional signal of scattered neutrons.

Here n_l is the index of refraction of the lens and R_1 and R_2 are the radii of curvature for the object side and image side of the lens [17, p. 138]. For neutrons n_l is given by the real part of the complex index of refraction

$$n_\mathrm{l} = \sqrt{1 - \frac{\eta\,\bar{b}\,\lambda^2}{\pi}} \approx 1 - \frac{\eta\,\bar{b}\,\lambda^2}{2\,\pi} \tag{2.84}$$

with the particle density η, the average coherent scattering length $\bar{b}$ and the neutron wavelength λ [18, p. 64]. For neutrons $n_\mathrm{l} < 1$ for all materials. Therefore a focusing lens for neutrons will have radii R_1 and R_2 with $R_1 < 0$ and $R_2 > 0$ corresponding to a concave or biconcave shape of the lens. If the neutron lens is symmetric and $R_1 = -R_2 = -R$, combining equations (2.83) and (2.84) leads to

$$\frac{1}{f} = \frac{\eta\,\bar{b}\,\lambda^2}{2\,\pi} \cdot \frac{2}{R} \tag{2.85}$$

Thus the focal length of the neutron lens is

$$f = \frac{\pi\,R}{\eta\,\bar{b}\,\lambda^2}\,. \tag{2.86}$$

Limitation in Q-range Due to the special geometrical arrangement of the apertures for USANS there is a limitation of the maximum Q-value, which can be detected without an overlap of the scattering signals. An overlap of two scattering signals occurs as soon as neutrons scattered to "positive" and "negative" Q-direction of two neighboring beams meet right in the middle. Thus the largest detectable Q-value Q_max is defined by half of the distance d_D between the maxima of the primary intensity and equation (2.35)

$$Q_\mathrm{max} = k\,\frac{\frac{1}{2}\,d_\mathrm{D}}{L_\mathrm{D}} \quad \text{or} \quad Q_\mathrm{max} = \frac{\pi\,d_\mathrm{D}}{\lambda\,L_\mathrm{D}}\,. \tag{2.87}$$

This means there is a minimum detectable particle size for a given wavelength.

SANS or USANS setups using multiple beam geometries like the ones described above produce intensity patterns of a total size, which is often less than 10 cm × 10 cm. Thus it is not possible to resolve the multiple peaks inside the patterns with standard SANS detectors offering only up to about 512 pixels for a length scale of 1 meter, corresponding to a resolution of several millimeters.
Standard neutron imaging detectors on the other hand easily offer the required spatial resolution of about 100 μm. Most of them are operated in an integrating detection mode, which enables to record the transmitted primary beam intensity along with the scattered signal. It is not necessary to place a beam stop blocking the primary beam, because (most) imaging detectors are capable to acquire images even at high neutron flux densities.[28]

[28] usually $10^6\ \frac{\mathrm{n}}{\mathrm{cm^2\,s}}$ to $10^{10}\ \frac{\mathrm{n}}{\mathrm{cm^2\,s}}$

Chapter 3

Neutron Imaging Detectors

Neutrons incident on any detection device may not be converted to an electronic signal directly, as they are uncharged particles. Hence it is necessary to make use of a nuclear detection reaction and at least one further conversion of the reaction products before an electronic or digital signal is available.[1] Neutron detectors can therefore be modeled as a cascade of single conversion steps. Some of the most common detection reactions for thermal and cold neutrons are listed in section 3.1. In section 3.2 concepts to describe cascaded neutron imaging detectors are introduced, namely the Detection Quantum Efficiency (DQE) and the Quantum Accounting Diagram (QAD). The focus of section 3.3 is put on neutron scintillation screens, which are optically coupled to digital imaging sensors. This kind of detectors is the most common one in the field of neutron radiography and tomography nowadays. Therefore this section is the most detailed section of this chapter. The detector described in section 3.4 uses a Multi Channel Plate (MCP) made of borated glass[2] to detect neutrons. A chevron stack of conventional multi channel plate (MCP)s is applied to amplify the generated electron signal. The readout stage is based on a Complementary Metal Oxid Semiconductor (CMOS) pixel sensor called Medipix.[3] Other types of neutron detectors have not been considered for this work. For example ^{3}He based detectors do not reach the required spatial resolution and they are often not capable to be operated at a neutron flux of more than $10^6 \frac{\mathrm{n}}{\mathrm{cm}^2\,\mathrm{s}}$, which is essential for dynamic measurements. A short summary is added at the end of the chapter.

3.1 Neutron detection

The weak interaction of neutrons with matter makes them hard to be detected. Neutrons do not have an ionizing power to directly generate an electric charge signal. But such a signal is necessary at some stage of the detection process to gain an electronic representation of the neutron signal. As there is no way for a direct detection of neutrons, a reaction resulting in ionizing secondary particles is required. Cold and thermal neutrons with energies $< 100\,\mathrm{meV}$ are detected by nuclear capture reactions.Isotopes with a large absorption cross section allow for an efficient conversion. It is obvious that this primary neutron conversion sets an upper limit to the overall detector performance (Sec. 3.2). Therefore the aim is to use isotopes having a high neutron conversion efficiency, which is equivalent to a large neutron absorption cross section. In figure 3.1 the absorption cross sections of isotopes commonly applied for position sensitive detectors are shown. Note the decrease of the neutron absorption cross section with increasing kinetic energy E of the neutrons. It follows a $\frac{1}{v}$-law in the cold and thermal energy range [18]. The corresponding detection reactions are [10,

[1] This is true for thermal and cold neutrons, while fast neutrons may as well be detected via recoil protons without any nuclear reaction being involved.

[2] The glass is doped with ^{10}B.

[3] `http://medipix.web.cern.ch/medipix/`

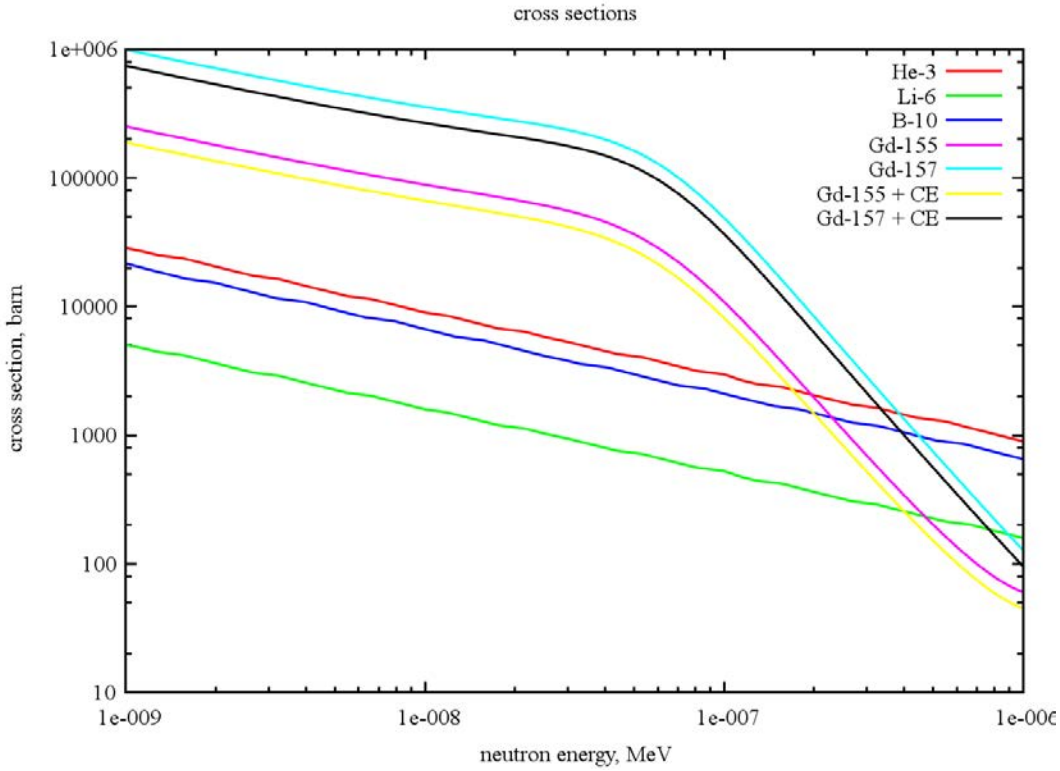

Fig. 3.1: Neutron absorption cross sections of isotopes commonly used for position sensitive detectors. For $^{155}_{64}$Gd and $^{157}_{64}$Gd the pure neutron absorption cross section as well as the effective absorption efficiency corrected for the branching ratio of the emission of a conversion electron are plotted.

p. 3.3-1], [19], [20], [21]:

$$^{3}_{2}\mathrm{He} + ^{1}_{0}\mathrm{n} \longrightarrow ^{3}_{1}\mathrm{H} + ^{1}_{1}\mathrm{H} + 0.77\,\mathrm{MeV} \tag{3.1}$$

$$^{6}_{3}\mathrm{Li} + ^{1}_{0}\mathrm{n} \longrightarrow ^{4}_{2}\mathrm{He} + ^{3}_{1}\mathrm{H} + 4.79\,\mathrm{MeV} \tag{3.2}$$

$$^{10}_{5}\mathrm{B} + ^{1}_{0}\mathrm{n} \longrightarrow \begin{cases} ^{4}_{2}\mathrm{He} + ^{7}_{3}\mathrm{Li} + 2.3\,\mathrm{MeV} + \gamma(0.48\,\mathrm{MeV}) & 93\% \\ ^{4}_{2}\mathrm{He} + ^{7}_{3}\mathrm{Li} + 2.8\,\mathrm{MeV} & 7\% \end{cases} \tag{3.3}$$

$$^{155}_{64}\mathrm{Gd} + ^{1}_{0}\mathrm{n} \longrightarrow ^{156}_{64}\mathrm{Gd}^{*} \longrightarrow ^{156}_{64}\mathrm{Gd} + \gamma + \mathrm{CE} + 39 - 199\,\mathrm{keV} \tag{3.4}$$

$$^{157}_{64}\mathrm{Gd} + ^{1}_{0}\mathrm{n} \longrightarrow ^{158}_{64}\mathrm{Gd}^{*} \longrightarrow ^{158}_{64}\mathrm{Gd} + \gamma + \mathrm{CE} + 29 - 182\,\mathrm{keV}\,. \tag{3.5}$$

CE denotes conversion electrons. Further detection reactions can be found in [19] or [21] for example. The use of $^{3}_{2}$He is common for neutron counting detectors, e.g. multi wire chambers. But such detectors are not used for neutron imaging, as they usually do not yield the desired spatial resolution. Most standard neutron imaging detectors for neutron radiography and tomography employ scintillation screens with phosphor materials like ^{6}LiF/ZnS and Gd_2O_2S. Formerly those materials have served as converters for film radiography. Today the emitted scintillation light is collected by an imaging sensor (Sec. 3.3). The detection reaction of gadolinium is special among the reactions listed above, as the secondary particles that allow for the actual signal detection are electrons instead of the much heavier ions generated by the other reactions. The average energy of these electrons is in the range of 100 keV and much lower than the kinetic energy of the particles produced by other detection reactions. This is reflected by the light output of Gd_2O_2S scintillation screens. The number of emitted photons per detected neutron of a gadolinium based phosphors is less than that of scintillators based on other detection reactions. The imaging system described in section 3.4 detects neutrons by a MCP made of glass containing ^{10}B. It is operated in a counting mode like standard $^{3}_{2}$He detectors.

3.2 Theory of Cascaded Detection Systems

Moving towards ever smaller pixel sizes and increasing time resolution of the detectors it gets more and more important to reach a reasonable neutron statistics of the measured data. It is essential therefore to optimize the neutron detection efficiency, as the final signal statistics will always be limited by the information virtually stored inside the detected single neutron signal. It has to be assured that the signal generated by the detected neutrons is transfered to the detector output with minimum loss of statistics. That is the number of quanta carrying information must not be less than the number of detected neutrons per pixel or evaluated area. For a combination of a scintillation screen and a radiographic film Ter M. Pogossian wrote in 1967: *"Under ideal conditions the screen can transfer to the emulsion as much information as was absorbed from the X-ray beam but never more. ..."* [22, p. 203] In fact this holds for any kind of detection system, including neutron detectors of course. And it is a contradiction to the basic principles of building an efficient detection system if a major part of information is lost at the first stage of a cascaded detector already. Therefore the neutron detection efficiency of the first stage must be as high as possible. The neutron imaging detectors applied for time resolved neutron imaging in chapter 4 as well as the detectors used for USANS described in chapter 5 use cascades of signal conversions before the signal is integrated and converted to a digital image. Each conversion contributes to the uncertainty of the final signal. This section will exemplarily focus on detectors with a scintillation screen optically coupled to an imaging sensor. But the underlying theory is valid for any kind of cascaded detection system. Due to practical limitations by detector or beam geometry, e.g. limited detection or conversion efficiencies, the beam divergence or the available neutron flux, there will always be a trade-off between spatial resolution, time resolution and neutron statistics. It is like a magic triangle of detector design [23]:

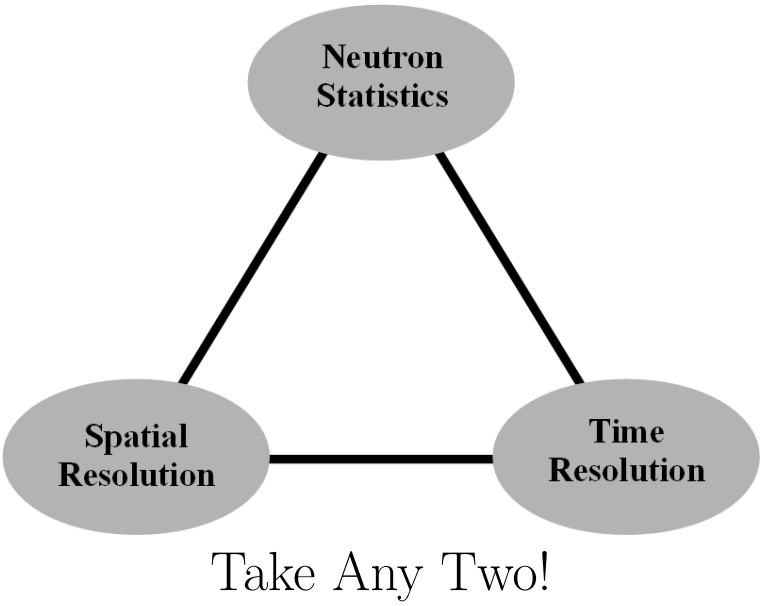

As the available neutron flux will always be limited, it will never be possible to reach the optimum for all three requirements at once. So one has to trim back the demands for one of them.
The concepts of the Detection Quantum Efficiency (DQE) and the Quantum Accounting Diagram (QAD) offer a way for a theoretical description of the signal statistics and signal propagation of detectors. These theoretical descriptions, e.g. introduced by Cunningham et al., are used to determinate conversion steps inside a signal chain, or components of cascaded detector elements that cause a limitation of the detector performance [24]. In principle the easiest way is to isolate each conversion stage to investigate its performance. But for real detectors it is not possible to get access to the signal after each conversion step. Thus some values have to be estimated from appropriate measurements or results gained by other groups. Cunningham et al. give an example

for a hypothetical system to demonstrate the influence of the spatial spread of a converter on the spatial-frequency dependent DQE of a detector. A QAD illustrates the number of quanta carrying information after each conversion step of the cascaded detector system. With the help of a QAD it is easy to determine the conversion step, where the lowest number of quanta contains information about the measured signal. This step is called a quantum sink [24]. If there is a step during the signal conversion, which involves a lower number of quanta than the primary detected number of quanta, this step is called a secondary quantum sink. If a detector does not posses a secondary quantum sink, its signal statistics is solely limited by the number of detected quanta. In this sense it would be limited by the number of absorbed neutrons or neutrons that triggered a nuclear detection reaction.

3.2.1 Contrast and Detective Quantum Efficiency

The term contrast is often used to describe the performance of detection system, especially imaging devices. But there are many ways to define it [25]:
≫
- Contrast (vision), difference in color and light between parts of an image
- Contrast (statistics), the difference between two means
- Contrast (literary), describing the difference(s) between two or more entities.

≪
And there are even more possibilities to derive a numerical value for it.
The contrast C is related to spatial resolution and resolution in terms of intensity.
A possible relation between neutron flux density ϕ, pixel size Δx, exposure time Δt and the contrast C is

$$C = \chi \underbrace{\left(\kappa \cdot \phi(x,y) \cdot (\Delta x)^2 \cdot \Delta t\right)}_{\text{detectable signal}} . \tag{3.6}$$

The function χ in equation (3.6) is taking into account that different signal thresholds are necessary for a given feature to be defined as detected depending on the definition of the term contrast. This makes the contrast a quite arbitrary value to describe the performance of an imaging detector.
In fact the contrast can be changed and optimized during post processing of data, e.g. to put the focus on a certain gray scale range. The factor κ on the other hand is a perfect measure to describe the detector performance, as it directly relates the detectable signal to the input signal of the detector determined by the incident flux ϕ, the pixel size Δx and integration time Δt.

DQE A standard parameter to measure the quality of a (neutron) detection system is its detective quantum efficiency(DQE). But this value does not take into account the spatial resolution of the detector. For position sensitive and in particular for imaging detectors it is very important to include the spatial resolution to the parameter determining the performance of the detector. The frequency dependent detective quantum efficiency (DQE) $DQE(\omega)$ offers a way to do so [26], [27]. Thus the frequency dependent DQE is ideal to replace the factor κ in equation (3.6). It is further independent of the definition of contrast and solely describes the detector performance. For zero frequency it describes the statistical behaviour of a neutron beam monitor for example, when a spatial resolution is not taken into account. In any case the DQE is defined as [28]

$$DQE = \frac{(\text{output signal to noise ratio})^2}{(\text{input signal to noise ratio})^2} = \frac{(SNR_{\text{out}})^2}{(SNR_{\text{in}})^2} . \tag{3.7}$$

Under ideal conditions the Signal to Noise Ratio (SNR) at the input and the SNR at the output of the detector would be the same and the DQE would be equal to 1. Barmakov et al. give a scheme of the physical processes involved in the detection of thermal neutrons by a CCD-detector including the effects of an image intensifier stage in combination with the CCD-sensor [28]. It is shown that the DQE of an Gd_2O_2S scintillator is higher for fields of view smaller than $10\,\text{x}\,10\,\text{cm}^2$

(or a pixel size of less than $10\,\mathrm{x}\,10\,\mu\mathrm{m}^2$) even at low neutron flux densities ($> 10^2\,\frac{\mathrm{n}}{\mathrm{cm}^2\,\mathrm{s}}$) [28]. For a small field of view (FOV) of approximately $1\,\mathrm{x}\,1\,\mathrm{cm}^2$ their simulations show that the DQE of a gadolinium based scintillation screen is higher than the one of a lithium based screen by up to a factor of three [28]. This effect is simply explained by the fact that only the detection efficiency plays a role here. Other system parameters like the light output of the screen and the optical coupling to the sensor are sufficient enough to not diminish the signal statistics. It is also stated that the best DQE is reached by a system without an intensifier in this case, while usually systems including an image intensifier achieve higher DQEs than detectors without one. This is caused by the fact that the optical coupling or light output of the scintillator is a limiting factor and may result in a quantum sink without an image intensifier. Cunningham et al. have a more detailed look at the signal and noise propagation in cascaded imaging systems [24]. They describe how the DQE differs for a zero-frequency noise propagation and a (non zero) spatial-frequency dependent noise propagation. For the non zero frequency case effects of blurring or spreading at the single stages of the imaging system are taken into account. Each stage may be modeled as a stage with gain only and a stage with stochastic spreading only. In this way even complicated systems can be represented. It is important though to keep the single stages in the right order. Otherwise the stage causing a quantum sink might not be recognized. The basic idea is to separate detectors to several, sequential stages. Each of these stages contributes to the total uncertainty of the output signal of the detector. The overall DQE DQE_{total} of a detector with M stages is calculated from the DQEs DQE_{i} of the single conversion steps via

$$DQE_{\mathrm{total}} = \prod_{\mathrm{i}=1}^{\mathrm{M}} DQE_{\mathrm{i}} = \prod_{\mathrm{i}=1}^{\mathrm{M}} \frac{(SNR_{\mathrm{i}})^2}{(SNR_{\mathrm{i}-1})^2} = \frac{(SNR_{\mathrm{M}})^2}{(SNR_0)^2}\,. \tag{3.8}$$

At each interface all effects altering the signal, like the conversion efficiency and the amplification, have to be considered. The error propagation of such cascaded systems has been described in [22], [26], [28], [29], [30], [31]. Let $\bar{N}_{\mathrm{i}-1}$ be the average number of quanta at the input of stage i, $\bar{N}_{\mathrm{i}}$ the average number of quanta at the output and $\bar{g}_{\mathrm{i}}$ the average gain of this stage. Further $\sigma^2_{N_{\mathrm{i}-1}}$, $\sigma^2_{N_{\mathrm{i}}}$ and $\sigma^2_{g_{\mathrm{i}}}$ are the variances of the variables $N_{\mathrm{i}-1}$, N_{i} and g_{i}. Then

$$\bar{N}_{\mathrm{i}} = \bar{g}_{\mathrm{i}}\,\bar{N}_{\mathrm{i}-1} \quad \text{and} \quad \sigma^2_{N_{\mathrm{i}}} = \bar{g}_{\mathrm{i}}^2\,\sigma^2_{N_{\mathrm{i}-1}} + \sigma^2_{g_{\mathrm{i}}}\,\bar{N}_{\mathrm{i}-1} \tag{3.9}$$

(App. A.6, [29]). According to Cunningham, Westmore and Fenster [24] the DQE of a single stage is given by

$$DQE_{\mathrm{i}} = \frac{(SNR_{\mathrm{i}})^2}{(SNR_{\mathrm{i}-1})^2} = \frac{\bar{N}_{\mathrm{i}}^2\,/\,\sigma^2_{N_{\mathrm{i}}}}{\bar{N}_{\mathrm{i}-1}^2\,/\,\sigma^2_{N_{\mathrm{i}-1}}}\,. \tag{3.10}$$

A spatial frequency dependency is not included here. It follows from the definition of the DQE equation (3.7) and the error propagation of a single stage, equation (3.9), that the DQE of stage i is

$$DQE_{\mathrm{i}} = \frac{\bar{N}_{\mathrm{i}}\,(1+\epsilon_{N_{\mathrm{i}-1}})}{\bar{N}_{\mathrm{i}-1}\,(1+\epsilon_{N_{\mathrm{i}}})} = \frac{\bar{g}_{\mathrm{i}}\,\bar{N}_{\mathrm{i}-1}\,(1+\epsilon_{N_{\mathrm{i}-1}})}{\bar{N}_{\mathrm{i}-1}\,\left[1+\bar{g}_{\mathrm{i}}\,(1+\epsilon_{N_{\mathrm{i}-1}})+\epsilon_{g_{\mathrm{i}}}\right]} = \frac{1+\epsilon_{N_{\mathrm{i}-1}}}{1+\epsilon_{N_{\mathrm{i}-1}}+\left[(1+\epsilon_{g_{\mathrm{i}}})\,/\,\bar{g}_{\mathrm{i}}\right]}\,. \tag{3.11}$$

Here $\epsilon_{N_{\mathrm{i}}}$ and $\epsilon_{g_{\mathrm{i}}}$ are defined as a so-called Poisson excess terms [24] with

$$\epsilon_{N_{\mathrm{i}}} = \frac{\sigma^2_{N_{\mathrm{i}}}}{\bar{N}_{\mathrm{i}}} - 1 \quad \text{and} \quad \epsilon_{g_{\mathrm{i}}} = \frac{\sigma^2_{g_{\mathrm{i}}}}{\bar{g}_{\mathrm{i}}} - 1\,. \tag{3.12}$$

$\epsilon_{N_{\mathrm{i}}}$ is equal to zero for a pure Poisson distribution, $\epsilon_{N_{\mathrm{i}}} = -1$ for deterministic stage, e.g. an amplification without a statistical variance and for a binary selection with $\sigma^2_{g_{\mathrm{i}}} = \bar{g}_{\mathrm{i}}\,(1-\bar{g}_{\mathrm{i}})$ the Poisson excess term $\epsilon_{g_{\mathrm{i}}} = -\bar{g}_{\mathrm{i}}$ [24]. Extended to a multi stage system of M stages

$$DQE_{1,\mathrm{M}} = 1 \Bigg/ \left[1 + \sum_{\mathrm{i}=1}^{\mathrm{M}} \left(\frac{1+\epsilon_{g_{\mathrm{i}}}}{P_{\mathrm{i}}}\right)\right] \quad \text{and} \quad P_{\mathrm{i}} = \prod_{\mathrm{j}=1}^{\mathrm{i}} \bar{g}_{\mathrm{j}} \tag{3.13}$$

This expression shows that all amplifying stages contribute to the uncertainty of the final signal. Their influence on the SNR can be reduced to a minimum though if the amplifications g_i of the single stages are high enough.

Frequency Dependent DQE The spatial frequency dependent DQE for a single stage $DQE_{\mathrm{i}(\omega)}$ is given by [24]

$$DQE_\mathrm{i}(\omega) = \frac{1+\epsilon_{\phi_{i-1}}}{1+\epsilon_{\phi_{i-1}}+\left[1+\epsilon_{g_i}\left|T_i(\omega)\right|^2\right]/\left[\bar{g}_i\left|T_i(\omega)\right|^2\right]} \tag{3.14}$$

where $|T_i(\omega)|$ is equivalent to the modulation transfer function of stage i. That way a signal spread is included to the spatial frequency dependent DQE $DQE_\mathrm{i}(\omega)$ representing a single stage of the detector [24]. $\epsilon_{\phi_\mathrm{i}}$ and ϵ_{g_i} are again Poisson excess terms like the ones known from the zero frequency DQE.
The expansion to a system built up from M stages results in the spatial frequency dependent DQE $DQE_{1,\mathrm{M}}(\omega)$ given by [24]

$$DQE_{1,\mathrm{M}}(\omega) = 1 \Bigg/ \left[1+\sum_{\mathrm{i}=1}^{\mathrm{M}}\left(\frac{1+\epsilon_{g_\mathrm{i}}\left|T_i(\omega)\right|^2}{P_\mathrm{i}(\omega)}\right)\right] \quad \text{and} \quad P_\mathrm{i}(\omega) = \prod_{\mathrm{j}=1}^{\mathrm{i}} \bar{g}_\mathrm{j}|T_j(\omega)|^2\,. \tag{3.15}$$

Including additional noise sources to the spatial frequency dependent DQE of the total system $DQE_{1,\mathrm{M}}(\omega)$ leads to [24]

$$\mathrm{DQE}_{1,\mathrm{M}}(\omega) = 1 \Bigg/ \left[1+\sum_{\mathrm{i}=1}^{\mathrm{M}}\left(\frac{1+\epsilon_{g_\mathrm{i}}\left|T_i(\omega)\right|^2 + S_{a_i}(\omega)/\bar{\phi}_i}{P_\mathrm{i}(\omega)}\right)\right] \tag{3.16}$$

$$\text{and} \quad P_\mathrm{i}(\omega) = \prod_{\mathrm{j}=1}^{\mathrm{i}} \bar{g}_\mathrm{j}|T_j(\omega)|^2 \tag{3.17}$$

where $S_{a_i}(\omega)/\bar{\phi}_i$ is the relative additive noise power spectrum.

3.2.2 Quantum Sinks

The transmitted neutron signal has to be multiplied by the $DQE(\omega)$ of the detector to get the final signal. While the error of the transmitted signal (the counting statistics of the transmitted neutrons) may be improved by using longer exposure times of by summing up images, it is not possible to overcome the inherent error which results from the neutron detection probability and the contributions of the single conversion steps. Thus it is not possible to overcome a certain noise level even by adding up an infinite number of images. The signal to noise ratio at the output of the detector is simply given by

$$SNR_\mathrm{out} = SNR_\mathrm{in} \cdot \sqrt{DQE(\omega)} \tag{3.18}$$

according to the definition of the DQE equation (3.7). The DQE is fixed for a given detector setup and independent of the incident neutron fluence.[4] Therefore summing up images only makes sens as long as the statistics of the output signal is not limited by the DQE but the statistics of the signal at the input. So there is a difference for the optimum number of images that should be summed up depending on the current detector configuration and neutron flux. One reason, why there is a limitation of the statistics is the detection efficiency of course. Another one is the occurrence of a secondary quantum sink.

[4]This only holds as long as no dead time effects have to be taken into account for counting detectors. For integrating detectors an overflow of single pixels caused by too long exposure times would also affect the overall detector behavior.

What is a quantum sink? "If there is multiplication of photons at some stage of the examination, such as occurs in the conversion of X-ray photons into light in an X-ray screen, the lower value of the photon flux determines the limit of the statistical perceptibility of the examined object. It should be noted that if, in a given image-forming system, the photon flux passes through a series of stages of high and low values, the lowest value of the flux determines the maximum image perceptibility allowed by statistical fluctuations." [22, p. 302] As stated by Michele M. Ter-Pogossian in 1967 aquantum sink is defined as that stage of the imaging system at which the statistical information reaches its lowest level, i.e. where the information is carried by the lowest number of quanta. A quantum sink limits the signal-to-noise-ratio of a single pixel, or in other words of each single detected neutron. There are two possible quantum sinks which are of top priority for radiography detector built from a scintillation screen optically coupled to an imaging sensor. The number of detected neutrons is a primary limitation for the achievable DQE. After the conversion to light, which is in general a conversion step of high gain, the optical coupling to the next stage is a step, where quanta carrying information are lost. This originates from the small solid angle accepted by the imaging optics. A further reduction of quanta is caused by the conversion efficiency of the imaging sensor (or the photocathode of an image intensifier). An optical quantum sink becomes severe for small pixels, equivalent to high spatial-frequencies, or scintillators of low light output like Gd_2O_2S screens. There are two effects which may cause a secondary quantum sink. Both result from a insufficient number of photons reaching the imaging sensor per detected neutron.

i) While the neutron detection reaction results in an isotropic emission of photons[5] in 4π, the solid angle accepted by the lens optically coupling the scintillation screen and the imaging sensor is limited.

ii) Spreading of the signal reduces the number of quanta per pixel that carry information.

The accepted solid angle $\Delta\Omega$ is given by (Fig. 3.2)

$$\Delta\Omega = 4\pi \cdot \frac{\pi\, D^2}{4 \cdot 4\pi \cdot g^2} = \frac{\pi\, D^2}{4\, g^2}\,. \tag{3.19}$$

The corresponding fraction of 4π is

$$p = \frac{\Delta\Omega}{4\pi} = \frac{D^2}{16\, g^2}\,. \tag{3.20}$$

Including the F-number $F\#$ of the lens, which is given by

$$F\# = \frac{f}{D} \quad \Longrightarrow \quad D = \frac{f}{F\#} \tag{3.21}$$

one gets

$$p = \frac{f^2}{16\, g^2\ (F\#)^2}\,. \tag{3.22}$$

This is independent of the focal length f if the FOV and the sensor size are kept the same, which is equivalent to a fixed magnification M. Then

$$p = \frac{f^2}{16\ (1+M)^2\ f^2\ (F\#)^2} = \frac{1}{16\ (1+M)^2\ (F\#)^2}\,. \tag{3.23}$$

A spatial spreading of the quanta carrying information causes a loss of resolution due to two facts. First of all the spread of the quanta introduces a loss of signal statistics. Secondly the overall background signal is increased due to the spread of quanta. Thus the signal to noise ratio of a single pixel is reduced and the minimum level a signal has to overcome before is is recognizable is increased. Or in other words the contrast is diminished by the increasing background signal.

[5] not taking into account attenuation of the emitted light by the phosphor itself

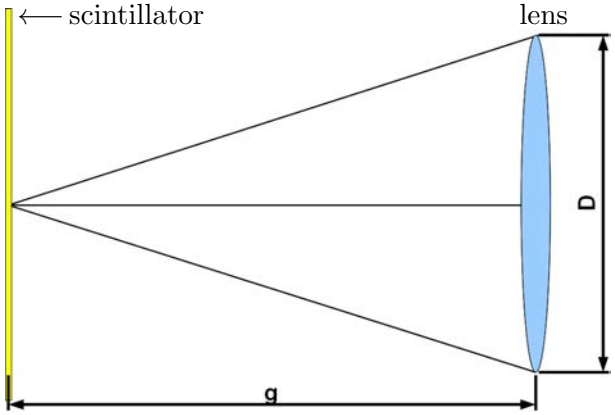

Fig. 3.2: The accepted solid angle of a lens system is defined by the diameter D of the entrance aperture of the lens and its displacement g from the scintillation screen.

3.2.3 Quantum Accounting Diagram

Plotting the number of quanta carrying information at each stage of the detector is a measure to illustrate the propagation of the signal from the input to the output side of a detector. Cunningham et al. call this kind of plot a Quantum Accounting Diagram (QAD) [24]. A QAD allows to estimate the fundamental noise limitations of different detector systems. Its interpretation is simple and the stages with few or the fewest quanta can directly be identified. In fact that stage limits the overall DQE of the cascaded system. Normalized to one incident neutron the stage limiting the DQE is easy to identify. Limitations of the QAD are, that it does not include effects of additional noise sources like gamma events or dark current signals and that a spatial spreading of the quanta can only be included by an reduction of the quanta carrying information. The additional background caused by a spatial spreading is not taken into account, but it is included for a frequency dependent DQE.

3.3 Neutron Detection by Phosphor Screens and Imaging Sensors

This section describes effects due to the nature of neutron detection by scintillation screens. It highlights some parameters of the scintillation screens and how it is possible to optimize them for dynamic neutron radiography investigations or standard radiography applications. Some of these issues are the neutron detection efficiency, the spatial resolution and the decay time of the phosphor effecting the time resolution. The sensitivity of ^{6}LiF/ZnS and Gd_2O_2S scintillators for gamma rays and X-rays is discussed, too. The basic principle of the detector design is shown in figure 3.3. Neutrons incident onto the scintillation screen are absorbed by the active isotope[6] inside the phosphor layer, the products of the detection reaction (Sec. 3.1) excite the phosphor and visible light is emitted. Often the light is optically coupled to an imaging sensor by a lens or a lens system.[7] This allows for a very high flexibility concerning the detector design, e.g. the active area of the detector. A front side coated mirror reflects the light. That way it is possible to keep the imaging sensor out of the direct neutron beam and to prevent from radiation damage. A lens maps the intensity distribution of light emitted at the surface of the scintillation screen to the pixel array of an imaging sensor. There are different kinds of sensors which may be used to detect light emitted by a phosphor screen. In the following the term imaging sensor represents any position sensitive area sensor, e.g. simple Charged-Coupled Device sensors (CCD sensors), Intensified Charged-Coupled Device sensors (ICCD sensors), electron multiplying Charge-Coupled Device sensors (EMCCD sensors) or Active Pixel Sensors (APS) also called Complimentary Metal Oxid Semiconductor (CMOS) sensors.

[6] An isotope is called active if its capture reaction of a neutron contributes to the detected signal.

[7] A coupling using a fiber optical taper is not discussed here, as it is rarely used for neutron imaging detectors.

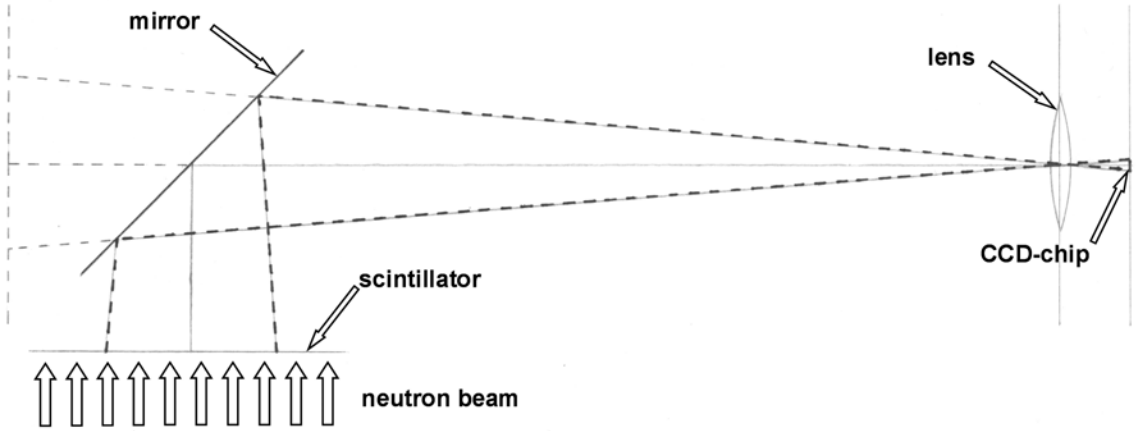

Fig. 3.3: The basic design of the most common neutron imaging detector consists of a neutron sensitive scintillator, a mirror, a lens and an imaging sensor, e.g. CCD-chip. The emitted scintillation light is collected via an optical coupling usually employing a mirror and a lens and recorded by the imaging sensor.

3.3.1 Neutron Detection Efficiency

A primary limitation of the detection efficiency of a system based on a phosphor screen is the probability of neutrons to be absorbed inside the phosphor layer by an active isotope of the phosphor. An isotope is called active if the neutron absorption is followed by a radioactive decay of the isotope that finally results in an excitation of the phosphor and a subsequent emission of scintillation light. The most important isotopes used for neutron scintillation screens are ^{6}Li, ^{10}B and ^{155}Gd/^{157}Gd [10], [20], [28], [32]. The probability to detect a neutron is proportional to the absorption cross section of the isotope, the particle density of the isotope inside the phosphor and the thickness of the phosphor layer. The absorption efficiency of neutron scintillation screens reaches from less than 10 % for thin ^{6}LiF/ZnS scintillators of 25 μm thickness up to more than 70 % for Gd_2O_2S screens of 20 μm thickness. As the absorption cross section obeys a $\frac{1}{v}$-law for cold and thermal neutrons, there is a dependency on the neutron wavelength or the neutron energy spectrum if a white neutron beam is used (Fig. 3.4). A standard composition of the phosphor materials

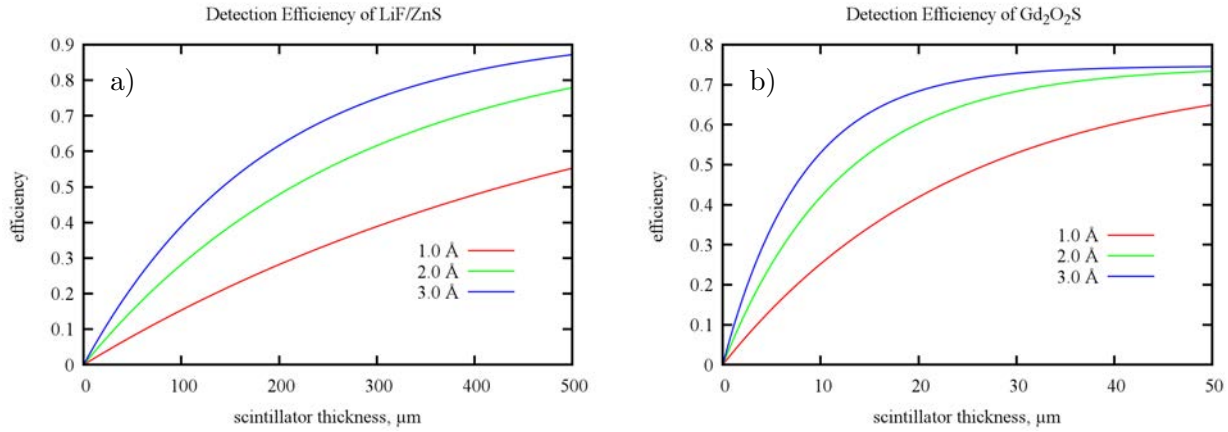

Fig. 3.4: Neutron detection efficiency plotted versus thickness of the phosphor layer of the neutron scintillator. a) The wavelength dependency is stronger for the ^{6}LiF/ZnS screen. b) The detection efficiency of the Gd_2O_2S screen is limited to 75 %, as this is the branching ratio for generating a conversion electron, which is necessary for the excitation of the phosphor and the subsequent emission of scintillation light.

^{6}LiF/ZnS and Gd_2O_2S is assumed for the following calculations. For ^{6}LiF/ZnS a mixture of ^{6}LiF and ZnS with a volume ratio of 1:1 and for Gd_2O_2S a density of 4.5 $\frac{g}{cm^3}$ have been used. LiF with

^{6}Li enriched to 100 % is assumed and Gd of natural abundance is used to calculate the particle densities and macroscopic cross sections for the phosphors.

3.3.2 Spatial Resolution and Scintillator Thickness

It is known from X-ray radiology that a higher resolution is achieved by scintillation screens of reduced thickness and smaller grain size of the phosphor particles. This has been stated by Michele M. Ter-Pogossian in 1967 already, when he said: *"For high resolution in a screen, lateral diffusion of the light photons must be prevented; this may be achieved by reducing the size of the phosphor particles, or by increasing the opacity of the phosphor layer to its own light."* [22, p. 200] Manufacturers of phosphors or scintillation screen use as small particles as possible. Increasing the opacity of the phosphor or binder material means that there is a significant loss of scintillation light due to self absorption. Only photons generated close to the surface of the phosphor will be emitted. Thus the effective thickness of the phosphor layer is reduced. Another way is to directly reduce the thickness of the phosphor layer to a minimum, while the opacity of the phosphor is kept low. This helps to improve the signal statistics for single neutron detection events, because more photons are emitted at the surface of the phosphor for each detected neutron. By reducing the thickness of the phosphor layer the spatial resolution is improved, too, as the maximum path length of the scintillation light inside the phosphor layer is inherently reduced [28]. As a rule of thumb the number of line pairs R_L per millimeter, that can be resolved, depending on the thickness of the scintillation screen is given by[8]

$$R_L = \frac{500}{d}\,,$$

where the thickness d of the phosphor layer is inserted in μm. This yields an resolution limit which is comparable to the thickness of the scintillator. The major drawback of using thinner scintillation layers is their lower detection efficiency. The only way to compensate this is to switch to detection materials with a high absorption cross sections for neutrons or to increase the particle density of neutron sensitive material inside the phosphor of the screen.
Another important parameter for the spatial resolution is the average absorption length of neutrons inside the phosphor of the scintillation screen. It is determined by total macroscopic cross section for neutron interaction and given by

$$\bar{x}_\mathrm{a} = \frac{1}{\Sigma_\mathrm{t}} - d \cdot \frac{\mathrm{e}^{-\Sigma_\mathrm{t}\, d}}{1 - \mathrm{e}^{-\Sigma_\mathrm{t}\, d}}\,. \tag{3.24}$$

Figure 3.5 shows that the average absorption length does not necessarily increase with the thickness of the phosphor layer. For phosphors like Gd_2O_2S that show high neutron attenuation the average absorption length does not change significantly with the thickness of the phosphor layer, but is mainly dependent on the neutron energy. Note the factor of 10 for the range of the axes between the plots for ^{6}LiF/ZnS and Gd_2O_2S. It is not advisable to use Gd_2O_2S screens of a thickness of more than 30 μm even for neutrons with wavelengths shorter than 2 Å. A strong deviation from a linear increase of the average absorption length especially for large neutron wavelengths is equivalent to the fact that enlarging the thickness of the phosphor layer does not result in a higher detection efficiency, as the neutron transmission of the scintillator has already reached a low value. From the average absorption length $\bar{x}_\mathrm{a}$ it is straight forward to derive the average path length of the scintillation light inside the phosphor. If the light exits the scintillator in reverse direction with respect to the neutron beam direction, the average path length of the light to reach the surface of the phosphor layer is equivalent to the average absorption length. In case the generated scintillation light exits the scintillator in neutron beam direction, the average distance $\bar{x}_\mathrm{l}$ of the reaction center of the neutron detection to the surface of the phosphor is given by

$$\bar{x}_\mathrm{l} = d - \bar{x}_\mathrm{a}\,, \tag{3.25}$$

where d is the thickness of the phosphor layer (Fig. 3.6). The average path length of the emitted

[8] `http://adweb.desy.de/mdi/documentation/Restgas_at/PETRA/phos.htm`

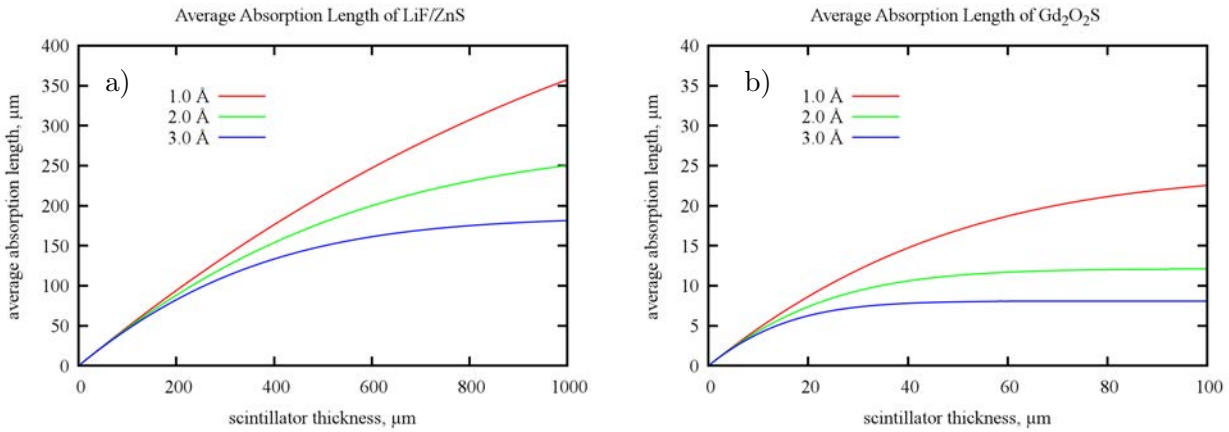

Fig. 3.5: a) For a ^{6}LiF/ZnS phosphor and a neutron wavelength of 2 Å or longer the average absorption length does not increase significantly for a phosphor thickness of more than 400 μm. b) For a Gd_2O_2S scintillator the average absorption length of neutrons of 3 Å already starts to saturate for a scintillator thickness of about 20 μm. A saturation of the average absorption length is equivalent to the fact that a major part of the neutron is already absorbed inside the phosphor layer. Increasing the thickness of the phosphor does not improve the absorption efficiency significantly then.

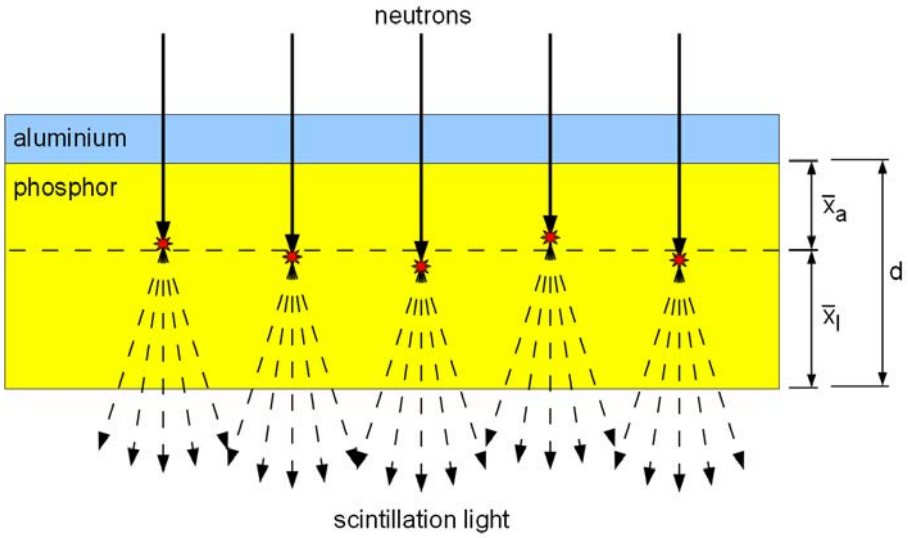

Fig. 3.6: The average absorption length $\bar{x}_a$ and the thickness of the phosphor layer d define the average path length $\bar{x}_l$ of the scintillation light inside the phosphor.

scintillation light inside the phosphor layer of the scintillator depends on the thickness d of the phosphor layer and the total macroscopic cross section Σ_t. For a fixed neutron wavelength it is given by

$$\bar{x}_\mathrm{l} = d \cdot \left(1 + \frac{\mathrm{e}^{-\Sigma_\mathrm{t}\, d}}{1 - \mathrm{e}^{-\Sigma_\mathrm{t}\, d}}\right) - \frac{1}{\Sigma_\mathrm{t}}\,. \tag{3.26}$$

This is valid only if the light exits the scintillation screen in the same direction as the neutron beam. As the absorption cross section $\Sigma_\mathrm{a}^\star$ of the active isotope(s) of the phosphor is usually much larger than the cross sections of all other constituents, it is possible to approximate Σ_t by $\Sigma_\mathrm{a}^\star$.

$$\bar{x}_\mathrm{l} = d \cdot \left(1 + \frac{\mathrm{e}^{-\Sigma_\mathrm{a}^\star\, d}}{1 - \mathrm{e}^{-\Sigma_\mathrm{a}^\star\, d}}\right) - \frac{1}{\Sigma_\mathrm{a}^\star}\,. \tag{3.27}$$

In order to get a minimum spread of the signal or scintillation light inside the phosphor layer one has to keep the average path length as short as possible. In principle this would afford an orientation of the scintillator and the mirror with respect to the neutron beam like the one shown in figure 3.7a. But for standard neutron imaging applications (neutron radiography) the sample is usually positioned close to the scintillation screen to minimize the effects of geometrical blurring due to the divergence of the neutron beam (Fig. 3.7). So there is not enough space to place a mirror between the sample and the scintillator.[9] Therefore neutron radiography detectors use a setup where the light emitted in neutron beam direction is detected (Fig. 3.7b). As soon as a certain detection efficiency of the scintillator is reached, about 70 % of the maximum absorption efficiency, a further increase of the thickness of the phosphor does only yield a minor increase of the detection efficiency. But the additional phosphor gives rise to a longer average path length for the emitted scintillation light. It is enlarged by nearly the full thickness of added phosphor layer. This results in a loss of resolution due to the spreading of light inside the phosphor and a diminished signal statistics, as the generated scintillation light is also attenuated by the additional phosphor material. Figure 3.8 shows the calculated, average path length light travels inside ^{6}LiF/ZnS and Gd_2O_2S scintillation screens for different thicknesses of the phosphor layer. Usually the optical coupling between the scintillator and the imaging sensor does not limit the overall performance of the detection system in terms of spatial resolution. This means that the modulation transfer function (MTF) of the coupling lens system does not cause a reduction of the total frequency dependent DQE of the detector due to a spreading of the signal. But the optical coupling may cause a secondary quantum sink due to a gain < 1 of the photon transfer to the imaging sensor. This in turn would of course give rise to a reduction of the DQE.

3.3.3 Time Resolution

The time resolution of a detection system based on a scintillation screen optically coupled to an imaging sensor is limited by the decay time of the phosphor and the minimum time the imaging sensor is exposed to light. There is also a third limitation which is common for all neutron measurements [33].

Physical Limitation Neutrons being massive particles have rather low velocities compared to X-rays or gamma-rays. According to their kinetic energies typical velocities of cold and thermal neutrons are within a range of 300 $\frac{\mathrm{m}}{\mathrm{s}}$ to 4000 $\frac{\mathrm{m}}{\mathrm{s}}$. Thus it takes time for the neutrons to pass the sample, or in other words it is possible for the sample to change its state during the "possible" interaction time. A similar effect is true for the time resolution of the detection of the neutrons. Depending on the size of the active detector volume[10] in neutron flight direction Δz, there is a

[9] For a setup like it is shown in figure 3.7a the distance between the sample and the scintillator must at least be of the same size as the FOV, i.e. the size of the scintillator. For neutron imaging applications this would already introduce a significant blurring due to the divergence of the neutron beam.

[10] the size of the matrix containing neutron sensitive material

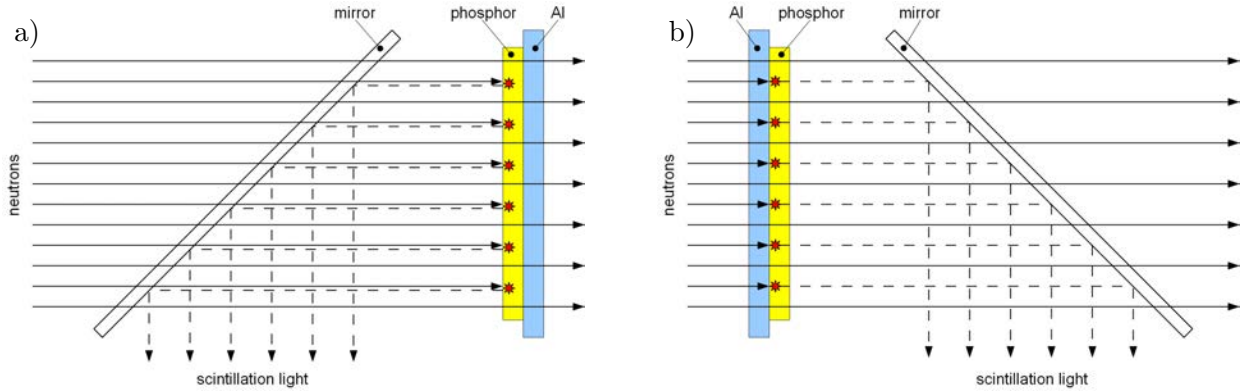

Fig. 3.7: There are two possibilities to put a neutron scintillation screen with respect to the neutron beam direction: a) The neutrons hit the phosphor layer of the scintillation screen first and the scintillation light is emitted in reverse direction with respect to the neutron beam. This orientation is preferred if the phosphor shows a high absorption efficiency for neutrons. Most neutrons are detected close to the surface of the phosphor layer that way keeping the average path length for the emitted scintillation light inside the phosphor short. b) In the standard geometry used for neutron radiography detectors the neutrons pass a support layer, made of aluminum most of the time, before they are absorbed by the phosphor material. In this configuration only scintillation light emitted in neutron beam direction reaches the imaging sensor. The average path length of the scintillation light inside the phosphor is always larger for this geometry. But it enables to position the sample closer to the detector for a minimized geometrical blur. Furthermore there is no attenuation of the neutron beam due to the mirror.

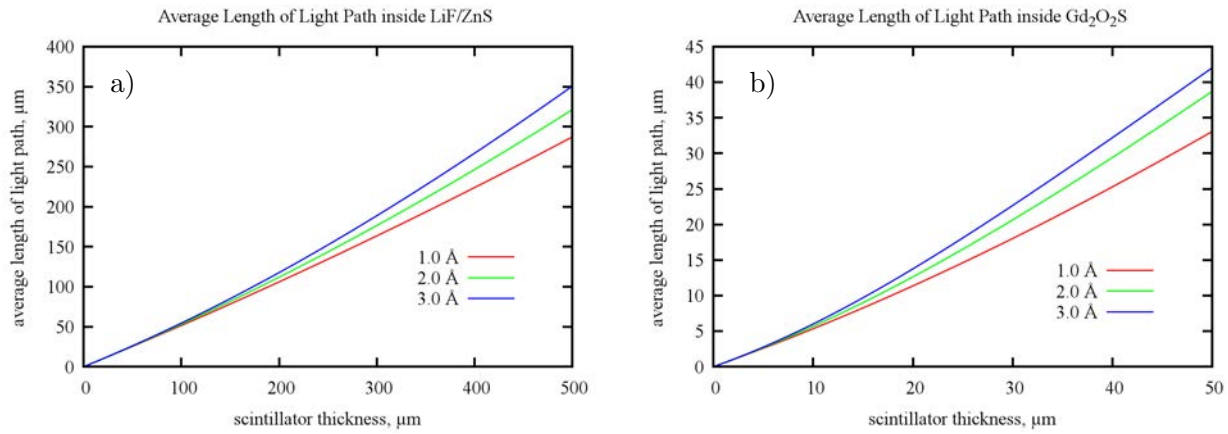

Fig. 3.8: For ^{6}LiF/ZnS the average path length the emitted scintillation light travels inside the phosphor is nearly independent on the neutron wavelength. This is caused by the low detection efficiency of ^{6}LiF/ZnS resulting in a linear increase of the average absorption length, which is approximately half of the thickness of the phosphor layer. b) For a phosphor of higher absorption probability, e.g. Gd_2O_2S, the average length of the light path inside the phosphor shows a faster increase with the thickness of the phosphor layer.

certain interval Δt given by $\Delta t = \frac{\Delta z}{v_n(\lambda)}$ when neutron interaction may take place. As the sample is often not in direct contact with the detector, it also takes time for the neutrons to traverse the distance from the sample to the detector. Thus a neutron radiograph acquired using a full neutron spectrum will always include information, of slightly different states of the sample, because it took the detected neutrons a time $\Delta t = \frac{d}{v_n(\lambda)}$ to pass the distance d from the sample to the detector. For the measurement on the injection nozzle the sample size is about 1 cm in neutron beam direction and the distance to the scintillator is about 2 cm. The effect due to the thickness of the scintillation screen is negligible. Therefore the expected timing error is approximated to be 100 μs, which is of the same order of magnitude as the exposure times.

Decay Time of the Phosphor Neutron detection reactions are prompt compared to the time scale of microseconds up to milliseconds it takes for the excited states of the phosphor to decay to the ground state accompanied by the emission of scintillation light. Thus the time resolution is primarily given by the decay time of the phosphor. To change the scintillation behavior of phosphor screens they are doped with different elements, so-called activators. These activators have an influence on the emission spectra and the decay time of the excited states of the phosphor [34]. For the dynamic radiography measurements with high spatial resolution a Gd_2O_2S scintillator doped with Pr/Ce/F has been chosen. Its optical decay time is specified to be 1 μs to 10 μs [35]. Hence the optical decay time of this Pr/Ce/F activated phosphor is less by about a factor of 100 compared to standard doping with Tb, for which the optical decay time is specified to be 1 ms [36]. As the doping not only affects the decay time but also the emitted light spectra of the phosphor, this must be kept in mind when selecting a scintillation screen. The wavelength peak of the emission spectra of the two phosphors are 513 nm for Pr/Ce/F doping and 544 nm for the Tb activated phosphor. Both wavelengths are well inside the spectral range where standard imaging sensors reach high efficiencies.

Minimum Exposure Time Mechanical shutter systems do not allow for exposure times down to 100 μs or even less if the entire area of the sensor has to be illuminated simultaneously. It is therefore necessary to use electronic shutters, e.g. an image intensifier, instead. These electronic shutters enable to reach exposure times as short as nanoseconds. This is about two orders of magnitudes less than the expected decay times of the excited states of the applied phosphors.

Thus the time resolution of this kind of detector is not limited by the minimum exposure time but the decay time of the phosphor and the error introduced due to the finite neutron velocity. There is a way though to overcome this limitations by a pulsed neutron beam irradiating the scintillation screen. The minimum exposure time is then determined by the width of the neutron pulse. For the measurements on the injection nozzle a timing error of 100 μs is acceptable, as the planed exposure times of 200 μs to 500 μs cause a time average of the recorded neutron signal anyway.

3.3.4 Readout Speed, Dead Time and Duty Cycle

It takes between 1 s to 5 s to read a full frame from a CCD type imaging sensor. This is not significant for steady state radiography or tomography, when exposure times are about 30 s to 300 s per image. But it gets a reasonable timing factor for dynamic radiography, when exposure times are shorter than 1 ms. Here it does not make sense for the imaging sensor to be readout after each exposure. On the one hand the signal acquired during these short time frames is not significantly higher than the readout noise of the detector or it does not overcome the digitization threshold.[11] On the other hand the duty cycle of such a system would be most wasteful. Less than $\frac{1}{1000}$ of the available neutrons would be used on a continuous neutron beam that way. Therefore

[11] There is a minimum signal that is necessary to cause a change of one bit at the analog to digital converter of the detector.

an on-chip integration method is used to sum up the incoming photons of multiple exposures on the imaging sensor before the accumulated signal is read out. This is a standard technique for time resolved investigations of periodic processes at continuous neutron beams or energy resolved neutron radiography at pulsed neutron sources [37], [38], [39]. The signal of several single exposures is integrated on the imaging sensor. An effective exposure time up to a few seconds is reached that way before the image is read. Because of low repetition rates of the investigated processes, the duty cycle is often still quite bad. For example a gate width of 500 μs for a single exposure and a repetition rate of 50 Hz, which is already a rather long gate width and a standard repetition rate for a periodic process, results in an effective exposure time of only 2.5 s during an acquisition time of 100 s. Thus the duty cycle is

$$\frac{\text{effective exposure time}}{\text{acqusition time}} = \frac{25\,\text{ms}}{1\,\text{s}} = \frac{1}{40}\,.$$

The readout time of 5 seconds is not considered here, as it is negligible compared to usual acquisition time of several minutes for an on chip integration.
Expressed in terms of dead time a detector operated at a duty cycle of $\frac{1}{40}$ is sensible for neutrons only 2.5 % of the time. This is a small fraction compared to the acquisition of a steady state radiograph, where typically more than 90 % of the acquisition time are used to integrate signal generated by neutrons, including losses due to the readout time already.

3.3.5 Gamma Background

There are two kinds of gamma background for scintillator based detectors. The first one is caused by gamma rays directly interacting with the imaging sensor of the detector. These gamma rays originate from the beam or neutrons interacting with the sample or structure material of the detector. The resulting hot spots or bright spots can be filtered by software to a certain amount [40]. But it is best to shield the imaging sensor against gamma rays in the first place. The second kind of gamma background is an additional signal resulting from gamma rays detected by the phosphor in parallel to the neutron signal. This gamma signal depends on the gamma sensitivity of the scintillator material and can be suppressed by the use of appropriate filters like lead and bismuth, which show high absorption for gamma rays but allow for neutron transmission. This problem could be circumvented if a pure neutron beam without any gamma contribution was available. It is important to minimize the contribution of gamma rays to the measured signal and keep the detected signal linked to neutrons only, because the detection of gamma rays along with the neutron signal has two negative effects:

(i) An Indirect Loss of Contrast Detected gamma rays add a background signal diminishing the overall DQE of the detector. This is especially true for gamma rays directly interacting with the imaging sensor.

(ii) A Direct Loss of Contrast A fact that makes gamma filtering even more crucial is the "inverse contrast" resulting from gamma ray attenuation compared to neutrons. Often neutron radiography and tomography is applied due to its unique contrast properties, penetrating metals easily while showing high attenuation for low Z materials or hydrogen containing materials. As it is vice versa for the attenuation of gamma rays, this will lead to an active reduction of contrast inside a neutron radiography. The transmission signal of the neutrons is superimposed by an inverse behaviour of the transmission for gamma rays having high attenuation values for most metals but very low attenuation values for low-Z material like hydrogen, carbon and oxygen most liquids are composed of. Thus the gamma ray signal leads to an active reduction of the contrast of the neutron radiograph. Gamma rays of energies above 100 keV do not cause trouble. Because the phosphor layer is usually very thin, the probability for X-rays or gamma rays to be absorbed inside the phosphor is close to zero even for phosphors containing high-Z elements like gadolinium

(Fig. 3.9). The transmission plots show dips, which may be attributed to absorption edges[12] of the elements the phosphors consist of. Neutron scintillation screens have only a low sensitivity

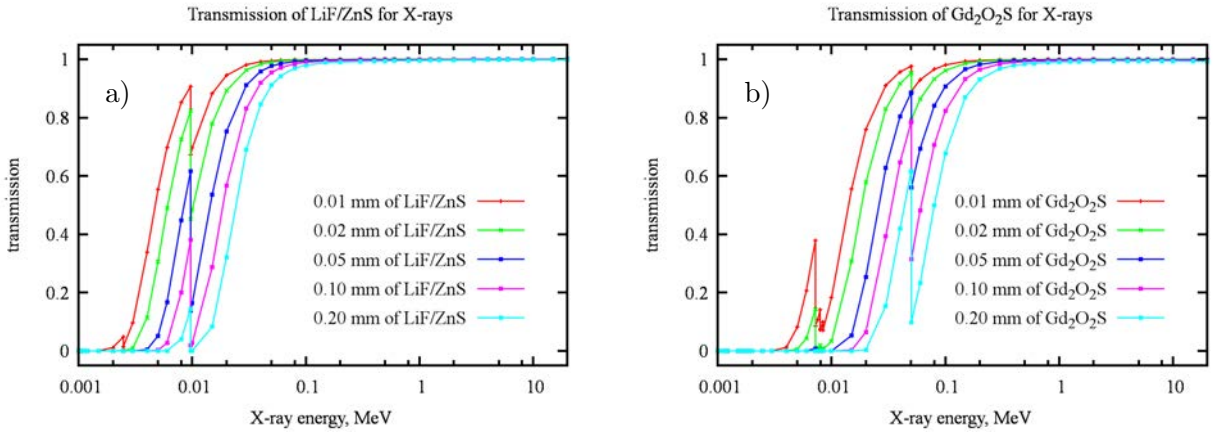

Fig. 3.9: ^{6}LiF/ZnS and Gd_2O_2S both show a low sensitivity for X-rays or gamma rays with energies above 100 keV. For those energies the transmission of the phosphors is close to 1 for typical thicknesses of the phosphor layer. Dips in the transmission plot below 100 keV are due to absorption edges.

for X-rays or gamma rays of energies above 100 keV. Mass attenuation coefficients[13] for typical components of phosphors are shown in figure 3.10. For energies around 1 MeV the attenuation is

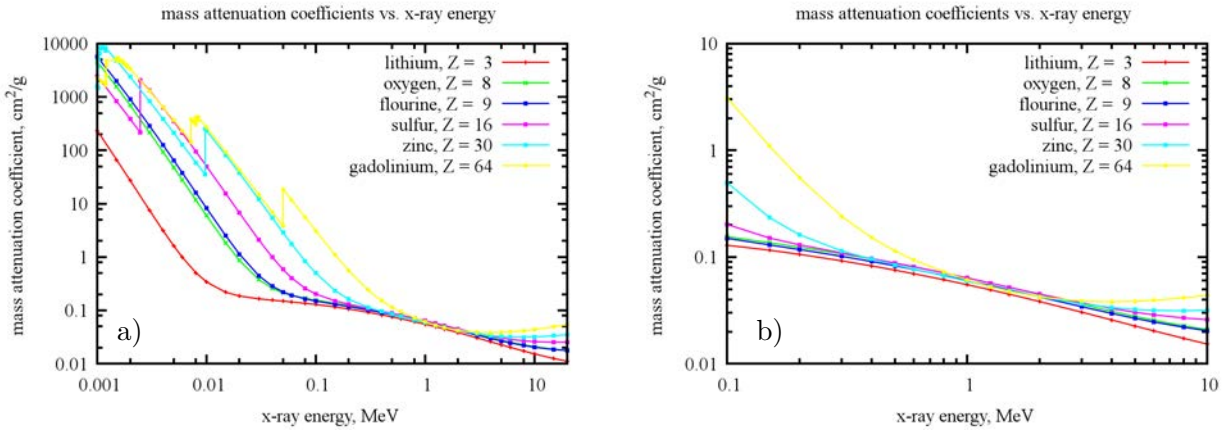

Fig. 3.10: Mass attenuation coefficients of the main elements contained in ^{6}LiF/ZnS and Gd_2O_2S screens: a) for X-ray energies from 1 keV to 20 Mev b) for X-ray energies form 100 keV to 10 Mev.

low and comparable for all phosphor materials. Thus only gamma rays of low energies will show in a significant detection efficiency for neutron scintillators. If it is possible to hinder gamma rays of energies below 1 MeV to reach the phosphor layer of the scintillator, there will be only a very small fraction of gamma rays that is still detected by the phosphor. Usually ^{6}LiF/ZnS and Gd_2O_2S phosphors are supported by a sheet of aluminum. This aluminum back plane of the scintillator has a thickness of 1 mm to 1.5 mm. It is not sufficient to block gamma rays with energies between 1 keV and 100 keV (Fig 3.11a). But these energies are most likely to be absorbed by the phosphor. It is advisable therefore to add a thin sheet of lead in front of the scintillator. A sheet of lead of a thickness of only 1 mm is enough to block nearly 100 % of X-rays with energies below 100 keV (Fig. 3.11b).

[12] X-ray Data Booklet, `http://http://xdb.lbl.gov/`

[13] form `http://physics.nist.gov/PhysRefData/XrayMassCoef/tab3.html`

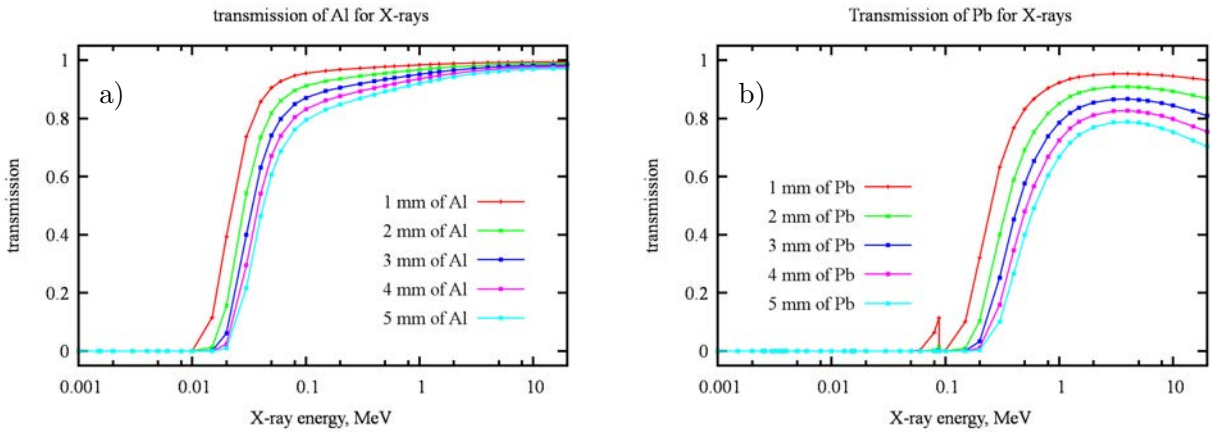

Fig. 3.11: a) transmission vs. X-ray energy for different thicknesses of the aluminum support, b) transmission of lead vs. X-ray energy for different thicknesses.

3.4 Neutron Detection by a Borated Multi Channel Plate

In 1990 Fraser and Pearson reported the detection of thermal neutrons by means of an imaging microchannel-plate electron multiplier where lithium incorporated inside the glass is responsible for the neutron detection [41]. A further development of this type of neutron detector has been applied for time resolved neutron imaging. This detector has been built by Tremsin et al. [42], [43]. Here ^{10}B is used inside the neutron sensitive MCP in contrast to the lithium used by Fraser and Pearson. Tremsin et al. added a chevron stack of unborated MCPs to the neutron sensitive MCP. Thus the electron signal is amplified before it reaches the readout stage consisting of an array of pixels (Fig. 3.12). After neutron absorption by a ^{10}B atom inside the glass of the neutron sensitive MCP, an α-particle and a Li-particle are emitted. If they cross the border from the borated glass towards a channel of the MCP, they release electrons. These electrons are accelerated by the voltage applied to the MCPs. The signal is amplified by generation of an electron avalanche, when

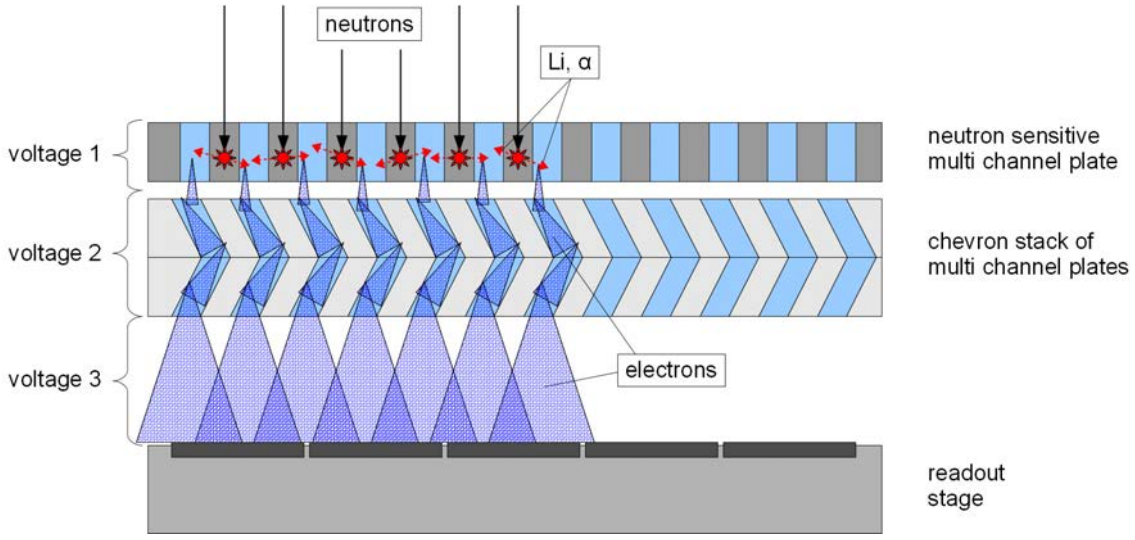

Fig. 3.12: Neutrons are absorbed inside the borated glass of the neutron sensitive MCP. The products of the detection reaction, a Li- and an α-particle, enter a channel of the MCP and release electrons. These electrons are accelerated and transfered to the chevron stack by voltage 1 applied to the first MCP. Inside the chevron stack the main amplification of the electron signal takes place. It is controlled via voltage 2 across the chevron stack. Finally voltage 3 is used to transfer the amplified electron signal to the readout stage and to control the spreading of the electron cloud. This enables to adjust the so-called footprint, which is the width of the electron cloud at the readout stage.

the electrons move along the channels of the MCPs and hit the channel walls [44]. The main signal gain is achieved inside the chevron stack. The glass of its MCPs does not contain ^{10}B. And it is therefore insensitive to neutrons. Thus they only serve for the amplification of the electron signal. At the exit side of the chevron stack the electron avalanche crosses a gap before it reaches the pixel array of the readout stage. The voltage applied between the chevron stack and the readout stage controls the size of the footprint[14] of the electron signal. This voltage has to be changed to switch between the counting mode and the centroiding mode of the detector. There are different readout electronics available to convert the electron signal to its digital representation [45], [46]: cross strip anodes, charge sensitive active pixels (ASIC), frame based active pixel sensors, Medipix2.[15] The Medipix readout using a CMOS array of 256×256 pixels is the standard readout of the neutron sensitive MCP detector. It is capable of count rates up to 20 MHz on the whole detector area [47]. In the following sections this detector is described in more detail concerning detection efficiency, spatial resolution, time resolution and gamma background.

3.4.1 Neutron Detection Efficiency of a Borated Multi Channel Plate

Tremsin et. al. describe the neutron detection efficiency Q_n of the borated MCP by

$$Q_\mathrm{n} = P_1 \cdot P_2 \cdot P_3 \,, \tag{3.28}$$

which is a product of three probabilities [44]. The probabilities P_1 to P_3 describe different steps of the detection process.

$\mathbf{P}_1$ is the probability of neutron absorption inside the neutron sensitive MCP, which means an absorption by ^{10}B. It is given by

$$P_1 = 1 - \mathrm{e}^{\left(-L_\mathrm{eff} \cdot \eta_{^{10}\mathrm{B}} \cdot \sigma_{^{10}\mathrm{B}}\right)} \quad \text{with} \quad \begin{array}{rl} \eta_{^{10}\mathrm{B}} & \text{particle density of } ^{10}\mathrm{B} \\ \sigma_{^{10}\mathrm{B}} & \text{absorption cross section of } ^{10}\mathrm{B} \\ L_\mathrm{eff} & \text{path length through bulk glass of the MCP.} \end{array}$$

The calculation of the effective path length L_eff is described in [44]. It depends on the incident angle of neutrons onto the MCP containing ^{10}B. If the neutron beam is perpendicular to the detector surface, the effective path length of the neutron is just the thickness of the borated MCP of 1 mm and the probability of neutron absorption may reach 52 % [44].

$\mathbf{P}_2$ is the probability of the reaction products to escape into an open channel of the MCP. It is 78 % for the commercial available MCPs of 8 μm pores and 2 μm channel walls. It is a unique feature of the MCP structure that the escape probability P_2 is not changed if the ^{10}B content or the thickness of the neutron sensitive MCP are changed to increase the neutron absorption probability [44, p. 284].

$\mathbf{P}_3$ describes the probability for creation of an electron avalanche in an adjacent channel of the MCP by one of the reaction products. It can be set to 1, as it is well-known from the operation of MCPs detecting other radiation, e.g. UV-light, that an electron avalanche is produced after every release of a primary electron or ion inside a channel [43].

The detection efficiency Q_n for thermal neutrons is then calculated to be $Q_\mathrm{n} = 0.52 \cdot 0.78 \cdot 1 = 0.41$. Higher detection efficiencies are possible by increasing the thickness of the neutron sensitive MCP.

[14] width of the electron could when it reaches the readout stage

[15] `http://medipix.web.cern.ch/medipix/pages/medipix2/medipix2.php`

3.4.2 Spatial Resolution

The range of the products of the detection reaction inside the neutron sensitive MCP does not limit the spatial resolution of the detector. Because they are produced inside the channel walls and can only reach the two adjacent channels of the MCP [44]. There is a spread of the signal though for the following amplification step. A primary amplification already takes place inside the neutron sensitive MCP. The generated electrons disperse to a larger number of channels at the interface to the following MCPs where the electron signal is further amplified before it is passed to the Medipix readout. But still the spread of the signal is limited by the structure size of the MCP, which is a big difference compared to detectors using a scintillation screen and an optical coupling. As the voltage bias between the output side of the amplifying chevron MCP stack and the readout allows to control the footprint of the electron avalanche signal, there are different readout modes available [42, p. 378]. For the counting mode[16] the footprint of the electron cloud is adjusted to match the pixel size of the Medipix sensor (Fig. 3.13a). A spread of the electron signal over more than one pixel would cause a blurring of the image here. The small footprint of the electron signal makes the pixel size of 55 μm the limiting factor for spatial resolution. In the Timepix mode where centroiding is used to determine the center of the electron cloud the footprint is set to a size of about 5×5 pixels [42, p. 378]. For single events it is possible that way to locate the position of the incident neutron with subpixel resolution at the centroid of the electron signal. The maximum resolution of the detector is now determined by the center to center distance of the pores inside the MCPs that are used to detect the neutrons and to amplify the electron signal (Fig. 3.13b). Centroiding is only possible as long as there are only few neutron events during one detector cycle,

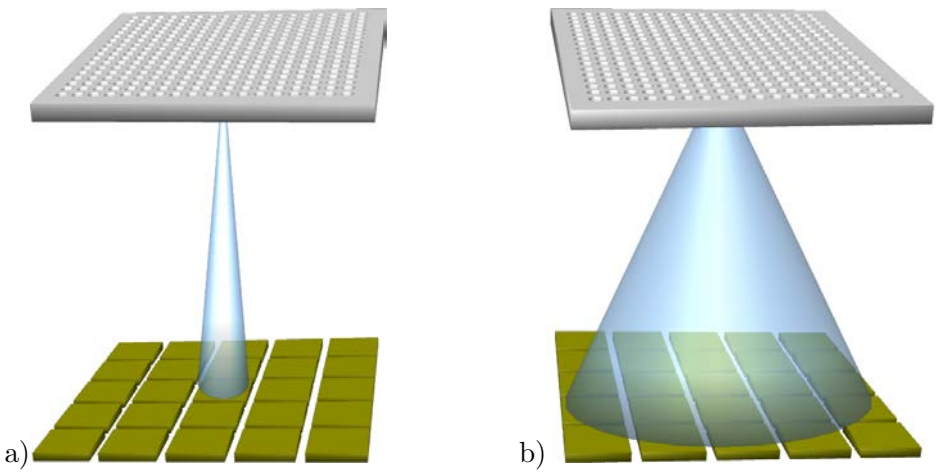

Fig. 3.13: Changing the voltage applied between the amplifying MCP and the readout stage allows to vary the footprint of the electron could: a) applying a high voltage keeps the charge cloud within one pixel of the readout for counting or integrating mode, b) applying a low voltage lets the electrons spread over many pixels of the readout in centroiding mode.

corresponding to one full frame readout. An overlap of two events would cause the centroiding to fail. So this mode may afford a reduced neutron flux, as the speed of the readout electronics is limiting the maximum neutron count rate. Centroiding can not be applied in combination with the high neutron flux necessary to reach sufficient statistics for dynamic radiography.
For the presented measurements the maximum readout rate has been 30 frames per second. An improved version using a parallel readout of the MediPix chip allows for 1200 frames per second [48]. The maximum frame rate is limited by the time it takes to readout the chip, which is 290 μs. The faster readout enables to reach higher time and spatial resolution at higher neutron flux densities.

[16] event counting per pixel

3.4.3 Time Resolution

The maximum time resolution of the MCP detector depends on neutron energy. Compared to X-rays neutrons have a low velocity, e.g. around 2200 $\frac{\mathrm{m}}{\mathrm{s}}$ for thermal neutrons. Thus it takes about 0.5 μs for the neutron to cross the detection layer of 1 mm thickness [42], [43]. As the point of interaction of the neutron inside the ^{10}B containing MCP is not know and can not be determined from the detected signal, the time resolution of the MCP detector is given by the time it takes for the neutron to cross the detection layer. Most applications of dynamic radiography aim for exposure times of 100 μs or longer. So this will only cause timing errors of less than 1 %. An electronic shutter to set the exposure time of the detector is realized by controlling the gate voltage of the amplifying MCP stack. Measurements with UV-light have shown that the timing of the gate voltage reaches an accuracy of 100 ps [42, p. 375].

3.4.4 Gamma Background

There are two reasons, why the use of neutron sensitive MCPs in combination with the MediPix readout can reach a sufficient suppression of gamma induced signals. On the one hand the sensitivity for gamma rays of the MCPs, neutron sensitive and amplifying, is kept low by the use of low-Z materials for their production. On the other hand detected gamma rays tend to generate much lower signals than neutron events. Neutrons are detected in the upmost MCP of the detector stack, as only this MCP is containing ^{10}B. Gamma rays are absorbed within the whole detector stack with approximately the same probability. The primary electron signal gets amplified on the way through the MCP stack towards the readout stage. The gain depends on the voltage applied across the MCPs and the total path through the MCP stack. Thus the average amplification of gamma induced signals is lower than the one for neutrons, which are always detected inside the first MCP. The neutron signal is always amplified by the complete chevron MCP stack. An electron multiplication of 10^6 to 10^7 is reached operating the MCP stack at standard voltages of about 1000 V to 1500 V across the channels [44, p. 280]. As gamma events result in a lower number of electrons at the readout stage, it is easy to discriminate between neutron and gamma signals by setting a threshold for the electron signal [46]. Gamma rays hitting the MediPix chip directly give rise to signals well below the threshold set for an electron avalanche signal corresponding to a neutron detection event.

3.5 Summary

Three ways are suggested by Cunningham et al. [24] to circumvent the problem of a secondary quantum sink:

≫
i) increasing the conversion efficiency of the phosphor by changing to a more efficient system
ii) improving the screen MTF to reduce optical blurring (spreading)
iii) increasing the optical coupling efficiency of the lens system by using optically "faster" (larger numerica
≪

These recommendations have been implemented to improve the detector systems applied for dynamic neutron radiography. For the scintillator based detection system following issues have been considered:

i) The use of a phosphor containing gadolinium instead of ^{6}Li as an active detection material gives rise to a higher neutron absorption efficiency. Owing to the huge neutron absorption cross section of gadolinium a Gd_2O_2S layer of only 10 μm thickness causes higher attenuation of the neutron beam than a ^{6}Li based scintillator of 150 μm thickness. Thus the primary statistics of the signal is increased and the initial loss of quanta is reduced. Unfortunately the improved detection efficiency can not compensate the lower light output per neutron of Gd_2O_2S. So there is a higher probability for generation of a secondary quantum sink.

ii) Minimizing the thickness of the phosphor layer is a straight forward approach to improve the MTF of a scintillation screen, because the spreading of light in the phosphor is proportional to its thickness. Although the light output of the scintillation screen will be reduced at the same time, the final frequency dependent DQE of the detector can be optimized, as the frequency dependent DQE is affected by the MTF to the power of two, while there is a more linear dependency of the DQE on the number of emitted photons [24], [28]. Thus it is possible that an improved MTF compensates the lower light output of the screen due to larger DQE. Given the same number of incident neutrons a better spatial resolution is reached that way as long as there is no secondary quantum sink caused by an insufficient optical coupling. This has been proven by acquiring radiographs of a resolution target using a ^{6}LiF/ZnS scintillator and a Gd_2O_2S scintillator. The same detector setup and exposure time have been applied for both radiographs (Fig. 3.14).

iii) The optical coupling between the scintillation screen and the intensified camera has been improved by bringing the imaging lens closer to the scintillation screen. At the same time the field of view of the detector has been reduced, resulting in an enlarged image of the screen on the CCD chip corresponding to a smaller pixel size on the screen. Using this detector geometry the solid angle of light, which is emitted from the converter and enters the lens, has been increased by a factor of 2.6 for a coupling lens of the same F-number. As an lens with an higher F-number has been used, this improvement has been spent to reach a higher resolution.[17]

All the effects described above are best exemplified by figure 3.14. Both radiographs have been acquired with the same settings: an exposure time of 150 s, a neutron flux of $2.6 \cdot 10^7 \frac{\mathrm{n}}{\mathrm{cm^2\,s}}$ and a FOV of 65 mm × 65 mm. The number of incident neutrons per pixel has been $3.9 \cdot 10^4$. Thus the signal statistics of the incident neutron fluence is the same for both radiographs. Only the scintillation screen is exchanged. The radiograph in figure 3.14a is taken with a ^{6}LiF/ZnS screen of 50 μm thickness and the radiograph in figure 3.14b is taken with a Gd_2O_2S screen of 10 μm thickness. The difference between the two radiographs is solely their effect on the total DQE of the detector. The images of figure 3.14 show normalized radiographs of a Gd-test-pattern. As the same scaling is applied to the normalized images to map the gray scale range from 0 to 1, the change of the contrast of the images is only due to a change of the frequency dependent DQE of the detector. There are several facts that cause a change of the frequency dependent DQE of the detector if the 50 μm ^{6}LiF/ZnS scintillation screen is replaced by 10 μm thick Gd_2O_2S one.

- An increase of neutron absorption by about a factor of 7 for the Gd_2O_2S screen compared to the ^{6}LiF/ZnS screen causes an improved detection efficiency for the first stage of the detector, because a larger number of neutrons is converted to light that way.

- Although the light yield for the ^{6}LiF/ZnS phosphor is about 40 times as high as the light yield of the Gd_2O_2S phosphor. An improved optical coupling helps to avoid a secondary quantum sink for the number of detected photons at the imaging sensor.

- A third difference between the two detector setups is the thickness of the phosphor layer of the scintillators. The 50 μm thick layer of the ^{6}LiF/ZnS scintillator causes a larger spreading of the scintillation light, which reduces the spatial frequency dependent DQE for high frequencies. This effect is visible as a loss of contrast for small features inside the test image due to the reduced signal statistics of a single pixel. The blurring is expected to be proportional to the average path length of the emitted scintillation light inside the phosphor. It is about 26 μm for the ^{6}LiF/ZnS screen and only 5.7 μm for Gd_2O_2S based one.

[17] Note that there is a difference, when talking about the number of photons emitted or transfered per detected neutron and the total number of detected neutrons. A minimum number of transfered photons causing a secondary quantum sink will limit the DQE or frequency dependent DQE of the detector. This can not be compensated by elongated exposure times or summing up images, while the total number of detected neutrons can always be increased by longer exposure times and adding up images.

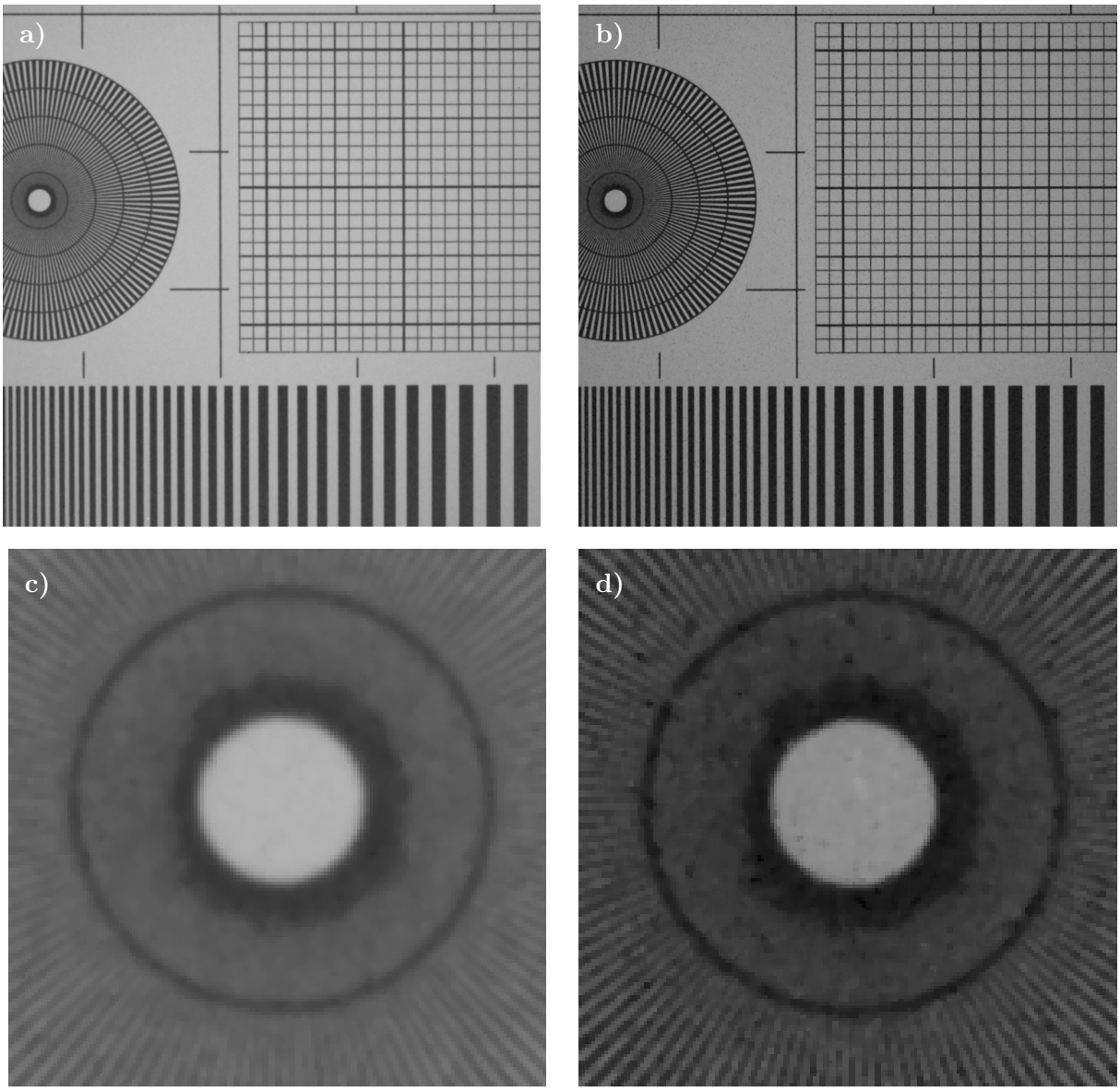

Fig. 3.14: Radiographs of a gadolinium test target (inverted gray scale): a) acquired using a ^{6}LiF/ZnS screen of 50 μm thickness, b) acquired using a Gd_2O_2S screen of 10 μm thickness, c) detail of figure a) showing the center part of the Siemens star and d) the corresponding region cut out of figure b).

Also the MCP detector has an improved characteristic in terms of DQE compared to a ^{6}LiF/ZnS based detector.

i) The detection efficiency of the detector is larger than the one of ^{6}Li phosphors, because the active MCP containing ^{10}B has a typical thickness of 1 mm, which is about ten times as thick as the phosphor layers of scintillators used for high-resolution neutron imaging [44]. After neutron detection the reaction products are directly converted to an electron signal, which is fed to an amplifying chevron stack of MCPs. This stack is mounted in direct contact to the neutron sensitive MCP. Thus there is no loss of signal statistics within the stacked MCPs [44].

ii) The spread of the signal inside the detecting MCP is inherently limited by the pore size of the channels. The center to center distance of the pores of 10 μm is even smaller than the FWHM of the light spread of thin ^{6}Li screens, or scintillation screens in general.

iii) As the amplifier and readout are in close contact to the converter there is no loss due to any coupling inefficiencies. Thus there is no secondary quantum sink, because only conversions amplifying the signal are involved.

Imaging detectors based on the principle of combining a scintillation screen and an imaging sensor with an optical coupling show benefits and drawbacks. There are three major aspects that support the application of scintillators in combination with an imaging sensor for neutron imaging.

- This kind of detector integrates the signal generated by the detected neutrons. Integrating detectors in contrast to counting ones can be operated at nearly any neutron flux. There is no limitation for high neutron flux applications as long as the imaging sensor is shielded against the present background radiation. A lower limit of the neutron flux density depends on the pixel size (integrated area), the exposure time and the background, which may be an internal background signal of the detector itself, e.g. the readout noise or the dark current signal of the sensor, or an instrument background.
- Systems using an optical coupling by a lens offer a high flexibility concerning the overall size of the detector and the field of view. This allows to change the spatial resolution of the detector quickly. For other detectors this is not possible, because the size of their sensitive area is fixed.
- Compared to other detector types they are easy to operate and do not afford complex auxiliary equipment like high voltage supplies or similar.

The major drawback is the gamma sensitivity of the imaging sensor and scintillator, which results in gamma spots generated inside the imaging sensor and a contribution of a gamma signal to the integrated signal of the detected neutrons. As this is caused by the inherent detection efficiency of the scintillation screen for gamma rays, it is not possible to differentiate between the neutron signal and the gamma signal like it is done by pulse shape analysis for single detection events inside glass scintillators coupled to photo multipliers or for the electron charge cloud detected by the MCP detector. Thus the acquired signal is not a pure neutron radiograph usually, because there is a flux contribution of gamma rays along with the neutron beam. A straightforward method to reduce the contribution of gamma radiation is to block it by filters made of lead or bismuth for example. But all filter materials have a limited transmission for neutrons, too, and filtering the gamma radiation is associated with a loss of neutron flux. Another approach is to apply neutron optical devices to redirect the neutrons but not the gamma rays, which hit a beam dump. Lowering the gamma content of the neutron beam will automatically reduce the number of gamma spots generated by gamma rays hitting the imaging sensor directly. But a filtering of gamma spots by software will always be necessary [40]. Depending on the detection reaction, the neutron wave length or spectrum and the thickness of the scintillation screen the detection efficiency of scintillator based systems is often less than 20 %. The conversion efficiency of Gd_2O_2S phosphors is limited by the branching ratio of the electron emission reaction, which is required for the emission of scintillation light subsequent to the absorption of a neutron by gadolinium. Thus the maximum neutron conversion efficiency of a gadolinium based phosphor is 75 % [21]. But it is a huge gain compared to the probability of neutrons to be absorbed by ^{6}Li inside a ^{6}LiF/ZnS layer of similar thickness. As it has already been stated by Barmakov et al. in [28] 2004 the use of thin Gd_2O_2S phosphors is advantageous whenever small FOVs, less than 10 cm by 10 cm, and high spatial resolution, below 50 μm, are required. In contrast to Barmakov et al. one should rather use the pixel size as a measure for the type of scintillator which should be applied for the measurements. In fact the pixel size, the exposure time and the conversion efficiency of the phosphor determine the incoming neutron statistics. Regardless of the DQEs of the single stages of the complete detector system this will always be the primary limitation of the detected signal. The optical coupling should be efficient enough to transfer at least several photons per detected neutron to the imaging sensor. The duty cycle of standard detectors used for dynamic radiography are very low, typically less than 1 %, when operated at continuous sources. At pulsed sources higher duty cycles could be reached even for short single exposures. But this is only possible if the process under examination can be synchronized to the pulse rate of the source, i.e. the process must be trigger-able or it has to be

operated at frequencies that are compatible with the pulse rate of the source. Only in case the optical coupling causes a secondary quantum sink it is reasonable to use a scintillation screen with higher light output per detected neutron to improve the overall frequency dependent DQE of the detector.

Chapter 4

Time Resolved Neutron Radiography

There is a steady progress of neutron imaging techniques towards higher resolution in space and time. It comes along with the improvement of detectors and the availability of more powerful neutron sources making it possible to perform measurements which were unthinkable before. There have been experiments using time resolved neutron radiography to visualize the injection process of fuel outside [38], [37] as well as inside a combustion engine or the injection nozzle [49]. But there will always be a need to push the limits a little bit further towards the desired optimum. Environment protection and fuel economy is a main aim of the improvement of modern combustion engines. This includes the fuel-mixture generation and the injection spray. Cavitation phenomena occurring inside the spray hole are important for the formation of the injection spray [50]. Many efforts are made to visualize these effects. Ambient conditions like heat, pressure or mechanical load should be close to real operation conditions of the injection nozzle. Optical methods are often not applicable, because windows or parts of the nozzle machined from optically transparent materials can not withstand the requirements of mechanical load or heat. Another standard tool for non destructive testing in industry are X-rays. They allow for an inspection of the nozzle body and the movement of the needle inside it. But they can not provide information about the behaviour of the fuel or test oil inside the injection nozzle due to a lack of contrast. Neutrons on the contrary offer a large interaction cross section for the hydrogen contained in fuel or test oil. Hence an attenuation contrast between the nozzle body made of steel and the test oil is obtained, which makes it possible to visualize the behavior of test oil inside an injection nozzle. Short time frames down to 100 μs and the necessity of high spatial resolution to resolve details inside the spray hole of a diameter of less than 200 μm are the challenges in this field of time resolved neutron radiography. Two facts opened up new possibilities to reinvestigate the behaviour of fuel or test oil inside an injection nozzle from a truck diesel engine. One is the availability of a new kind of detector which has already been described in section 3.4. It is capable to reach a spatial resolution of less than 15 μm [42], [51]. Its time resolution can be as good as 1μs for neutrons [52]. The neutrons are detected by a borated MCP and the generated signal is readout by CMOS sensor, called Medipix[1]. The second fact is that recently many neutron radiography facilities switched to scintillation screens that use Gd_2O_2S based phosphors instead of the ^{6}LiF:ZnS phosphors. The thickness of the active layer of the Gd_2O_2S phosphor is in the range of 10 μm to 20 μm. Such screens yield the highest achievable resolutions for detectors with a scintillation screen optically coupled to an imaging sensor [53]. Scintillation screens made of Gd_2O_2S are especially superior to ones made of ^{6}LiF:ZnS mixtures, when small fields of view and pixel sizes are used [28]. They offer a higher detection efficiency and reduced spatial spreading of the emitted light. This is caused by the larger absorption cross section of gadolinium compared to the enriched ^{6}Li inside the ^{6}LiF/ZnS screens and thinner phosphor layers. Section 4.1 gives an overview of the experimental setup. It is followed by section 4.2 describing the various measurements carried out using three different detector setups. The data evaluation and its results are presented in section 4.3. Finally the summary in section 4.5 completes this chapter.

[1] `http://medipix.web.cern.ch/medipix/pages/medipix2/medipix2.php`

Some suggestions for further improvements are added to the conclusions in chapter 6.

4.1 Experimental Setup

4.1.1 Radiography Facility

All time resolved radiography experiments have been carried out at the radiography and tomography facility ANTARES[2] at Forschungs-Neutronenquelle Heinz Maier-Leibnitz (FRM II)[3]. A cross sectional view of the ANTARES facility is shown in figure 4.1. At FRM II neutrons are

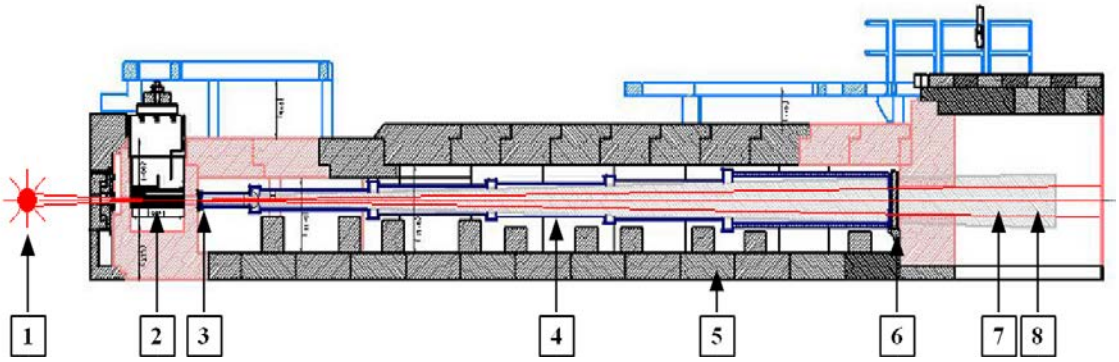

Fig. 4.1: Cross-sectional view of the radiography and tomography facility ANTARES: (1) neutron source (reactor with heavy water moderator and cold source), (2) collimator and secondary shutter, (3) optional filters and fast shutter, (4) evacuated flight tube, (5) shielding (heavy concrete), (6) beam limiter, (7) sample position, (8) detector position.

generated by fission of enriched 235-Uranium. Heavy water inside the moderator tank at a temperature of about 300 K delivers a thermal neutron spectrum. ANTARES is positioned at a beam tube looking at the cold source, which is a vessel filled with liquid deuterium at a temperature of 25 K and placed inside the heavy water moderator. The resulting neutron energy spectrum is close to a combination of two Maxwell spectra, one for thermal neutrons ($\bar{E} \approx 0.025\,\mathrm{meV}$) and one for cold neutrons ($\bar{E} \approx 0.002\,\mathrm{meV}$). The main part of the beam collimator is mounted inside the secondary shutter system. This hydraulic system allows to select three different positions: a closed position, a high collimation with a L/D ratio of 800 (effective aperture diameter: 2.15 cm) and a high flux option with a L/D ratio of 400 (effective aperture diameter: 4.05 cm). The selected aperture defines the L/D ratio according to its effective diameter. The corresponding integral neutron flux at the sample position is $2.6 \cdot 10^7 \frac{\mathrm{n}}{\mathrm{cm^2\,s}}$ for L/D 800 and $1.0 \cdot 10^8 \frac{\mathrm{n}}{\mathrm{cm^2\,s}}$ for L/D 400 [4]. A fast pneumatic shutter allows to block up to 98 % of the cold and thermal neutron flux [4]. It consists of an aluminum housing filled with boron carbide. By closing this shutter during sample positioning and detector readout the activation of the sample is minimized. A multi filter wheel allows to reduce the background of gamma radiation by lead or bismuth filters or the contribution of fast neutrons by a sapphire filter [5]. The largest effect is achieved by the Beryllium filter. It leaves a spectrum of low energy neutrons due to a Bragg edge at 3.96 Å [54]. In order to minimize transmission losses the neutron beam is guided inside an evacuated flight tube.

4.1.2 Injection Nozzle Setup

For the investigation of the injection process, more precisely the visualization of the fuel inside the injection nozzle, a dedicated sample environment is necessary, which ensures to get close to real operation conditions of the nozzle. The injection nozzle is supplied with pressurized test oil at a pressure of 1600 bar ($\widehat{=}$160 MPa) by a high pressure pump. The injection process is controlled by a

[2] ANTARES, `http://www.frm2.tum.de/en/science/radiography/antares/description/index.html`
[3] Forschungs-Neutronenquelle Heinz Maier-Leibnitz (FRM II), `http://www.frm2.tum.de`

current pulse applied to the injector. A dedicated electronic circuit generates the required signal. Adjusting three timing parameters and the corresponding current levels allows to simulate different operation modes of the injector. After the injection the atomized spray of test oil is removed by a retaining system. A vacuum pump keeps a steady flow of air around the nozzle inside the spray chamber positioned in front of the detector. Thus a build up of droplets of test oil on the walls of the spray chamber is effectively reduced. Also a deposition of the test oil inside the experimental chamber is avoided. A recuperation tank is directly attached to the spray chamber. Up to 5 liters of test oil have to be recycled during a single run of 1 hour depending on the operation conditions of the injector. Two additional oil separators, one prior and one past the vacuum pump filter remains of oil to hinder it from reaching the waste gas system. Figure 4.2 shows a sketch of the sample environment. The different components and their functions are described below. The **Fuel**

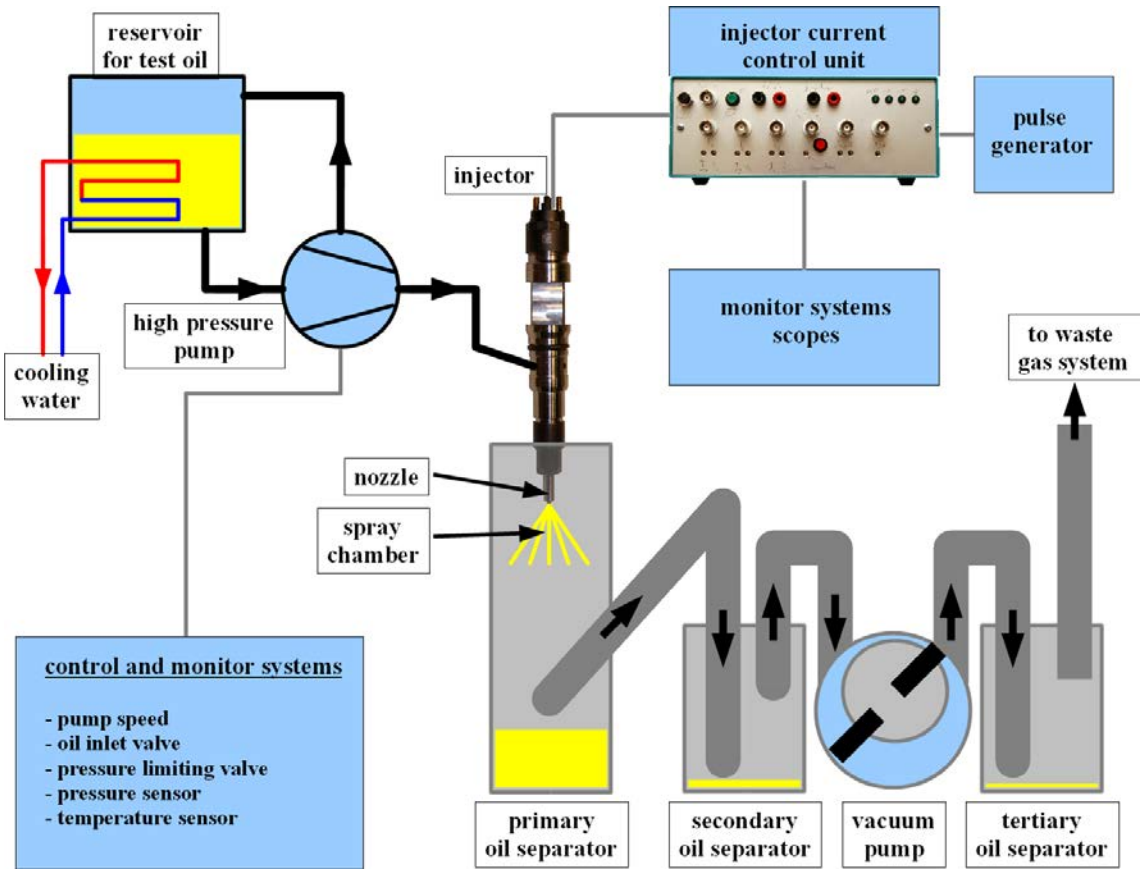

Fig. 4.2: Schematic of the sample environment necessary to operate the injection nozzle inside the experimental chamber of ANTARES. It may be divided into three major subsystems: a supply unit for pressurized test oil, the electronics for timing and control of the injector current and a retaining device for the atomized spray of test oil.

Reservoir has a capacity of approximately 15 liters. This is enough to allow for a continuous operation of the nozzle up to 1 hour. About 10 liters of test oil remain inside the tank, which is enough to secure a circulation of test oil through the pump and a thermal contact to the heat exchanger inside the reservoir. The high pressure pump is operated at an inappropriate condition of a low fuel consumption. Instead of 6 to 8 injection nozzles of 6 spray holes each only 1 nozzle with 1 spray hole is connected to the pump. This leads to an unfavorable ratio between the volume flow of consumed test oil at the nozzle and of oil recirculated to the reservoir. A high back flow rate in combination with the small volume (less than 15 liters) of test oil inside the reservoir gives rise to a fast increase of the temperature. Therefore a **Water Cooled Heat Exchanger** is mounted inside the reservoir and helps to keep the temperature of the test oil between 60 °C and 80 °C. The heat exchanger has been connected to the cooling water circulation inside the experimental hall

of FRM II. The **High Pressure Pump** is usually powered directly by the combustion engine it is attached to. But during the measurements it has been driven by an electric motor. There are two pumps built into one housing. A feed pump supplies test oil at low pressure to a second stage. This second stage is the actual high pressure part capable to produce pressures up to 2000 bar[4]. The pressurized test oil is fed to the so-called common rail and forwarded to the injector. The pressure is adjusted by the speed of the driving motor, the opening of the inlet valve of the pump and the opening of the outlet valve mounted at the common rail. The electric motor powering the pump is controlled by a variable frequency drive[5]. A remote control for the frequency drive allows to operate it from the control desk of the instrument or from inside the experimental chamber. A standard injector has been used for the measurements. Only the nozzle had been exchanged by a nozzle with one spray hole instead of 6 spray holes. This allows for a more compact layout of the spray chamber. Normally the injector is mounted inside the cylinder head of the diesel engine. The connections to the pressurized fuel and to the fuel back flow line are part of the geometry of the cylinder head. For the measurements a **Custom-Built Mounting** had been designed for the injector. Only due to this mounting is has been possible to reach a distance of less than 20 mm between the detector and the nozzle and to supply it with pressurized test oil. The **Spray Chamber** hinders test oil to hit the detector. A **Recuperation Tank** is directly attached to it acting as a primary oil separator. Via a connection to an external can the test oil can be recycled after each run. A **Secondary Oil Separator** is mounted in front of the vacuum pump to assure that no test oil enters the vacuum pump. The **Vacuum Pump** guarantees a continuous flow of air through the spray chamber. Hence the fuel spray is quickly removed from the investigated area close to the nozzle tip and the risk of of test oil condensing on the walls of the spray chamber in front of the detector is minimized. Finally a **Tertiary Oil Separator** is mounted subsequent to the vacuum pump. Rotary vane pumps may reach extreme temperatures especially if they are operated at high air throughput. Evaporating oil from inside the pump is filtered out before the air is fed to the waste gas installation. According to the data sheet of the injector the current pulse to control the opening of the injector follows a specific characteristic. This current profile can be split into three steps. For each step a different current is fed through the injector. An initial boost current causes the injection needle to be lifted. It is followed by two phases where a constant current is applied to keep the needle opened. By variation of the timing of the constant current phases it is possible to change the duration of the injection process and therefore the amount of fuel injected by a single spray. Only a single current profile has been used for the measurements at high pressures. It is illustrated by figure 4.3. Within the first 110 μs the current increases to a boost value of 25 A. During an idealized fast drop the current is then reduced to a first hold value of 15 A within 15 μs. This current is kept constant for 450 μs. Then the current is reduced to 11 A within 40 μs and is kept at this level for another 360 μs. Finally the current falls off to 0 A within 30 μs, and the needle is closed again. A custom-built **Injection Control Unit** allows to select the durations and current values for each of the three current steps during the injection. The rise and fall times are slightly tunable around a basic value set by the selected the electronic components. The principal ideas of the circuit design and its behaviour was simulated using LTspice[6]. A **Pulse Generator** sets the repetition rate of the injection process by triggering the injector control unit. The gate electronics of the detector is synchronized to this pulse, too. Several parameters of the experiment are monitored and controlled manually. Some of them are the pressure of the test oil inside the common rail, the temperature of the test oil at the outlet valve, the speed of rotation of the pump, the current through the inlet valve of the pump and the current through the outlet valve at the common rail. The timing of the detector and the proper operation of the injector are monitored by scopes. In detail these signals are the injection rate acting as trigger signal for the detector at the same time, the delay of the detector, the gate width of the detector, which

[4] Up to 3000 bar are possible under special operating conditions [55]. But standard parts are not rated to withstand such high pressure values.

[5] Toshiba VF-S7 400V-15kW

[6] LTspice IV is a high performance SPICE simulator: `http://www.linear.com`

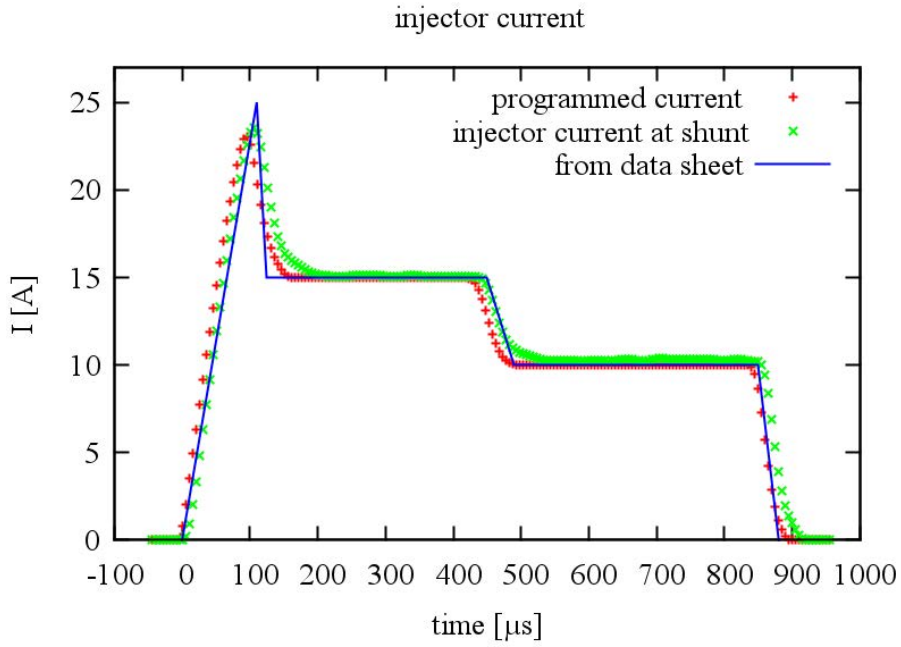

Fig. 4.3: The programmed current and the current through the injector measured at a shunt resistor are close to the idealized current characteristics taken from the data sheet of the injector.

determines the exposure time, and the control current of the injector. An automation has not been reasonable for this first test setup, as it had to be watched during operation due to safety reasons anyway.

4.1.3 Detectors

Three different detector setups have been used for time resolved neutron radiography on injection nozzles during three beam times. In-between the single beam times the injection and the detector setups have been changed to improve the results. The first detector uses neutron sensitive MCPs with CMOS readout (section 3.4). Its FOV is fixed to 14.1 x 14.1 mm^2 by the size of the Medipix readout. The second system detects neutrons by a scintillation screen with a Gd_2O_2S phosphor layer of 20 μm thickness doped with Pr,Ce,F. Two configurations of this detector system have been used, which are different with respect to the optical coupling of the scintillation light to the intensified Charge-coupled Device (iCCD) camera. The iCCD-highRes configuration employed a Nikon lens with a focal length of 85 mm and a f-number of 1.4 and the FOV has been 14.4 x 14.4 mm^2. This FOV is comparable to the one of the MCP detector. In order to improve the spatial resolution the iCCD-highRes configuration uses a modified optical coupling. A Leica APO-Macro-Elmarit-R lens with a focal length of 100 mm and a f-number of 2.8 has been used in this case, because it offered a higher optical accuracy. It has been mounted in reverse direction close to the scintillation screen. The FOV of this configuration has only been 3.47 x 3.47 mm^2. The imaged area on the scintillator is magnified by nearly a factor of 4 to the chip size of the intensified Charge-coupled Device (CCD) camera of 13.3 x 13.3 mm^2. A special mounting for the Leica APO-Macro-Elmarit-R had been designed and machined to hinder stray light to enter the intensifier of the iCCD-camera[7]. More details about this setup are found in appendix A.1. The three detector setups are shown in figure 4.4. Table 4.1 gives an overview of the detector parameters.

[7]ANDOR iStar DH734, `http://www.andor.com/`

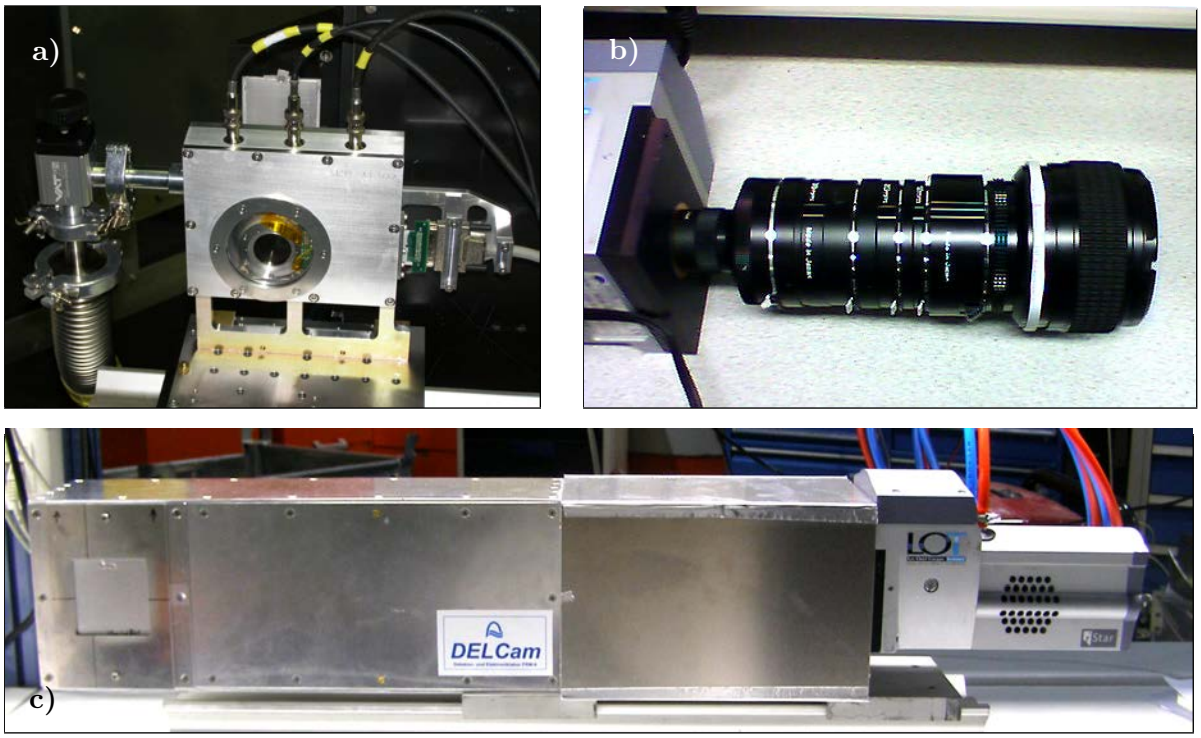

Fig. 4.4: a) MCP detector, b) iCCD-lowRes, Nikon lens mounted on the camera using extension tubes, c) iCCD-highRes setup already mounted inside the optical box.

beam time	1	2	3
detector configuration	MCP	iCCD-lowRes	iCCD-highRes
imaging sensor	CMOS	iCCD	iCCD
sensor size	$14.1 \times 14.1\,\mathrm{mm}^2$	$13.3 \times 13.3\,\mathrm{mm}^2$	$13.3 \times 13.3\,\mathrm{mm}^2$
field of view	$14.1 \times 14.1\,\mathrm{mm}^2$	$14.4 \times 14.4\,\mathrm{mm}^2$	$3.47 \times 3.47\,\mathrm{mm}^2$
magnification	1.00	0.92	3.83
active pixels	256×256	1024×1024	1024×1024
pixel size	$55.0\,\mu\mathrm{m}$	$14.1\,\mu\mathrm{m}$	$3.39\,\mu\mathrm{m}$

Table 4.1: Comparison of the detector parameters of the three individual beam times.

	average pressure bar	average temperature °C	repetition rate Hz	duration μs
MCP	372 ± 5	59 ± 3	30	400
iCCD-lowRes	1662 ± 19	62 ± 13	50	900
iCCD-highRes	1637 ± 7	77 ± 5	50	900

Table 4.2: The temperatures and pressures during the three runs of the radiography.

4.2 Measurements

This section will describe all parameters set for the injection and the detectors during the measurements. An overview and comparison of all parameters is given in table 4.3 at the end of this section.

4.2.1 Parameters for Injection Measurements

The basic parameters for the operation of the injection nozzle were discussed with the Lehrstuhl für Verbrennungskraftmaschinen (LVK) at Technische Universität München (TUM) [55], [56]. A frequency converter controlled the speed of rotation of the electric motor driving the high pressure pump. It has been set to 12.4 Hz which is equivalent to 744 rpm. This speed resulted in a minimum vibration of the pump on the sample table. The current of the inlet valve of the high pressure pump has been varied between 1.1 A and 1.4 A to adjust the supply rate of test oil fed into the pump. If the amount of test oil supplied to the pump is too low, the designated pressure at the nozzle can not be reached. Supplying the pump with too much test oil results in a large volume flow through the outlet valve of the common rail and an excessive heating of the test oil. Temperatures above 80 °C are reached within a few minutes that way. The current through the outlet valve of the common rail had to be readjusted to keep the pressure at the nozzle at a constant value. The average pressure and temperature of the test oil during the measurements is shown in table 4.2.

The pressure settings of the data acquired by the MCP detector are lower than the ones acquired with the iCCD-lowRes and iCCD-highRes configuration, because the tubing that supplied the injector with pressurized test oil could only withstand pressures up to 500 bar. By changing the tubing for the later beam times, the pressure of the test oil could be increased to 1600 bar. This pressure is comparable to the one, which is applied if the injector is mounted on an combustion engine. At the same time the standard injection nozzle with six spray holes was replaced by one with only one spray hole. In between the measurement cycles of a duration of about half an hour up to one hour the test oil had to be refilled to the reservoir of the high pressure pump. From time to time the oil separators mounted before and after the vacuum pump had to be emptied, too. Refilling the test oil including the time to stop and restart the whole setup took about half an hour. If all oil separators had to be cleaned, the measurements had to be interrupted for about one hour. It was necessary to do so after about three hours of operating the pump.

4.2.2 MCP Detector

First tests of the MCP detector to estimate the spatial resolution and signal statistics for later measurements at ANTARES had been carried out in advance at the radiography facility ICON at PSI[8]. For the measurements at ANTARES an upgraded version of the MCP detector has been available. The housing of the detector had been redesigned to bring the neutron sensitive MCP closer to the entrance window. A smaller distance of the neutron sensitive MCP to the entrance window of the detector allows to reduce the distance between the sample and the detection layer. Thus blurring effects due to the beam divergence are minimized. As the parallel readout of the

[8] `http://neutra.web.psi.ch/facility/icon_index.html`

Medipix sensor had not been available at that time, the maximum frame rate was limited to 15 frames per second. The injector was operated at a pressure of 375 bar instead of 1600 bar, which is the standard pressure of this kind of common rail injection. This limitation was caused by the preliminary tubing of the test setup, because it was rated to withstand pressures up to 500 bar only. The pressure has been kept below 400 bar to add an additional safety margin, as pressure variations had to be expected along the tubing caused by the pulsation of the injection and the mechanical stability of the tubes had been reduced by bending them to fit them to the geometry of the assembly. The electric motor of the high pressure pump has been set to a speed of 5 Hz, which is equivalent to 300 rpm. A pressure of 375 bar could be measured by the sensor mounted at the common rail already if no current was applied to the inlet valve of the high pressure pump. The current through the outlet valve of the common rail was close to 0.5 A.
A nozzle with 6 spray holes was used, which is the serial-production version of the nozzle. It was operated at 30 Hz. The distance of the injection nozzle to the neutron sensitive MCP of the detector was 4 cm. This distance could not be measured directly as the MCP was mounted inside an evacuated housing. To reduce the gamma flux at the detector position the lead filter of the ANTARES multi filter device was used. The background caused by gamma rays was determined acquiring images, while the fast shutter was closed but the primary and secondary shutter of the instrument were opened. This way the thermal and cold neutron flux was suppressed considerably and the detected signal was related to gamma rays mainly. First of all a time series using different delays was recorded to determine the start and end of the injection process. For this series the delay of the detector with respect to the trigger pulse of the injection was increased from 0 μs to 1500 μs in steps of 250 μs. The gate width was set to 500 μs. The best overlap of the gate width and the injection was observed for a delay of 750 μs. Using a fixed delay of 750 μs a larger number of on-chip integrations, 54000 trigger events, was recorded. The gate width of 500 μs was kept unchanged.

4.2.3 iCCD, Low Resolution Configuration

After an optical focusing of the detector the resolution test pattern was replaced by the scintillation screen and neutron radiographs of a Gd-test target were taken. The focus of the optical coupling of the detector was not readjusted for the neutron measurements. To check the correct operation of the gate electronics of the image intensifier radiographs were acquired using an internal trigger and an external trigger signal[9]. A series of radiographs for different time frames of the injection process was acquired starting with a delay of 200 μs up to a maximum delay of 2000 μs in steps of 200 μs. The gate width was set to 250 μs and 20 images of 60 s acquisition time each were recorded. In addition to the radiographs recorded using the full ANTARES spectrum radiographs were taken with the beryllium filter inside the neutron beam, which suppresses the neutron flux of wavelengths shorter than 4 Å effectively. Radiographs of the empty nozzle were acquired for a later normalization canceling out the nozzle material. But it turned out that the test oil can not be removed from the injector completely without disassembling it. Open beam images were taken using different settings. In order to improve the neutron statistics of the recorded data the gate width was increased to 500 μs for a series of images at a fixed delay of 800 μs. That is the same gate width as set for the measurements using the MCP detector. A total of 680 images were taken with an acquisition time of 30 s each and a repetition rate of the injection of 50 Hz. The duration of the injection was set to 950 μs. Finally open beam and dark current images were acquired again.

4.2.4 iCCD, High Resolution Configuration

The focusing of the high resolution configuration of the iCCD detector was done in two steps. First the imaging distances were adjusted with the help of an optical test target. In a second step the

[9]The gate of the image intensifier is know to fail if the high level of the trigger signal does not exceed 4.0 V, although the input is rated to accept a TTL signal.

optical test target was replaced by a scintillation screen and neutron radiographs of a gadolinium test pattern were acquired varying the imaging distances in between the radiographs. Radiographs of the gadolinium test pattern were acquired using two different scintillators in order to compare the light emission and spatial resolution. One of them employed a Tb doped Gd_2O_2S phosphor with a thickness of 10 μm. The other one had a thickness of 20 μm and was made from a Gd_2O_2S phosphor doped with Pr,Ce,F. Figure 4.5 shows the resulting images from the optical focusing, the gadolinium test pattern before the focus was readjusted with neutrons and the images after readjusting using the two different scintillators. A Gd_2O_2S scintillator doped with Pr,Ce,F of 20 μm

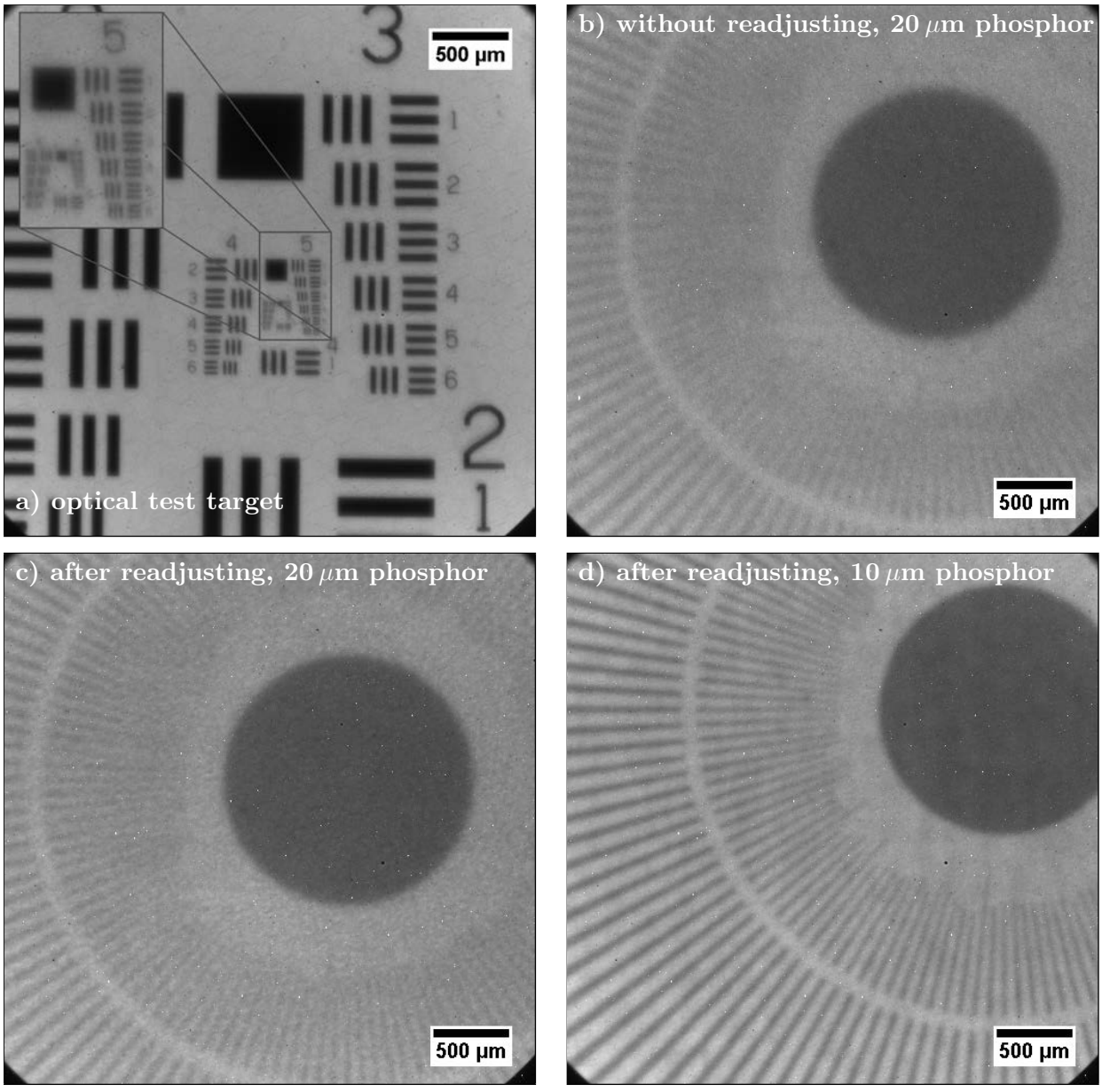

Fig. 4.5: a) The optical image of a 1951 USAF resolution test chart shows a contrast of less than 10 % for elements of group 5, which have line widths of less than 10 μm. b) Before readjusting of the focus the neutron radiograph of a Siemens star shaped gadolinium test pattern reveals that the resolution is reduced to a line width of about 50 μm. c) After readjusting the focus the resolution of the neutron radiograph acquired with a scintillator of 20 μm thickness is improved but it does not show the smallest features of the test pattern. d) When a scintillator with a phosphor coating of only 10 μm thickness is used, the smallest features of the test pattern are resolved. Their line width is about 25 μm.

thickness was mounted for the time resolved measurements, because it offered shorter decay times by more than a factor of ten than the one with a standard doping by Tb [35], [36]. When the high

pressure pump was running, vibrations originating from the pump were forwarded to the injector through the tubing supplying it with test oil. To improve this situation the common rail, which is placed between the pump and the injector and connected to either one through a thin supply tube, was mounted on a separate support instead of keeping it fixed to the pump setup (Fig. 4.6). That way it was possible to reduce the movement of the injector significantly. Figure 4.7a shows a differential image before the mechanical decoupling of the common rail. For this purpose two radiographs of the tip of the injection nozzle were acquired, one with the pump in operation and one when the pump was stopped. Measuring the width of the black and white border line allows to estimate the amplitude of the movement to be 80 μm. After the mechanical decoupling this procedure was repeated to get figure 4.7b. This shows that the decoupling has been successful.

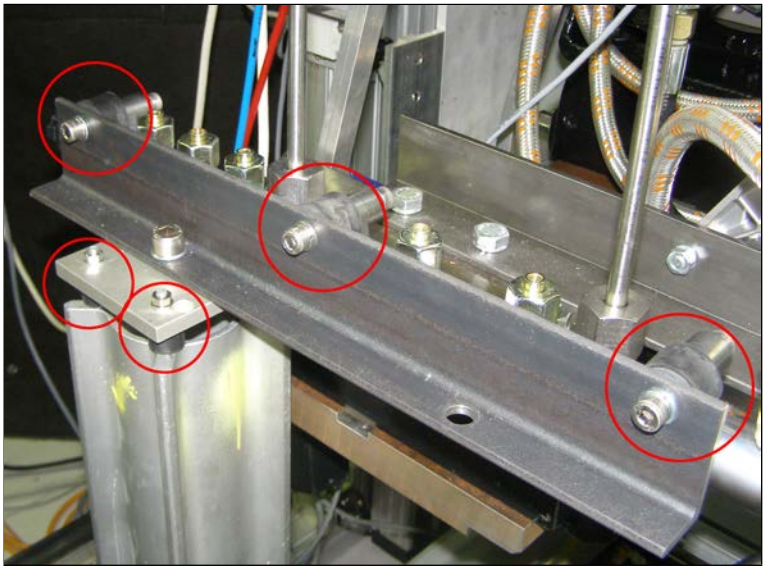

Fig. 4.6: By isolating the common rail from the mounting frame of the pump and fastening it using rubber cushions it has been possible to reduce the vibrations forwarded to the injector via the tubing.

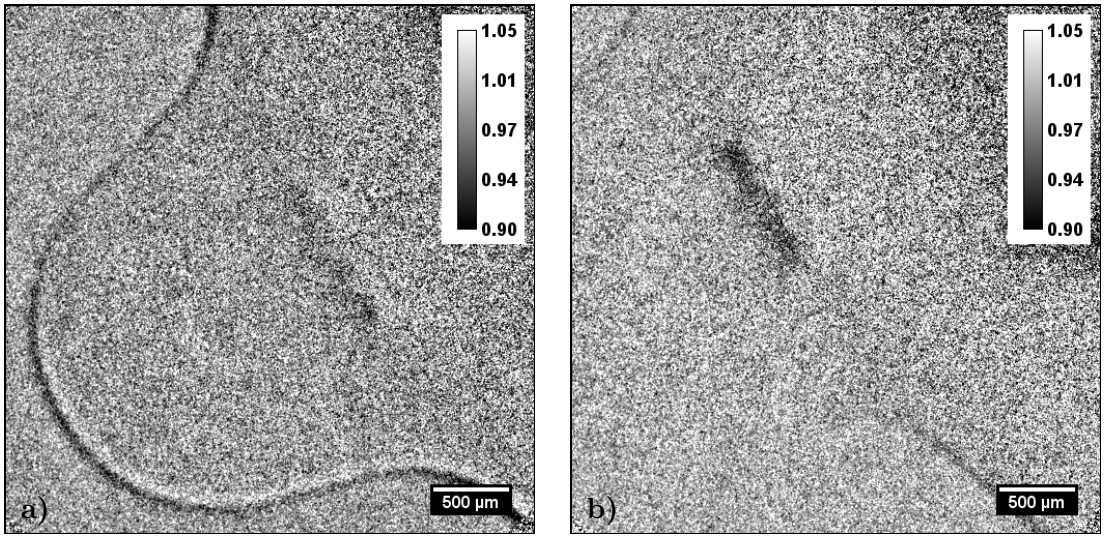

Fig. 4.7: Both images show the difference between a neutron radiograph taken while the pump for the high pressure supply of the nozzle was running and a neutron radiograph acquired while the pump was turned off. a) Before the decoupling a clear outline of the nozzle is visible inside the differential image, because of its vibrations when the pump is operated. b) After decoupling the injector from the pump the vibration of the nozzle is reduced. The outline of the nozzle is less prominent in the differential image. Note that the position of the nozzle is slightly changed after the decoupling.

parameter	MCP	iCCD lowRes	iCCD highRes
L/D ratio	400 (800)	400 (800)	400 (800)
FOV	$14.1 \times 14.1\,\mathrm{mm}^2$	$14.4 \times 14.4\,\mathrm{mm}^2$	$3.47 \times 3.47\,\mathrm{mm}^2$
detector type	borated MCP	Gd_2O_2S:Pr,Ce,F	Gd_2O_2S:Pr,Ce,F
resolution	8.1 lp/mm	8.0 lp/mm	16.4 lp/mm
	62 μm	63 μm	30 μm
imaging device	MCP	Nikon lens 85 mm	Leica lens 100 mm
magnification	1.00	0.92	3.83
pixel size	55.0 μm	14.1 μm	3.39 μm
binning	1×1	1×1	2×2
trigger delay	750 μs	800 μs	800 μs
gate width	500 μs	500 μs	200 μs
repetition rate injection	30 Hz	50 Hz	50 Hz
on-chip integrations	54000	1500	10050
effective exposure time	27.0 s	0.75 s	2.01 s
number of radiographs	4	680	300
total integration time	108 s	510 s	603 s
corresponding beam time	2.0 h	5.67 h	16.75 h
average test oil temperature	$59\,^\circ\mathrm{C} \pm 3\,^\circ\mathrm{C}$	$62\,^\circ\mathrm{C} \pm 13\,^\circ\mathrm{C}$	$77\,^\circ\mathrm{C} \pm 5\,^\circ\mathrm{C}$
average test oil pressure	372 ± 5 bar	1662 ± 19 bar	1637 ± 5 bar
control current of injector	0.0 A to 25 A	0.0 A to 25 A	0.0 A to 25 A
duration of injection	$\approx 400\,\mu$s	$\approx 900\,\mu$s	$\approx 900\,\mu$s

Table 4.3: The instrumental parameters as they were set for the measurements using the MCP detector setup and the two setups with the intensified CCD camera. The resolution was determined using an ImageJ-plugin[10].

With the high resolution configuration only radiographs for a fixed delay of 800 μs and a gate width of 200 μs were recorded. This corresponds to only one time frame of the injection process. The small FOV and the high time resolution would have required much more beam time to get data of different delays. For normalization, images of the dry injection nozzle were taken subsequent to the dynamic images. As it had not been possible to remove all the oil from the nozzle without its disassembly, the radiographs could not be taken with the nozzle at exactly the same position as during its operation. Therefore a later normalization is quite difficult. Table 4.3 gives an overview of the detector parameters and the parameters used for the operation of the injection nozzle.

4.3 Data Evaluation

4.3.1 Spatial Resolution

Radiographs of a gadolinium test target [57] have been acquired in order to determine the detector resolution. Figure 4.8 presents the images taken with the MCP detector offering a fixed FOV of $14.1 \times 14.1\,\mathrm{mm}^2$, the iCCD-lowRes configuration adjusted to a FOV of $14.4 \times 14.4\,\mathrm{mm}^2$ for comparison and the iCCD-highRes configuration with a FOV of only $3.47 \times 3.47\,\mathrm{mm}^2$.[11] The best results have been achieved by the iCCD-highRes configuration using a Leica APO-MACRO-ELMARIT-R lens with a focal length of 100 mm and an intensified CCD camera set to a field of view of $3.47 \times 3.47\,\mathrm{mm}^2$ in combination with a Terbium doped Gd_2O_2S scintillator of 10 μm thickness. All features present on the resolution test target down to about a period of 50 μm are resolved. This is equivalent to a resolution of 20 line pairs per millimeter. For a direct comparison of the

[11] Note that a different test target has been used for the measurements carried out with the MCP detector.

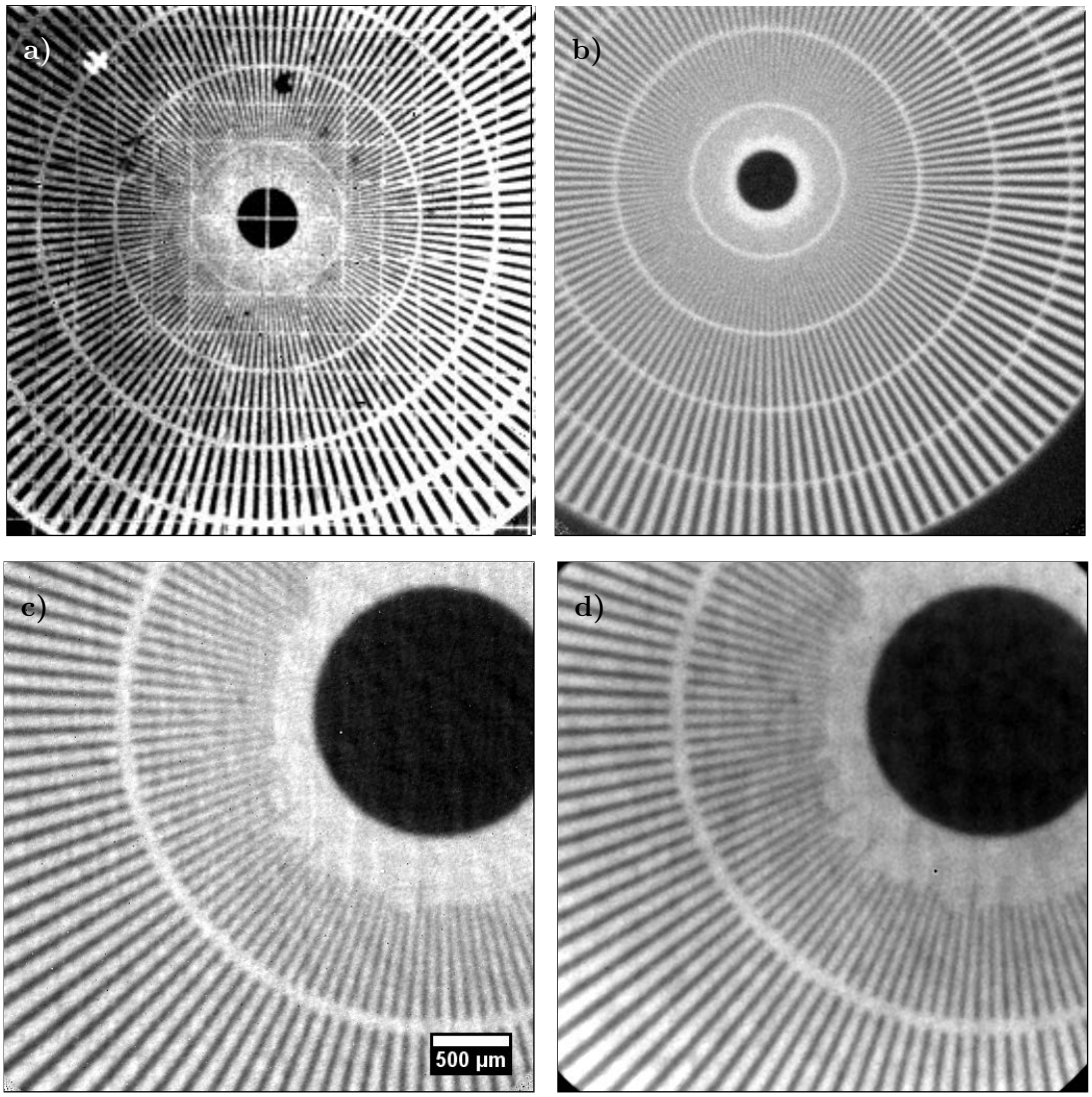

Fig. 4.8: a) Resolution test pattern acquired with the MCPdetector using standard readout corresponding to a pixel size of the detector of 55 μm and a fixed field of view of 14.1 $\times$ 14.1 mm^2. b) Radiograph of the test pattern measured using an intensified CCD camera in combination with a Gd_2O_2S scintillation screen. The field of view was set to 14.4 $\times$ 14.4 mm^2 (iCCD-lowRes) to allow for an investigation of a similar section of the sample. c) To improve the spatial resolution the field of view was reduced to 3.47 $\times$ 3.47 mm^2 (iCCD-highRes). All features of the Siemens star that are present on the test target are clearly visible now. Unfortunately the elements indicating the resolution limit of 50 μm are missing on the target. The resolution has to be determined therefore by fitting an edge spread function to the edge of the center mark. The Fit results in a width of the fitted step function of $\sigma = 20\,\mu$m. d) Same image as c) but without normalization.

different detector configurations figure 4.9 displays similar cutouts with the same scale. Therefore all images correspond to the same area of 3.47 $\times$ 3.47 mm^2, which is just the FOV of the iCCD-highRes configuration. For this configuration two gadolinium based scintillators of varied thickness and phosphor composition have been applied. Due to the larger grain size of the phosphor and the thicker phosphor layer of 20 μm the Pr/Ce/F doped phosphor [35] caused an obvious reduction of the contrast and resolution (Fig. 4.9d) compared to the Tb doped standard phosphor with a thickness of 10 μm. The MCP detector (Fig. 4.9a) shows a clear limitation due to its pixel of 55 μm. This could be overcome by operating it in a high resolution, a so-called centroiding mode. But this operation mode is not available in combination with the high time resolution that is necessary for the injection measurements. For the iCCD-lowRes configuration (Fig. 4.9b) the spatial resolution is limited by the optical coupling. The blurring introduced by the lens and the image intensifier lead to spatial resolution inferior to the one of the MCP detector although the pixel size of the

type	exposure time	incident neutrons	absorbed neutrons	total gray levels	gray levels per inc. n.	gray levels per abs. n.
100 μm, LiF/ZnS	40	6003	1381	55029	9.17	39.8
50 μm, LiF/ZnS	90	13506	1486	53480	3.96	36.0
10 μm, Gd_2O_2S	350	52522	39917	58825	1.12	1.47

Table 4.4: Depending on the thickness and the type of the phosphor of the scintillation screen different exposure times are necessary to reach the same number of gray levels at the detector output. For each detector configuration an absorbed neutron gives rise to average number of generated gray levels. In any case this number should be greater than unity. For values less than unity a secondary quantum sink causes a loss of information.

iCCD-lowRes configuration is only about one forth of the pixel size of the MCPdetector.

4.3.2 Noise and Signal Statistics

Applying a serial median or minimum filter to an image series easily filters for gamma events or hot spots on single pixels. It should be taken into account that the mean and therefore also the median gray level of each pixel inside the series is shifted to higher levels than the expected value due to the fact that gamma radiation contributes an additional signal. Thus the distribution of the gray levels for a single pixel of the series should be visualized by a histogram. A further possibility to get a corrected pixel gray level is to use the value of the highest frequency of occurrence. Especially hot spots or gamma events are not described by a Gaussian noise term of zero mean but are rather additive noise causing a shift of the mean or median to higher values [40]. Here noise is more likely to affect the mean value than the median. Using a minimum filter does certainly remove all additive noise, but it does not allow to balance the Gaussian noise.
For open beam images with uniform illumination of the detector the spread of the signal can be disregarded. It has no influence on the determination of the gray levels per detected neutron at the output of the detector, because the spread of the signal equalizes for a large homogeneous area and one gets an average signal for each pixel. This signal corresponds to the one of a zero frequency DQE without taking the spreading of light into account.
Three different scintillators have been investigated, two ^{6}LiF/ZnS screens with a thickness of 100 μm and 50 μm and a Gd_2O_2S screen with a phosphor layer of only 10 μm thickness. The filed of view (FOV) of the detector and the beam geometry has been constant only the scintillators have been exchanged. Due to different detection efficiencies and light yields the exposure times to reach approximately the same number of gray levels at the output of the detector differ for the various scintillators (tab. 4.4). In case of these measurements a simple model can be applied for the cascaded detection system splitting it into just four steps of the QAD: starting from one incident neutron, including the neutron detection efficiency of the converter, the generation of photons inside the phosphor and finally a combined step for the transfer of photons to the imaging sensor and their conversion to a charge signal expressed in gray levels. The only step including a multiplication of the number of quanta is the generation of light at the scintillator. As long as there is more than one gray level generated per one detected neutron, there is no implicit secondary quantum sink inside the detector system. This means, that the lowest number of quanta carrying information is reached directly after neutron detection. After this step the number of quanta is always larger than the number of detected neutrons. The QAD for the cascaded system described above is shown in figure 4.10. It suggests that the best statistics is reached for the Gd_2O_2S scintillator, although the signal at the output of the detector is lower than the signal of the ^{6}LiF/ZnS scintillators. The reason why the Gd_2O_2S reaches such good statistics is that the number of detected neutrons at stage 2 is higher than the one for the two ^{6}LiF/ZnS scintillators. If the diffusion of light inside the phosphor is included photons emitted at the scintillator are spread over several pixels on the detector (Fig. 4.11), e.g. assuming a Gaussian spread with a standard deviation equal to the average

a) pixel size 55.0 μm, MCP detector

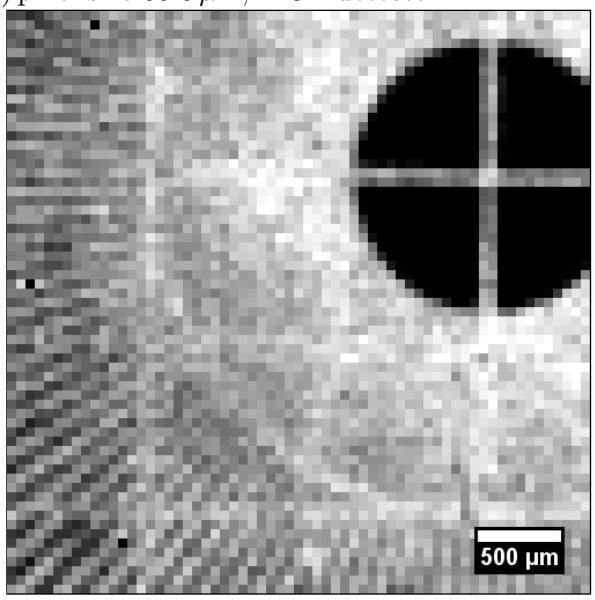

b) pixel size 14.1 μm, iCCD-lowRes

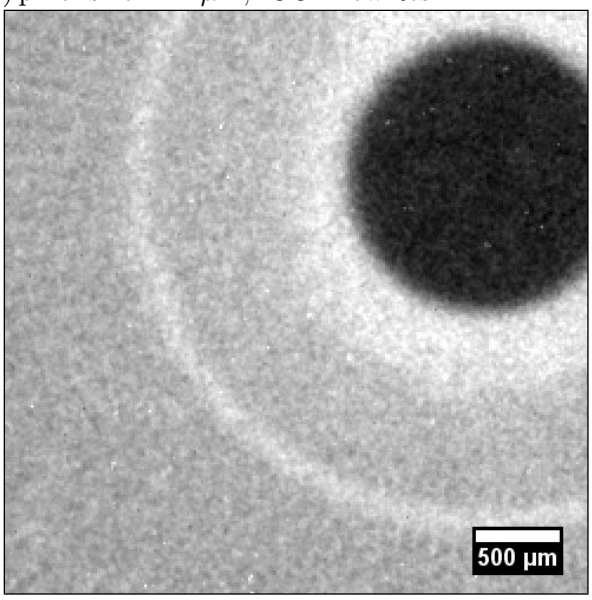

c) pixel size 3.39 μm, iCCD-highRes, 10 μm Gd_2O_2S:Tb scintillator

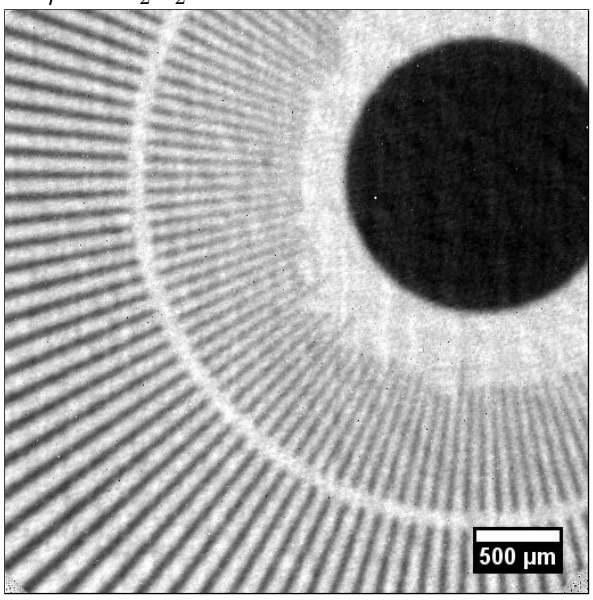

d) pixel size 3.39 μm, iCCD-highRes, 20 μm Gd_2O_2S:Pr/Ce/F scintillator

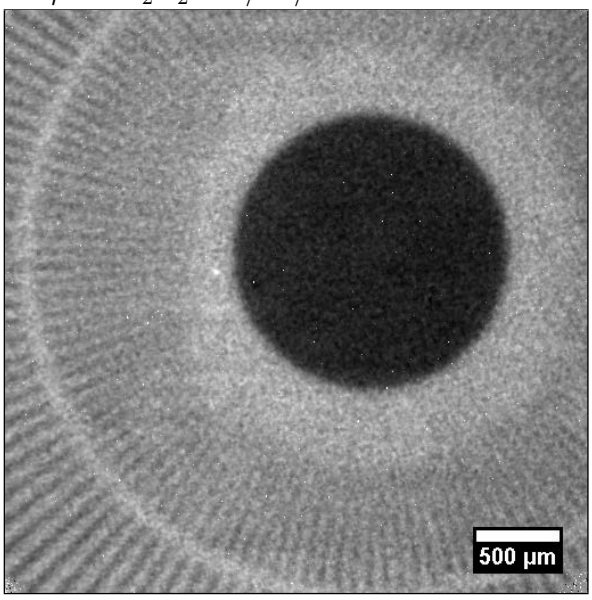

Fig. 4.9: All radiographs show the center part of a gadolinium test pattern (Siemens star). Each image corresponds to an area of $3.47 \times 3.47\,\mathrm{mm}^2$. a) The radiograph acquired with the MCP detector in normal readout mode has a clear limitation due to the pixel size of 55.0 μm. b) For the iCDD-lowRes configuration the pixel size of 14.1 μm did not restrict the spatial resolution, but two facts namely the optical coupling including the image intensifier and the inherent spread of the signal inside the phosphor layer did. c) By reducing the pixel size to only 3.39 μm and improving the optical coupling the spatial resolution could be improved for the iCCD-highRes configuration. Unfortunately the features corresponding to a period of less than 50 μm were not present on the available test pattern. d) A Gd_2O_2S scintillator doped with praseodymium, cerium and fluorine was used to reach a higher time resolution. The thickness of its phosphor layer of 20 μm caused a reduction of the spatial resolution.

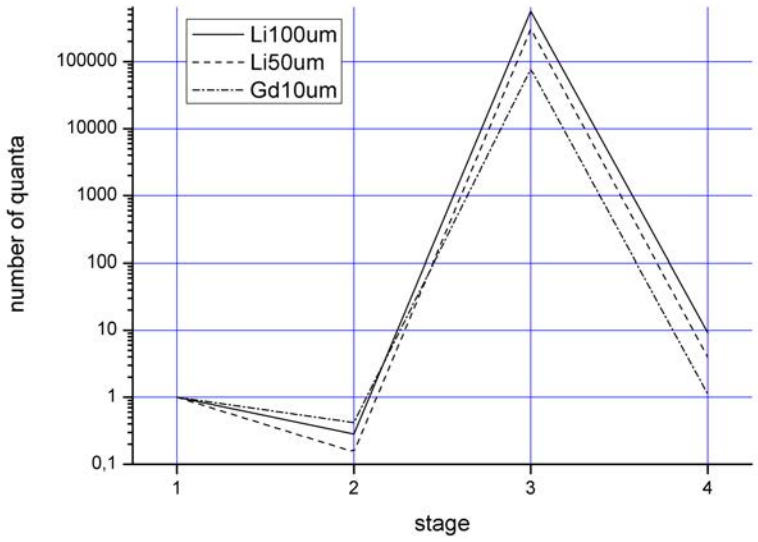

Fig. 4.10: The QAD plot shows, that the minimum number of quanta carrying information for all scintillators is reached for stage 2 and corresponds to the number of absorbed neutrons. This is the case as long as a blurring inside the scintillation screen is not taken into account. The best choice would be the Gd_2O_2S screen here.

path length of the light inside the phosphor (Sec. 3.3.2), an additional step is included to the QAD plot after the generation of light. This is closer to the situation for real radiographs, when the

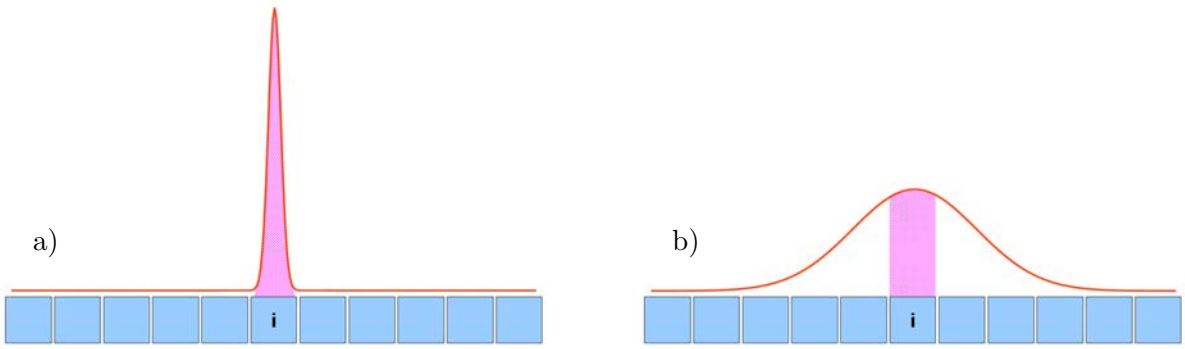

Fig. 4.11: a) If there is no spread of the signal, all photons emitted at the scintillation screen will reach pixel i of the detector. b) Including a spread of the signal only a fraction of the photons emitted by an area corresponding to pixel i will reach this pixel.

spread of light inside phosphor or a blurring caused by the the optical coupling reduces the number of quanta, photons here, that reach the pixel at the imaging sensor. The reduced number of quanta at the output of the detector results in a reduction of the SNR at the output of the detector due to two effects: The spread of the signal diminishes the number of quanta carrying information that reach the detector pixel they correspond to and therefore the signal is reduced. The signal that does not reach its corresponding pixel, but is detected by a neighboring pixel instead, acts as a background signal. Thus the background of these pixels is increased while the detected signal is lower. In total the SNRis reduced. For a corresponding QAD including the diffusion of light see figure 4.12. A model for the signal spread due to the blurring caused by the scintillation screen is based on the following assumptions: The diffusion of light inside the phosphor layer of the

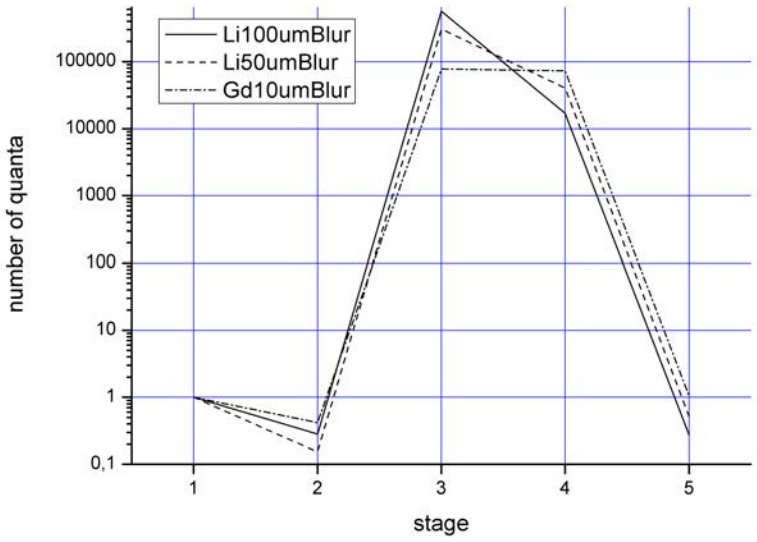

Fig. 4.12: If the diffusion of light inside the phosphor layer of the scintillation screen is included. The number of photons generated at stage 3 is now reduced at stage 4 to the number of photons that reach the pixel they correspond to. At output of the detector, stage 5, the highest signal is now reached by the Gd_2O_2S scintillator.

scintillation screen causes a Gaussian shaped spread of the signal with a standard deviation σ given by the average path length of the light inside the phosphor layer of the applied scintillator, as the scintillator is the main source causing a spread of the signal. The percentage of quanta that still reach the appropriate pixel is estimated by an integral of this point spread function over the area of one pixel. The remaining number of quanta contribute to the background signal of the other pixels. The again illustrates the progress of the signal statistics from the input of the detector to the output. In contrast to evaluating a region of interest, only the signal statistic of single pixels is of interest here. It is important to keep the focus on a single pixel, or in other words on the DQE for high frequencies if the aim is to achieve the best resolution.

4.3.3 Visualization of Fuel Inside the Injection Nozzle

The visualization of fuel inside an injection nozzle, while it is operated at standard parameters, has been the main aim of the dynamic neutron radiography measurements. Instead of diesel oil, Shell V-oil 1404[12], has been used during the measurements due to security issues. Like diesel oil or petrol this test oil shows a high attenuation of the neutron beam. This is caused by the large scattering cross section of the hydrogen, $82,02$ barn [10], contained in the test oil. The orientation of the injection nozzle with respect to the neutron beam is shown in figure 4.13. The primary intention for this alignment of the nozzle was, that the spray hole of the nozzle could be positioned nearly vertically that way. This is necessary to allow for a quick removal of the spray from the spray chamber. To do so the whole injector was turned around the neutron beam axis with respect to its upright position. A second reason for such an orientation of the nozzle was to bring the spray hole as close to the detector as possible to reduce the effect of geometric blurring due the (local) divergence of the neutron beam. Therefore the nozzle was turned around the center axis of the spray hole. This rotation allowed to bring the tip of the nozzle closer to the detector. Due to the geometry of the nozzle body such an orientation may cause an overlay of the spray hole and different edges of the nozzle tip inside the radiograph. Figure 4.14 shows cuts through the tip of the injection nozzle for a plane parallel to the neutron beam and the center line of the spray

[12]This is a special test oil for diesel injection systems. It has a higher flash point than diesel oil.

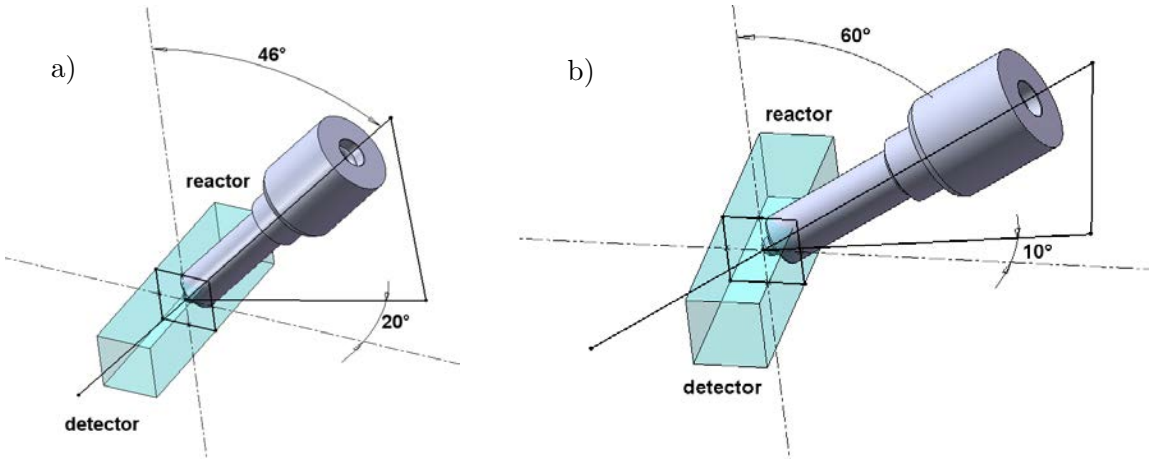

Fig. 4.13: Different orientations of the injection nozzle with respect to the neutron beam have been used for the two beam times with the intensified CCD camera: a) orientation of iCCD-lowRes, b) orientation of iCCD-highRes.

hole. The variation of the neutron path length through the steel body is illustrated by red lines for some rotation angles around the center axis of the spray hole. Here larger angles allow to bring the nozzle tip closer to the detector. But at the same time the neutron path length through steel is increased by up to a factor of four. For any orientation the nozzle body itself produces a

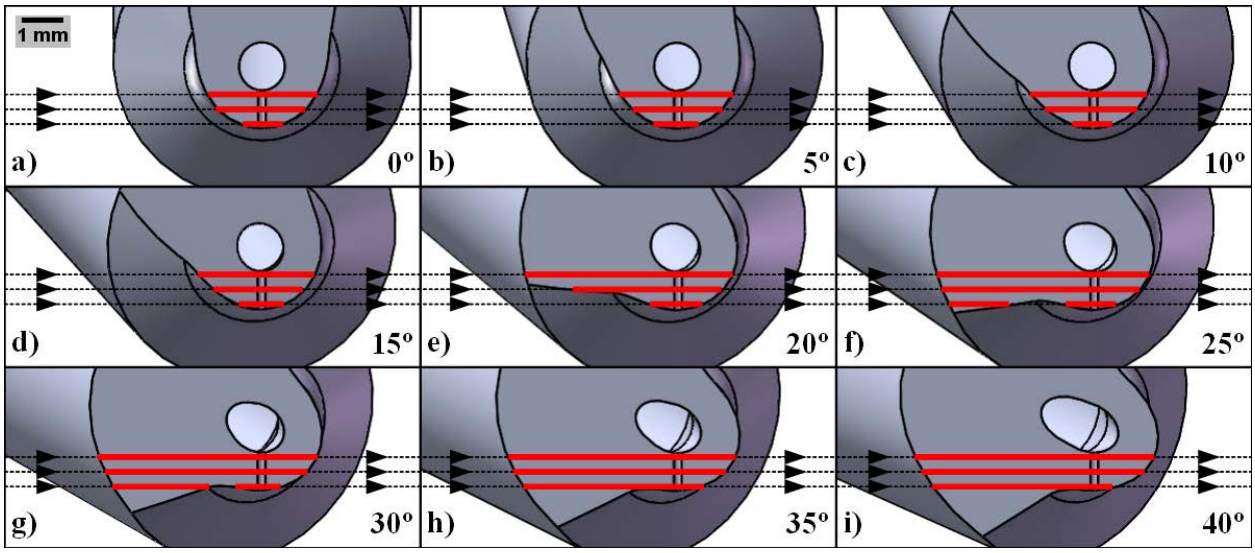

Fig. 4.14: The injection nozzle is inclined towards the detector to minimize the projection distance in order to reach a higher spatial resolution. Each of the images corresponds to a cut through the nozzle tip at the center of the spray hole in neutron beam direction. The path length for three example paths (red lines) is shown depending on the angles the nozzle is inclined with respect to the detector plane. For angles in the range of 0 ° to 15 ° there is only minor change of the path lengths: images a) to d). But as soon as the angle gets larger than about 20 ° the neutrons have to cross much more material of the nozzle body: images e) to i).

non uniform transmission signal. The intensity variations of the transmitted neutron beam due to this effect are higher than the attenuation caused by the test oil inside the spray hole. Although already a thin layer of test oil gives a good contrast in front of a uniform background, the intensity variations caused by the nozzle body hinder to set a narrow window for the transmission values in order to enhance the contrast of the test oil inside the spray hole. For a comparison of the expected attenuation some calculated values for steel up to a thickness of 4 mm and for test oil up to a thickness of 200 μm are shown in table 4.5. The attenuation is calculated according to the

(a)

thickness of steel d, mm	0.5	1.0	1.5	2.0	2.5	3.0	3.5	4.0
attenuation $A(d)$, %	6.76	13.1	18.9	24.4	29.5	34.3	38.7	42.9
ΔA, %	±0.33	±0.61	±0.85	±1.05	±1.23	±1.38	±1.50	±1.60

(b)

thickness of oil d, μm	10	20	50	100	200
attenuation $A(d)$, %	0.64	1.3	3.1	6.2	12
ΔA, %	±0.03	±0.06	±0.15	±0.28	±0.53

Table 4.5: Attenuation caused by steel (a) and test oil (b) for different thicknesses.

linear attenuation law

$$A(d) = 1 - \exp\left(-\Sigma_\mathrm{t}\, d\right). \tag{4.1}$$

A neutron wavelength of 4 Å is assumed for neutron absorption. As the composition of the steel the nozzle is made of and the test oil is not known precisely, the uncertainty of the total macroscopic cross section $\Delta\Sigma_\mathrm{t}$ is assumed to be ±5 %. The variation of the attenuation is given by

$$\Rightarrow \Delta A = \frac{\mathrm{d}A}{\mathrm{d}\Sigma_\mathrm{t}}(d) \cdot \Delta\Sigma_\mathrm{t} = d \cdot \exp\left(-\Sigma_\mathrm{t}\, d\right) \cdot \Delta\Sigma_\mathrm{t}\,. \tag{4.2}$$

The different thicknesses of steel close to the position of the spray hole gives rise to variations of the neutron transmission signal of more than 40 %. Small changes of the transmitted neutron signal in the order of only a few percent due the test oil are hard to be recognized. Therefore it is important to have a possibility to correct the acquired data for a variation of the neutron attenuation caused by structure material, like the steel body of the nozzle, which is not of interest for detailed investigations. Three options are compared to remove the influence of the nozzle material inside the radiographs taken from the injection nozzle: a normalization using a second radiograph, a normalization using a calculated radiograph and a normalization using a simulated radiograph.
The basic idea of all these methods is to emphasize the attenuation signal caused by the test oil. According to equation (2.20) the transmitted neutron signal at position (x, y) at the detector may be written as:

$$T(x,y,t) = I_0(x,y,t)\, \exp\left(-\int_{C_\mathrm{S}} \Sigma_\mathrm{t}(x,y,s,t)\,\mathrm{d}s\right). \tag{4.3}$$

Where $\Sigma_\mathrm{t}(x,y,s,t)$ includes the attenuation caused by the nozzle body as well as the attenuation caused by the test oil inside the nozzle. Splitting $\Sigma_\mathrm{t}(x,y,s,t)$ into contributions of the oil $\Sigma_\mathrm{oil}(x,y,s,t)$ and the nozzle body $\Sigma_\mathrm{body}(x,y,s,t)$ allows to rewrite equation (4.3).

$$T(x,y,t) = I_0(x,y,t)\, \exp\left(-\int_{C_\mathrm{S}} \Sigma_\mathrm{body}(x,y,s,t)\,\mathrm{d}s\right)\, \exp\left(-\int_{C_\mathrm{S}} \Sigma_\mathrm{oil}(x,y,s,t)\,\mathrm{d}s\right). \tag{4.4}$$

From this it is obvious that it is possible to solve the equation for the transmission of the test oil if the transmission signal of the empty nozzle

$$T_\mathrm{empty}(x,y,t) = I_0(x,y,t)\, \exp\left(-\int_{C_\mathrm{S}} \Sigma_\mathrm{body}(x,y,s,t)\,\mathrm{d}s\right) \tag{4.5}$$

is known. Then the transmission of the test oil is given by

$$\begin{aligned}\frac{T(x,y,t)}{T_\mathrm{empty}(x,y,t)} &= \frac{I_0(x,y,t)\, \exp\left(-\int_{C_\mathrm{S}} \Sigma_\mathrm{body}(x,y,s,t)\,\mathrm{d}s\right)\, \exp\left(-\int_{C_\mathrm{S}} \Sigma_\mathrm{oil}(x,y,s,t)\,\mathrm{d}s\right)}{I_0(x,y,t)\, \exp\left(-\int_{C_\mathrm{S}} \Sigma_\mathrm{body}(x,y,s,t)\,\mathrm{d}s\right)} \\ &= \exp\left(-\int_{C_\mathrm{S}} \Sigma_\mathrm{oil}(x,y,s,t)\,\mathrm{d}s\right)\end{aligned}$$

which is the transmission signal acquired with oil inside the nozzle divided by the transmission signal without oil inside the nozzle. This normalization is similar to the standard data correction of neutron imaging described in section 2.1.2. There are different ways though to get the transmission values corresponding to an empty nozzle.

Normalization by a Second Radiograph The easiest and straight forward approach is to use a radiograph of the empty nozzle without oil inside the spray hole. A radiograph of the empty nozzle can be taken in steady state mode, which allows for a better signal statistics, because the effective exposure time is equal to the acquisition time and a duty cycle close to 100 % is reached. Compared to a duty cycle of only 2.5 %, when the camera is operated in a stroboscopic mode to acquire the dynamic neutron radiographies. The number of detected neutrons is increased by a factor of 40 for the same acquisition time that way. The average of the radiographs of the injection process acquired at a certain time delay is then normalized using the steady state radiograph. Another possibility is to use the average of an image series taken in dynamic mode at different delays to normalize single images of this series. The resulting normalized image will only enhance the differences between the two time frames. Instead of using a radiograph of the empty nozzle a radiograph with a different delay corresponding to a different time frame of the injection process can be used. That way it is possible to highlight only deviations from the average. In case of the injection measurements this might be reduced density of test oil inside the nozzle due to cavitation or an irregularity of the movement of the needle inside the nozzle. In practice a normalization using a radiograph of the empty nozzle has a drawback, as the attenuation of the neutron beam by the steel of the injection nozzle results in a reduced statistics of the measured signal. This leads to a higher noise contribution for parts of the radiograph where a lower transmitted signal is used to normalize the radiograph of the nozzle filled with oil. To keep the error during the normalization at a minimum one should use the raw data of the filled and the empty nozzle without prior corrections for the beam profile or the detection efficiency. For the normalization one has to ensure that the position of the filled and the empty nozzle match with high accuracy. When it comes to visualization of fuel inside the spray hole, whose diameter is less than 200 μm, an exact positioning of the empty nozzle is most important. Already a shift of only a few micrometers is comparable to the pixel size of the high resolution configuration iCCD-highRes. Even if the nozzle is kept mounted during the whole time, shifts of the injection nozzle of a few micrometers can hardly be avoided. For example a thermal expansion of the injector may cause the nozzle to move. Assuming that the injector can reach temperatures equal to the temperatures of the test oil of 60 °C, a temperature difference ΔT of 20 K between individual runs is realistic. Due to this temperature change the whole injector may expand by approximately 50 μm (App. A.3). This can already cause a movement of the spray hole by 25 % of its diameter. Even an expansion of the injection nozzle due to the applied pressure should be taken into account. The pressure of the oil reaches 1600 bar, which will result in an increase of the inner diameter of the injection nozzle by 5.06 μm and a change of the outer diameter by 3.16 μm (App. A.4). Any shift of the nozzle during the measurement makes it necessary to align the projections of the nozzle by software for normalization. This causes patterns to be enhanced which arise from inhomogeneities of the neutron beam or the detector efficiency, e.g. a structure of the scintillator (Fig. 4.15a). The resulting pattern inside the corrected radiograph has a standard variation of 1.8 %. A line profile of the open beam region marked in figure 4.15a is shown in figure 4.15b. This variation is already comparable to the attenuation associated with the test oil inside the spray hole. It is therefore necessary to normalize the radiographs of the filled and the empty nozzle by open beam images first to correct for the patterns due to an inhomogeneous detection efficiency or inhomogeneities of the detector readout. It is difficult to acquire a radiograph of the nozzle without oil inside it. This is due to the fact that it is impossible to remove all test oil from the nozzle without disassembling the injector. The series of images in figure 4.16 shows the progress of cleaning the nozzle tip several times. Remains of oil inside the nozzle cause artifacts during the normalization process. These artifacts suggest areas of low attenuation inside the oil filled areas and might be misinterpreted e.g. as air bubbles, which are not present in reality. As

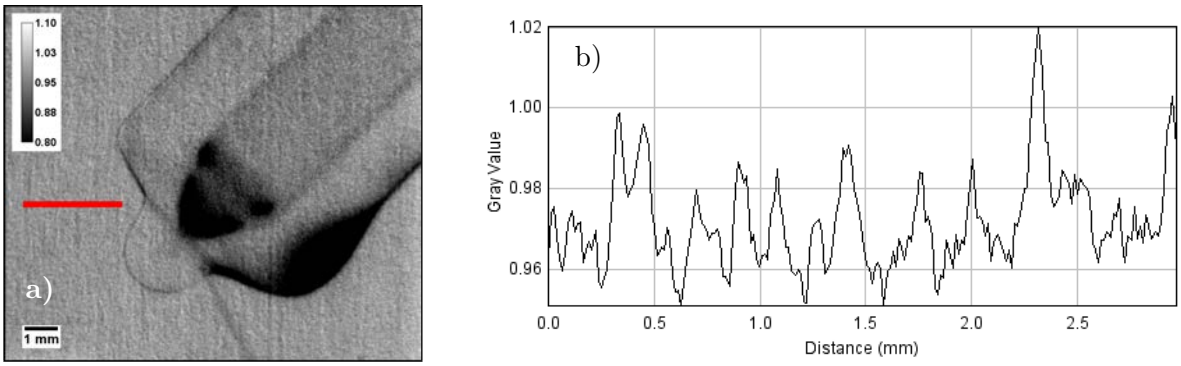

Fig. 4.15: a) Normalized radiograph corrected using a radiograph of the empty nozzle. The structure of the phosphor layer of the scintillation screen gets visible, because it is necessary to shift one of the two images to achieve an overlay of the nozzle body. b) Line profile (corresponding to red line on the left) showing the variation of the background caused by the structure of the scintillation screen.

one of the principle interests of such investigations is the visualization of cavitation phenomena, those artificial voids would completely corrupt the results. Disassembling the nozzle to remove the oil means to remove it from its mounting at the instrument. It is not possible then to place the injection nozzle at the same position with an accuracy of a few micrometers after reassembling it.

Normalization by a Calculated Radiograph Using calculated values for data treatment has some advantages. First of all calculated data show less noise. Thus the errors introduced by data treatment are small compared to the uncertainties associated with measured signals. A second benefit of calculated data is the possibility to restrict them to certain parts of the sample. Thus some parts may be masked during the evaluation in order to enhance the contrast for the parts of interest. In case of the injection nozzle for example it is possible to use a model with or without test oil inside the nozzle. Further not all details of the sample have to be modeled. This helps to enhance those features inside the radiograph which were not included in the calculation. For example the spray hole at the tip of the injection nozzle can be omitted for the calculation, so it and especially the test oil inside it will be enhanced. A third point that should be considered in this context is the possibility to change the parameters for absorption and scattering of each material inside the model. That way the influence of both effects can easily be separated. Based on this technique it is also possible to estimate the scattered intensity that reaches the scintillation screen. This is of interest for samples where the main part of attenuation is caused by scattering rather than absorption. As the scattered intensity is calculated separately, the measured data may be corrected for the expected scattered intensity during the evaluation process. A drawback of this method is, that it is necessary to create a detailed model of the sample including its physical dimensions and elemental composition of all parts. Here the determination of the composition can be a quite challenging part. Only if the geometry of the model is in good agreement with the geometry of the sample, the normalization does not yield artifacts at the edges of the sample.

Normalization by a Simulated Radiograph A simulation of the radiographic image of the sample by Monte Carlo methods and using it to normalize the measured data provides similar advantages as the normalization by a calculated radiograph. The effort to prepare a model of the sample is comparable to the one necessary to create the model for calculation. But the simulation is more time consuming than the calculation. This is due to the fact that effects like multiple scattering and an energy dependency of the interaction of the neutrons with the sample are taken into account, too. Thus the simulation is kept closer to the real experiment than the calculation. Data based on Monte Carlo methods still posses statistical fluctuations. But spending an adequate time for computing these fluctuations can be minimized, so that the standard deviation of the simulated transmission values is much smaller than the noise of the transmission values of the

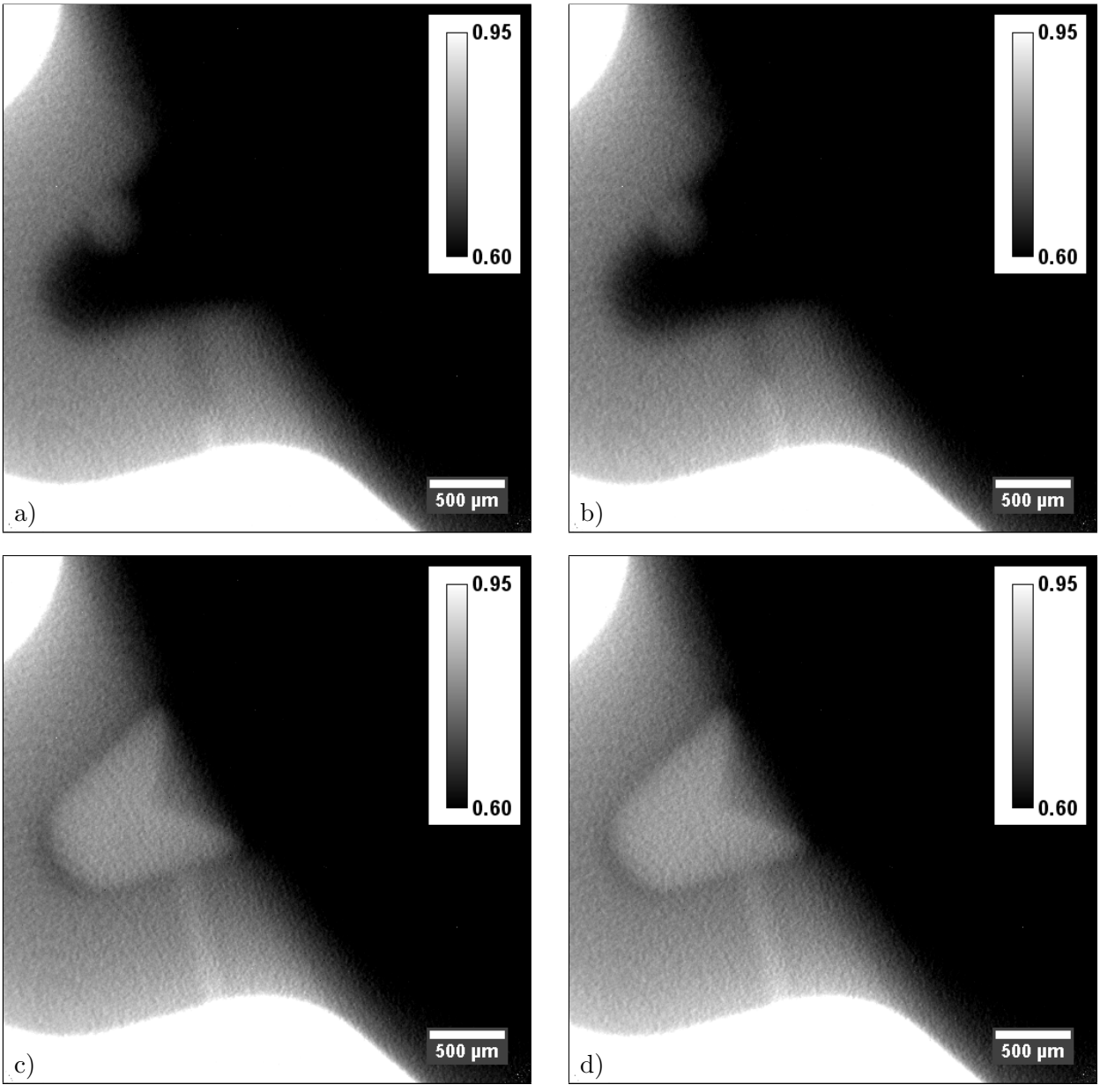

Fig. 4.16: a) nozzle wiped clean by cloth, still there is oil inside the nozzle tip and the spray hole; b) cleaned again using cloth, some of the oil inside the spray hole could be removed; c) nozzle tip cleaned with alcohol and pressurized air, some remains of oil are still visible inside the nozzle tip; d) once again pressurized air and alcohol were used to clean the nozzle tip, nearly all oil is removed, but not completely.

measured data. Therefore the simulated data do not add a significant uncertainty to the final result of the normalization process.

4.4 Results

4.4.1 MCP Detector

For data taken with the MCP detector the normalization process differs slightly from the standard described in section 2.1.2. The Medipix readout uses a threshold to discriminate between neutron signals and gamma signals. Single neutron events are counted instead of integrating the generated charge signal. As each count is equivalent to a detected neutron, there is no need to subtract a background signal or to correct for dark current signals. But it is important to correct for inhomogeneities of the detection efficiency. Burn in effects may occur if the detector is not preconditioned and directly used in a high neutron flux density with long exposure times. In figure 4.17a an open beam image with a non-uniform detection efficiency is depicted. Such effects, also called burn up, are known for detectors working with scintillation screens, too [37, p. 32]. For a MCP-detector with a preconditioned multi channel plate the detection efficiency is quite homogeneous. Figure 4.17b shows a radiograph acquired during 1800 s, which corresponds to an effective exposure time of only 27 s due to the repetition rate of 30 Hz and the gate width of 500 μs. The delay was set to 750 μs for a time frame during the injection process. For the raw data the burn in structure of the detector is still visible. It is removed after normalization with the open beam image (Fig. 4.17c). The circular and line shaped structures in the normalized image are caused by additional covers, which had to be used, because the nozzle for this first test was from serial production and equipped with six spray holes instead of only one. There is an overlay of the six injection sprays. Thus there seem to be only three sprays: one to the left, one to the bottom and one in neutron beam direction towards the detector. The result of a normalization using a second radiograph is shown in figure 4.17d. The second radiograph has been acquired for a delay of 0 μs before the start of the injection. Therefore the injection sprays are enhanced here. As the second radiograph has been acquired with the beryllium filter in the beam, the edges of the nozzle body are highlighted, too. This is caused by the different absorption and refraction behaviour of the two neutron spectra with and without the beryllium filter. The only limitation for MCP detector is its fixed spatial resolution defined by the pixel size of the readout. Due to the counting mode of the detector there is a good contrast for the injection spray for short exposure times already. For the MCP data only a normalization using a second radiograph has been applied, because the models for calculation or simulation of a radiograph of the nozzle have only been built for the final setup using a nozzle with only one spray hole.

4.4.2 iCCD-lowRes

The measurements with the intensified CCD camera in the low resolution configuration iCCD-lowRes have been carried out using a FOV equivalent to the one of the MCP. A radiograph normalized by an open beam image and the same radiograph corrected for the attenuation of the nozzle body using a calculated radiograph are presented in figure 4.18. The normalized radiograph corresponds to the median of 50 radiographs each composed of 1500 on-chip integrations acquired for a delay of 800 μs while the nozzle has been in operation with a repetition rate of 50 Hz. All images use a logarithmic scale for the representation of the color scheme. The corrected image (Fig. 4.18b) does not yield a perfect extinction of the nozzle body, but it helps to improve the visibility of the test oil inside the nozzle. Some reasons why the outline of the nozzle is still clearly visible are the deposition of test oil on the outside of the and possibly a slight mismatch of the nozzle geometry or the parameters used to model the steel of the nozzle body. The corresponding images for a correction with a simulated radiograph are shown in figure 4.19. The Monte Carlo simulation models the transmission signal of an injection nozzle without test oil inside and without the geometry of the spray hole (Fig.4.19b). As the simulation resulted in an upright position of the

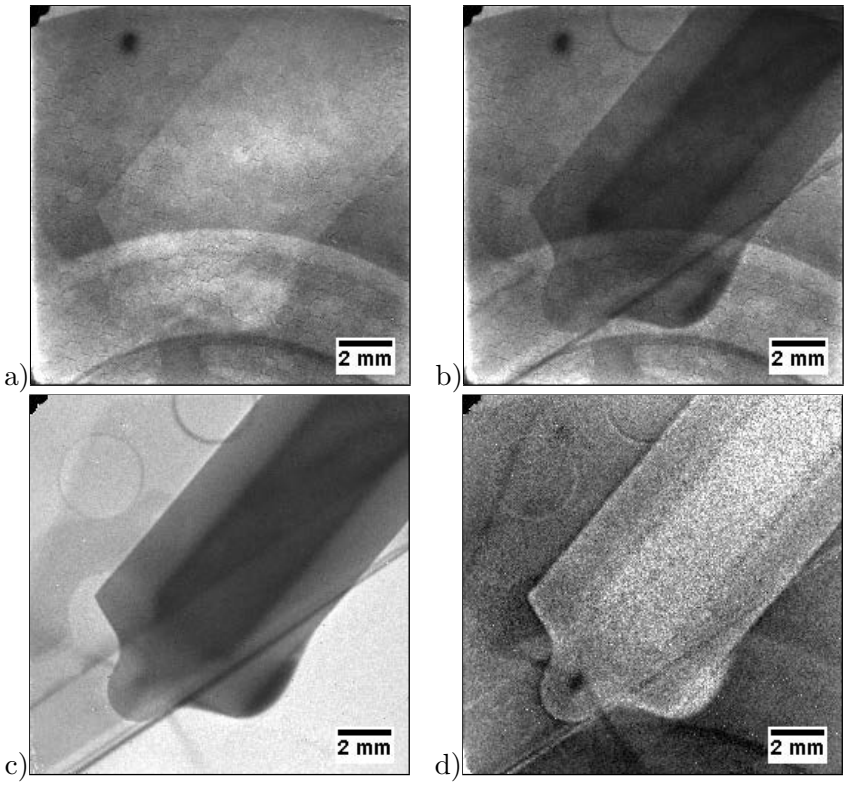

Fig. 4.17: a) open beam image with burn in effect, b) radiograph acquired during the injection process, c) normalized radiograph of the injection process with visible injection spray, d) normalized radiograph corrected for the effects of the nozzle material using a second radiograph, which was acquired with the beryllium filter in the beam.

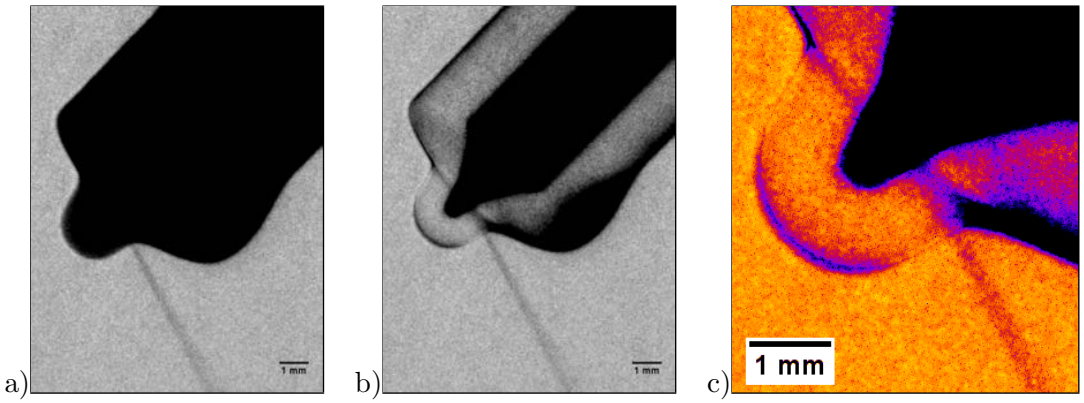

Fig. 4.18: Radiographs using a logarithmic scale for the gray values of the images. A calculated model of the injection nozzle has been used for the correction of the geometry of the nozzle body. a) A normalized radiograph without any correction of the geometry of the nozzle body. b) The same radiograph including the correction of the geometry of the nozzle body. c) An enlarged detail of b) using a different color scheme.

nozzle, the normalized radiograph (Fig. 4.19a) has been rotated accordingly. Therefore he spray hole marked by the injection spray outside of the nozzle is now orientated to the right side of the image. After the correction the transmission of the structure material of the nozzle is close to unity (Fig. 4.19c). Thus the right material composition has been assumed for the steel of the nozzle body. Also the geometry of the model used to calculate and simulate the radiographs must precise enough, as the outline of the nozzle body is only slightly visible. But the position of the spray hole and the test oil is vaguely perceptible although the same calibration and a logarithmic scale are applied for the corrected image. Differences between the calculated and the simulated radiograph may arise from the fact that the simulation includes scattered neutrons and energy

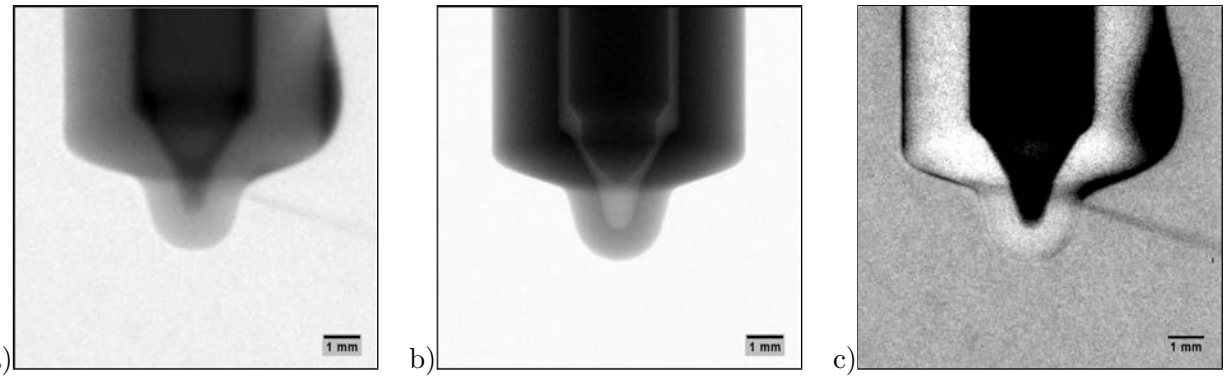

Fig. 4.19: a) The median of a series of radiographs taken while the injection nozzle has been in operation. b) This simulated radiograph has been generated using Monte Carlo methods. c) The result after normalization of the measured radiograph using the simulated radiograph (logarithmic scale).

dependent neutron interaction effects.

4.4.3 iCCD-highRes

The results of a normalization using and radiograph of an empty nozzle and a calculated radiograph are presented in figure 4.20. A standard normalization using an open beam image does not yield a good contrast (Fig. 4.20a). If the calibration for the mapping of the transmission values to the displayed gray scale levels is changed, the visibility of the injection spray outside of the nozzle is enhanced but the attenuation due to the test oil inside the spray hole is masked by a larger attenuation caused by the nozzle body and remains of test oil on the outside of the nozzle (Fig. 4.20b). A correction for the attenuation of the nozzle body is carried out by a normalization with a second radiograph of the "empty"[13] nozzle (Fig. 4.20c) and a normalization with a calculated radiograph (Fig. 4.20d). The correction based on the second radio results in a better contrast for the test oil inside the spray hole.

4.5 Summary

The signal and noise behaviour of single pixels has to inspected in order to reach the highest possible resolution of pixel based detectors. Using an area of pixels, often called region of interest (ROI), does not reflect the effects of blurring or allow to determine the signal statistics of the detected neutrons. The use of region of interest (ROI)s is useful though to give a statement concerning the homogeneity of the primary neutron beam, the conversion processes inside the neutron converter and the pixel array of the detector. For detectors using an optical coupling by a lens system the FOV does affect the DQE of the detector, as it changes the effective pixel size on the scintillator. Removing or avoiding a secondary quantum sink improves the DQE of the detection system. Although the thickness of the phosphor layer of the Gd_2O_2S scintillator has been increased from $10\,\mu$m to $20\,\mu$m in order to reach a detection efficiency of more than $60\,\%$[14], only a limited number of neutrons is detected per pixel. This is caused by the small pixel size of only $3.39 \times 3.39\,\mu\text{m}^2$ for the iCCD-highRes configuration. It gives an average of 11 incident neutrons per second and pixel even at a neutron flux of $1 \cdot 10^8\,\frac{\text{n}}{\text{cm}^2\,\text{s}}$, which is equivalent to a probability of only 0.006 for a single pixel to be hit by a neutron during an exposure time of $500\,\mu$s of a single time frame of the stroboscopic measurement. While the zero frequency DQE of the detector is improved by the increased thickness of the phosphor layer, is has a negative effect on

[13] As the nozzle has not been disassembled and cleaned, it can not be assured that the test oil has been been removed completely.

[14] The maximum is limited to $75\,\%$ due to the branching ratio of the internal conversion of gadolinium which is necessary for neutron detection and light emission inside the Gd_2O_2S phosphor.

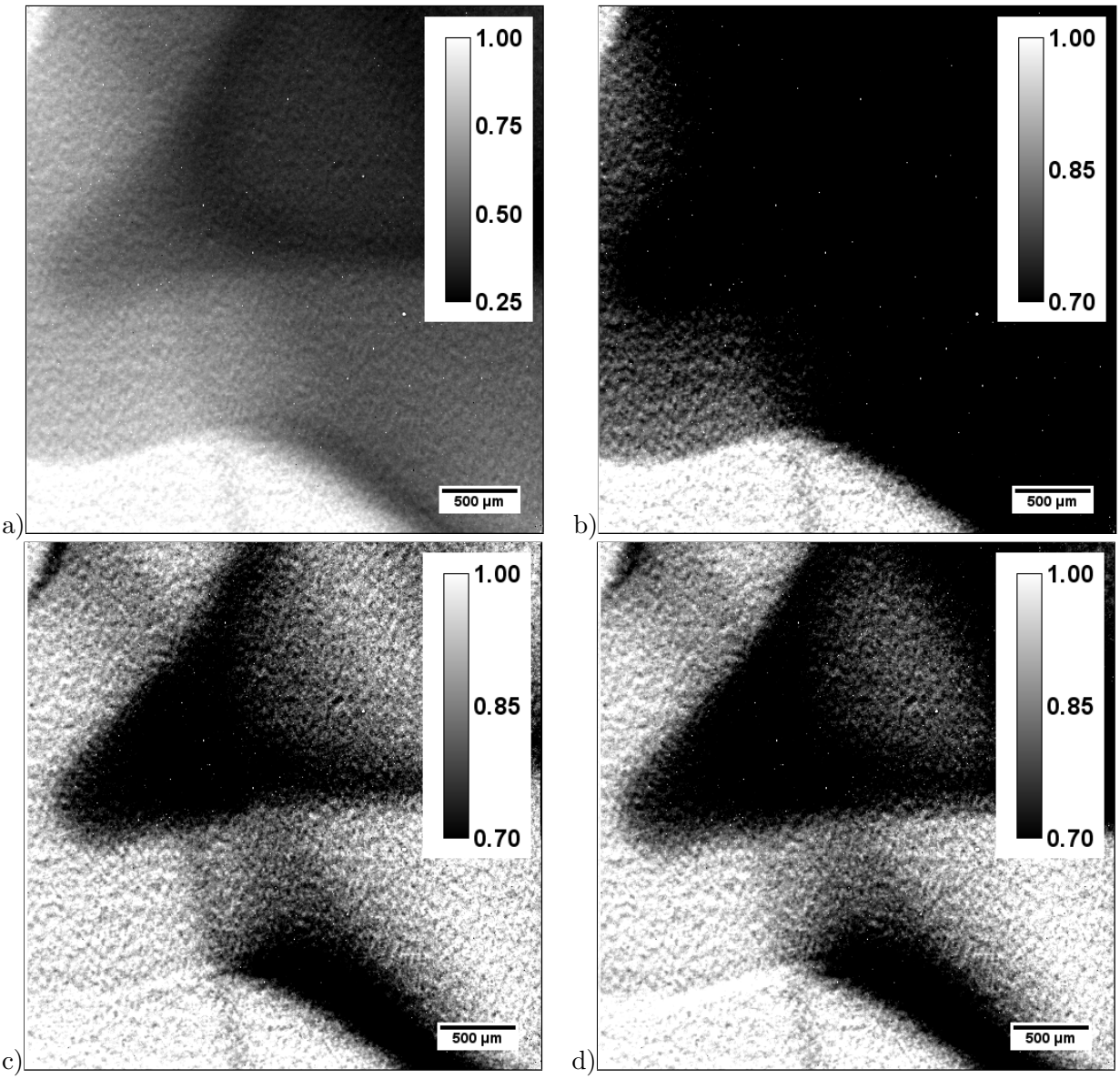

Fig. 4.20: a) radiograph of the injection normalized by an open beam image, calibration setting 0.25 to 1.00, b) same image but calibration setting 0.7 to 1.00, c) radiograph of the injection process normalized by an radiograph of the "empty" nozzle, d) same radiograph but normalized by a calculated radiograph of the nozzle.

the frequency dependent DQE resulting in a lower spatial resolution of the detector. For example the detection efficiency increases from 42 % to 60 % for a neutron wavelength of 2 Å if the thickness of the gadolinium phosphor layer is changed from 10 μm to 20 μm. But this comes along with an increase of the mean path length of the light inside the phosphor by 121 %, from 5.7 μm to 12.6μm. This effect is even more pronounced for long neutron wavelengths, which means that there is only a small gain in detection efficiency, while the spreading of the signal inside the scintillation screen is enhanced proportional to the average light path by more than a factor of two. The spreading of light causes a blurring which in turn reduces the signal to noise ratio of the detector output for a single pixel. Thus this effect should always be taken into account if thicker phosphor layers are employed. Depending on the neutron wavelength there is an optimum thickness, where a thickening of the phosphor layer does not yield an improvement of the detection efficiency large enough to compensate the reduction of the overall DQE caused by the additional signal spread induced by the thicker phosphor layer. For thermal neutrons the thickness of a Gd_2O_2S screen can be reduced to 10 μm without a significant loss of detection efficiency.

The MCP detector has the best DQE and operating it in centroiding mode also allows to reach the highest spatial resolution of 10 μm. Unfortunately the event centroiding is only applicable up to a fixed neutron detection frequency, which is determined by the maximum speed of the serial CMOS readout. Thus there is a upper limit of the neutron flux for high resolution imaging using the MCP detector. An improved readout electronic offering a parallel readout promises to solve this [48]. In the triggered mode of the detector operation, when it is synchronized to the injection process, the spatial resolution of the detector is reduced to the pixel size of the CMOS readout of $55 \times 55\,\mu m^2$. Due to the fixed field of view of 14.08 mm × 14.08 mm of a single readout chip its application is limited to small samples. There is the possibility though to increase the field of view by putting several chips in close contact to each other. Up to now it is more complex to operate the MCP detector than to use detectors combining a neutron scintillation screen and a camera readout. The MCP detector can not be bought off-the-shelf. Besides a computer and readout electronics a vacuum pump and external power supplies for the high voltage potentials applied to the MCP stack are needed to operate the detector. Although the setup using the intensified CCD camera with a FOV of 14.4 mm × 14.4 mm has a smaller calculated pixel size than the MCP detector, only 14 μm instead of 55 μm, it does not reach a resolution which is competitive to the one of the MCP detector. The image intensifier of the camera already reduces the effective number of pixels by about a factor of four from 1024×1024 pixels to 512×512 pixels. In combination with the optical coupling between the scintillation screen the intensified camera it causes a blurring that limits the spatial resolution to 63 μm (8.0 lp/mm). Reducing the FOV to only 3.47 mm × 3.47 mm and improving the optical coupling it has been possible to increase the spatial resolution to 30 μm (16.4 lp/mm) even if the camera readout is operated at a 2×2 binning mode. In that case the calculated pixel size on the scintillator is 6.8 μm. For this setup only about 100 neutrons reached one pixel of the detector during 200 seconds of acquisition time at a neutron flux of $1.0 \cdot 10^8 \frac{1}{cm^2\,s}$. Without the readout being set to the 2×2 binning mode there would be less than 25 neutrons contributing to the signal of a single pixel during one acquisition. It has turned out that the increased thickness of the phosphor layer of 20 μm for the Gd_2O_2S:Pr/Ce/F scintillator has induced a major limitation of the spatial resolution of this detector configuration. This has been shown by comparison with a standard type Gd_2O_2S:Tb scintillator of only 10 μm thickness. When the thicker scintillator has been used, the detector resolution was reduced to 42 μm (12.0 lp/mm).

Three different methods have been applied to normalize the radiographs acquired from the injection process. The data have been corrected for the attenuation of the nozzle body by a second radiograph of the empty nozzle, a calculated radiograph and a simulated radiograph of the nozzle body. The biggest advantage when using a second radiograph of the empty nozzle for normalization is, that the measurements show definitely the same attenuation behaviour for

the nozzle body. Drawbacks of this method are that it can not be assured that the nozzle is really empty, as it is only possible to remove all test oil from the nozzle if it is disassembled. Furthermore the operating nozzle seems to be enlarged compared to the empty one. A "virtual" enlargement may be caused by the vibration of the injector when the pump is in operation. Other reasons for the movement of the nozzle are a thermal expansion of the injector due to the elevated temperature of the nozzle during operation and an expansion caused by the pressure applied to the nozzle. This change of the geometry of the nozzle body does also introduce artifacts during the normalization. The corrections based on a calculated or a simulated radiograph of the empty nozzle body are very similar. The calculation can be carried out much faster than the simulation. But the simulation offers a more precise result as it includes a wavelength dependency of the neutron interaction with the sample and multiple scattering of neutrons. Of course the spectrum of the neutron beam and the material composition have to be known. For both methods offered a good cancellation of the attenuation caused by the nozzle body, which allowed to increase the contrast for the test oil inside the spray hole and the nozzle. The advantage of these type of corrections is that they do not add a significant additional error during the evaluation of the data and that the model of the sample may be adapted to ones needs to enhance a specific feature, e.g. the test oil. Disadvantages are that the sample geometry and the sample orientation has to be known very precisely to prevent artefacts during the correction and that it is time consuming to built the model of the sample and to carry out the necessary calculations. As the Monte Carlo simulation took too long to get simulated radiographs for different configurations only the one corresponding to the iCCD-lowRes has been used for corrections, while calculated radiographs were available for the iCCD-lowRes and iCCD-highRes configurations.
Comparing the three evaluation techniques using a second radiograph is of course the most straight forward one. And it is also the fastest way. Even if it may take some time to acquire the additional radiographs, it is much more time consuming to generate the models necessary for the calculation or the simulation. For some samples having a much more complicated geometry it might be impossible to create the corresponding model.
Calculating the transmission signal is fast. So it is possible to use a set of different parameters, e.g. to model the energy dependency of the neutron absorption or to check effects due to various material compositions. If the scattered intensity is calculated with the same resolution like the transmitted intensity, it may take more than one day depending on the number of voxels inside the evaluated sample volume. But it is surely enough to evaluate the scattered intensity using lower resolution.
As a final remark one could sum up that it has been possible to visualize the test oil inside the spray hole. But the available signal statistics and spatial resolution did not allow for a detailed view of the test oil during the injection process. Further improvements of the experimental setup and data evaluation are promising to get close to the spatial resolutions reached with X-rays while neutron radiography has the benefit to gain a contrast for the test oil.

Chapter 5

Ultra Small Angle Neutron Scattering

This chapter starts with a description of the USANS setup proposed by Roland Gähler [14] which was installed in a preliminary version at the instrument D11 at the Institute Laue-Langevin (ILL) in Grenoble, France. Therefore the standard apertures were replaced by a multi slit array used as source aperture and an array of cylindrical lenses at the sample position. The aim of these changes was to reach a neutron flux at the sample position which is comparable to the flux of standard SANS measurements, while the divergence of each of the resulting multiple neutron beams is reduced by about factor of 50. Thus the accessible Q-range is $5 \cdot 10^{-6}\,\text{Å}^{-1}$ to $2 \cdot 10^{-4}\,\text{Å}^{-1}$ instead of $1\,\text{Å}^{-1}$ to $3 \cdot 10^{-4}\,\text{Å}^{-1}$ for the standard setup. Section 5.2 explains some of the measurements carried out with the advanced setup. It covers the adjustment of the focal length of the neutron lenses by varying the neutron wavelength, the formation of the primary intensity profile at the detector and measurements of calibration standards. Section 5.3 will show two different ways of data evaluation. One of them is similar to the standard SANS data treatment. It allows to evaluate data for larger Q-values, which do not posses a large overlap with the primary beam profile. The second evaluation makes use of fitting a model of the expected intensity profile to the measured data. It is especially useful to evaluate data close to $Q = 0$ in the Guinier range. It may be used even if there is an overlap of the scattered intensities originating from different peaks of the primary multiple beam pattern. Section 5.4 gives an overview of the results of the evaluated data. A summary on the USANS measurements carried out the D11 at the ILL ends this chapter.

5.1 USANS Setup

A sketch of the instrumentation at the D11 is shown in figure 5.1. For standard SANS measurements the collimation offers six positions with distances from 1.5 m to 40.5 m for the source aperture. Computer controlled aperture changers enable to define the divergence of the incident neutron beam at the sample position[1]. The primary intensity profile at the detector results from a combination of the source aperture and a corresponding sample aperture (Sec 2.2). For USANS measurements special source and sample aperture arrays were used. They replaced the standard apertures of the collimation. There have been different setups for the two beam times when preliminary USANS configurations have been installed at D11. They are called USANS I and USANS II from now on. For both configurations the source aperture was positioned 20.5 m upstream with respect to the sample position, the sample aperture was put directly in front of the sample at the sample position and the detector was placed 22.5 m downstream from the sample position.

Source Apertures For USANS I the source aperture consists of two sheets of cadmium of 1 mm thickness and an identical pattern of slits (Fig. 5.2 a and 5.2 b). The width of the slits is 2 mm and their effective height is 23 mm. The center to center distance of the slits is 4.79 mm. There are two

[1] For further details please visit the instrument homepage `http://www.ill.eu/instruments-support/instruments-groups/instruments/d11/` .

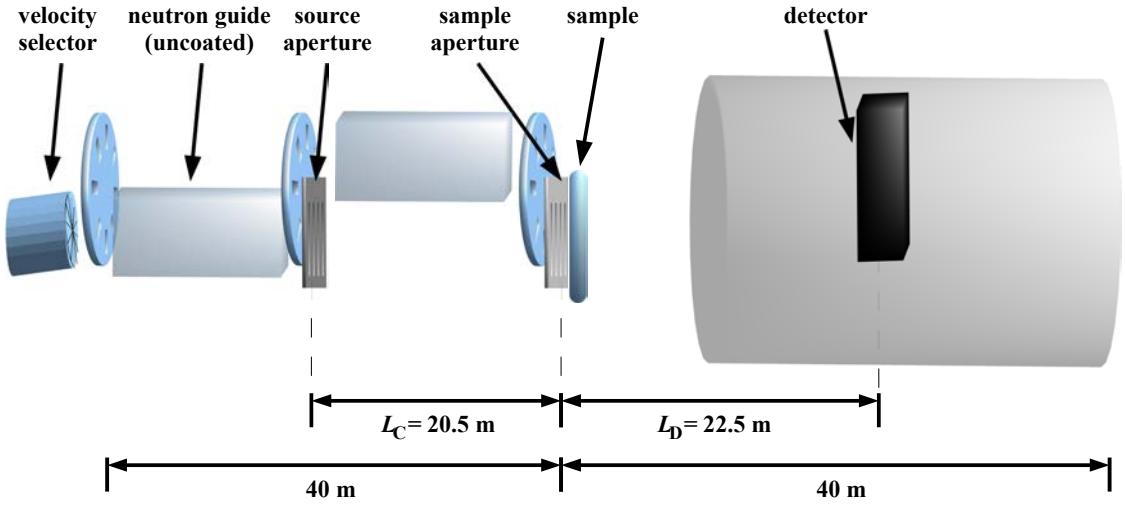

Fig. 5.1: Aperture arrays replace the source aperture and the sample aperture of the standard collimation at the D11. The source aperture is placed 20.5 m upstream of the sample aperture, which is positioned right in front of the sample. A neutron imaging detector is set up 22.5 m downstream of the sample position. It replaces the standard detector of the D11.

rows of six slits each. By shifting one of the two cadmium sheets it is possible to adjust the width of the aperture from 0 mm up to the full width of the slits of 2 mm. A width of 0.5 mm has been set for the measurements with the USANS I setup at the D11. This results in a total area of the source aperture of

$$A_{S,I} = 12 \cdot 0.5\,\text{mm} \cdot 23\,\text{mm} = 138\,\text{mm}^2 = 1.38\,\text{cm}^2\,. \tag{5.1}$$

The source aperture of USANS II is made of boron nitride and has a thickness of 3.175 mm (Fig. 5.2 c). There are only 4 slits with a center to center distance of 8.5 mm. Their width is fixed to 0.5 mm and their height is 55 mm. Thus the total source area is reduced to

$$A_{S,II} = 4 \cdot 0.5\,\text{mm} \cdot 55\,\text{mm} = 110\,\text{mm}^2 = 1.10\,\text{cm}^2\,. \tag{5.2}$$

Photos of the source aperture array of the USANS I configuration mounted on the aperture

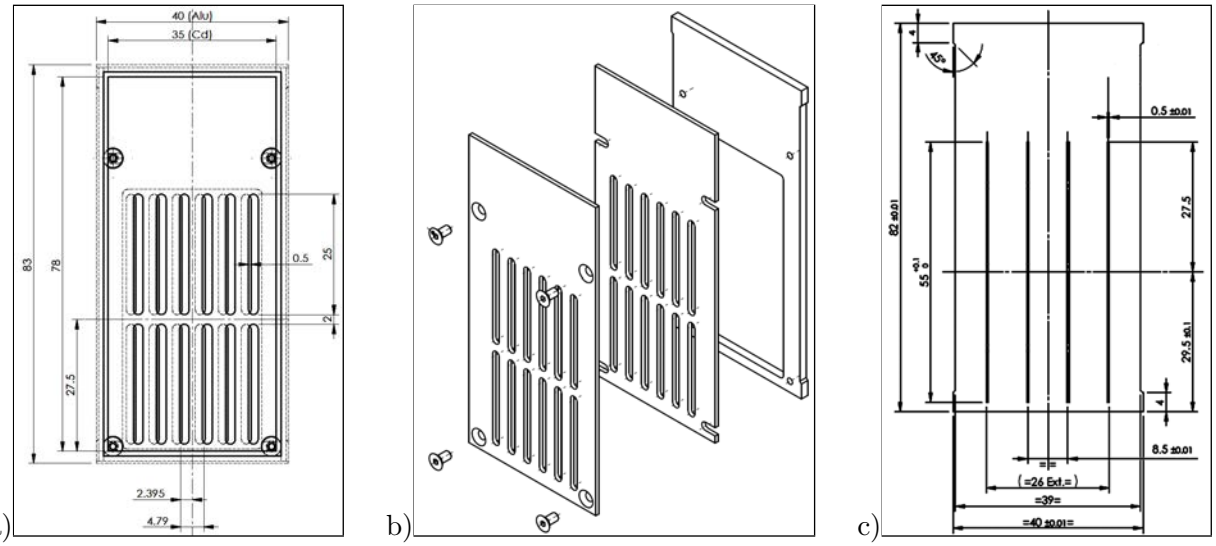

Fig. 5.2: The source aperture for USANS I with 12 slits of variable width, adjustable from 0 mm to 2 mm: a) mounted and b) disassembled; c) the source aperture for USANS II: 4 slits with a fixed width of 0.5 mm.

exchanger of D11 are shown in figure 5.3.

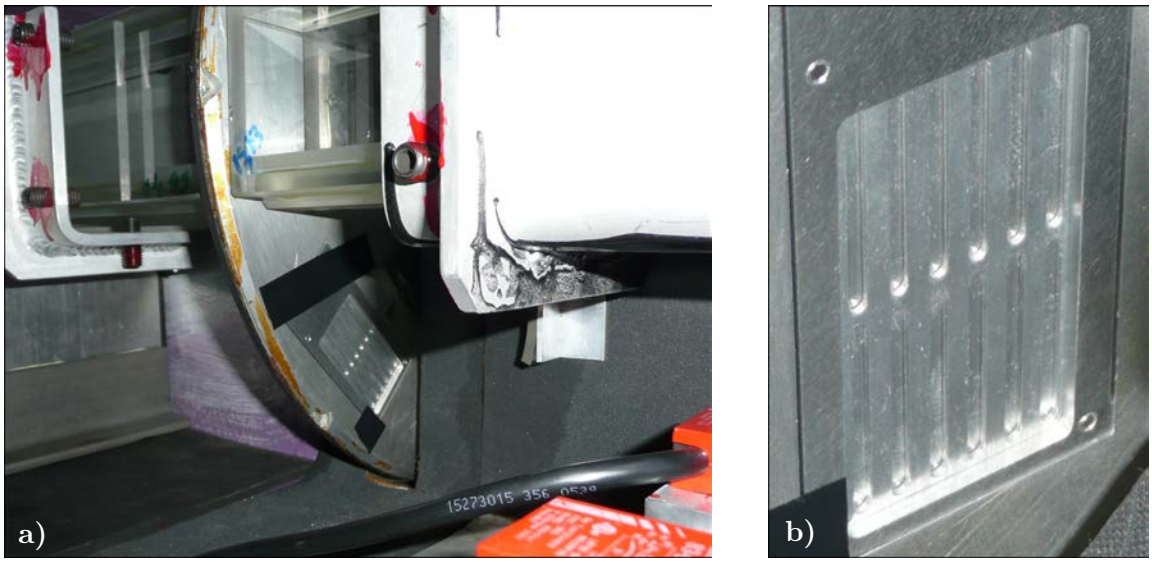

Fig. 5.3: a) The source aperture of the USANS I setup mounted on the aperture exchanger of the D11 at the ILL, b) a close-up view of the USANS I source aperture array.

Sample Aperture - Lens Arrays Arrays of lenses with a cylindrical geometry were used as sample apertures. As the focal length of a neutron lens is inversely proportional to the square of the neutron wavelength (Eqn. (2.86)), a stack of lenses is used instead of a single lens to reduce the effective focal length for short neutron wavelengths. The number of the stacked lenses and their geometry allows for a rough choice of the wavelength. The position of the source aperture, the sample aperture and the detector are fixed for multiple beam setups to fulfill the requirements for an overlay of a multiplicity of the single neutron beams at the detector (Sec 2.2.3). Thus the focal length of the stack of lenses at the sample position has to be adjusted to meet the imaging conditions. A fine tuning of the focal length via the neutron wavelength is necessary to get a sharp image of the source aperture at the detector position. The geometries of the lens arrays of USANS I and USANS II are shown in figure 5.4 and figure 5.5. For USANS I the center to center distance of the cylindrical lenses is 2.5 mm and the lenses have a radius of curvature of 1.5 mm. According to

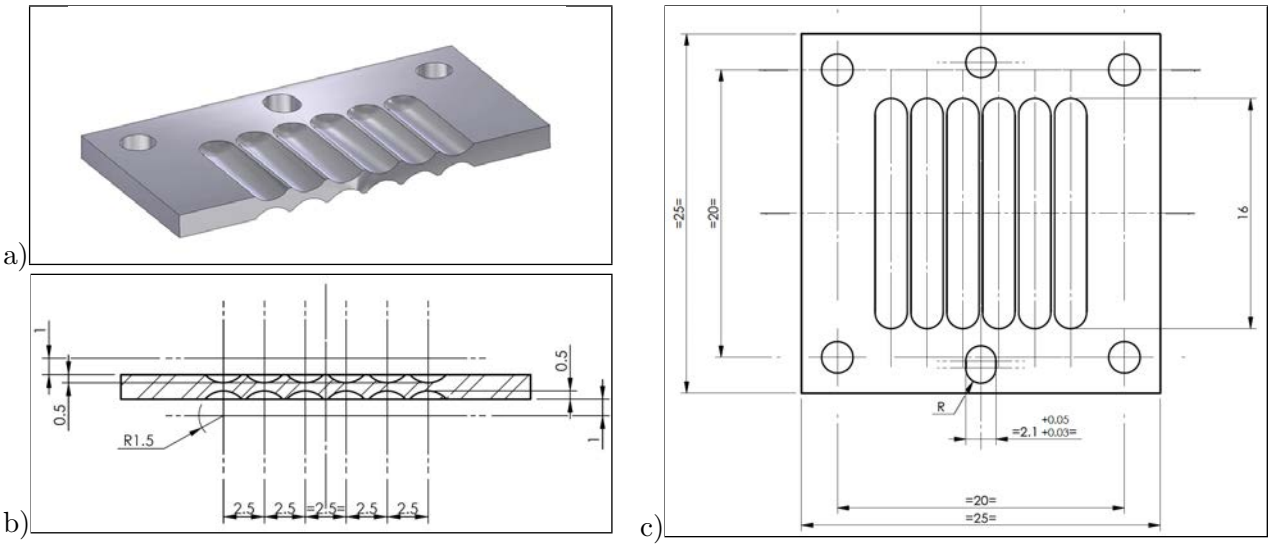

Fig. 5.4: a) Cut through a three dimensional view of a neutron lens array applied for the USANS I setup. b) Cross sectional view of the aluminum lens array with dimensions. c) A top view of the same lens array. The center to center distance of the lenses is 2.5 mm [14].

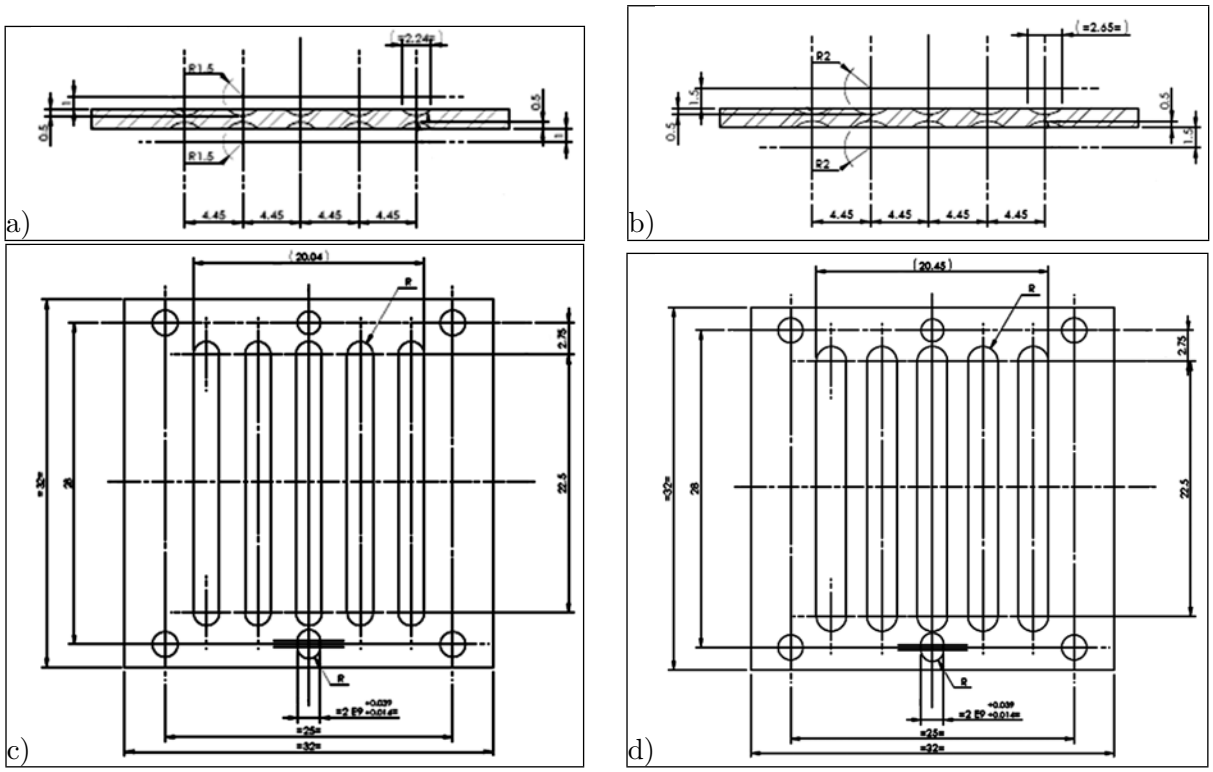

Fig. 5.5: Cross sections of aluminum lens arrays for the USANS II setup with an radius of curvature of a) 1.5 mm and b) 2.0 mm; c) and d) corresponding top views of the lens arrays . Note that the center to center distance of the lenses has been increased to 4.45 mm compared to 2.5 mm of USANS I [14].

expected wavelength in Å	lens curvature (radii in mm)	number of lenses
14.5	1.5	1
10.2	1.5	2
8.34	1.5	3
7.23	1.5	4
16.7	2.0	1
11.8	2.0	2
9.63	2.0	3
8.34	2.0	4

Table 5.1: The wavelenght for USANS measurements is determined by the curvature of the lens and the number of lenses that are stacked to reach a focal length of 10.7 m for different neutron wavelengths [15].

a larger center to center distance of the source aperture for USANS II the center to center distance of the lenses is increased to 4.45 mm. There have been two radii of curvature, 1.5 mm and 2.0 mm, available for the USANS II setup. For an overview of the expected neutron wavelength depending on the number of stacked lenses see table 5.1. The inactive area of the aluminum lens arrays was covered by a gadolinium frame. The dimensions of the gadolinium frame for USANS II are shown in figure 5.6. The thickness of the gadolinium was 0.125 mm. The sample aperture array mounted at the sample position is shown in figure 5.7.

Neutron Flux at Sample Position The neutron flux Φ at the sample position is defined by [14], [15]: the total area of the source aperture $A_{\mathrm{S,i}}$, the accepted solid angle $\Delta\Omega$ given by the area of the sample aperture $A_{\mathrm{A,i}}$ and the distance L_{C} from the source aperture to the sample,

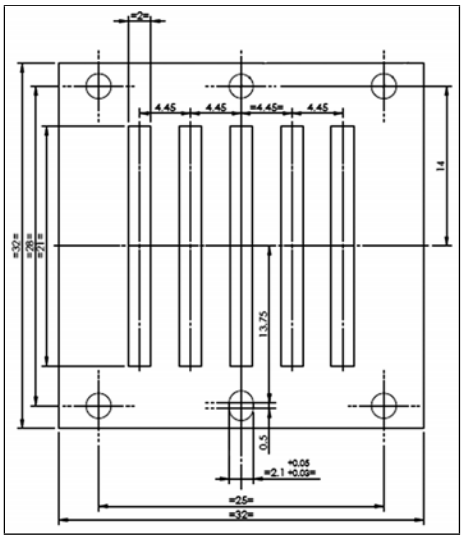

Fig. 5.6: Dimensions of the gadolinium frame covering the inactive part of the aluminum lenses of the USANS II setup.

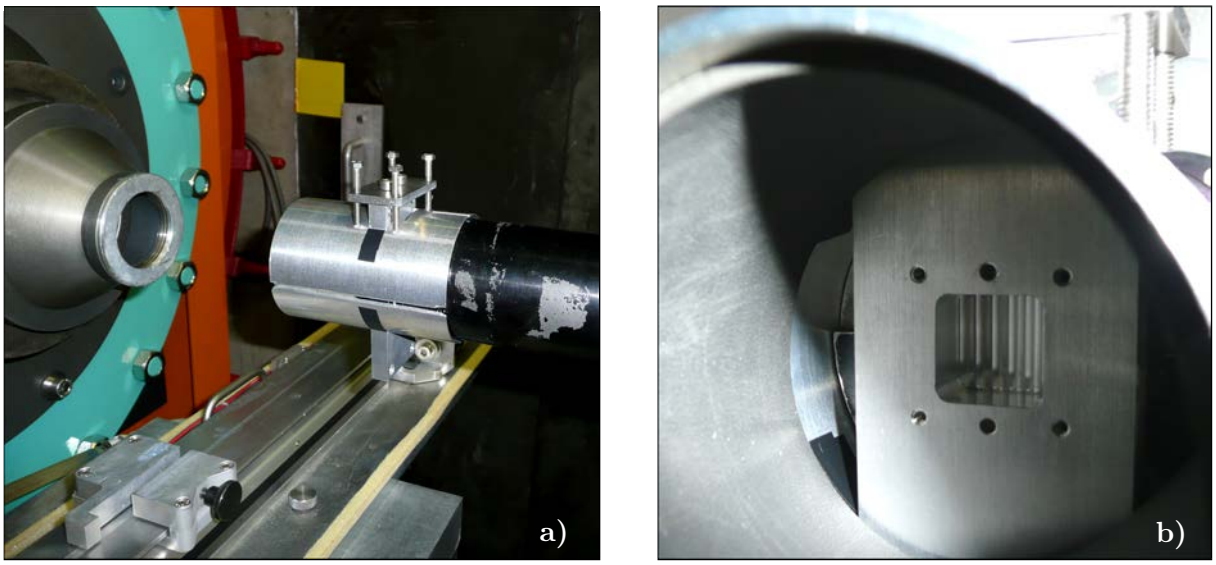

Fig. 5.7: a) The USANS I sample aperture mounted at the sample position of the D11 at the ILL, b) a view onto one of the neutron lens arrays of the sample aperture from the sample position.

the transmission through the sample aperture $T_{\mathrm{A,i}}$, the selected wavelength λ and the wavelength band $\Delta\lambda$. It is estimated by the formula [15]

$$\Phi(\lambda) = \left(\frac{\mathrm{d}^2\Phi}{\mathrm{d}\lambda\,\mathrm{d}\Omega}\right)(\lambda) \cdot \Delta\lambda \cdot \mathrm{d}\Omega \cdot A_{\mathrm{S,i}} \cdot T_{\mathrm{A,i}}\,. \tag{5.3}$$

The total areas of the source apertures for USANS I and USANS II calculated above, equations (5.1) and (5.2), are

$$A_{\mathrm{S,I}} = 1.38\,\mathrm{cm}^2 \quad \text{and} \quad A_{\mathrm{S,II}} = 1.10\,\mathrm{cm}^2\,. \tag{5.4}$$

The solid angle defined by the area covered by the lens array is about $2\,\mathrm{cm}^2$ for USANS I and $5\,\mathrm{cm}^2$ for USANS II. The distance from the source aperture to the sample position is 20.5 m and the corresponding solid angles are

$$\Delta\Omega_{\mathrm{I}} = \frac{2\,\mathrm{cm}^2}{(20.5\,\mathrm{m})^2} = 4.8 \cdot 10^{-7}\,\mathrm{sr} \tag{5.5}$$

and

$$\Delta\Omega_{\mathrm{II}} = \frac{5\,\mathrm{cm}^2}{(20.5\,\mathrm{m})^2} = 1.2 \cdot 10^{-6}\,\mathrm{sr}\,. \tag{5.6}$$

The transmission $T_{\mathrm{A,i}}$ through the sample aperture, i.e. a stack of lens arrays, includes the opening ratio of the lens array and the loss due to absorption of neutrons. For the cylinder geometry of the lenses the opening ratio τ is given by the width of a single lens divided by the center to center distance of the lenses. The opening ratio [15] of the different lens geometries are

$$\tau_{\mathrm{I}} = \frac{2.2\,\mathrm{mm}}{2.5\,\mathrm{mm}} = 0.88 \tag{5.7}$$

for USANS I with lenses of 1.5 mm radius of curvature and

$$\tau_{\mathrm{II}} = \frac{2.0\,\mathrm{mm}}{4.45\,\mathrm{mm}} = 0.45 \tag{5.8}$$

for USANS II where the lenses are covered by a gadolinium frame (Fig. 5.6). The average thickness of the aluminum inside the active lens area is approximately 1 mm. It is the same for both versions of the lenses. The neutron transmission through a single lens of aluminum at a neutron wavelength of 10 Å is

$$\exp\left(-\Sigma_{\mathrm{Al,10\,\mathring{A}}} \cdot d\right) = \exp\left(-7.86\,\mathrm{m}^{-1} \cdot 0.001\,\mathrm{m}\right) = 0.992\,. \tag{5.9}$$

if only neutron absorption is taken into account for attenuation [10]. A stack of two lenses is used for an wave length close to 10 Å. Thus the total transmission through the lens array including the opening ratio is

$$T_{\mathrm{A,I}} = 0.88 \cdot 0.992 \cdot 0.992 \approx 0.87 \tag{5.10}$$

and

$$T_{\mathrm{A,II}} = 0.45 \cdot 0.992 \cdot 0.992 \approx 0.44\,. \tag{5.11}$$

The wavelength band $\Delta\lambda = 1.0\,\mathring{\mathrm{A}}$ at a wavelength of 10 Å. With the differential flux $\left(\frac{\mathrm{d}^2\Phi}{\mathrm{d}\lambda\,\mathrm{d}\Omega}\right)$ taken from the ILL yellow book[2] the neutron flux at the sample is calculated using equation (5.3) for the USANS I and USANS II:

$$\Phi_{\mathrm{I}} = 1 \cdot 10^{11}\,\frac{1}{\mathrm{cm}^2\,\mathrm{s}\,\mathring{\mathrm{A}}\,\mathrm{sr}} \cdot 1\,\mathring{\mathrm{A}} \cdot 4.8 \cdot 10^{-7}\,\mathrm{sr} \cdot 1.38\,\mathrm{cm}^2 \cdot 0.87 = 6 \cdot 10^4\,\frac{1}{\mathrm{s}} \tag{5.12}$$

[2] http://www.ill.eu/instruments-support/instruments-groups/yellowbook/

and

$$\Phi_{\mathrm{II}} = 1 \cdot 10^{11} \, \frac{1}{\mathrm{cm^2\,s\,\mathring{A}\,sr}} \cdot 1\,\mathring{\mathrm{A}} \cdot 1.2 \cdot 10^{-6}\,\mathrm{sr} \cdot 1.10\,\mathrm{cm^2} \cdot 0.44 = 6 \cdot 10^4 \, \frac{1}{\mathrm{s}} \, . \tag{5.13}$$

This is only valid if the divergence of the neutron beam at the source aperture is sufficient to allow for a full illumination of the sample aperture and the full area of sample aperture is used. The average output signal of the detector per incident neutron is

$$\frac{\text{integrated gray levels of full beam profile at the detector}}{\text{flux} \cdot \text{exposure time}} \, . \tag{5.14}$$

It depends on the gain setting of the detector and the neutron wavelength, as the detection efficiency of the scintillation screen varies with neutron energy.

Detector The detector is placed 22.5 m downstream from the sample position. The spatial resolution of the detector has to be high enough to resolve shifts that are smaller than the peak width of the primary intensity profile of 0.6 mm. For the desired Q-resolution down to $5{\cdot}10^{-6}\,\mathring{\mathrm{A}}^{-1}$ at a wavelength of 10 Å the shift of scattered neutrons at the detector is 180 μm. A standard neutron imaging detector based on a scintillation screen and CCD camera system is sufficient to resolve such shifts[3]. The detector for USANS I and USANS II was equipped with a ^{6}LiF/ZnS scintillation screen to detect the neutrons. Its phosphor layer had a thickness of 300 μm and is deposited on a sheet of aluminum of 1.5 mm thickness. A Nikon lens with a focal length of 50 mm and a F-number of 1.2 images the light emitted by the phosphor onto the sensor of the camera. The detector was slightly changed for the USANS II configuration. For USANS I the neutrons reach the phosphor layer after passing through the sheet of aluminum the phosphor is deposited on. For a neutron wavelength of 10 Å the loss of neutrons due to absorption inside the aluminum is only 1.2 %. But for this configuration a major part of the neutrons interacting inside the phosphor is absorbed close to the aluminum far from the surface where the light is emitted towards the camera (Fig. 5.8). This results in two drawbacks. Light generated far from the surface of the phosphor layer is subject to attenuation reducing the effective light output. Diffusion of light on its way to the surface degrades the spatial resolution of the detector. For the USANS II configuration the detector box had been equipped with a thin aluminum window of 0.1 mm thickness at the backside. The front side coated mirror made of glass had been replaced by an aluminum coated silicon substrate. With neutrons entering form the back side now and passing through the mirror the scintillator was illuminated from the surface of the phosphor layer. Thus the neutrons were absorbed close to the surface of the scintillator and the effective path length of the scintillation light to exit the phosphor layer was reduced (Fig. 5.8). A second but marginal change was the use of a different camera. An Andor iXon DU 888[4] has been used for USANS I. It has been replaced by a Princeton Instruments ProEM 1024B[5] for USANS II. As both cameras use the same EM-CCD sensor, "e2v CCD 201"[6], this does not affect the specifications of the detector, like field of view, spatial resolution or sensitivity of the sensor. The imaging sensor has an active area of 13.3 x 13.3 mm^2 and 1024 x 1024 pixels. This results in a field of view of 82 x 82 mm^2 and a pixel size of 80 x 80 μm^2 on the scintillator.

5.2 USANS Measurements

5.2.1 Formation of the Primary Intensity Profile

For the USANS II configuration with only 4 slits as a source aperture the complete aperture arrangement at the sample position had been removed except for a circular aperture of 7 mm in

[3] For a sketch of the detector geometry see section 3.3

[4] http://www.andor.com/pdfs/specifications/Andor_iXon_888_Specifications.pdf

[5] http://www.princetoninstruments.com/Uploads/Princeton/Documents/Datasheets/Princeton_Instruments_ProEM+_1024B_eXcelon3_Rev_P1_7.20.2012.pdf

[6] http://www.e2v.com/products-and-services/high-performance-imaging-solutions/space---scientific-imaging/imaging-sensor-datasheets/

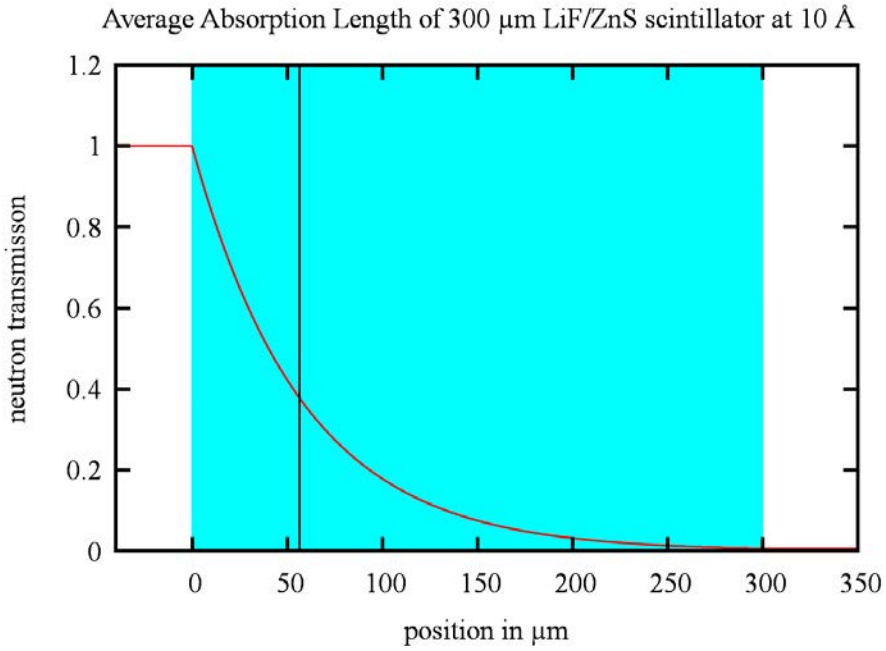

Fig. 5.8: Transmission of neutrons through a ^{6}LiF/ZnS phosphor layer of 300 μm thickness for a neutron wavelength of 10 Å. The average absorption length is indicated by the vertical line at 56 μm. For a standard configuration, like USANS I, the scintillation light is emitted to the right resulting in a large spread of the scintillation light inside the phosphor due to the long average path length form the point of neutron absorption to the surface of the scintillator. If in the contrary the scintillation light is emitted to the left, comparable to the USANS II configuration, the scintillator acts more like a scintillator of only 100 μm thickness.

diameter that restricted the beam size to the size of the sample. The resulting intensity profile is shown in figure 5.9a. It had been expected to form a flat intensity profile corresponding to the superposition of 4 beams fully illuminating the sample area. Hence also the irradiated area of the detector should show a quite homogeneous intensity profile. Instead three prominent peaks have been observed (Fig. 5.9d). An explanation for the measured profile is discussed in section 5.3. It was caused by the circular aperture placed at the sample position. Repeating the same measurement with an additional gadolinium mask which restricts neutron transmission at the sample aperture to the active lens area only, revealed that this mask blocked a large part of the area where the initial beam reached its maximum intensity (Fig. 5.9b and 5.9e). Thus the neutron flux at the sample and the detector was reduced significantly, when the gadolinium mask was used in combination with the 7 mm aperture (Fig. 5.10). When finally the arrangement of two neutron lens arrays and the gadolinium frame was placed at the sample position in combination with the circular aperture of 7 mm in diameter[7], the maximum intensity of the much narrower peaks was increased, while the intensity between the peaks was reduced due to the focusing nature of the lenses (Fig. 5.9c and 5.9f).

5.2.2 Neutron Wavelength Adjustment

As the distances between the source aperture, the sample aperture and the detector were fixed by the geometry constraints to yield an overlay of the multiple neutron beams, the focal length of the neutron lenses had to be adjusted by changing the neutron wavelength. A rough selection of the neutron wavelength was possible by the number of lenses that were stacked to reach shorter focal

[7]This small aperture cuts down the beam size to the actual sample size.

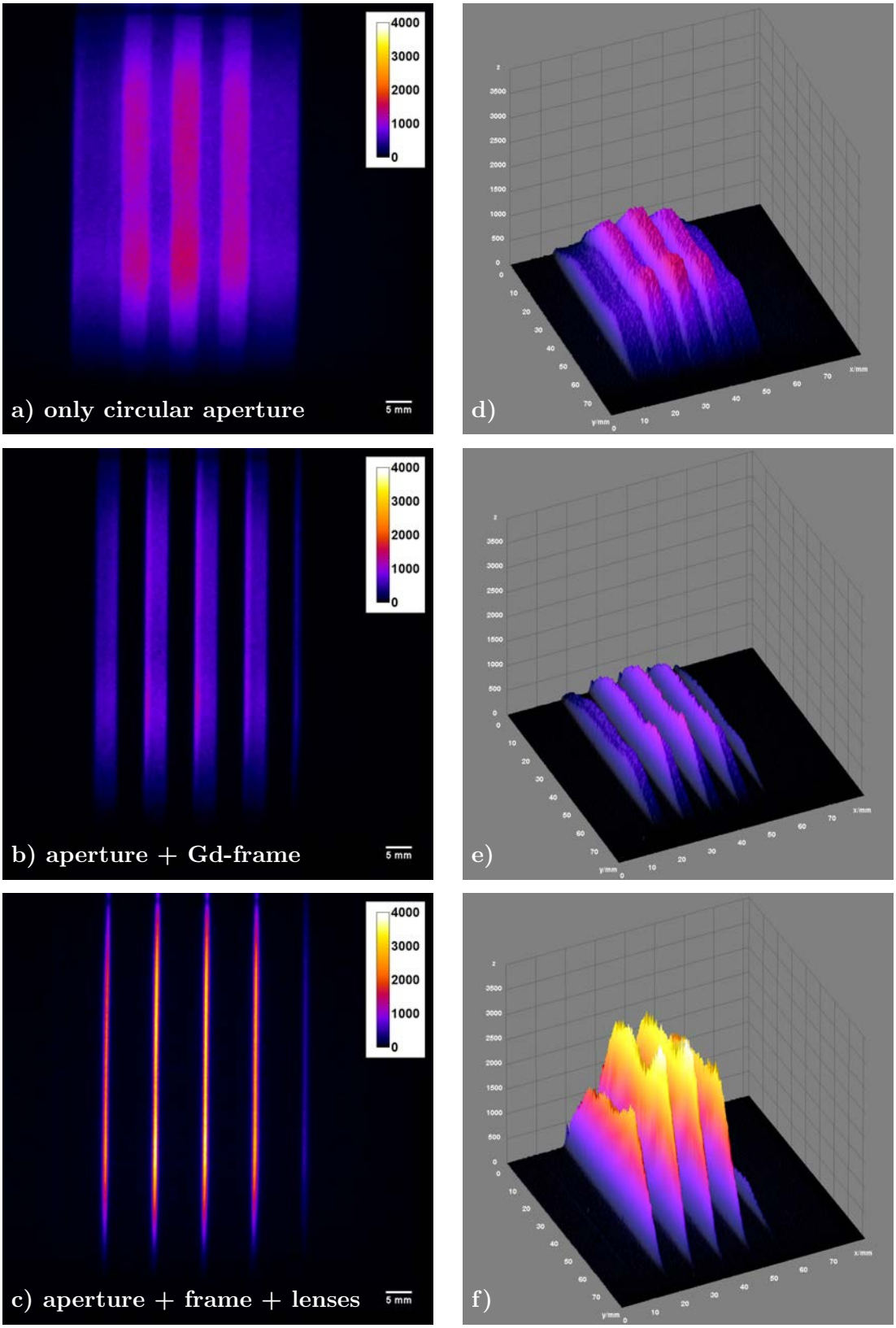

Fig. 5.9: Measured intensity distribution at the USANS detector (left column): a) with a circular aperture of 7 mm diameter at the sample position, b) when putting the gadolinium frame that covers the inactive area of the lens arrays in addition to the circular aperture, c) with a stack of two lens arrays, the gadolinium frame and the circular aperture inside the neutron beam. The corresponding three-dimensional surface plots are shown in the right column images d) to f). All images were acquired using the same exposure time. The same contrast settings and color schemes are applied.

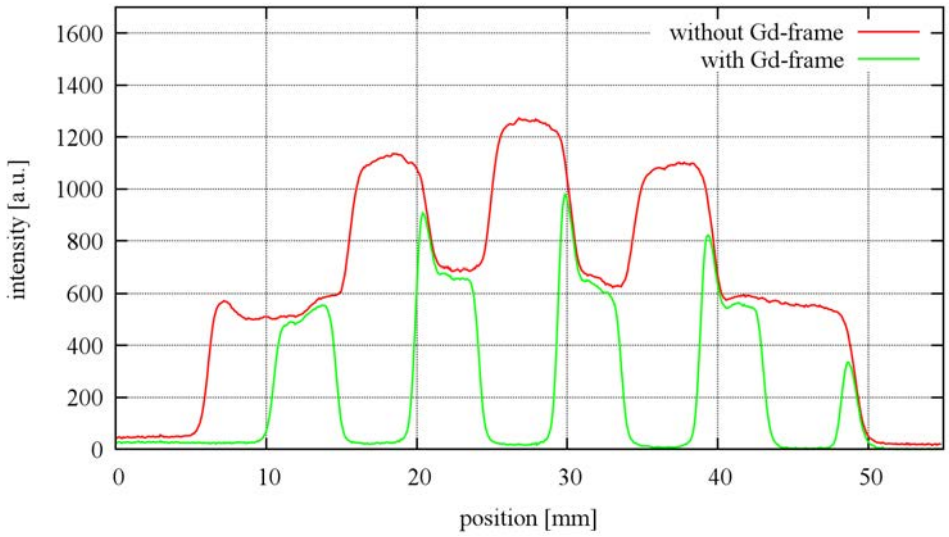

Fig. 5.10: The gadolinium mask at the sample position blocks the maxima of the intensity profile resulting form the source aperture array with four slits in combination with an additional circular aperture of 7 mm in diameter. A simple shift of the Gd-frame by a few millimeters would increase the neutron flux by about a factor of two, as the maxima of the red curve are not blocked but transmitted then.

lengths[8]. The images in figure 5.11 were acquired using the USANS I configuration. A stack of two neutron lens arrays with a radius of curvature of 1.5 mm and a gadolinium frame covering the inactive parts of the lens arrays were used as sample aperture. The distance L_C from the source aperture to the neutron lenses was 20.5 m. The distance L_D from the neutron lenses to the detector was 22.5 m. The intensity distribution of the empty beam, without any sample inside the neutron beam, was used to set the wavelength which fulfilled the imaging condition for the stack of neutron lenses best. At the same time the cylindrical lenses were aligned parallel to the slits of the source aperture. This step is comparable to the focusing of an optical lens system. The measured two-dimensional intensity profiles and profile plots for different wavelengths are shown in figure 5.11. An influence of gravity on the neutron beam is visible, too, as the center of the integral intensity is shifted to a lower position on the detector with increasing neutron wavelength. The optimum wavelength is set, when the peak width at the detector reaches a minimum. Such a focusing procedure or the adjustment of the neutron wavelength is necessary each time the arrangement or position of the source aperture, the sample aperture or the detector is changed.

5.2.3 Calibration Standards

Artificial gratings were used as standard samples to check the calibration of the detector (Fig. 5.12). These gratings had been provided by Christian Grünzweig [58]. The ΔQ-value corresponding to one pixel of the detector is calculated from the neutron wavelength λ, the distance L_D from the sample to the detector and the size of a single detector pixel on the scintillation screen Δd (Eqn. (2.35))

$$\Delta Q = \frac{2\,\pi\,\Delta d}{\lambda\,L_D}\,. \tag{5.15}$$

There have been three phase gratings with periods of 4.0 μm, 8.5 μm and 12 μm. The expected Q-values defined by the known periodicity of the gratings are $1.6 \cdot 10^{-4}$ Å^{-1}, $7.4 \cdot 10^{-5}$ Å^{-1} and $5.2 \cdot 10^{-5}$ Å^{-1}, respectively. The acquired intensity profiles are shown in figure 5.13 for the 8.5 μm and the 12 μm grating. The integration time was 60 s for the empty beam and 300 s when the gratings were placed in the beam. The gain of the EMCCD camera detector was set to 50. The

[8]Stacking several lenses in beam direction reduces the overall focal length of the stack for a fixed neutron wavelength.

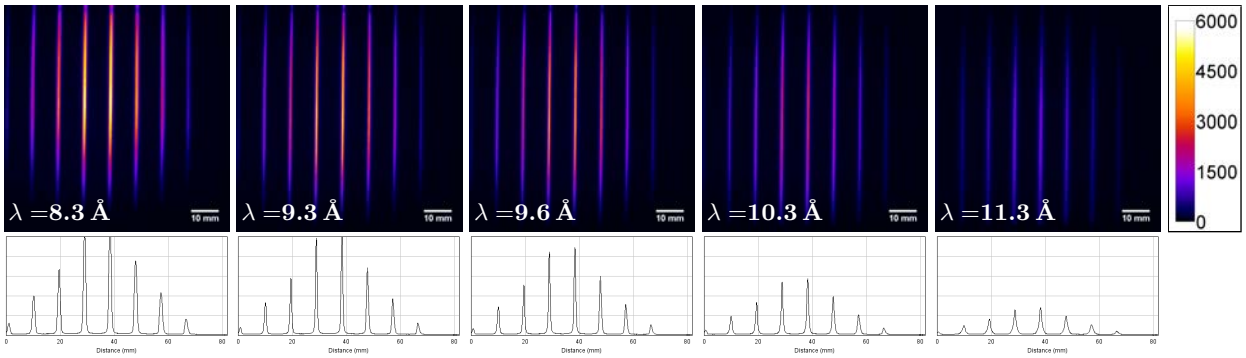

Fig. 5.11: Measured intensity profiles for different neutron wavelengths when using a stack of 2 lenses as a sample aperture. The two-dimensional profiles show the spatial distribution of the primary intensity. For longer neutron wavelengths a influence of gravity is recognizable, as the center of the primary intensity profile moves downwards. The one-dimensional line profiles show the change of the peak to background ratio for different wavelength settings. For USANS measurements the peak width is of special importance here.

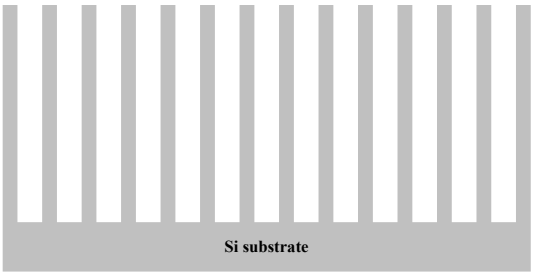

Fig. 5.12: The neutron phase gratings used for the calibration measurements consist of silicon bars on a silicon substrate [58]. Neutron pass through the gratings from the top to the bottom.

selector was set to a wavelength of 9.5 Å for both gratings. For the images acquired with the 4 μm grating placed in the neutron beam and without it see figure 5.14. Here the neutron wavelength was 7.7 Å and the exposure time for the images was 300 s again.

5.3 USANS Data Treatment

There are different ways to evaluate the data acquired by an imaging detector in combination with multi aperture or lens system at a SANS instrument. They are described in the following subsections. Which of the methods is the best to evaluate the measured intensity profile, is highly dependent on the scattering characteristics of the sample. For example summing up the scattering intensities for the multiple scattering peaks is only possible if it is assured that there is no overlap of the scattering signals originating from different peaks of the primary intensity profile. An overlap of signals originating from different primary intensity peaks would lead to a misinterpretation of the scattered intensity profile. Only Q-values corresponding to half of the distance between the peaks of the primary can be evaluated. Summing up the scattering signal of the multiple beams is a straight forward adaption of a standard pinhole SANS data evaluation (Sec 2.2.2). It includes steps to correct for detector effects and the geometry of the multiple slit apertures. This correction is based on the steps shown in *"Neutorns, X-rays and Light: Scattering Methods Applied to Soft Condensed Matter"* edited by P. Lindner and Th. Zemb [11, p. 23]. A second method is to fit an appropriate model of the scattered intensity profile and the transmitted primary intensity to the measured data. This method helps to evaluate data for small Q-values in the Guinier-range close to $Q = 0$. As the fit function is evaluated for the whole multiple beam pattern, it is possible to evaluate the data even if there is an overlap of the scattered intensity profiles or if some of the

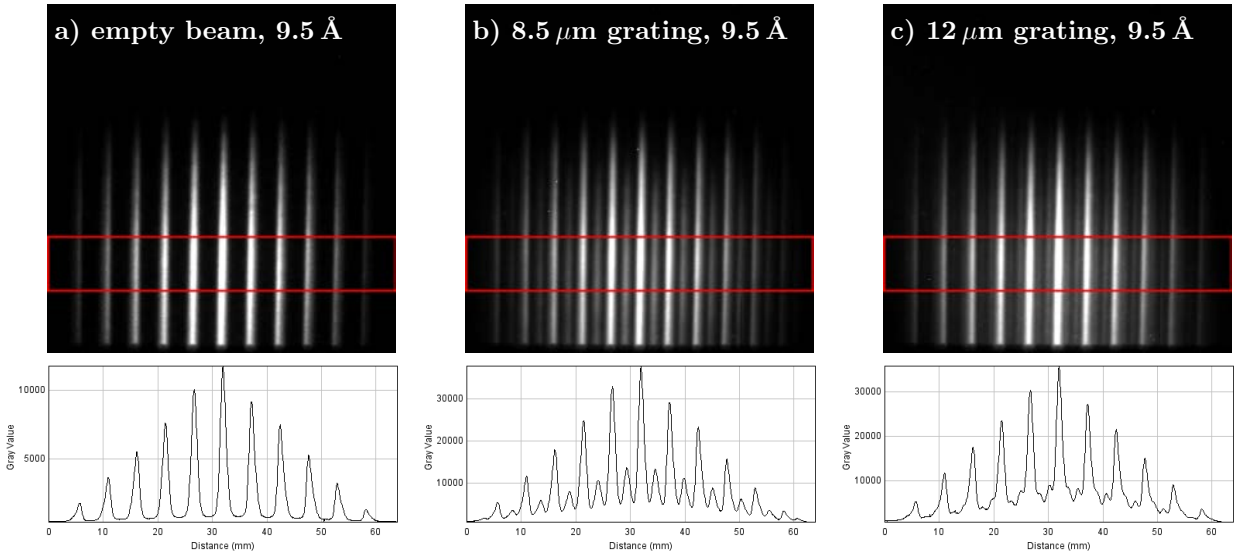

Fig. 5.13: Measured intensity acquired at a neutron wavelength of 9.5 Å and a stack of two neutron lens arrays as sample aperture: a) the empty beam, b) with a 8.5 μm grating placed in the neutron beam and c) with a 12 μm grating placed in the neutron beam. The line profiles correspond to the regions marked inside the images above.

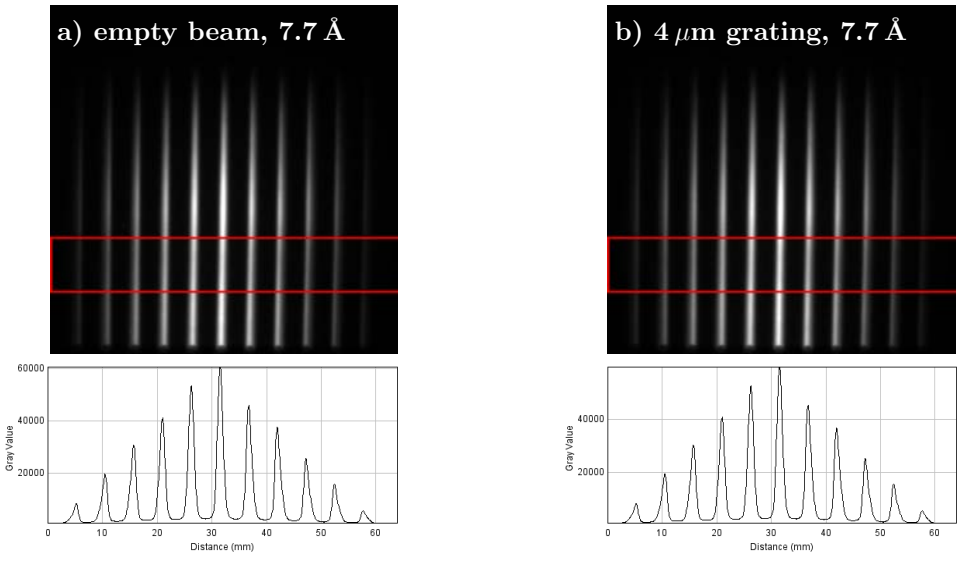

Fig. 5.14: Measured intensity profiles at a neutron wavelength of 7.7 Å using a stack of three neutron lens arrays as sample aperture: a) empty beam, b)profile with a 4 μm grating placed in the neutron beam. The line profiles correspond to the marked regions of the images above. As this grating shows high neutron transmission and the scattered signal caused by it is close to the neighboring maximum of the transmitted primary beam, there is nearly no difference between the image taken without the grating and the one taken with the grating inside the neutron beam.

multiple neutron beams miss the sample [9].

5.4 Evaluation of the Measured Data

5.4.1 Formation of the Primary Beam Profile

Intensity Profile for Multiple Neutron Beams with reduced Divergence The primary multiple neutron beam pattern of the USANS II setup, which has been observed, shows an intensity profile at the detector (Sec 5.2) that differs from the expected one. To investigate this effect a closer look at the formation of the primary intensity profile at the detector is necessary. The effects of all components forming the sample aperture configuration will be taken into account. Therefore models are built which describe the single steps that caused each of the intensity profiles shown in section 5.2.1. A simple model for the expected intensity at the detector would suggest a superposition of four single neutron beams emitted from the four slits of the source aperture of the USANS II setup. The divergence of each of these neutron beams is equal to the divergence that reaches the source aperture array positioned inside the collimation of the SANS instrument. A sample aperture may block parts of some of the multiple neutron beams and alter the intensity profile at the detector (Fig. 5.15). In any case the expected intensity profile at the detector has a

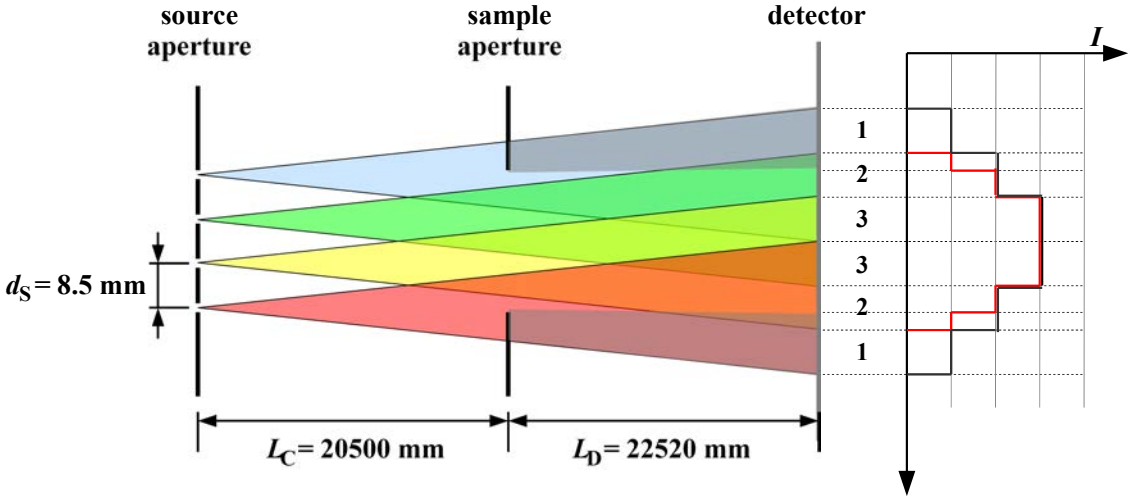

Fig. 5.15: The beam profile at the detector is expected to be formed by a superposition of 4 individual beams emitted from a source aperture array of four slits. The corresponding intensity profile is shown on the right (black line). Taking into account a restriction of the beam size due to the cross section of the exit of the collimation at the sample position or a sample aperture results in the intensity profile plotted in red color. The numbers indicate how many neutron beams are superimposed to form the black intensity profile.

flat region of maximum intensity at the center and falls off towards the left and the right margin. However the measured intensity profile shows three distinct maxima. Their intensity is about twice as high as the intensity of the plateau below (Sec. 5.2). In figure 5.16 the geometries for three different divergences of the neutron beams emitted at the source aperture array are illustrated. For a quite low divergence of 0.02 ° the expected intensity profile does indeed show three maxima, whose intensities are twice as high as the plateau below (Fig. 5.16a). For larger divergences the expected intensity profiles at the detector do not show separated maxima. Thus the measured intensity profile could be explained by a reduced divergence of the single neutron beams. There is a perfect agreement of the measured intensity profile for a divergence of 0.02 ° with respect to the width of the peaks and the intensity ratio between the peaks and the plateau. But in that case already a factor of two would be lost for the maximum intensity compared to the maximum

[9] If a beam hits the sample only partially, the evaluated profile is altered due to the sample transmission. This will cause an asymmetry of the measured beam profiles.

intensity reached for a divergence of 0.13 ° if all four beams emitted by the source aperture array overlap on the detector (Fig. 5.16c). Possible reasons that might yield a restricted beam divergence are the entrance of the collimation, which is given by the cross section of the end of the coated neutron guide ($\approx 0.089°$), the slits of the source aperture acting like a collimator ($\approx 8.9°$), the neutron velocity selector placed in front of the collimation ($\approx 2°$), the reflectivity of the coated neutron guide in front of the collimation ($\approx 1.9°$) and the reflectivity of the uncoated neutron guide in front of the source aperture ($\approx 0.62°$).[10] Thus none of these components is limiting the beam divergence to a value low enough to allow for an explanation of the observed intensity profile.

Real Beam Geometry A closer look to the measured intensity profile reveals that the real maxima have a center to center distance of 9.5 mm rather than the expected 8.5 mm corresponding to the geometric model above. Still the shape of the intensity profile suggests that the divergence of each of the multiple neutron beams is only 0.02 °. Only that way the overlap of the single neutron beams is small enough to allow for the separated maxima that have been observed. A limitation of the beam divergence to 0.02 ° is reached if an aperture of 7 mm in width is placed at a distance of 20 m from the source aperture. In fact an additional aperture of 7 mm in diameter was place close to the sample position. It was used to restrict the incident neutron beam at the sample position to the sample size. Here this aperture acts like an imaging device. It generates a blurred image of the source aperture at the detector plane. That way it may also be explained, why the center to center distance of the observed peak structure at the detector differs from 8.5 mm. The geometry for the overlay of four neutron beams emitted by the source aperture and passing through the aperture placed at the sample position is shown in figure 5.17. There is a problem though for neutrons crossing the outer slits of the source aperture. Neutrons are for example crossing the left and the right slit of the source aperture at an average angle of 0.036 ° with respect to the beam axis. This is only possible, because an uncoated glass guide allows for an reflection of neutrons, which in turn is virtually enlarging the size of the entrance area of the collimation (Fig. 5.18). It also explains, why the outer peaks of the measured intensity profile have a lower intensity than the center peak. The neutron beams originating from the outer slits of the source aperture array undergo one additional reflection at the side walls of the uncoated glass guide inside the collimation. Therefore these beams are less intense. The center peak on the other hand originates from the two center slits of the source aperture array, which are directly illuminated by neutrons emitted at the exit of the coated neutron guide (Fig. 5.18).

Effects due to a Combination of Sample Apertures A gadolinium frame with five slits covers the inactive areas of the aluminum lenses. When it is placed at the sample position a second effect is observed. The new intensity profile at the detector resulting from a combination of two sample apertures now, the gadolinium frame and the 7 mm aperture, has a strong dependence on the relative position of the two apertures with respect to each other. A shift of the gadolinium frame causes a change of the effective transmission area. Some transmission areas for different shifts have been calculated. They are shown in figure 5.19. For a coincidence of the centers of the two apertures and for a shift of 2.25 mm the effective sample apertures are symmetric. This results in a symmetric intensity distribution at the detector (Fig. 5.20 a and b). For a shift of 3 mm the intensity distribution at the detector shows a clear asymmetry (Fig. 5.20 c). It seems that for the layout during the measurement the cadmium mask has accidentally been positioned in a way that it blocked the maxima of the intensity distribution resulting from the correlation of the 7 mm aperture and the source aperture array (Sec. 5.2). In order to reach the maximum available intensity at the sample and the detector the combination of two apertures must result in a maximum transmission area. The effective opening function for a combination of two apertures

[10] Details about the way the transmitted divergences of each component have been estimated are found in the appendix A.11.

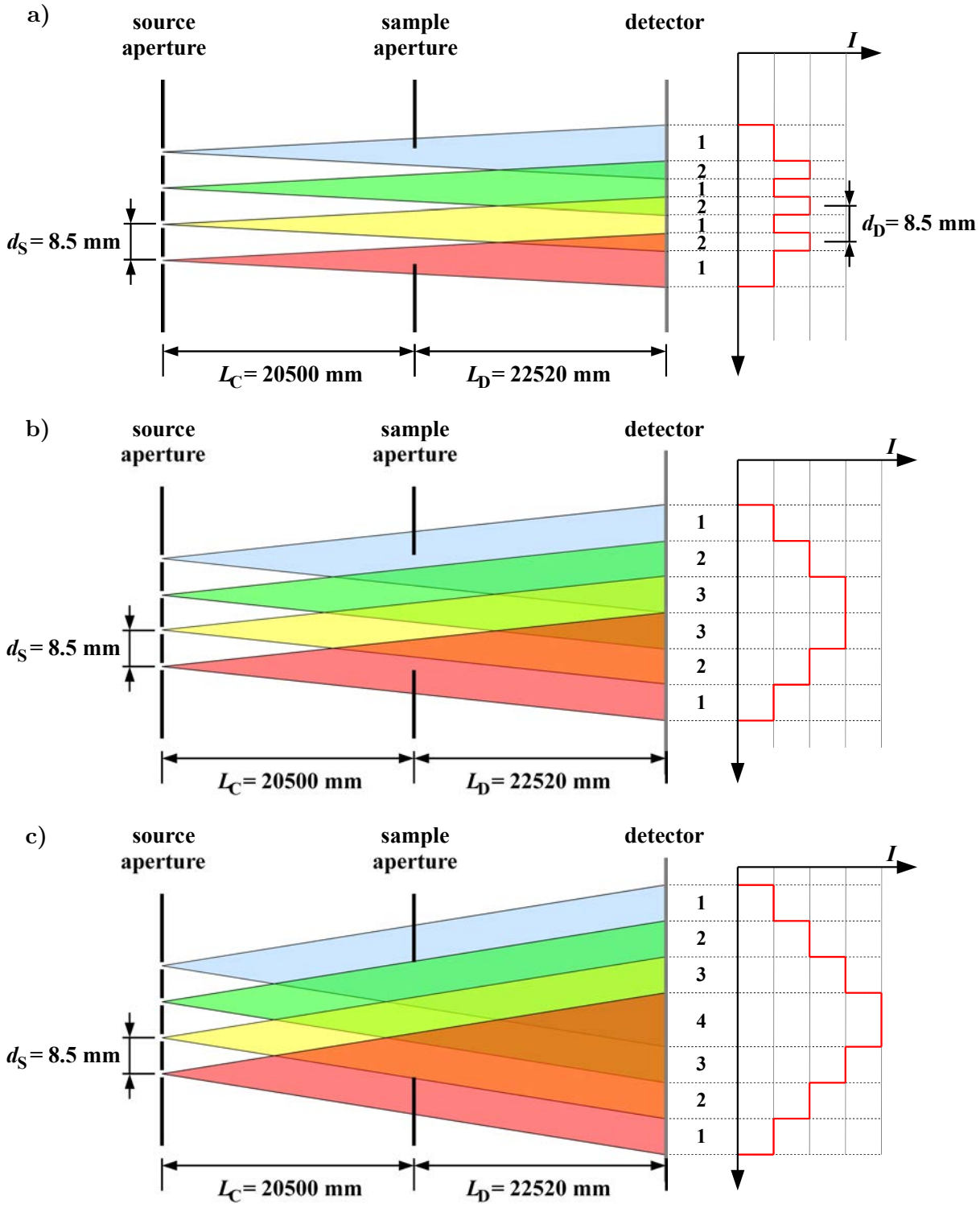

Fig. 5.16: The expected intensity profile at the detector is shown for three different neutron beam divergences at the source aperture: a) 0.02 °, b) 0.086 °, and c) 0.13 °. The numbers between the beam geometry on the left and the intensity profile on the right indicate the number of source slits that contribute to the intensity at the detector. For larger beam divergences the shape of the beam profile gets more and more triangular. Note, that the presence of a sample aperture (not taken into account here) may restrict the size of the single neutron beams. This will also alter the intensity profile at the detector.

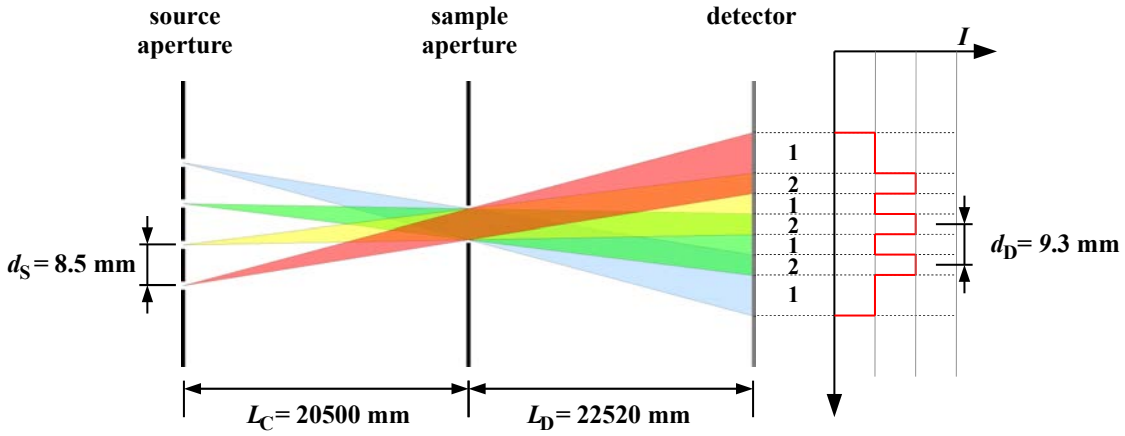

Fig. 5.17: An explanation for the low divergence accepted by the aperture configuration is an additional aperture of 7 mm placed at or close to the sample position.

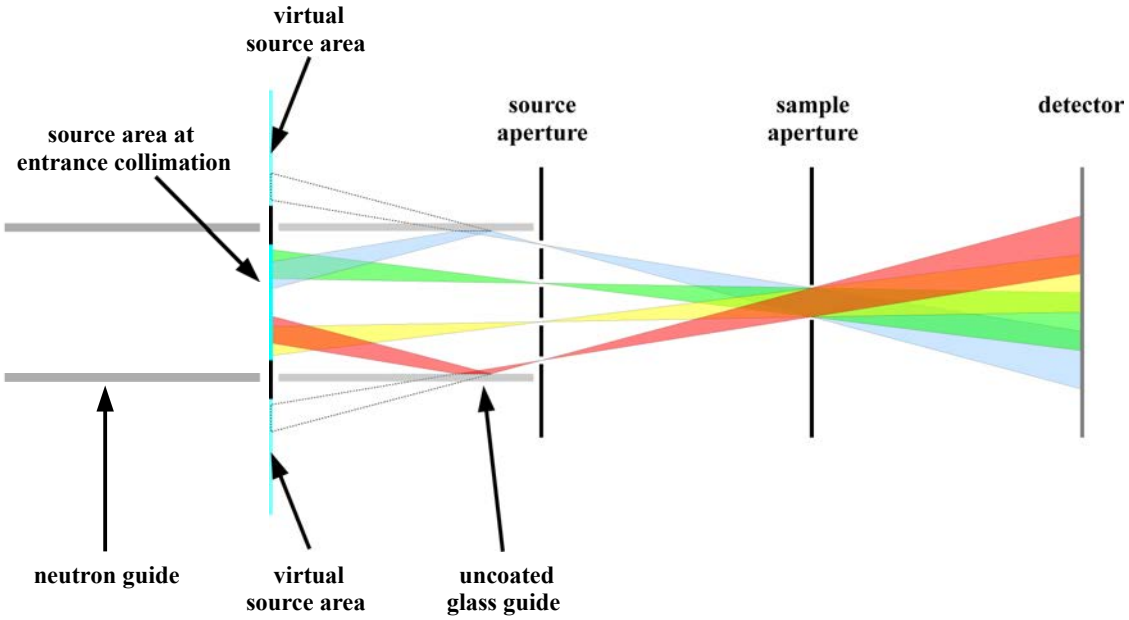

Fig. 5.18: The uncoated glass guide in between the entrance of the collimation and the source aperture array of the USANS setup gives rise to virtual source areas illuminating the source aperture array. Without the uncoated glass guide only the center part of the source aperture array would contribute to the neutrons reaching the sample and the detector.

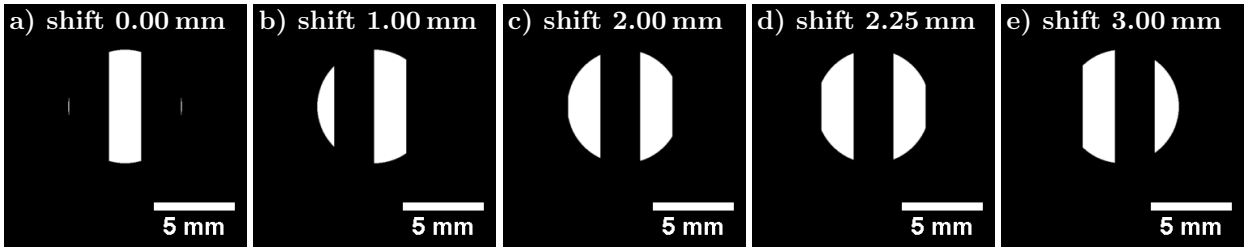

Fig. 5.19: The effective transmission areas for a combination of the gadolinium frame and a circular sample aperture of 7 mm diameter are indicated by the bright regions of the images above: a) for a coincidence of the centers of the combined apertures; and shifts of: b) 1 mm, c) 2 mm, d) 2.25 mm and e) 3 mm.

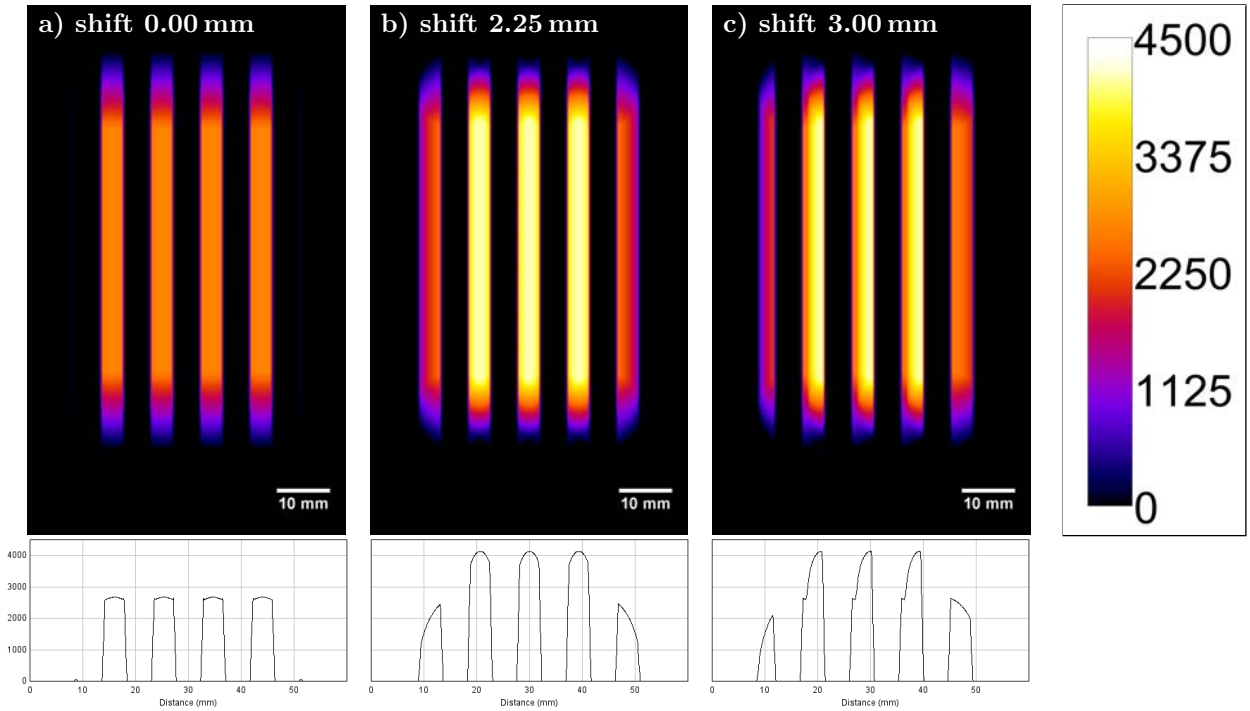

Fig. 5.20: If a combination of sample apertures defines the effective transmission area at the sample position, the intensity profile at the detector is very sensitive to shifts of these apertures relative to each other. The expected intensity distributions at the detector for three of the effective transmission areas of figur 5.19 are shown above: a) coincidence of the centers of the two apertures, b) a shift of 2.25 mm and c) a shift of 3 mm. The calibration bar represents the color scheme for the calculated intensities in arbitrary units. The corresponding line profiles are added below each image. The optimum is reached for b) a shift of 2.25 mm, when the effective transmission area of the combined apertures reaches a maximum and is symmetric. The situation shown in c) is close to the measured intensity profile of the USANS II setup and has an asymmetric peak shape.

configuration	peak intensity, a.u.	integral intensity, a.u.
7 mm aperture (circular)	1554	308514767
7 mm aperture and Gd-frame (slits)	1233	108196838
7 mm aperture, Gd-frame and neutron lenses	3926	118881492

Table 5.2: Peak intensities and integral intensities at the detector for different configurations of the sample aperture.

A_1 and A_2 is

$$A_{\text{eff}}(Q_\text{x}, Q_\text{y}) = A_1(Q_\text{x}, Q_\text{y}) \cdot A_2(Q_\text{x}, Q_\text{y})\,. \tag{5.16}$$

The intensity distribution at the detector plane is

$$\hat{I}_0(Q_\text{x}, Q_\text{y}) = \frac{(A'_\text{sc} \star A'_\text{eff})\,(Q_\text{x}, Q_\text{y})}{\int\int A'_\text{sc}(u,v)\text{d}u\,\text{d}v} \tag{5.17}$$

$$= \frac{\int\int A_\text{sc}(u\cdot\alpha, v\cdot\alpha)\cdot A_\text{eff}\left((Q_\text{x}+u)\cdot\beta, (Q_\text{y}+v)\cdot\beta\right)\,\text{d}u\,\text{d}v}{\int\int A_\text{sc}(u\cdot\alpha, v\cdot\alpha)\,\text{d}u\,\text{d}v}\,. \tag{5.18}$$

The factors

$$\alpha = -\frac{L_\text{C}}{L_\text{D}} \quad \text{and} \quad \beta = -\frac{L_\text{C}}{L_\text{C}+L_\text{D}} \tag{5.19}$$

are used to take into account a scaling of the apertures due to there position with respect to the source aperture and the detector. Thus the evaluated profile is directly given in coordinates Q_x and Q_y corresponding to a position on the detector plane.

Beam Profile Including the Neutron Lenses Adding a stack of 2 neutron lens arrays to the sample aperture arrangement of the USANS II configuration reduces the width of the peaks at the detector. As expected from the transmission calculations of section 5.1 the neutron lenses do not really change the integral intensity. The peak intensities and the integral intensity at the detector for different aperture configurations at the sample position are listed in the table 5.2. The measured integral intensity with the neutron lens arrays inside the neutron beam is increased slightly, although a reduction would be expected due to the transmission losses. This can be explained by a small shift of the gadolinium frame, when the stack consisting of the two neutron lens arrays and the gadolinium frame had been assembled and remounted at the sample position. It has been shown already that the transmission area formed by the 7 mm aperture and the gadolinium frame is very sensitive for small shifts of the two apertures with respect to each other. Thus the increase of about 10 % of the integral intensity for the measurement with the neutron lenses inside the beam is attributed to a different position of the gadolinium frame. A plot of the resulting line profiles for the different sample aperture configurations is shown in figure 5.21.

5.4.2 Focusing

The correct neutron wavelength must be selected to optimize the imaging of the source aperture onto the detector via the lens arrays at the sample position. In order to determine the optimum neutron wavelength Gaussian profiles are fitted to the center peaks of the USANS primary intensity patterns, which have been acquired for different neutron wavelengths (Fig. 5.22). The aim is to select the neutron wavelength, that results in the smallest peak width or rather the optimum peak to background ratio. The optimum neutron wavelength for the current combination of the source aperture array, the stack of lens arrays is not only dependent on the number of neutron lenses that have been stacked to reach a shorter total focal length, but also on the imaging distances between the source aperture, the neutron lenses and the detector. The fits for profiles resulting from neutron

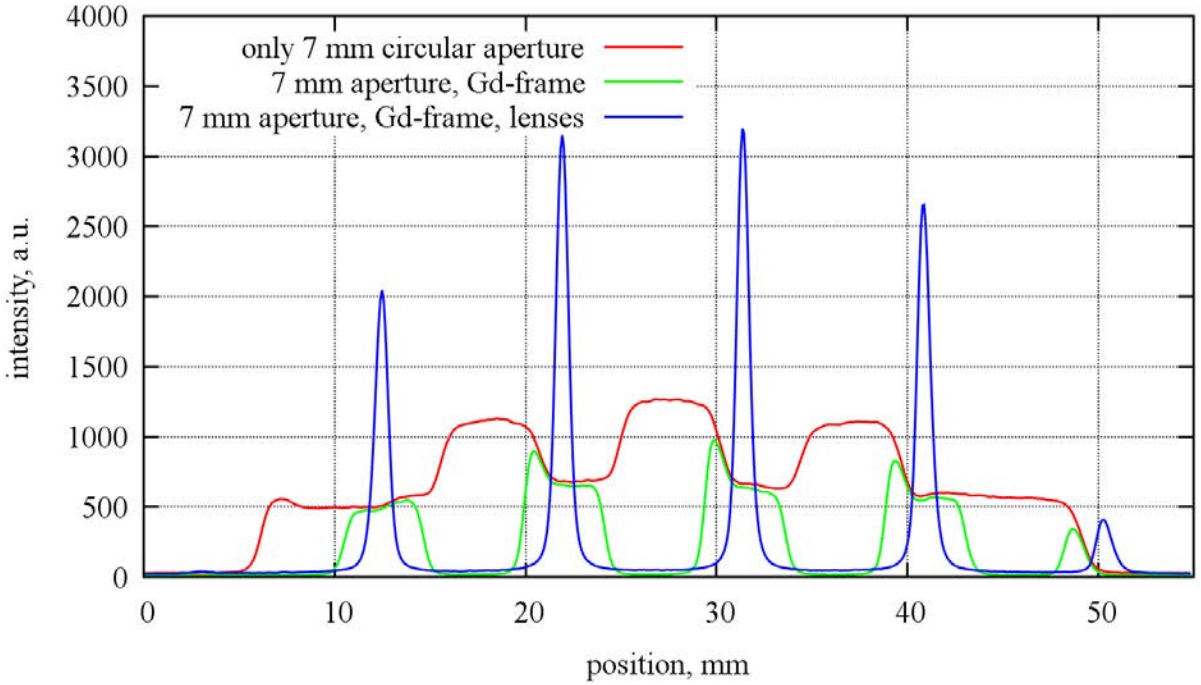

Fig. 5.21: The intensity profiles measured at the detector for different sample aperture configurations of USANS II: red - only a circular aperture of 7 mm in diameter, green - the 7 mm aperture and an array of 5 slits made of gadolinium, blue - the 7 mm aperture, the gadolinium frame and two neutron lens arrays. The imaging of the sample aperture array onto the detector plane by the 7 mm circular aperture results in three maxima. Due to an unfavorable positioning of the gadolinium frame these maxima are nearly blocked by the gadolinium. When the neutron lenses are added the transmitted intensity is concentrated to narrow peaks, which correspond to the superposition of the multiple images of the slits of the source aperture array.

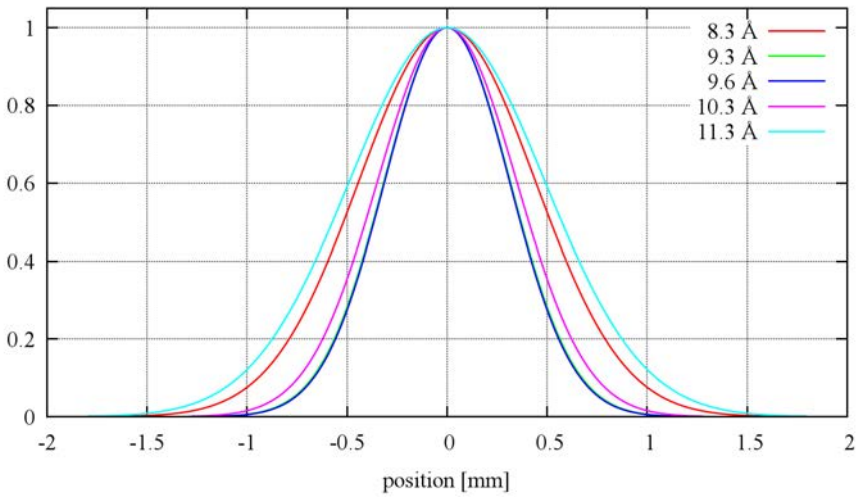

Fig. 5.22: The line profiles for the center peak of the USANS intensity pattern of the empty beam have been measured at different neutron wavelengths. The fitted Gaussian profiles are normalized to an amplitude of 1 and centered at zero. The narrowest peak shape is reached for 9.6 Å. There is a nearly perfect overlap for 9.3 Å

wavelength	σ width of Gaussian	FWHM
8.3 Å	0.440 mm ± 0.004 mm	1.036 mm ± 0.009 mm
9.3 Å	0.314 mm ± 0.002 mm	0.739 mm ± 0.005 mm
9.6 Å	0.311 mm ± 0.002 mm	0.732 mm ± 0.005 mm
10.3 Å	0.347 mm ± 0.005 mm	0.817 mm ± 0.012 mm
11.3 Å	0.487 mm ± 0.011 mm	1.147 mm ± 0.026 mm

Table 5.3: A Gaussian profile is fitted to the primary beam in order to determine the neutron wavelength, which fulfills the imaging condition best.

wavelengths of 8.3 Å, 9.3 Å, 9.6 Å, 10.3 Å and 11.3 Å and $\frac{\Delta\lambda}{\lambda} = 10\,\%$ are plotted in figure 5.22. The σ values for the Gaussian profiles and the calculated full width at half maximum (FWHM) are listed in table 5.3. A wavelength of 9.6 Å has been selected for the stack of two lens arrays, where the radius of curvature of the cylindrical lenses has been 1.5 mm. The expected width of the image of the source aperture at the detector is given by the width of the source aperture scaled to the detector plus a blurring induced by the chromatic aberration of the neutron lenses and a blurring due to the thickness of the phosphor layer of the scintillation screen of the detector. The scaled width of the source aperture is

$$0.50\,\text{mm} \cdot \frac{22.52\,\text{m}}{20.5\,\text{m}} = 0.55\,\text{mm}\,. \tag{5.20}$$

The additional blurring caused by chromatic aberration is equal to the width of the circle of least confusion for the image of an object point at the detector (App A.9), [14], [15]

$$\Delta w = \frac{D\,s_\text{i}}{f} \cdot \frac{\Delta\lambda}{\lambda} = \frac{2.1\,\text{mm} \cdot 22.52\,\text{m}}{10.731\,\text{m}} \cdot 0.10 = 0.44\,\text{mm}\,. \tag{5.21}$$

The detection inside the scintillation screen causes a blurring approximated by a σ equal to the path length it takes the scintillation light to reach the surface of the phosphor. For the USANS II configuration the average path length for a neutron wavelength of 10 Å is calculated to be 56 μm, which corresponds to a FWHM of 0.11 mm. The width of the image at the detector is therefore

$$\sqrt{(0.55\,\text{mm})^2 + (0.44\,\text{mm})^2 + (0.11\,\text{mm})^2} = 0.71\,\text{mm}\,. \tag{5.22}$$

The measured FWHM of the image of 0.732 mm for the selected wavelength of 9.6 Å is 3.1 % larger than the expected width.

5.4.3 USANS Background of Aluminum Lenses

The lenses made of aluminum[11] cause a background due to small angle neutron scattering. This is shown for some data taken with the USANS II configuration using a single lens array with a radius of curvature of 2 mm and a neutron wavelength of 16.47 Å. Figure 5.23a shows the result of fitting a single Gaussian to each peak of the primary beam profile. The corresponding fit function is given by

$$f(x) = o + o_1 \cdot x + \sum_\text{i} a_\text{i} \cdot \text{e}^{-\frac{(x-c_\text{i})^2}{2\,b_\text{i}^2}}\,, \tag{5.23}$$

where the parameters o and o_1 model the offset and background $B(x)$ of the measured data and the parameters a_i, b_i and c_i describe the amplitude, width and position of the peaks of the primary beam. In order to ease the fit routines and to generalize them all positions are represented in pixel

[11] AG3-NET

values rather than Q-values. The mapping to Q-values may be done afterwards. Note that the detector offset o is close to 1800. The residual values reach ± 50. This raises the question whether a USANS/SANS signal contributed by the neutron lenses has to be included for the fit of the primary beam profile. The plot in figure 5.23b results from fitting two Gaussians to each peak of the primary beam profile. In a first step the fit function $f(x)$ for the single Gaussian (Eqn. (5.23)) is used to

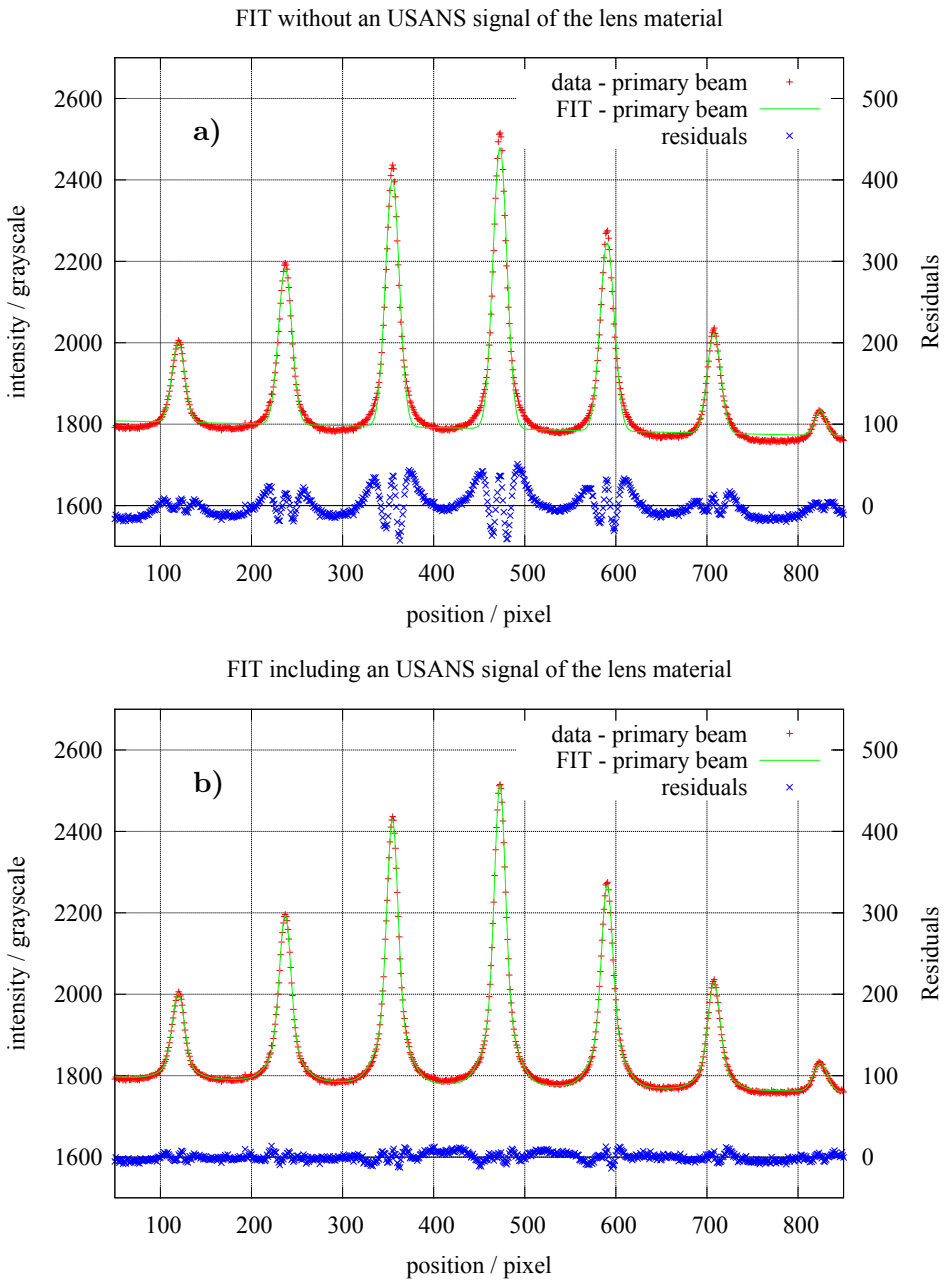

Fig. 5.23: a) The fit of the primary beam intensity profile using a single Gaussian for each peak of the multi peak pattern. There are large residuals, because the USANS signal caused by the aluminum (AG3-NET) of the neutron lenses is not taken into account. b) If two Gaussian profiles are fitted for each peak including a contribution of scattered neutrons due to the lens material, the fit is improved a lot.

determine the positions c_i and basic values for the width b_i and amplitude a_i of the peaks. The second step makes use of these predefined values and adds terms representing the USANS signal of the neutron lenses. Keeping the position of the primary beam profile constant a second Gaussian profile is added for each peak of the measured intensity pattern to describe the scattered intensity

	empty beam	10 mm aluminum	8 mm aluminum	18 mm Suprasil
a_3	564 ± 5	270 ± 2	209 ± 2	440 ± 4
a_4	636 ± 5	299 ± 2	230 ± 2	509 ± 4
as_3	60 ± 4	75 ± 2	71 ± 2	40 ± 3
as_4	66 ± 3	89 ± 2	86 ± 3	53 ± 3
$\frac{\bar{as}}{\bar{a}}$	0.105 ± 0.004	0.288 ± 0.005	0.358 ± 0.007	0.099 ± 0.004

Table 5.4: Comparison of the USANS signal caused by the neutron lenses themselves (empty beam) and for different types and amounts of aluminum and Suprasil inside the neutron beam. a_3 and a_4 correspond to the amplitudes of the "transmitted" intensity of the two center peaks. as_3 and as_4 are the corresponding amplitudes of the fitted USANS signal. $\frac{\bar{as}}{\bar{a}}$ gives the ratio for the USANS signal and the transmitted neutron beam averaged over the two center beams.

by a Guinier approximation for small Q-values [12, p. 11]. Here the fit function is called $g(x)$ given by

$$g(x) = o + o_1 \cdot x + \sum_{\mathrm{i}} a_{\mathrm{i}} \cdot \mathrm{e}^{-\frac{(x-c_{\mathrm{i}})^2}{2\,b_{\mathrm{i}}^2}} + \sum_{\mathrm{i}} as_{\mathrm{i}} \cdot \mathrm{e}^{-\frac{(x-c_{\mathrm{i}})^2}{2\,(b_{\mathrm{i}}^2+f^2)}} \tag{5.24}$$

where as_{i} stands for the amplitude of scattered intensity of peak i and the parameter f describes the additional broadening of the peaks due to the USANS/SANS signal caused by the lenses. To further quantify this effect the same fit technique has been applied to data acquired with aluminum samples of a thickness of 10 mm and 8 mm and a sample of 18 mm Suprasil for comparison. Here the function $f(x)$ is fit to the empty beam as before but the function $g(x)$ is fit to the data with the samples put in the neutron beam. A comparison of the scattered signal caused by different types of alumina and Suprasil is given in table 5.4. The ratio between the amplitudes as_{i} of the broadened peaks and the amplitudes a_{i} of the "transmitted" intensity is used to determine the scattering contribution. Only averaged values for the two center peaks are taken into account here, as the outer peaks have lower statistics and may be affected by the slight asymmetry of the peaks. The two aluminum samples exhibit a clear increase of the scattered signal compared to the one of the neutron lenses. On the contrary the 18 mm of Suprasil do not show a significant change. In order to get a more detailed information on the scattering behaviour of the three samples the fit function $g(x)$ is now used to solely describe the primary beam profile including the broadening due to the neutron lenses. Using the Guinier approximation again the scattering function of the sample is approximated by Gaussian

$$\hat{S}(Q) = a \cdot \mathrm{e}^{-\frac{Q^2\,R^2}{3}} \tag{5.25}$$

with R being the radius of gyration. A new fit function $h(x)$ expands $g(x)$ (Eqn. (5.24)) with parameters t_{i} describing the transmission signal of each of the primary peaks and two new terms resulting from the convolution of the primary beam profile and the Gaussian approximation of the scattering function

$$h(x) = o + o_1 \cdot x + \sum_{\mathrm{i}} t_{\mathrm{i}} \cdot a_{\mathrm{i}} \cdot \mathrm{e}^{-\frac{(x-c_{\mathrm{i}})^2}{2\,b_{\mathrm{i}}^2}} + \sum_{\mathrm{i}} t_{\mathrm{i}} \cdot as_{\mathrm{i}} \cdot \mathrm{e}^{-\frac{(x-c_{\mathrm{i}})^2}{2\,(b_{\mathrm{i}}^2+f^2)}} + \sum_{\mathrm{i}} ss_{\mathrm{i}} \cdot a_{\mathrm{i}} \cdot \mathrm{e}^{-\frac{(x-c_{\mathrm{i}})^2}{2\,(b_{\mathrm{i}}^2+s^2)}} + \sum_{\mathrm{i}} ss_{\mathrm{i}} \cdot as_{\mathrm{i}} \cdot \mathrm{e}^{-\frac{(x-c_{\mathrm{i}})^2}{2\,(b_{\mathrm{i}}^2+f^2+s^2)}}. \tag{5.26}$$

The parameters ss_{i} characterize the amplitude of the scattering signal for each peak. s is related to the radius of gyration via

$$R = \sqrt{\frac{3}{2\,(s \cdot \Delta Q)^2}} \tag{5.27}$$

PAR	transmission	uncertainty	rel. ERR	PAR	USANS	uncertainty	rel. ERR
t_1	0.720	±0.007	(0.97%)	ss_1	0.00538	±0.01126	(209.3%)
t_2	0.772	±0.003	(0.39%)	ss_2	0.00038	±0.00275	(723.7%)
t_3	0.774	±0.002	(0.26%)	ss_3	0.00005	±0.00443	(8860%)
t_4	0.794	±0.002	(0.25%)	ss_4	0.01072	±0.00188	(17.54%)
t_5	0.827	±0.003	(0.36%)	ss_5	0.00163	±0.00603	(369.9%)
t_6	0.811	±0.005	(0.62%)	ss_6	0.00452	±0.00523	(115.7%)
t_7	0.841	±0.020	(2.38%)	ss_7	0.02572	±0.03099	(120.5%)

Table 5.5: Transmission signal and USANS signal caused by Suprasil. Large errors are observed for the USANS signal, especially for off center peaks, indexes 1, 2, 3, 5, 6 and 7. Also a deviation of the evaluated sample transmission from the one of the center peak t_4 is found.

PAR	transmission	uncertainty	rel. ERR	PAR	USANS	uncertainty	rel. ERR
t_1	0.481	±0.007	(1.46%)	ss_1	0.117	±0.007	(5.98%)
t_2	0.489	±0.003	(0.613%)	ss_2	0.089	±0.003	(3.37%)
t_3	0.482	±0.002	(0.415%)	ss_3	0.081	±0.002	(2.47%)
t_4	0.470	±0.002	(0.426%)	ss_4	0.087	±0.002	(2.30%)
t_5	0.485	±0.003	(0.619%)	ss_5	0.093	±0.002	(2.15%)
t_6	0.471	±0.005	(1.06%)	ss_6	0.103	±0.005	(4.85%)
t_7	0.465	±0.020	(4.30%)	ss_7	0.195	±0.021	(10.8%)

Table 5.6: The aluminum sample of 10 mm thickness shows nearly the same transmission for all seven evaluated peaks. The larger deviation of the transmission and USANS signal for the off center peaks, indexes 1, 6 and 7 may be attributed to their asymmetric peak shape and lower intensity.

where ΔQ is just the Q-value corresponding to a single pixel of the detector. The plots resulting form fitting $h(x)$ to the data acquired from Suprasil and the aluminium samples are shown in figure 5.24. The evaluated fit parameters for the transmission t_i signal and the USANS signal ss_i are listed in table 5.5 for 18 mm of Suprasil, table 5.6 for 10 mm of aluminum and table 5.7 for 8 mm of the aluminum the neutron lenses are made of. The width of the peaks has been found to differ especially for the outer peaks on the detector. Besides a tilt of the sample aperture [15] a spherical aberration, coma, introduces an asymmetry for peaks having a large distance to the center of the multi beam pattern [17, p. 221ff]. The broadening of the peaks given by the parameter s in equation (5.26) is now used to derive the corresponding radius of gyration R via equation (5.27). As all fit-parameters are expressed in pixels first a mapping to the corresponding Q-values is necessary. It is not possible to assign a definite Q-value in $\mathrm{Å}^{-1}$ to the detector pixels directly, because the

PAR	transmission	uncertainty	rel. ERR	PAR	USANS	uncertainty	rel. ERR
t_1	0.353	±0.006	(1.70%)	ss_1	0.094	±0.007	(7.45%)
t_2	0.381	±0.003	(0.787%)	ss_2	0.082	±0.003	(3.66%)
t_3	0.371	±0.002	(0.539%)	ss_3	0.073	±0.002	(2.74%)
t_4	0.362	±0.002	(0.552%)	ss_4	0.080	±0.002	(2.50%)
t_5	0.379	±0.003	(0.792%)	ss_5	0.088	±0.003	(3.41%)
t_6	0.365	±0.004	(1.10%)	ss_6	0.086	±0.005	(5.81%)
t_7	0.385	±0.017	(4.42%)	ss_7	0.123	±0.020	(16.3%)

Table 5.7: The transmission and USANS signal evaluated for AG3-NET, the aluminum used for the neutron lenses, show larger deviations for the off center peaks again. The transmission is lower than the one of the standard aluminum, while the USANS signal is comparable.

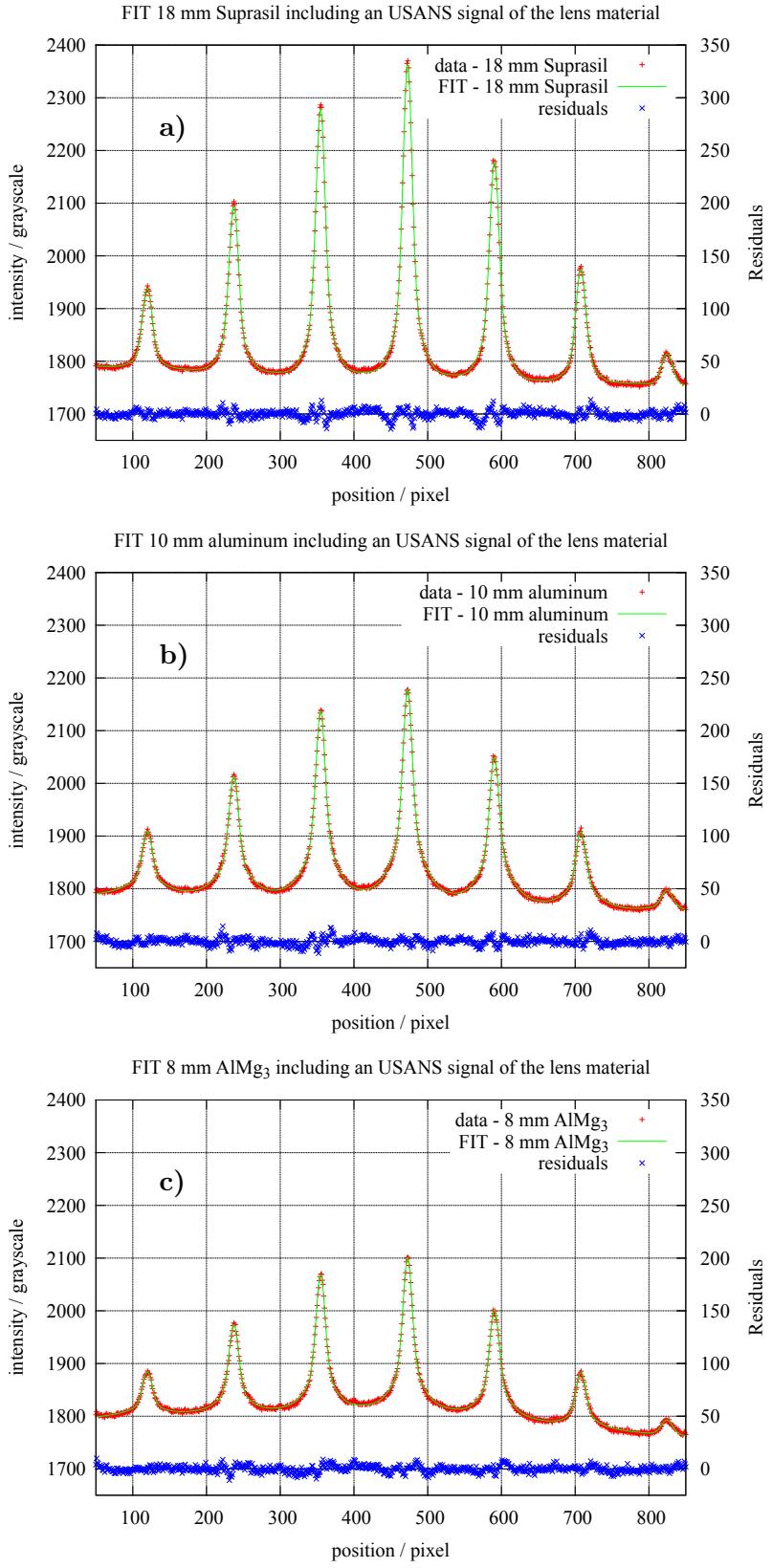

Fig. 5.24: a) 18 mm Suprasil does not show a significant scattering pattern b) 10 mm of pure aluminum c) 8 mm of AG3-NET

center position of each peak of the multi peak pattern on the detector corresponds to $Q = 0$. But all parameters given in pixel can be converted to Q-values in Å^{-1} by a simple multiplication with ΔQ corresponding to a single detector pixel. For the given setup

$$\Delta Q = \frac{2\,\pi}{\lambda \cdot L_{\mathrm{D}}} \cdot \Delta d = \frac{2\,\pi}{16.47\,\text{Å} \cdot 22.52\,\mathrm{m}} \cdot 80 \cdot 10^{-6}\,\mathrm{m} = 1.36 \cdot 10^{-6}\,\text{Å}^{-1} (\pm 0.03 \cdot 10^{-6}\,\text{Å}^{-1}) \,. \quad (5.28)$$

For the Suprasil sample the fit resulted in a broadening $s = 73.43 \pm 23.32$ ($\pm 31.76\,\%$) and the corresponding radius of gyration is

$$R_{\mathrm{Suprasil}} = \sqrt{\frac{3}{2\,(s \cdot \Delta Q)^2}} = \sqrt{\frac{3}{2\,\left(73.43 \cdot 1.36 \cdot 10^{-6}\,\text{Å}^{-1}\right)^2}} = 1.23\,\mu\mathrm{m}\,(\pm 0.39\,\mu\mathrm{m}) \,. \quad (5.29)$$

The amplitudes of the USANS signal for Suprasil are less than one percent of the transmission signal and the relative error of the amplitudes is huge. This and the high uncertainty values of all fit-parameters of the Suprasil USANS signal suggest that there is no ultra small angle neutron scattering caused by Suprasil. At least it is much smaller than the contribution of the lens material to the total USANS signal at the detector.
For 10 mm of aluminum in the neutron beam the broadening is given by $s = 33.79 \pm 0.41$ ($\pm 1.21\,\%$). The error of the fit-parameter is much less here and the radius of gyration

$$R_{10\,\mathrm{mmAl}} = \sqrt{\frac{3}{2\,(s \cdot \Delta Q)^2}} = \sqrt{\frac{3}{2\,\left(33.79 \cdot 1.36 \cdot 10^{-6}\,\text{Å}^{-1}\right)^2}} = 2.67\,\mu\mathrm{m}\,(\pm 0.07\,\mu\mathrm{m}) \,. \quad (5.30)$$

Finally the radius of gyration $R_{\mathrm{AG3-NET}}$ is derived from $s = 44.46 \pm 0.49$ ($\pm 1.10\,\%$).

$$R_{\mathrm{AG3-NET}} = \sqrt{\frac{3}{2\,(s \cdot \Delta Q)^2}} = \sqrt{\frac{3}{2\,\left(44.46 \cdot 1.36 \cdot 10^{-6}\,\text{Å}^{-1}\right)^2}} = 2.03\,\mu\mathrm{m}\,(\pm 0.05\,\mu\mathrm{m}) \,. \quad (5.31)$$

The evaluated values for the radius of gyration of the two aluminum samples are reasonable and consistent with an expected scattering signal of aluminum in the Q-range of 10^{-4}Å^{-1} [14], [59].

5.4.4 Check of Detector Calibration

The measured intensity profiles for the phase gratings are used to check the calibration of the USANS setup. They are evaluated by two methods. The first one is an evaluation in analogy to the initial data reduction of standard pinhole SANS data. A dedicated analysis software, μSANS is used to extract line profiles from the measured intensities resulting from the multiple beam geometry (App A.12). It automatically determines the positions of the maxima of the primary intensity, and corrects the scattered intensity pattern for effects like: the transmission of the sample and the sample container, background resulting from the sample container or a solvent the sample is embedded in, a hall background and artefacts arising from the detector due the inhomogeneity of the detection efficiency of the scintillation screen or the darkcurrent signal and offset of the imaging sensor. After the corrections the line profiles of the evaluated region of interest are summed up along the direction of the slits and saved. The second method is similar to the fit-procedure from above. Here a model of the expected intensity distribution is directly fit to the multi beam pattern summed along the slits. For the given geometry the model consists of 11 peaks for the primary intensity and 11 peaks each for the intensity scattered in positive and negative Q-direction with respect to the primary peaks.

μSANS Evaluation For the evaluations using μSANS the line profiles are summed for a large and a small area of the intensity pattern of the USANS data to see if the neutron statistics of parts with lower intensity effects the results. For the large area the whole detector area is used as an input for μSANS. The program then uses the peaks of the primary intensity, which exceed a certain threshold, to determine the position of $Q = 0$ for each line of the acquired image. The width of the extracted line profiles is set to half of the distance between the primary peaks, as larger scattering angles cause an overlap of the left and right profile for two neighboring primary peaks. This effect is visible in figure 5.25, where the extracted line profiles of the scattered intensities for different calibration gratings are plotted.[12] The full Q-range corresponding to the distance between two peaks of the multi-peak pattern is plotted. $Q = 0$ corresponds to the position of one peak and the maximum Q-value of the plot is equivalent to the position of the neighbouring peak and therefore equivalent to $Q = 0$. The right line profile is plotted in positive Q-direction starting from $Q = 0$. And the left line profile is plotted in negative Q-direction starting from the maximum Q-value. For the 12 μm grating the left and the right line profile only show a slight overlap (Fig. 5.25c). For the 8.5 μm grating the intensity scattered to the left and to the right of the primary peaks forms a nearly perfect single peak centered between the peaks of the transmitted primary intensity (Fig. 5.25b). For the 4 μm grating the scattering angle is that large that the scattered peaks are close to the position of the neighboring primary peak already. If it was not known that these peaks originate from a 4 μm grating, their position would suggest that the scattered intensity corresponds to a grating with a period of 27 μm (Fig. 5.25a). The results of the evaluation are summarized in table 5.8 at the end of this chapter.

Fit to USANS Data As shown in section 5.4.3 the neutron lens arrays used instead of standard sample apertures give rise for a small angle scattering signal, which should be taken into account for a description of the primary beam profile. In order to see whether there is an influence of this additional scattering signal on the evaluated parameters two sets of fit-functions have been used to model the measured intensity distributions with and without a sample. One assumes that there is no contribution of a scattering signal caused by the neutron lenses and the other one includes the scattering signal of the neutron lenses for the profile of the primary beam similar to the fit function $h(x)$ defined by equation (5.26) but adapted to 11 primary peaks instead of 7. In case the scattering of the neutron lenses is disregarded the fit function $f'(x)$ for the primary intensity is composed from 11 Gaussian peaks. For each peak the amplitude a_i, the peak width b_i and the peak position c_i are free parameters for the fit.

$$f'(x) = o + a_1 \exp(-\frac{(x-c_1)^2}{2\,(b_1)^2}) + a_2 \exp(-\frac{(x-c_2)^2}{2\,(b_2)^2}) + \ldots + a_{11} \exp(-\frac{(x-c_{11})^2}{2\,(b_{11})^2})\,. \quad (5.32)$$

An offset o allows to fit $f'(x)$ directly to the measured line profile without a correction of the detector offset. The fit function $g'(x)$ for the scattered intensity profile uses 11 Gaussian peaks for the transmitted signal and 22 additional Gaussian profiles describing the intensity scattered by the gratings, 11 peaks for neutrons scattered in positive Q-direction and 11 peaks for neutrons

[12] The corresponding measured intensity profiles are found in section 5.2.3, figures 5.13 and 5.14.

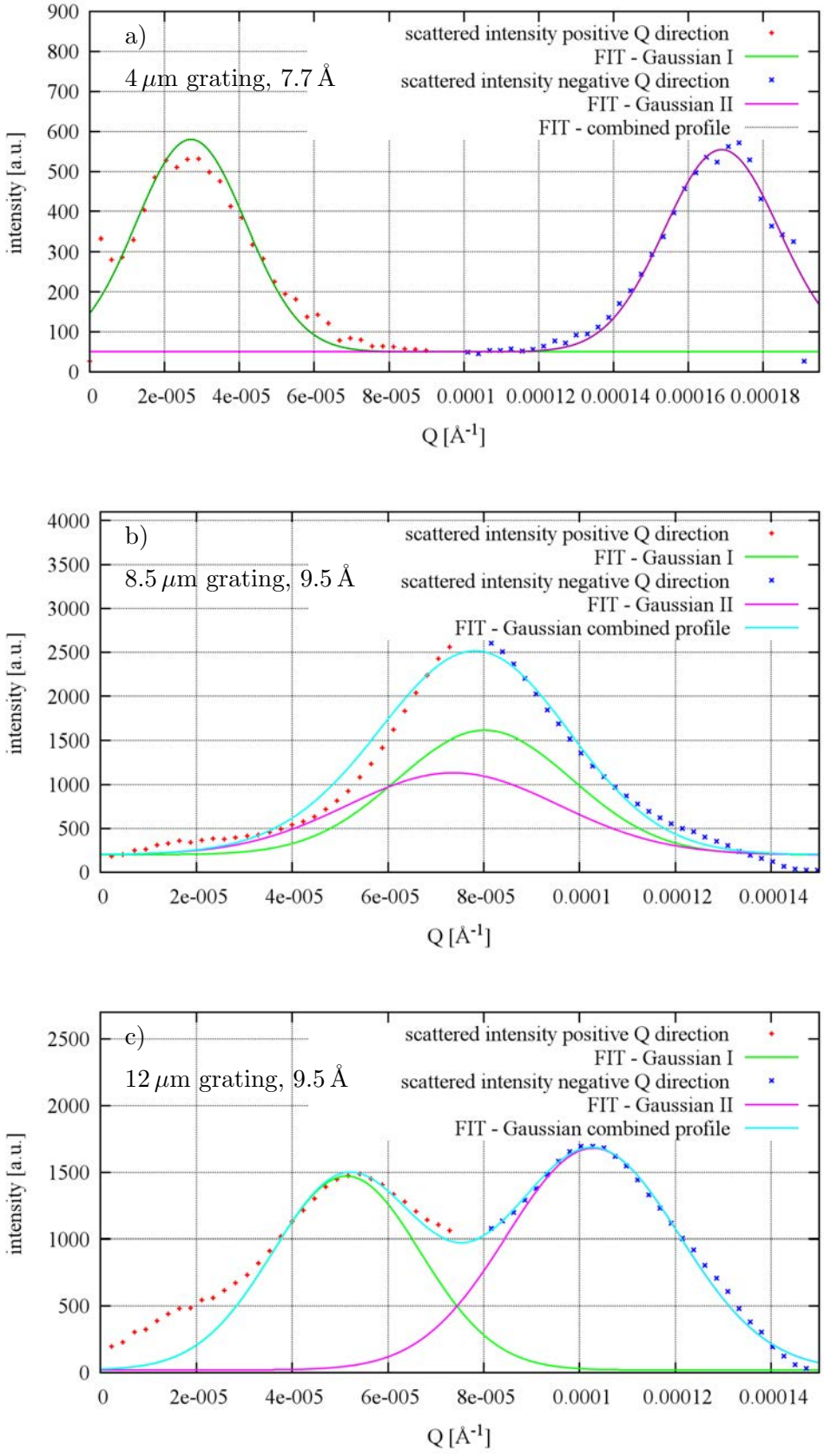

Fig. 5.25: Two Gaussian profiles are fitted to the measured line profiles resulting from the evaluation using μSANS, one for the positive Q-direction and one for the negative. The line profiles are corrected for the sample transmission and the transmitted primary intensity. The corrected data points, the fitted single Gaussian profiles and their sum are shown for: a) a 4 μm phase grating, b) a 8.5 μm phase grating and c) a 12 μm phase grating. Note that for the 4 μm grating the scattered intensity already starts to overlap with the neighbouring peak of the primary intensity.

scattered in negative Q-direction.

$$
\begin{aligned}
g'(x) \;=\; & \underbrace{o + a_1\,\exp(-\frac{(x-c_1)^2}{2\,(b_1)^2}) + \ldots + a_{11}\,\exp(-\frac{(x-c_{11})^2}{2\,(b_{11})^2})}_{\text{transmitted intensity}} \\
& + \underbrace{als_1\,\exp(-\frac{(x+d_\mathrm{s}-c_1)^2}{2\,(f_1)^2}) + \ldots + als_{11}\,\exp(-\frac{(x+d_\mathrm{s}-c_{11})^2}{2\,(f_{11})^2})}_{\text{intensity scattered to negative } Q} \\
& + \underbrace{ars_1\,\exp(-\frac{(x-d_\mathrm{s}-c_1)^2}{2\,(f_1)^2}) + \ldots + ars_{11}\,\exp(-\frac{(x-d_\mathrm{s}-c_{11})^2}{2\,(f_{11})^2})}_{\text{intensity scattered to positive } Q}\,. \qquad (5.33)
\end{aligned}
$$

The positions c_i and the widths b_i of the transmitted intensity are not varied and correspond to the parameters of the fit of $f'(x)$ to the primary intensity profile. A change in the amplitudes a_i of the transmitted signal takes into account the sample transmission. The amplitudes als_i and ars_i for the intensity scattered in positive and negative Q-direction are fitted independent of each other. The width of the peaks for scattering in positive and negative Q-direction are the same. The Q-value corresponding to the spacing of the grating is determined from the shift d_s. This shift is expected to be the same for the positive and negative Q-direction. The fit process is carried out in three steps: At first line profiles are extracted from the acquired images of the primary intensity and the intensity distribution with the sample, here the grating. Then $f'(x)$ is fitted to the primary intensity to determine the position and the width of the primary peaks. The third step is to fit $g'(x)$ to the profile containing the scattered intensity. The measured profiles and the fitted functions for the 4 μm are plotted in figure 5.26. There is an obvious deviation of the fit for the primary beam profile (Fig. 5.26a), because a single Gaussian fitted to each peak is not enough to included scattering signal of the neutron lenses. There is less deviation for $g'(x)$ when the terms representing the scattered signal are added. But this improvement is only due to the fact that the additional terms compensate the effects of the scattering signal contributed by the lenses. This causes a large error for the evaluated Q-value of the 4 μm grating. The situation is different for the 8.5 μm and 12 μm gratings, because here the scattered intensity has only a small overlap with the transmitted primary intensity. The measured intensity distributions and the corresponding fits are presented in figure 5.27 and figure 5.28. Both fits reveal imperfections for the outer peaks of the recorded intensity patterns. This is due to the asymmetry of these peaks. The 12 μm grating shows an obvious asymmetry for the intensities scattered in positive and negative Q-direction. Possible reasons for this behaviour might be an off-center position of the lens array or additional apertures at the sample position like they have been discussed in section 5.4.1 already or a misplaced sample, e.g. that some of the multiple beam did not pass through the sample or only partially hit it. As the 12 μm grating has been faked by rotating the 8.5 μm grating by 45° around the neutron beam axis, this fact might also give rise for the asymmetric behaviour. The sample transmission has been determined from the amplitudes of the primary peaks and the amplitudes of the transmitted signal of each peak of the primary beam profile. There is a transmission value for each single peak of the multi-peak pattern. If there is an evident difference between these values, it is a hint that the sample has not been covering the hole area of the sample aperture array and some of the multiple neutron beams did not hit the sample. The transmission values for the single peaks of the 4 μm grating, the 8.5 μm grating and the 12 μm grating are listed in table A.5, table A.6 and table A.7 in appendix A.13. For an evaluation of the calibration of the detector only the shift d_s is of interest. After the fit-process d_s is given in pixel values and mapping is used again to transform to a Q-value corresponding to the position of the scattered intensity peak for a further evaluation. A comparison of the expected Q-values of the calibration gratings and the evaluated Q-values for different evaluation methods are given in table 5.8.

The best agreement is reached for the 8.5 μm grating (method 2). This is surprising, as the peak of the scattered intensity for the 8.5 μm grating is positioned at the center between the peaks of the

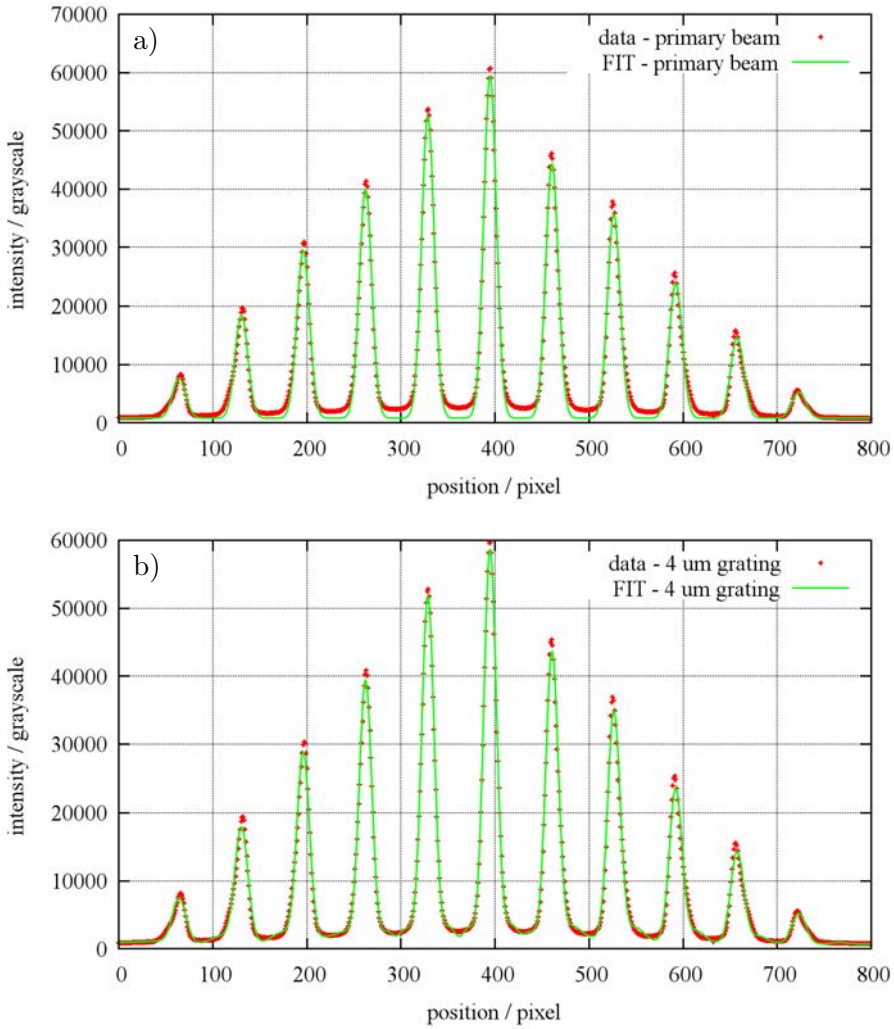

Fig. 5.26: a) measured intensity distribution of the primary beam profile and FIT using a single Gaussian for each peak. b) With a grating of 4 μm periodicity placed at the sample position the intensity profile does not show a big difference as the scattered intensity has a strong overlap with the transmitted primary beams. Three Gaussians are fitted for each peak of the primary intensity profile, one for the transmitted intensity and two for the scattered intensity caused by the 4 μm grating in the neutron beam.

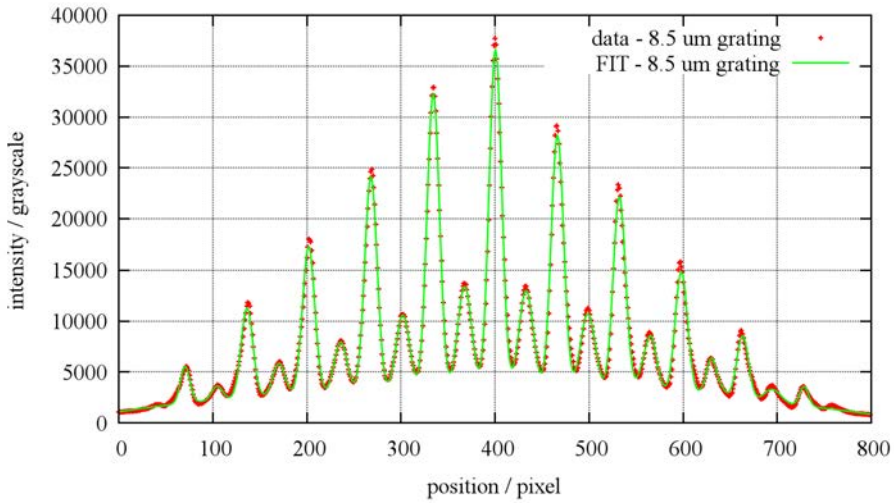

Fig. 5.27: For the 8.5 μm grating neutron scattered to positive and negative Q-values form a nearly perfect peak centered between the transmitted peaks of the primary beam profile. Due to the symmetric composition of the fit function $g'(x)$ built from Gaussian profiles only the asymmetric peak shape of the outer peaks described adequately.

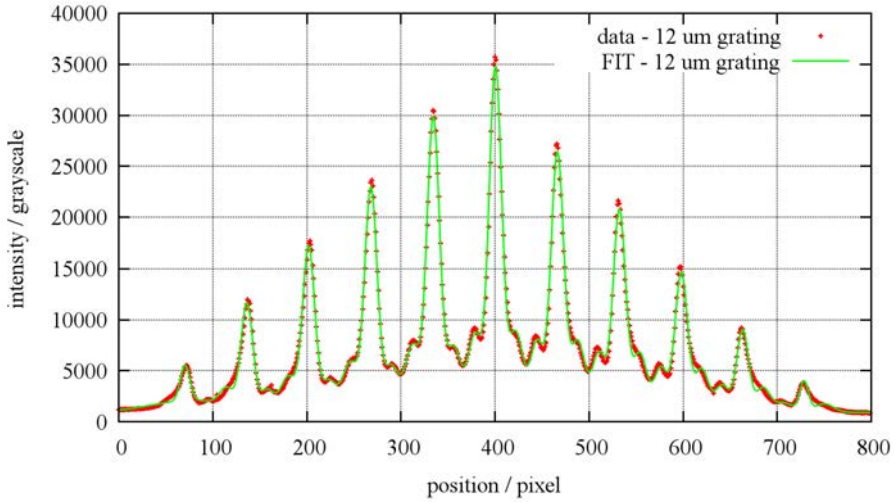

Fig. 5.28: The scattered intensity of the 12 μm grating is close to the transmitted primary beam. An asymmetric scattering behaviour has not been found for the positive and negative Q-direction.

#	evaluation method	4 μm grating	8.5 μm grating	12 μm grating
	expected Q-value, 10^{-5} Å^{-1}	15.71	7.392	5.236
1	μSANS large area, 10^{-5} Å^{-1}	16.38 ± 0.06	7.1 ± 0.6	5.1 ± 0.1
	deviation from expected value	4.26 %	4.0 %	2.6 %
2	μSANS small area, 10^{-5} Å^{-1}	16.54 ± 0.07	7.4 ± 0.2	5.15 ± 0.08
	deviation from expected value	5.28 %	0.1 %	1.64 %
3	FIT of peak model, 10^{-5} Å^{-1}	12.5 ± 0.1	7.45 ± 0.09	5.08 ± 0.02
	(neglecting the USANS signal of the lenses)			
	deviation from expected value	20.4 %	0.78 %	2.98 %
4	FIT of peak model, 10^{-5} Å^{-1}	15.2 ± 0.4	7.26 ± 0.08	5.17 ± 0.03
	(including the USANS signal of the lenses)			
	deviation from expected value	3.25 %	1.79 %	1.26 %

Table 5.8: Result of the evaluation of the measured data acquired from the gratings used to check the detector calibration.

primary intensity. The two peaks corresponding to a positive and a negative Q-value are overlapping nearly completely. In fact the evaluated values show a large uncertainty for the μSANS method. The smallest uncertainties are reached for the 12 μm grating. But there is a larger deviation from the expected Q-value than for data of the 8.5 μm grating. This might be explained by the fact that the 12 μm grating has been faked by tilting the 8.5 μm around the beam axis. An angle of tilt of 45° with respect to the direction of the slits of the source aperture or the sample aperture would result in an effective spacing of $8.5\,\mu\text{m} \cdot \sqrt{2} = 12\,\mu\text{m}$ perpendicular to the apertures, because the current geometry of the USANS setup is only sensitive to scattering along the Q_x direction. If the tilt angle has not been set to 45° exactly, there is a different effective spacing of the grating, of course. The measured Q-values suggest a spacing of the grating of $12.30\,\mu\text{m} \pm 0.16\,\mu\text{m}$. This is equivalent to an angle of tilt of $46.3° \pm 0.7°$ instead of 45 °. As the grating was placed at the sample position by hand, it is indeed possible that the tilt angle is not 45 ° but off by one or two degrees. For the intensity pattern measured with the 4 μm grating in the neutron beam the scattering angle is already that large that the peak corresponding to the scattered intensity is close to the center of the neighboring peak of the transmitted primary intensity. The average transmission of the 4 μm phase grating is evaluated to be 97 %. Thus the USANS signal caused by the grating is much smaller than the intensity transmitted through the grating (Tab. A.5), which makes it hard to fit the profiles for the scattered intensity. The deviation from the expected peak position is 4 % to 5 % for the evaluation with the μSANS software, when the line profiles are summed up for a large and a small area (methods 1 and 2). These methods do inherently include a correction for the USANS signal of the neutron lenses, because the transmitted primary beam profile is subtracted from the intensity measured with the sample inside the beam. In contrary approximating each peak of the primary beam profile by only a single Gaussian does not correct for the USANS signal caused by the neutron lenses. Here the deviation of the measured Q-values from the expected one for the 4 μm grating is more than 20 %(method 3). If now an effect due to scattering of neutrons by the aluminum lenses is included to the fit function, the fit results in a Q-value whose deviation from the expected value is only 3.25 %(method 4). Still the expected Q-value is not within the uncertainty of the measured value.

For the μSANS evaluation (methods 1 and 2) values not too close to $Q = 0$ and without an overlap in the proximity of Q_max defined by half the distance between two maxima of the primary intensity pattern the uncertainties are small either for a large or a small evaluated area. There is a larger deviation for the evaluated Q-values close to $Q = 0$. This seems to be caused by the correction used for the transmitted signal, as it does not allow for a scattered intensity at $Q = 0$ often resulting in negative values for the corrected scattered intensity profile close to $Q = 0$. The μSANS evaluation should not be used for the evaluation of signals which show an overlap of the scattered

intensity corresponding to neighboring peaks of the primary intensity, nor should it be used for signals with a distinct overlap with the transmitted primary beam profile. Fitting a peak model to the measured profiles (methods 3 and 4) may be used for nearly any Q-range in between two neighboring maxima of the primary intensity pattern. But it is important to include a correction for the scattered intensity due to the lens material (method 4).[13] Otherwise the evaluated Q-value is altered by the contribution of this additional scattered intensity (method 3, 4 μm).

5.5 Summary USANS

The current setup was limited to a one-dimensional evaluation of the data due to the slit shaped apertures, that only make the scattering signal perpendicular to the slit direction accessible. But this geometry allows to reach a much higher neutron flux at the sample. Thus carrying out two measurements to determine the scattering behaviour of a sample in x-direction and y-direction may be faster and result in a better signal statistics than using a two-dimensional geometry. Another advantage of the vertical slit geometry is that gravitational effects are automatically canceled out by summing along the slit direction. A two-dimensional setup on the contrary would afford special measures, i.e. prisms, to correct for these effects. Neutron lenses allow to increase the neutron flux at the sample and the detector proportional to the transmission area or active area of the lenses, while their ability to image the source aperture onto the detector plain does still result in an improved Q-resolution. As long as the imaging equation is fulfilled, the behaviour of a neutron lens used as a sample aperture may in a first approximation be described as follows:

- With respect to the imaging of the source aperture onto the detector lenses act like a nearly perfect pinhole aperture.
- The neutron flux forwarded to the sample is determined by the active area of the lens and equivalent to the one of a standard aperture of the same size.

These theoretical estimates of the performance of the lenses could be confirmed by a comparison of the integral intensities at the detector measured with and without a neutron lens array placed at the sample position. The attenuation of the neutron beam by the lenses made from aluminum is negligible. A major drawback of neutron lenses is that a certain configuration of lens arrays may only be used in combination with a fixed neutron wavelength. This is due to the necessity to fulfill the imaging equation in order to get an optimized peak shape of the primary intensity profile on the detector. A second constraint for multiple beam geometries is that the distances between the source aperture array, the sample aperture array and the detector plane are fixed to yield an overlay of the multiple neutron beam at the detector plane. The neutron wavelength is the only free parameter that can be adjusted for focusing the setup. Using a fixed neutron wavelength and a fixed distance from the sample to the detector automatically results in a limited Q-range. There is a possibility though to change the total focal length by stacking a different number of neutron lenses or the geometry of the multiple beam configuration by using different center to center distances for the source aperture or the lens arrays. Thus the distance from the sample aperture array, i.e. the sample, to the detector or the neutron wavelength can be varied, which in turn allows to access a modified Q-range. One has to be careful when placing additional apertures at the sample position, e.g. to restrict the size of the neutron beam to the size of the sample. In combination with the aperture or lens array such a configuration results in an effective aperture with reduced transmission area. This not only yields a much lower intensity at the sample and the detector but may also prevent an overlap of the multiple neutron beams. At worst the idea of a multiple beam geometry might be reduced to a single neutron beam geometry of poor performance. In that case an optimized single beam geometry might be a better choice. For the sample aperture geometry analyzed in section 5.4.1 it can be concluded that an improper positioning of the second aperture

[13] This correction might not be necessary if the neutron lenses are fabricated from a material which does not show such large SANS or USANS effects as AG3-NET.

reduced the neutron flux at the sample position by a factor of two compared to the one if it was placed in an optimized way. The major part of the peak intensity resulted from a combination of on source aperture and one neutron lens each. Thus the multi peak profile did not have the character of a real multiple beam SANS or USANS anymore, as there was only a partial overlay of two neutron beams for the center peaks. In fact the additional circular aperture caused the multiple lens array consisting of 5 lenses to appear like a single lens only. A maximum number of 20 neutron beams reaching the detector would be possible for a combination of 4 source apertures and 5 neutron lenses. But effectively only 4 beams have been able to pass through the combination of the two apertures. If an aperture combination has to be applied to restrict the incident neutrons to the sample cross section one has to optimize it to yield a maximum transmission area. Of course it would be best to use samples large enough to cover the whole sample aperture array. Otherwise the theoretical gain factor for multi apertures has to be reconsidered. In theory one assumes that all slits or holes of the sample aperture array are illuminated by each slit or hole of the source aperture array and that all beams passing through the sample aperture array hit the sample. Only that way the theoretically possible maximum number of multi peaks and therefore the expected gain factor by summing up all peaks is reached. In practice there might be a limitation due to the beam divergence of the single neutron beams emitted by the source aperture, which will not allow for a full illumination of the sample aperture array no matter if a one-dimensional slit geometry or a two dimensional layout using a multi pinhole geometry is chosen. Further more the sample itself might cause a reduction of the number of contributing neutron beams if its cross section is less than the size of the sample aperture array. In that case neutron beams not hitting the sample at all or only partially will result in no scattering signal or an asymmetric contribution to the overall signal after summation.

Artificial gratings of known periodicity have been used to check the calibration of the detector, which means the ΔQ that has been calculated to correspond to a single pixel of the detector. Data of three gratings have been evaluated using four different methods. In all cases but one the deviations of the evaluated periodicity from the real value have been less than 5 %. Five results have even been within a range of less than 2 %. A deviation of more than 20 % has been observed for a fit of the 4 μm grating. Here the scattered intensity showed a large overlap with the transmitted primary intensity and was weaker than for the other gratings. As there was no correction for the additional USANS signal caused by the aluminum the lenses were made of, the deviation can be attributed to that signal. As soon as the USANS signal of the lens material was taken into account, the deviation could be reduced to only 3.25 %. This means that the additional USANS signal of the lenses has to be taken into account during the evaluation. As this effect alters the shape of the primary beam profile, it must be included for the description of the primary beam profile. Neutron lenses made from aluminum have only been used for the preliminary experiments, because it has been possible to machine the lenses in the local workshop using standard computer controlled machines and the aluminum has been available easily and inexpensive, too. Further improvements are possible if the neutron lenses are produced from other materials, that do not give rise to an USANS signal. Possible materials are Suprasil, magnesium, magnesium oxide, magnesium fluoride, sapphire, beryllium, bismuth ... [10, p. 3.2-19].

In principle the evaluation of the multiple beam USANS data was carried out based on two different principles. One of them is actually a kind of preprocessing in order to apply standard techniques afterwards. Using the μSANS software the intensities of the multi peak pattern are not only summed along the stripe shaped peaks resulting for the source slits and the cylindrical neutron lenses, but also the individual peaks were combined to a single line profile. The resulting line profile may then be evaluated using standard SANS software.

The second evaluation method used dedicated and adapted functions which were fitted to the multiple peak pattern. This allowed to evaluate diffraction patterns even if there is an overlap of the signals, e.g. of scattered neutrons and the transmitted primary intensity or arising from scattered neutrons corresponding to neighboring primary peaks. This kind of evaluation may often yield better results than summing up the integrated intensities of all peaks to a single line profile.

Disadvantages of a standard evaluation in combination with μSANS are: If the sample does not cover the whole sample aperture array, some of the multiple neutron beams miss the sample. Therefore the transmission correction must fail. As the final line profile is averaged over all peaks, asymmetries of the peak profiles far from the center of the multiple beam pattern will be included. This alters the results of data evaluation.
Advantages of this evaluation method are: It is possible to sum up and correct the acquired USANS data without a prior knowledge of the scattering behaviour or the sample. The line profile of the scattered intensity is extracted without the need of a model. The line profile, which is available at the end of the evaluation process, is equivalent to the line profiles of a standard SANS measurements. The evaluation is therefore straightforward.
Using the FIT-method to evaluate the data is favorable if there is a model for the expected distribution of scattered neutrons. The main advantages of this method are: An overlap of the transmitted primary intensity and neutrons scattered in forward direction can be included to the fit function. Thus it is even possible to evaluate data that have a large overlap with the primary intensity pattern close to $Q = 0$. The transmission signal and the signal corresponding to scattered neutrons are represented by separate parts of the fit function. A separation of the two signals after the fitting is easy. The sample transmission is evaluated separately for each peak of the primary intensity pattern. This allows to determine and to exclude peaks which show a too large transmission compared to the other peaks, because there is a contribution of neutrons beams that do not pass through the sample. Also the scattering signal is not necessarily deduced from the fit parameters of all peaks. For example fit parameters of peaks that show a clear asymmetry can be excluded.
Drawbacks of the FIT-method are: It is not a universal method to evaluate USANS data, because the fit function must be adapted to the current sample. The evaluation does not result in a line profile of the scattered intensity versus Q like it is known from standard pinhole SANS evaluations. A large number of peaks, e.g. for a two-dimensional configuration of holes instead of slits, gives rise to huge number of parameters that have to be fitted including much more complicated fit functions than the ones presented in here. An evaluation method like μSANS summing up all data to a single line profile can give a first view of the scattered neutron intensity. As it is much faster than the fit-method, it can be used in parallel during the measurements. Using fit functions is the preferred method to get a more precise information of the sample characteristic.

Chapter 6

Conclusions

Neutron imaging detectors have successfully been applied for measurements in real space and reciprocal space, more precisely for a time resolved investigation of test oil inside an injection nozzle and Ultra Small Angle Neutron Scattering using a multiple beam geometry in combination with neutron lens arrays. In case of neutron radiography the main aim has been to simultaneously reach a maximum in time and spatial resolution. Here the spatial resolution has been improved by a factor of two from 63 μm to 30 μm without a trade-off for the time resolution. For the USANS applications the spatial resolution of a standard neutron imaging detector offering a pixel size of 80 μm has been sufficient to get access to Q-values in the range of $5 \cdot 10^{-6}$ Å^{-1} to $2 \cdot 10^{-4}$ Å^{-1}. This is equivalent to maximum of the evaluated lateral coherence length of 126 μm. For detectors based on scintillation screens without the need for precise timing and short exposure times spatial resolutions even below 10 μm have been reported [60]. The MCP detector is capable to reach a spatial resolution of 15 μm, too, as long as there is no need for high time resolution [52]. Thus it has been shown that neutron imaging and neutron diffraction provide a clear overlap on micrometer length scales.

Within the scope of the time resolved neutron radiography on an injection nozzle three different detector configurations have been used and their characteristics have been compared with respect to their spatial resolution and their noise and signal statistics. This includes effects due to a gamma background in form of direct detection probabilities by the neutron absorbing converter in the first place and in form of a direct detection by the imaging sensor of the detector. An emphasis is put on detectors with neutron scintillation screens and an optical coupling to the imaging sensor via a lens system. The evolution of the number of quanta carrying information form the input side to the output side of such cascaded detection systems has been illustrated with the help of a Quantum Accounting Diagram (QAD). By means of the QAD for a given detector configuration one can easily determine the conversion step or process which is most likely to limit the detector performance. Along with a standard technique for the normalization based on measured data only two techniques making use of calculated or simulated radiographies representing the full sample or only parts of it have been used during the evaluation to mask or extinct certain features of the sample, here the nozzle body, in order to enhance the contrast of other ones like the test oil inside the spray hole of the nozzle. It has been possible to visualize the test oil inside the spray hole of the injection nozzle. But the spatial resolution has not been good enough to yield detailed information about its behaviour during the injection process. The decision to employ a Gd_2O_2S scintillator with a phosphor layer of 20 μm thickness in order to improve the primary neutron statistics has been wrong. The detection efficiency of a phosphor layer of only 10 μm thickness would have been sufficient, while the spatial resolution could have been improved. For the measurements with the MCP detector the fixed detector resolution given by the pixel size of the Medipix readout of 55 μm has been a limiting factor for the spatial resolution.

A major part of the chapter about USANS is concerned with the formation of the primary beam profile. Especially the interplay of the neutron lens arrays with standard aperture arrays and additional apertures has been discussed. It has been found that under certain preconditions the

primary beam profile may be described by a correlation of the opening function of the source aperture and the sample aperture including appropriate scaling factors determined by the distances between the apertures and the detector plane to obtain the intensity distribution of the primary beam profile directly in coordinates of the detector plane. This allows for a fast and simple way to estimate the primary beam profiles for different aperture configurations. In this context also effects resulting from a combination of different apertures forming an effective aperture have been discussed. For a combination of standard apertures and aperture arrays of a multiple beam geometry one should be aware that the resulting effective aperture may render the whole multiple beam geometry useless as only very few of the expected multiple beams are actually forwarded to the sample. As such additional aperture are primarily used to restrict the cross section of the multiple beam geometry to the size of the sample, it would be a better choice to use a sample of a larger cross section or to reconsider the layout of the beam geometry to reach a smaller cross section of the neutron beam at the sample position comparable to a standard sample size. For the evaluation of the acquired data using slit shaped apertures and cylinder lenses forming the multiple beam USANS geometry two concepts have been applied. The μSANS software has been developed to correct intensity profiles composed of the transmitted primary beam and a scattered neutron signal for the sample transmission and background contributions. Finally the scattered intensity is converted to an intensity profile versus Q. The images recorded by the neutron imaging detector can directly be used as input files for this software. The correction steps follow a standard evaluation for SANS adapted to the use of an imaging detector and slit shaped apertures. For a large overlap of the scattered intensity with the transmitted primary beam μSANS should not be used. Therefore a second method of fitting dedicated functions directly to the multiple beam intensity distributions has been applied. This method is much more flexible and allows for a detailed investigation of the behaviour of individual peaks and an evaluation of scattering signals with large or direct overlap with the transmitted primary beam. In principle Q-values down to $Q = 0$ may be evaluated limited by the detector resolution and the quality of the fit functions. Data of calibration gratings of $4\,\mu$m, $8.5\,\mu$m and $12\,\mu$m spacing have been evaluated with an average deviation from the expected value of 2.5 %. The neutron lenses made of aluminum (AG3-NET) have shown an inherent contribution of an USANS/SANS signal. It has been possible to compensate this by including the scattered intensity to the description of the primary beam profile. Neutron lenses for a permanent instrumentation should be fabricated from different material with less or no contribution to the scattered neutron intensity. The shape of the neutron lenses should be optimized to reduce the effects of spherical aberration like coma. It could already be an improvement if the biconcave lenses are replaced by plano-concave ones. Similar measures are applied to overcome such problems for visible light as well. Due to the fact that a well collimated beam is available at the sample position of SANS instruments a neutron imaging detector may be used to check for the correct illumination of the sample and its homogeneity within a few minutes. An additional detector installed could also be used to gain more information about the sample, e.g. for a combination of imaging and diffraction on the micrometer length scale on a single instrument.

Many improvements of converters have been made and new imaging sensors have been invented since Rossmann,[61] concluded in 1966: *"It is difficult ... to develop a general technique for measuring radiographic image quality which holds for all types of images under any condition."* This is still true and will be in future. It is therefore due to the experience of the examiner to choose the correct instrumentation or due to his patience to optimize the experimental setup until the available signal statistics and resolution either in real space or reciprocal space allow for a contrast high enough to detect the detail he or she is looking for. A better understanding of all processes involved in signal generation for neutron imaging detectors is surely helpful here.

Appendix A

Appendix

A.1 Optical Setup for iCCD-highRes

The detector for the high resolution configuration iCCD-highRes is based on the optical box of the DELCam[1]. In order to reach the desired FOV of only $3.5 \times 3.5\,\mathrm{mm}^2$ the has been mounted in reverse direction where the distance between the flange of the lens and the imaging sensor of the camera had been calculated to be 552 mm. For this purpose and to prevent stray light from entering the camera extension tubes had been built in the local workshop (Fig. A.1a). This mounting is also used for focusing the detector system, as the focus setting of the lens had to be kept at ∞. The largest dimension of the light cone from the scintillator to the lens is determined from the diagonal of the field of view and the diameter of the entrance pupil of the lens[2]. The estimated light cone for the LEICA APO-MACRO-ELMARIT-R inside the optical box of the detector is shown in figure A.1b.

a) 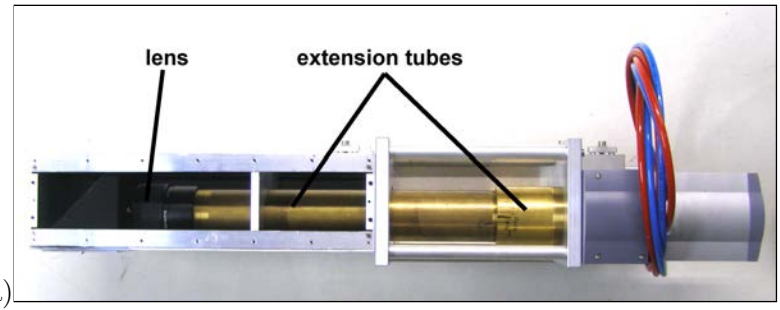

b) 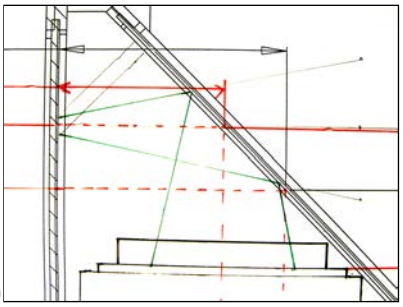

Fig. A.1: a) The intensified CCD camera mounted on the optical box of a DELCam. The lens is attached to the camera by custom-made extension tubes. b) The estimated light cone inside the optical box.

Light having a perpendicular inclination on the mirror is directly reflected back onto the scintillator. This causes an unwanted illumination of the scintillator and a background signal due to diffuse reflection of the light. Based on the estimated light cone that enters the lens a strip of black cardboard has been attached on the mounting frame of the mirror to cover parts of the mirror that are not needed for imaging the FOV on the scintillation screen onto the imaging sensor but likely to cause reflexions of the emitted scintillation light back onto the scintillation screen (Fig. A.2a). As only light emitted from a very small part of the scintillator is recorded by the imaging sensor, the remaining surface of the scintillator has been shielded by black cardboard, too (Fig. A.2b). Thus an illumination of the phosphor by emitted light being reflected back onto the the phosphor again is prevented.

[1] This is a compact neutron imaging detector built in a small series at the detector lab of FRM II. The prototype of this detector is described in [62].

[2] For the definition of the entrance pupil see [17, p. 149ff].

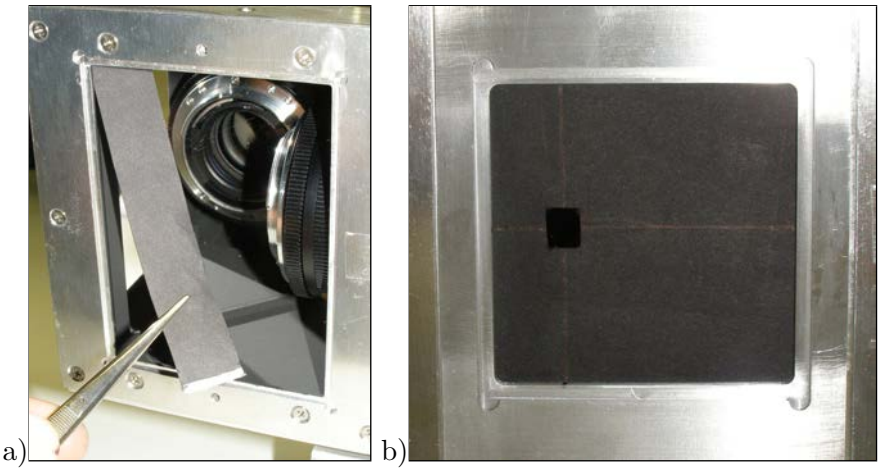

Fig. A.2: Black cardboard is used to shield areas of the mirror and the scintillator surface. Thus reflections of light emitted by the scintillator back onto the phosphor layer are avoided. Otherwise this light would contribute to the background signal by diffuse reflexion at the surface of the phosphor layer.

A.2 Water Cooling of the Intensified CCD Camera

For a basic operation the intensified CCD camera is equipped with a fan to remove the waste heat from the Peltier colling via the ambient air. This limits the minimum temperature reach at the CCD sensor to -30 °C. When cooling water is connected to the heat exchanger of the internal Peltier cooling, the lowest temperature of the CCD sensor at stable operation conditions is -40 °C (fig A.3). Thus it is possible to reduce the dark current signal of the detector especially for long integration

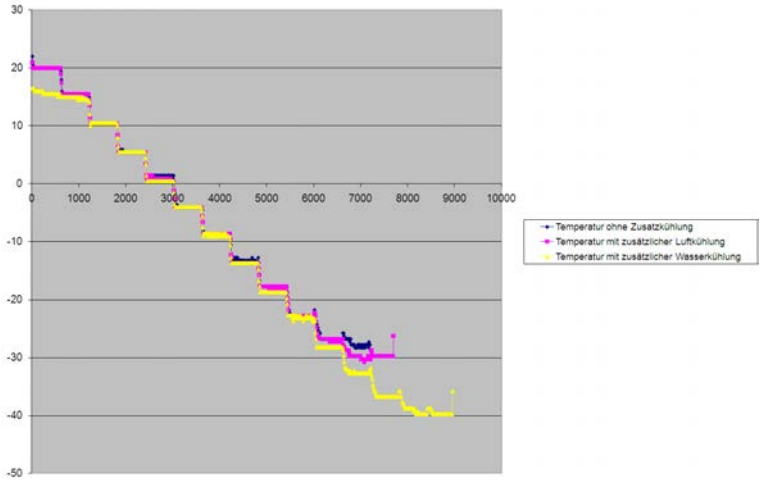

Fig. A.3: Temperature of the CCD sensor plotted versus time for a series of cooling cycles with a stepwise decrease of the set temperature. The cooling of the camera is improved by connection to a water circulation.

times. The temperature dependence of the dark current D in electrons per pixel and second is given by the empirical formula[3]

$$D = 2.5 \cdot 10^{15} \cdot A \cdot I_{\mathrm{d}} \cdot T^{1.5} \cdot \mathrm{e}^{-\frac{E_{\mathrm{g}}}{k_{\mathrm{B}} T}} \tag{A.1}$$

when the bulk dark current of the sensor I_{d} at a temperature of 300 K is given in $\frac{\mathrm{nA}}{\mathrm{cm}^2}$. It is proportional to the pixel area A in cm^2 and term describing the probability of thermal excitation

[3]reference: `http://www.kodak.com/go/imagers` , Application Note, MTD/PS-0233, Revision No. 2: "CCD Image Sensor Noise Sources"

of an electron inside the silicon substrate. A temperature dependence of the bandgap of the silicon substrate is also taken into account here:

$$E_{\mathrm{g}} = 1.1557\,\mathrm{eV} + \frac{7.021 \cdot 10^{-4}\,\frac{\mathrm{eV}}{\mathrm{K}} \cdot T^2}{1108\,\mathrm{K} + T} \tag{A.2}$$

According to this temperature dependent term the dark current signal can be reduced by a factor of 20 if the operating temperature of the CCD sensor is lowered by 13 K to −40 °C [63]. The integrated dark current signal is only 4.7 % of the charge generated at −27 °C.

A.3 Thermal Expansion of Injector

During its operation the injector may reach temperatures equivalent to the ones of the test oil. With the injector having a length l of approximately 0.2 m and the coefficient of thermal expansion α of steel[64, p. 725] the elongation Δl of the injector can be estimated to be

$$\Delta l = l\alpha\Delta T = 0.2\,\mathrm{m}\,1.2 \cdot 10^{-5}\,\mathrm{K}^{-1}\,20\,\mathrm{K} = 4.8 \cdot 10^{-5}\,\mathrm{m} = 48\,\mu\mathrm{m} \tag{A.3}$$

This is about 25 % of the diameter of the spray hole. The expansion in radial direction due to temperature change is

$$\Delta r = r\,\alpha\,\Delta T = 7.0 \cdot 10^{-3}\,\mathrm{m}\,1.2 \cdot 10^{-5}\,\mathrm{K}^{-1}\,20\,\mathrm{K} = 1.7 \cdot 10^{-6}\,\mathrm{m} = 1.7\,\mu\mathrm{m}\,. \tag{A.4}$$

This is already the size of half a pixel for the high resolution setup using the intensified CCD camera.

A.4 Expansion of the Injector due to the Applied Pressure

The expansion of the nozzle due to the pressure applied by the test oil is given by [4]

$$\Delta r_{\mathrm{x}} = \frac{p_{\mathrm{i}}\,r_{\mathrm{a}}\,(r_{\mathrm{i}})^2}{E\,\left(r_{\mathrm{a}}^2 - r_{\mathrm{i}}^2\right)} \cdot \left(\frac{(r_{\mathrm{a}})^2}{(r_{\mathrm{x}})^2}\,(1+\nu) + (1-\nu)\right)\,. \tag{A.5}$$

Δr_{x}	:	change of radius at a radial position r_{x}
r_{i}	:	inner radius of the nozzle
r_{a}	:	outer radius of the nozzle
r_{x}	:	arbitrary radial position
p_{i}	:	pressure inside the nozzle
E	:	elastic modulus (of steel)
ν	:	Poisson's ratio.

For the outer radius of the nozzle

$$\begin{aligned}\Delta r_{\mathrm{i}} &= \frac{160\,\frac{\mathrm{N}}{\mathrm{mm}^2}\,3.5\,\mathrm{mm}\,(1.68\,\mathrm{mm})^2}{2.0 \cdot 10^4\,\frac{\mathrm{N}}{\mathrm{mm}^2}\,((3.5\,\mathrm{mm})^2 - (1.68\,\mathrm{mm})^2)} \cdot \left(\frac{(3.5\,\mathrm{mm})^2}{(3.5\,\mathrm{mm})^2}\,(1+\nu) + (1-\nu)\right) \\ &= 1.68 \cdot 10^{-3}\,\mathrm{mm} \;=\; 1.68\,\mu\mathrm{m}\,.\end{aligned}$$

For the inner radius of the nozzle

$$\begin{aligned}\Delta r_{\mathrm{i}} &= \frac{160\,\frac{\mathrm{N}}{\mathrm{mm}^2}\,1.68\,\mathrm{mm}\,(1.68\,\mathrm{mm})^2}{2.0 \cdot 10^4\,\frac{\mathrm{N}}{\mathrm{mm}^2}\,((3.5\,\mathrm{mm})^2 - (1.68\,\mathrm{mm})^2)} \cdot \left(\frac{(3.5\,\mathrm{mm})^2}{(1.68\,\mathrm{mm})^2}\,(1+\nu) + (1-\nu)\right) \\ &= 2.53 \cdot 10^{-3}\,\mathrm{mm} \;=\; 2.53\,\mu\mathrm{m}\,.\end{aligned}$$

Both values are comparable to the pixel size of the iCDD-highRes configuration. Therefore it might be one explanation why the nozzle seems to be enlarge during the operation.

[4] `http://www.schweizer-fn.de/rohr/festigkeit/festigkeit.htm`

A.5 Calculated Radiography

Based on a cross section model of the injection nozzle, the injection needle and the oil inside the injection nozzle the transmission values for each pixel on the detector are calculated. It has been realized by writing an ImageJ-Plugin[5]. The software is evaluating a given parameter set in the following steps:
In a first step a set parameters has to be entered concerning the final radiograph. These parameters are the dimension of the radiograph, width and height, the position of the center of the sample, here the tip of the nozzle, the distance of the center of the sample to the detector and the pixel size of the radiography (Fig. A.4a). In the following step a cross section model of the injection nozzle / sample is selected. It is necessary for the further evaluation that each material inside the cross section is assigned to a specific grey level inside the standard range of an 8-bit gray scale image. The current version of the program assumes a cylindrical symmetry of the sample and a rotation axes along the y-direction[6]. The center point which will coincident with the center selected in the first step is assumed to be at $x = 0$ and $y = 0$. All parameters for a definition of the materials are set during step 3 (Fig. A.4b).

a)

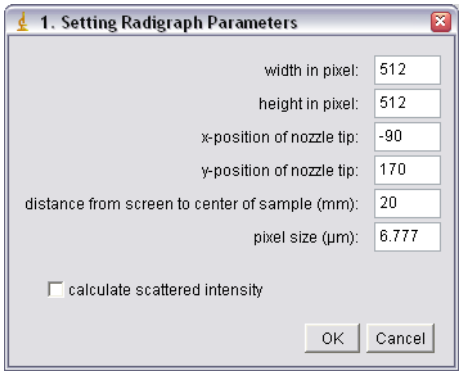

b)

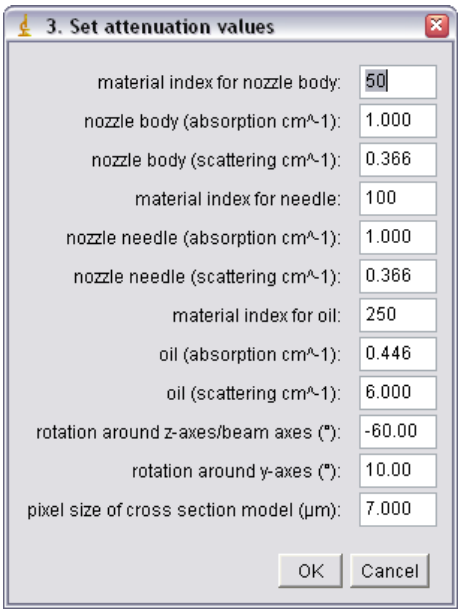

Fig. A.4: Step 1 and step 3, setting parameters for the calculation.

The attenuation coefficients for absorption and scattering are set separately for each material. The material index must match the value given inside the cross section model. Two rotation angles allow for a rotation of the sample around the beam axis and a vertical axes through the selected center inside the radiograph. After this step several windows are generated. Three of them are used to show the cross section model of the sample; one with material indices, one with the attenuation coefficients corresponding to the different materials for absorption and one with the attenuation coefficients for scattering. A group of four windows show different contributions of the calculated radiograph.[7] The upper left window contains the final radiograph which is a combination of the attenuation caused by absorption and scattering. The transmission accounting only for absorption or scattering are shown in the lower left or lower right window respectively. Calculating the scattered intensities is very time consuming and should be optimized in a future version. This may be done by reducing the resolution for the image representing the scattered intensity and increasing the step size for evaluating the scattering centers inside the model of the sample. To keep the coding

[5] `http://rsbweb.nih.gov/ij/`
[6] The y-axes is perpendicular to the neutron beam and vertical.
[7] Only three windows if no scattered intensities are calculated.

property	Shell V-Oil	Benzol	Decan	Dodecan	Hexadecan
chemical formula	—	C_6H_6	$C_{10}H_{22}$	$C_{12}H_{26}$	$C_{16}H_{34}$
mass density $\frac{\mathrm{kg}}{\mathrm{m}^3}$	826	880	730	750	773
flash point °C	95		46	71	135
cloud point °C	-18				
pour point °C	-27				
viscosity at 40 °C $\frac{\mathrm{mm}^2}{\mathrm{s}}$	2.55				
viscosity at 20 °C $\frac{\mathrm{mm}^2}{\mathrm{s}}$	3.8		0.92	1.35	3.34
boiling interval / boiling point °C	220 - 360	80	174	216	287

Table A.1: Physical properties of the test oil, Shell V-Oil 1404[66], and selected hydrocarbons[67].

element	mass fraction	density	molar mass	particle density
C	0.15 %	$0.0117\,\frac{\mathrm{g}}{\mathrm{cm}^3}$	12.0107	$5.866 \cdot 10^{20}\,\mathrm{cm}^{-3}$
Si	1.15 %	$0.0897\,\frac{\mathrm{g}}{\mathrm{cm}^3}$	28.0855 g	$1.923 \cdot 10^{21}\,\mathrm{cm}^{-3}$
Cr	25.5 %	$1.99\,\frac{\mathrm{g}}{\mathrm{cm}^3}$	51.9961 g	$2.305 \cdot 10^{22}\,\mathrm{cm}^{-3}$
Mn	1 %	$0.078\,\frac{\mathrm{g}}{\mathrm{cm}^3}$	54.9380,g	$8.550 \cdot 10^{20}\,\mathrm{cm}^{-3}$
Fe	67.7 %	$5.28\,\frac{\mathrm{g}}{\mathrm{cm}^3}$	55.854 g	$5.694 \cdot 10^{22}\,\mathrm{cm}^{-3}$
Ni	4.5 %	$0.351\,\frac{\mathrm{g}}{\mathrm{cm}^3}$	58.6934 g	$3.601 \cdot 10^{21}\,\mathrm{cm}^{-3}$

Table A.2: Composition of the steel used for the nozzle and the needle.

simple and straight forward and for an easier evaluation of the results all images have the same size and resolution in the current version of the program. As the scattered intensity does not show any detailed structure, it is not necessary to evaluate the scattered intensity with the same resolution as the radiograph. The final results are used to correct the measured data. The composition of the steel used for the nozzle and the nozzle needle is assumed to be X20CrNiSi25-4, a high alloy steel with high temperature stability [65]. There were no details available about the mixture of the test oil, Shell V-Oil 1404 unless the product data sheet [66]. Therefore the properties of different carbon hydrides were compared with the physical properties of the test oil. It was found that Dodecan ($C_{12}H_{26}$) is very close them (Tab. A.1). The attenuation coefficients used to calculate the neutron radiography are based on the values of table A.2 for the nozzle and needle material and table A.3 for the test oil. The density of Dodecan at 15 °C was set to be $826\,\frac{\mathrm{kg}}{\mathrm{m}^3}$, which is the density of the test oil given in the data sheet [66]. For an atomic ratio of

$$C : H = 12 : 26$$

the mass ratio of hydrogen to carbon of one Dodecan molecule can be evaluated to be

$$\frac{m_\mathrm{H}}{m_\mathrm{C}} = \frac{26 \cdot 1\,\mathrm{u}}{12 \cdot 12\,\mathrm{u}} = \frac{13}{72}\,.$$

Thus the estimated mass fraction of hydrogen and carbon inside the test oil is 15.3 % and 84.7 % respectively. The corresponding particle densities are given in table A.3. An overview of the

element	mass fraction	density	molar mass	particle density
C	84.7%	12.0107 g	$0.6996\,\frac{\mathrm{g}}{\mathrm{cm}^{-3}}$	$3.508 \cdot 10^{22}\,\mathrm{cm}^{-3}$
H	15.3%	1.00794 g	$0.1264\,\frac{\mathrm{g}}{\mathrm{cm}^{-3}}$	$7.552 \cdot 10^{22}\,\mathrm{cm}^{-3}$

Table A.3: Composition assumed for the test oil.

scattering and absorption cross sections for some elements is found in table A.4 [10]. For an effective absorption cross section a mean neutron wave length of 4 Å was assumed. To yield the effective absorption cross section $\sigma_{\mathrm{a,eff}}$ the absorption cross section σ_{a} corresponding to a neutron energy of 0.0253 meV [10] were multiplied by the factor $\frac{4\,\text{Å}}{1.78\,\text{Å}}$.

$$\sigma_{\mathrm{a,eff}} = \frac{\bar{\lambda}}{\lambda_{\mathrm{therm}}} \cdot \sigma_{\mathrm{a}}$$

element	σ_{c}	σ_{i}	σ_{s}	σ_{a}	$\sigma_{\mathrm{a,eff}}$	σ_{t}
H	1.7568	80.26	82.02	0.3326	0.7474	82.77
C	5.551	0.001	5.552	0.0035	0.00786	5.560
Si	2.1633	0.004	2.167	0.171	0.384	2.551
Cr	1.660	1.83	3.49	3.05	6.85	10.34
Mn	1.75	0.40	2.15	13.3	29.89	32.04
Fe	11.22	0.40	11.62	2.56	5.75	17.37
Ni	13.3	5.2	18.5	4.49	10.09	28.59

Table A.4: Scattering and absorption cross sections of selected elements.

A.6 Fluctuations of a Single Stage of a Detector

In principle this section is copied from the appendix of L. Mandel's paper from 1959 [29]. But it seemed to be worth to do so, as the whole derivation of cascaded detection systems is based on the following relations. The notation is kept close to the one used by Mandel. Some annotations were made were it was supposed to be helpful. Mandel shows how to derive the relations

$$\overline{\mu} = \overline{n}\overline{\lambda} \tag{A.6}$$

$$\text{and} \quad \sigma_\mu^2 = \overline{\lambda}^2\sigma_n^2 + \overline{n}\sigma_\lambda^2\,. \tag{A.7}$$

Here n stands for a number of primary particles entering a stage of a detector. It is considered that each of these particles gives rise to λ secondary particles. Finally μ is the total number of secondary particles at the output of the stage of the detector. A bar denotes the average and σ the standard deviation. For the standard deviation the corresponding signal is given by the index.
The probability distributions of n and λ are assumed to be $P(n)$ and $p(\lambda)$ for λ secondaries arising from any primary particle.
According to Mandel:
If $P_n(\mu)$ is the conditional probability that n primaries give rise to μ secondaries, then from first principles, provided the interactions are independent:

$$P_n(\mu) = \sum_{\lambda_1=0}^{\infty}\sum_{\lambda_2=0}^{\infty}\dots\sum_{\lambda_{n-1}=0}^{\infty} p(\lambda_1)p(\lambda_2)\dots p(\lambda_{n-1})p(\mu-\lambda_1-\lambda_2-\dots\lambda_{n-1}) \tag{A.8}$$

where it is to be understood that $p(\lambda) = 0$ for any $\lambda < 0$.

NOTE: There are only $(n-1)$ summations but n factors of $p(\ )$, as the λ_{i} are not independent and have to fulfill the condition

$$\mu = \sum_{\mathrm{i}=1}^{n}\lambda_{\mathrm{i}}\,. \tag{A.9}$$

The conditional mean is therefore:

$$\begin{aligned}\overline{\mu_n} &= \sum_{\mu=0}^{\infty} \mu P_n(\mu) \\ &= \sum_{\lambda'=0}^{\infty}\sum_{\lambda_1=0}^{\infty}\cdots\sum_{\lambda_{n-1}=0}^{\infty}(\lambda'+\lambda_1+\lambda_2+\ldots\lambda_{n-1})p(\lambda')p(\lambda_1)p(\lambda_2)\ldots p(\lambda_{n-1}) \\ &= n\overline{\lambda} \end{aligned} \tag{A.10}$$

where the substitution $\mu - \lambda_1 - \lambda_2 - \ldots \lambda_{n-1} = \lambda'$ *has been used.*

NOTE: One gets $\overline{\lambda}$ by summing

$$\sum_{\lambda'=0}^{\infty}\sum_{\lambda_1=0}^{\infty}\cdots\sum_{\lambda_{n-1}=0}^{\infty}\lambda_{\mathrm{i}}\, p(\lambda')p(\lambda_1)p(\lambda_2)\ldots p(\lambda_{n-1}) \tag{A.11}$$

for each of the n λs (λ', λ_1, λ_2 $\ldots$ λ_{n-1}).
Hence

$$\overline{\mu} = \sum_{n=0}^{\infty}\overline{\mu_n}P(n) \tag{A.12}$$

and, from equation (A.10)

$$\overline{\mu} = \overline{n}\overline{\lambda}\,. \tag{A.13}$$

The conditional mean square follows similarly:

$$\begin{aligned}\overline{\mu_n^2} &= \sum_{\mu=0}^{\infty}\mu^2 P_n(\mu) \\ &= \sum_{\lambda'=0}^{\infty}\sum_{\lambda_1=0}^{\infty}\cdots\sum_{\lambda_{n-1}=0}^{\infty}(\lambda'+\lambda_1+\lambda_2+\ldots\lambda_{n-1})^2 p(\lambda')p(\lambda_1)p(\lambda_2)\ldots p(\lambda_{n-1}) \\ &= n\overline{\lambda^2} + n(n-1)\overline{\lambda}^2 \end{aligned} \tag{A.14}$$

so that

$$\begin{aligned}\overline{\mu^2} &= \sum_{n=0}^{\infty}\mu_n^2 P(n) \\ &= \overline{n}\overline{\lambda^2} + (\overline{n^2} - \overline{n})\overline{\lambda}^2\,. \end{aligned} \tag{A.15}$$

Hence from equations (A.13) and(A.15)

$$\begin{aligned}\sigma_\mu^2 &= \overline{\mu^2} - \overline{\mu}^2 \\ &= \overline{\lambda}^2(\overline{n^2} - \overline{n}^2) + \overline{n}(\overline{\lambda^2} - \overline{\lambda}^2) \\ &= \overline{\lambda}^2\sigma_n^2 + \overline{n}\sigma_\lambda^2\,. \end{aligned} \tag{A.16}$$

A.7 Beam Profile Calculation

The beam profile at the detector for a given arrangement of the neutron source area and an aperture can easily be calculated by a correlation of the opening functions of the source A_S and the aperture A_A if the appropriate scaling is applied.

$$\hat{I}_0(x,y) = \frac{\int\int A_\mathrm{S}\left(\alpha\cdot u, \alpha\cdot v\right)\; A_\mathrm{A}\left(\beta\cdot(u+x), \beta\cdot(v+y)\right)\,\mathrm{d}u\,\mathrm{d}v}{\int\int A_\mathrm{S}(\alpha\cdot u, \alpha\cdot v)\,\mathrm{d}u\,\mathrm{d}v}\,. \tag{A.17}$$

The scaling parameters α and β are given by

$$\alpha = -\frac{L_\mathrm{C}}{L_\mathrm{D}} \tag{A.18}$$

$$\beta = -\frac{L_\mathrm{C}}{L_\mathrm{D}+L_\mathrm{C}}\,. \tag{A.19}$$

For the following considerations only a one-dimensional configuration of the source and the aperture is discussed. The problem is even further reduced to point like source and a point like aperture represented by a delta function each. Thus for the source positioned at $x_{\mathrm{S},0} = a$ on the source plane, the aperture positioned at $x_{\mathrm{A},0} = b$, the distance $L_\mathrm{C} = c$ and the distance $L_\mathrm{S} = d$ we get from a simple geometrical consideration that the position x of the resulting intensity spot on the detector plane is found at

$$x_0 = (a-b)\cdot\left(-\frac{d}{c}\right) + b\,. \tag{A.20}$$

A sketch of this configuration is shown in figure A.5. The source as well as the aperture may be

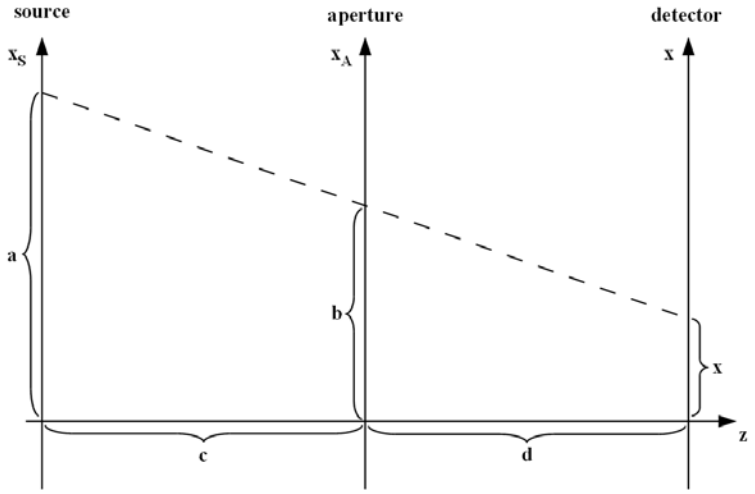

Fig. A.5: A simplified beam geometry for idealized point like pinhole apertures. Clearly there is only one defined position on the detector, where neutrons are registered.

described by delta function, using $f(x) = \delta(x_\mathrm{S} - a)$ for the source and $g(x) = \delta(x_\mathrm{S} - b)$ for the aperture. Using equation A.17 replacing opening function for the source and the aperture and reducing the integral to a one-dimensional case the intensity distribution $\hat{I}(x)$ at the detector plane

is given by

$$\hat{I}(x) = \frac{\int f\left(-\frac{L_C}{L_D}\cdot u\right)\cdot g\left(-\frac{L_C}{L_D+L_C}\cdot(u+x)\right)\mathrm{d}u}{\int f\left(-\frac{L_C}{L_D}\cdot u\right)\mathrm{d}u} \tag{A.21}$$

$$= \frac{\int f\left(-\frac{c}{d}\cdot u\right)\cdot g\left(-\frac{c}{d+c}\cdot(u+x)\right)\mathrm{d}u}{\int f\left(-\frac{c}{d}\cdot u\right)\mathrm{d}u} \tag{A.22}$$

$$= \frac{\int f\left(-\frac{c}{d}\cdot u\right)\cdot g\left(-\frac{c}{d+c}\cdot(u+x)\right)\mathrm{d}u}{1} \tag{A.23}$$

$$= \int \delta\left(-\frac{c}{d}\cdot u - a\right)\cdot\delta\left(-\frac{c}{d+c}\cdot(u+x) - b\right)\mathrm{d}u \tag{A.24}$$

$$= \delta\left(-\frac{c}{d+c}\cdot\left(\frac{a\cdot d}{c}+x\right)-b\right). \tag{A.25}$$

This is equivalent to an intensity spot at position

$$x_0 = \frac{b\cdot(c+d)-ad}{c}, \tag{A.26}$$

which is just the same value as we got from the geometrical consideration equation (A.20). Due to the fact that any source or aperture of finite area may be described by a finite number of points, i.e. delta functions, and the linear behaviour of the integral equation A.25 holds for any shape of the source or the aperture. Furthermore each point or position of the source might be modified by an emission factor corresponding to the emitted neutron flux, while each point of the aperture might be characterized not only by values of 1 and 0 representing holes or material, respectively, but real transmission values instead. Thus not only an estimate of the expected intensity values might be possible, but even inhomogeneities of the source area and imperfections of the aperture due to a partial transparency can be included to the calculation.

A.8 Imaging by a Lens

The object distance and image distance can easily be calculated by the Gaussian lens equation [17, p. 144]. The simple imaging principles known for thin lenses are sufficient for a basic layout of a neutron radiography detector with optical coupling or for the design of neutron beam geometries including neutron lenses. The imaging of the light emitting surface of the scintillation screen to an imaging sensor obeys the imaging equation even if a lens system is used. But all distances have to be measured with respect to the principal plane of the lens system in this case. For a thin lens the principal plane coincides with the center of the lens (Fig. A.6). An optical coupling of the scintillator and the imaging sensor makes this kind of detectors very flexible in terms of spatial resolution and field of view. In principle the field of view can have any desired size, as the magnification of the imaging can be selected at ones wish. The transverse magnification M_T[8] is defined as [17]

$$M_T \equiv \frac{y_i}{y_o} \tag{A.27}$$

by the length of corresponding distances y_i at the image plane (the detector) and y_o at the object plane (the scintillator). The sign convention is[17, p. 144]:

[8] Note that $M_T < 0$ and $M_T > -1$ for a minified, real and inverted image.

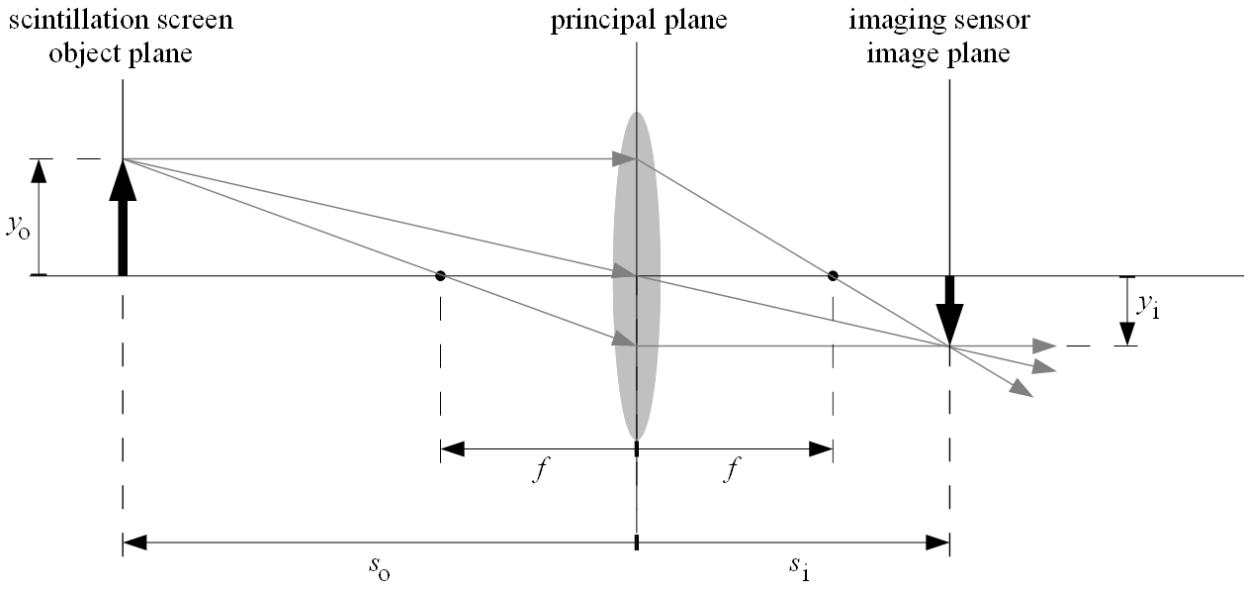

Fig. A.6: Basic imaging by thin lens.

Quantity	Sign	
	+	−
s_o	Real object	Virtual object
s_i	Real image	Virtual image
f	Converging lens	Diverging lens
y_o	Erect object	Inverted object
y_i	Erect image	Inverted image
M_T	Erect image	Inverted image

The width and height of the field of view are then given by the dimension of the active area of the imaging sensor. Let $y_{i,w}$ and $y_{i,h}$ be the width and height of the imaging sensor and $y_{o,w}$ and $y_{o,h}$ the width and hight of the field of view respectively. Then the size of the field of view is given by

$$y_{o,w} = \frac{y_{i,w}}{M_T} \qquad \text{and} \qquad y_{o,h} = \frac{y_{i,h}}{M_T}$$

Most of the times the transversal magnification M_T is chosen to be the free parameter, as the size of the field of view is determined by the size of the sample or the desired pixel size on the scintillator. Given a magnification M_T by

$$M_T = \frac{y_{i,w}}{y_{o,w}} \qquad \text{or} \qquad M_T = \frac{y_{i,h}}{y_{o,h}}\,.$$

The dimensions of the detector are determined by the focal length f of the lens (or lens system), which determines the imaging distance s_i and the object distance s_o. They have to fulfill the imaging equation

$$\frac{1}{f} = \frac{1}{s_o} + \frac{1}{s_i} \tag{A.28}$$

and the correlation for the transversal magnification

$$M_T = -\frac{s_i}{s_o} \quad \Leftrightarrow \quad M_T \cdot s_o = -s_i\,. \tag{A.29}$$

By a combination of equations (A.28) and (A.29) one gets

$$\frac{1}{f} = \frac{1}{s_o} - \frac{1}{M_T \cdot s_o} \quad \Leftrightarrow \quad \frac{1}{f} = \frac{M_T - 1}{M_T \cdot s_o} \quad \Leftrightarrow \quad f = \frac{M_T \cdot s_o}{M_T - 1} \tag{A.30}$$

$$s_\mathrm{o} = \frac{M_\mathrm{T} - 1}{M_\mathrm{T}} \cdot f \tag{A.31}$$

$$s_\mathrm{i} = -s_\mathrm{o} \cdot M_\mathrm{T} = -\frac{M_\mathrm{T} - 1}{M_\mathrm{T}} \cdot f \cdot M_\mathrm{T} = (1 - M_\mathrm{T}) \cdot f \tag{A.32}$$

which is sufficient to design a detector of fixed field of view or to set the distances if a detector of variable field of view is used. After a fine tuning using the focus drive of the lens one ends up at the desired FOV within about 1 % of error.

A.9 Chromatic Aberration

The index of refraction is dependent on the neutron wavelength. Thus the focal length f of neutron lenses is also varying with the neutron wavelength λ.

$$f = \frac{\pi R}{\rho \bar{b} \lambda^2} \tag{A.33}$$

It makes it impossible to yield a focused image of an object, here the source aperture, at the detector plane for different wavelengths at the same time. This effect is called chromatic aberration and well known from light optics [17]. A typical wavelength spread $\frac{\Delta\lambda}{\lambda}$ for SANS and USANS measurements is 10 %. For fixed distances between the object, the lens and the detector the neutron wavelength has to be selected to yield a circle of least confusion[9] at the detector (Sec. 5.2.2 and Sec. 5.4.2). The full width Δw of this circle is illustrated by figure A.7. It is defined by the diameter of the lens D,

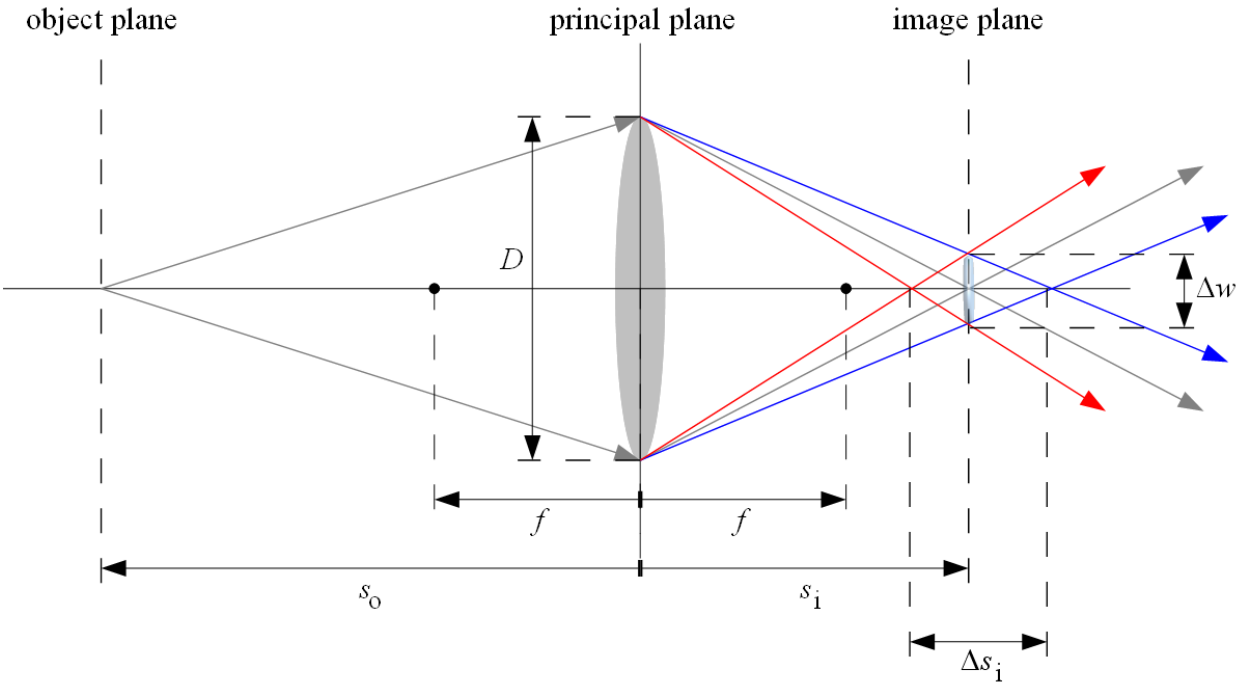

Fig. A.7: A change of the focal length for different neutron wavelengths results in a variation of the imaging distance s_i.

the imaging distance s_i and the variation of the imaging distance Δs_i. If the imaging distance is large compared to its variation, Δw can be approximated by

$$\Delta w = \frac{D}{s_\mathrm{i}} \cdot \frac{\Delta s_\mathrm{i}}{2} \,. \tag{A.34}$$

[9] More general it is an area of least confusion.

From the imaging equation (A.28) one gets

$$s_\mathrm{i} = \frac{1}{\frac{1}{f} - \frac{1}{s_\mathrm{o}}} \,. \tag{A.35}$$

Thus Δs_i for a variation of the focal length by Δf is given by

$$\Delta s_\mathrm{i} = \frac{s_\mathrm{i}^2}{f^2} \cdot \Delta f \,. \tag{A.36}$$

Δf in turn is derived from equation (A.33) including the known wavelength spread $\frac{\Delta\lambda}{\lambda}$

$$\Delta f = |-f| \cdot \frac{\Delta\lambda}{\lambda} \,. \tag{A.37}$$

Combining equations (A.34), (A.36) and (A.37)

$$\Delta w = \frac{D\, s_\mathrm{i}}{f} \cdot \frac{\Delta\lambda}{\lambda} \,. \tag{A.38}$$

A.10 Slit shaped Apertures

The effective area of the source and the sample aperture array can be increased by using slit shaped apertures instead of circular ones. For slit shaped apertures the Q-resolution along the slit direction is poor and only Q-values perpendicular to the slits can be measured, but this is compensated by a much higher flux at the sample position due to the enlarged transmission area of the apertures. If the slits of the source and the sample aperture array are parallel to each other and their width is matched according to equation (2.45), the theoretical beam profile for each peak at the detector plane has a triangular shape perpendicular to the slits. A misalignment of one aperture due to a rotation around the z-axis, beam axis, causes a reduction of the peak intensity and a broadening of the primary beam profile. The primary beam profile at the detector plane is described by a correlation of the opening function of the source aperture array and the sample aperture array including a scaling to take into account the distances between the apertures and their distance to the detector (Sec. 2.2.2 and App. A.7). Here the characteristics for the center of the intensity distribution at the detector are of primary interest. The shape of the beam profile for slit shaped apertures can be derived from a simple model of two rectangular areas shifted with respect to each other. To describe the intensity distribution at the detector the x-axis is perpendicular to the source aperture, the first one of the two slits, and the y-axis is parallel to this slit. The transmitted intensity is proportional to the overlap of the two rectangles. The shift Δx along the x-direction, perpendicular to the first rectangle, slit, is equivalent to a position at the detector. If the rectangular slits have a width b and a length l and the tilt angle of the second slit with respect to the first one is α, one has to distinguish different cases (Fig. A.8):

$\alpha = \mathbf{0}\,^\circ$ This is the beam profile for slit shaped apertures in case of an ideal,parallel alignment. It has a triangular shape in the direction of the slits and in the direction perpendicular to the slits. The FWHM is l in direction of the slits and b perpendicular to the slits. It is important to note here that the shape of the line profile in x-directions does not change for different values of y and its FWHM and the total width of the profile are constant in y-direction, too. They are b and $2\,b$, respectively. Thus it is possible to sum along the y-axis without causing a change of the shape of the profile in x-Direction. There are two intervals to describe the profiles:

$$\begin{array}{lrcll} \text{Interval I:} & -b & < \Delta x \leq & 0, & \text{Fig. A.9a} \\ \text{Interval II:} & 0 & < \Delta x \leq & b, & \text{Fig. A.9b} \end{array}$$

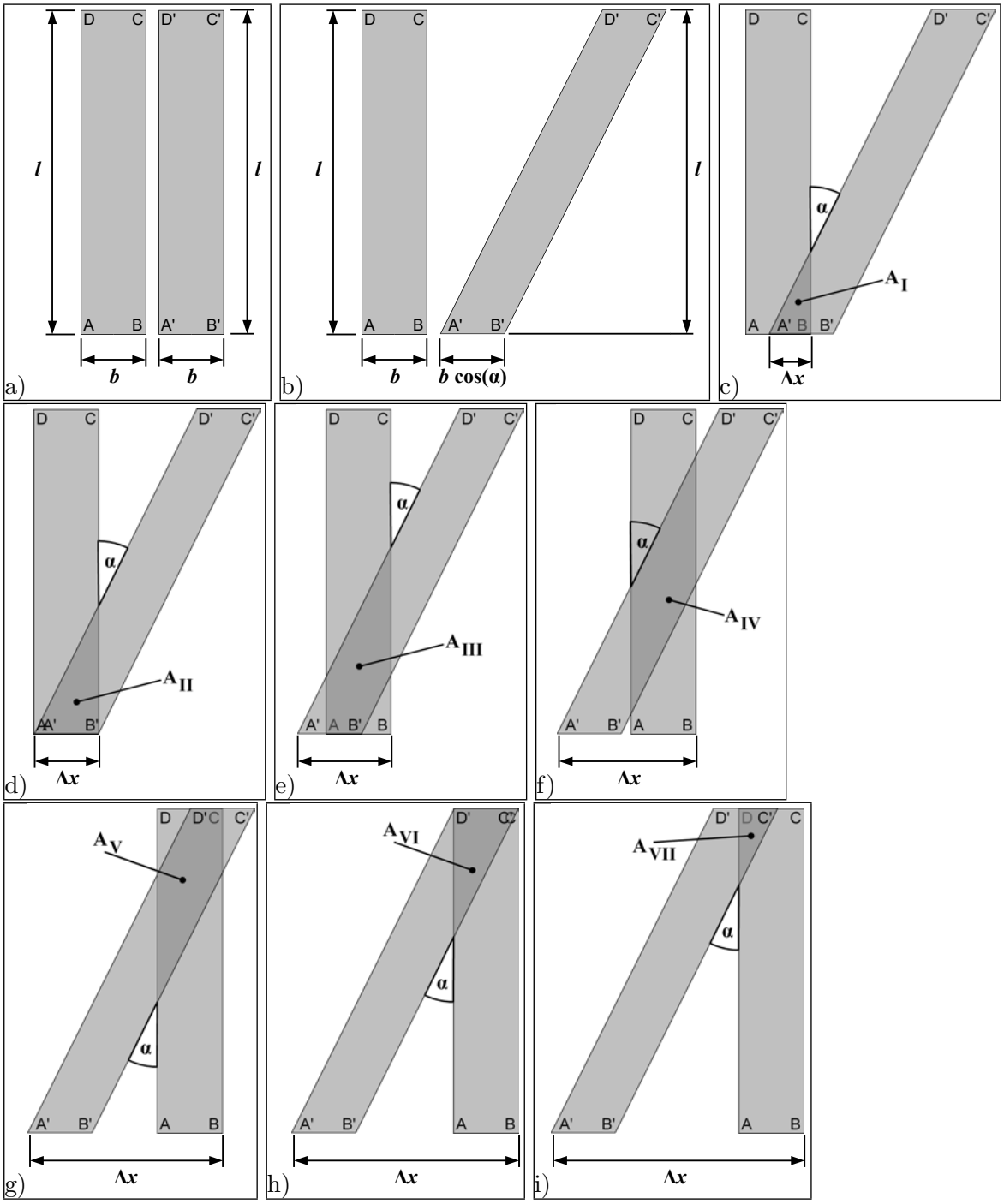

Fig. A.8: The intensity profile resulting from slit shaped apertures can be calculated in analogy to the area of the intersection of two rectangles. In case one of the apertures is tilted with respect to the other one, this aperture is approximated by an parallelogram to simplify the calculations, (a) and (b). In order to conserve characteristics of the resulting profile in x-direction (perpendicular to the first slit) the x-coordinates of the edges A',B',C' and D' are equal to the ones of the second rectangle, when it is tilted by an angle α. Depending on the angle α there are seven different intervals for the shift parameter Δx corresponding to seven different formula to calculate the area of the intersection: c) A_I: the edge A' is inside the rectangle ABCD, d) A_{II}: the edges A' and B' are inside the rectangle ABCD, e) A_{III}: the edge B' is inside the rectangle ABCD, f) A_{IV}: no edge of the parallelogram is inside the rectangle, g) A_V: the edge D' is inside the rectangle ABCD, h) A_{VI}: the edges D' and C' are inside the rectangle ABCD, i) A_{VII}: the edge C' is inside the rectangle ABCD.

Interval I describes a linear increase of the intensity starting from the begin of the overlap of the two apertures at $\Delta x = -b$ until the peak intensity is reached for the maximum overlap of the two apertures at $\Delta x = 0$. For $\Delta x = 0$ to $\Delta x = b$ there is a linear decrease of the intensity. Assuming an additional shift of Δy in y-direction the area $\mathrm{A}(\Delta x, \Delta y)$ of the intersection of the two apertures is given by

$$\mathrm{A}(\Delta x, \Delta y) \;=\; (l - |\Delta y|) \cdot (b - |\Delta x|)\,. \tag{A.39}$$

And the intensity profile at the detector is proportional to this area. For the center of the profile at $\Delta y = 0$ this can be split to stepwise defined function for the two intervals from above

$$\mathrm{A_I} \;=\; l \cdot (b + \Delta x) \tag{A.40}$$

$$\mathrm{A_{II}} \;=\; l \cdot (b - \Delta x) \tag{A.41}$$

The positions x and y at the detector with respect to the center of the detector plane or the source

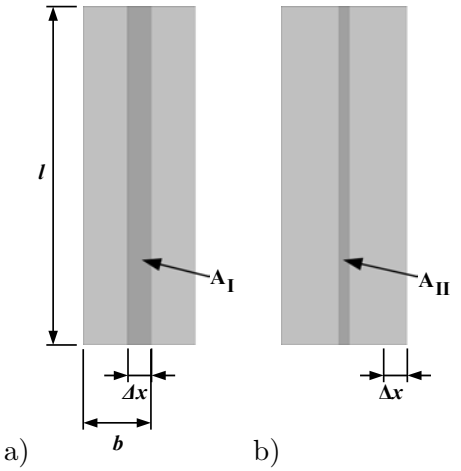

Fig. A.9: Overlap of slit shape apertures for a tilt angle $\alpha = 0$.

aperture correspond to a shift of the projection of the second slit, the sample aperture. For small tilt angles the second aperture is approximated by a parallelogram. To get a similar characteristics for the resulting line profile in x-direction the positions of the edges of the parallelogram in x are identical to the ones of the tilted rectangle describing the second aperture. The y-position of the edges is approximated by the y-position of the original edge. So there is only a small shift of $b \cdot \sin\alpha$ in y-direction between the original position of the edges of the tilted rectangle and the approximated position of the edges of the parallelogram. To compensate the reduced area of the parallelogram compared to rectangle the calcualted cross section of the rectangle and the parallelogram is multiplied by $\frac{1}{\cos(\alpha)}$. With respect to the center of the first slit at $(0, 0)$ the coordinates of the edges of the parallelogram are dependent on the position (x, y) at the detector and the tilt angle α. They are given by

$$\mathrm{A}\,(\,x - 0,5 \cdot (b\,\cos\alpha + l\,\sin\alpha)\,/\,y - 0,5\,l\,) \tag{A.42}$$

$$\mathrm{B}\,(\,x + 0,5 \cdot (b\,\cos\alpha - l\,\sin\alpha)\,/\,y - 0,5\,l\,) \tag{A.43}$$

$$\mathrm{C}\,(\,x + 0,5 \cdot (b\,\cos\alpha + l\,\sin\alpha)\,/\,y + 0,5\,l\,) \tag{A.44}$$

$$\mathrm{D}\,(\,x - 0,5 \cdot (b\,\cos\alpha - l\,\sin\alpha)\,/\,y + 0,5\,l\,) \quad . \tag{A.45}$$

If there is a shift in y-direction, the parallelogram may be replaced by a parallelogram representing the effective area of the parallelogram which actually gives rise to the area corresponding to the intersection of the parallelogram and the rectangle representing the first slit. For positive values of y with $0 \le y \le l$ C and D are replaced by C' and D'

$$\mathrm{C'}\,(\,x + 0,5 \cdot (b\,\cos\alpha + l\,\sin\alpha) - y\,\sin\alpha\,/\,y + 0,5\,l\,) \tag{A.46}$$

$$\mathrm{D'}\,(\,x - 0,5 \cdot (b\,\cos\alpha - l\,\sin\alpha) - y\,\sin\alpha\,/\,y + 0,5\,l\,)\,. \tag{A.47}$$

If y is negative and $-l \leq y < 0$, the edges A and B are replaced by A' and B'

$$\mathrm{A}'\,(\,x - 0,5 \cdot (b\,\cos\alpha + l\,\sin\alpha) + |y|\,\sin\alpha\,/\,y - 0,5\,l\,) \tag{A.48}$$

$$\mathrm{B}'\,(\,x + 0,5 \cdot (b\,\cos\alpha - l\,\sin\alpha) + |y|\,\sin\alpha\,/\,y - 0,5\,l\,)\ . \tag{A.49}$$

A stepwise defined function is used to describe the line profile in x-direction for a given value of y. Depending on y, the tilt angle α, the width b of the slits and their length l the range of the possible values for x is split into intervals where the functional relation between (x, y, b, l, α) and the area of the intersection of the parallelogram A,B,C,D can be described by a simple formalism.
For a shift in y direction the effective height of the the parallelogram is reduced from l to $(l - |y|)$. This also results in a reduction in a decrease of the total width of the parallelogram in x-direction from $(b\,\cos\alpha + l \cdot \sin\alpha)$ to $(b\,\cos\alpha + (l - |y|)\,\sin\alpha)$. There are six cases for small tilt angles that have to be examined by a case-by-case analysis:

- Case 1: $\{(l - |y|)\,\sin\alpha \leq b\,\cos\alpha\} \wedge y \in [0, l] \Rightarrow$ parallelogram A,B,C',D'
  Here D' is "left" of B.
- Case 2: $\{(l - |y|)\,\sin\alpha \leq b\,\cos\alpha\} \wedge y \in [-l, 0[\Rightarrow$ parallelogram A',B',C,D
  Here D is "left" of B'.
- Case 3: $\{b\,\cos\alpha < (l - |y|)\,\sin\alpha \leq b\} \wedge y \in [0, l] \Rightarrow$ parallelogram A,B,C',D'
  Here D' is "right" of B.
- Case 4: $\{b\,\cos\alpha < (l - |y|)\,\sin\alpha \leq b\} \wedge y \in [-l, 0[\Rightarrow$ parallelogram parallelogram A',B',C,D
  Here D is "right" of B'.
- Case 5: $\{b\,\cos\alpha < (l - |y|)\,\sin\alpha \leq b + b\,\cos\alpha\} \wedge y \in [0, l] \Rightarrow$ parallelogram A,B,C',D'
  Here D' is "right" of B.
- Case 6: $\{b\,\cos\alpha < (l - |y|)\,\sin\alpha \leq b + b\,\cos\alpha\} \wedge y \in [-l, 0[\Rightarrow$ parallelogram A',B',C,D
  Here D' is "right" of B'.
- Case 7: $\{b + b\,\cos\alpha < (l - |y|)\,\sin\alpha\} \wedge y \in [0, l] \Rightarrow$ parallelogram A,B,C',D'
  Here D' is "right" of B.
- Case 8: $\{b + b\,\cos\alpha < (l - |y|)\,\sin\alpha\} \wedge y \in [-l, 0[\Rightarrow$ parallelogram A',B',C,D
  Here D' is "right" of B'.

The intervals for each of the cases are:

Case 1: $\{(l - |y|)\,\sin\alpha \leq b\,\cos\alpha\} \wedge y \in [0, l]$

I	$-0.5\,(+b + b\,\cos\alpha + l\,\sin\alpha) + y\,\sin\alpha$	$<$	$x \leq$	$-0.5\,(+b + b\,\cos\alpha - l\,\sin\alpha)$
II	$-0.5\,(+b + b\,\cos\alpha - l\,\sin\alpha)$	$<$	$x \leq$	$-0.5\,(+b - b\,\cos\alpha + l\,\sin\alpha) + y\,\sin\alpha$
III	$-0.5\,(+b - b\,\cos\alpha + l\,\sin\alpha) + y\,\sin\alpha$	$<$	$x \leq$	$-0.5\,(-b + b\,\cos\alpha + l\,\sin\alpha) + y\,\sin\alpha$
IV	$-0.5\,(-b + b\,\cos\alpha + l\,\sin\alpha) + y\,\sin\alpha$	$<$	$x \leq$	$+0.5\,(-b + b\,\cos\alpha + l\,\sin\alpha)$
V	$+0.5\,(-b + b\,\cos\alpha + l\,\sin\alpha)$	$<$	$x \leq$	$+0.5\,(+b - b\,\cos\alpha + l\,\sin\alpha)$
VI	$+0.5\,(+b - b\,\cos\alpha + l\,\sin\alpha)$	$<$	$x \leq$	$+0.5\,(+b + b\,\cos\alpha - l\,\sin\alpha) + y\,\sin\alpha$
VII	$+0.5\,(+b + b\,\cos\alpha - l\,\sin\alpha) + y\,\sin\alpha$	$<$	$x \leq$	$+0.5\,(+b + b\,\cos\alpha + l\,\sin\alpha)$

Case 2: $\{(l - |y|)\,\sin\alpha \leq b\,\cos\alpha\} \wedge y \in [-l, 0[$

I	$-0.5\,(+b + b\,\cos\alpha + l\,\sin\alpha)$	$\leq$	$x \leq$	$-0.5\,(+b + b\,\cos\alpha - l\,\sin\alpha) + y\,\sin\alpha$
II	$-0.5\,(+b + b\,\cos\alpha - l\,\sin\alpha) + y\,\sin\alpha$	$<$	$x \leq$	$-0.5\,(+b - b\,\cos\alpha + l\,\sin\alpha)$
III	$-0.5\,(+b - b\,\cos\alpha + l\,\sin\alpha)$	$<$	$x \leq$	$-0.5\,(-b + b\,\cos\alpha + l\,\sin\alpha)$
IV	$-0.5\,(-b + b\,\cos\alpha + l\,\sin\alpha)$	$<$	$x \leq$	$+0.5\,(-b + b\,\cos\alpha + l\,\sin\alpha) + y\,\sin\alpha$
V	$+0.5\,(-b + b\,\cos\alpha + l\,\sin\alpha) + y\,\sin\alpha$	$<$	$x \leq$	$+0.5\,(+b - b\,\cos\alpha + l\,\sin\alpha) + y\,\sin\alpha$
VI	$+0.5\,(+b - b\,\cos\alpha + l\,\sin\alpha) + y\,\sin\alpha$	$<$	$x \leq$	$+0.5\,(+b + b\,\cos\alpha - l\,\sin\alpha)$
VII	$+0.5\,(+b + b\,\cos\alpha - l\,\sin\alpha)$	$<$	$x \leq$	$+0.5\,(+b + b\,\cos\alpha + l\,\sin\alpha) + y\,\sin\alpha$

Case 3: $\{b\cos\alpha < (l-|y|)\sin\alpha \leq b\} \wedge y \in [0,l]$

I	$-0.5\,(+b+b\cos\alpha+l\sin\alpha)+y\sin\alpha$	$< x \leq$	$-0.5\,(+b-b\cos\alpha+l\sin\alpha)+y\sin\alpha$
II	$-0.5\,(+b-b\cos\alpha+l\sin\alpha)+y\sin\alpha$	$< x \leq$	$-0.5\,(+b+b\cos\alpha-l\sin\alpha)$
III	$-0.5\,(+b+b\cos\alpha-l\sin\alpha)$	$< x \leq$	$-0.5\,(-b+b\cos\alpha+l\sin\alpha)+y\sin\alpha$
IV	$-0.5\,(-b+b\cos\alpha+l\sin\alpha)+y\sin\alpha$	$< x \leq$	$+0.5\,(-b+b\cos\alpha+l\sin\alpha)$
V	$+0.5\,(-b+b\cos\alpha+l\sin\alpha)$	$< x \leq$	$+0.5\,(+b+b\cos\alpha-l\sin\alpha)+y\sin\alpha$
VI	$+0.5\,(+b+b\cos\alpha-l\sin\alpha)+y\sin\alpha$	$< x \leq$	$+0.5\,(+b-b\cos\alpha+l\sin\alpha)$
VII	$+0.5\,(+b-b\cos\alpha+l\sin\alpha)$	$< x \leq$	$+0.5\,(+b+b\cos\alpha+l\sin\alpha)$

Case 4: $\{b\cos\alpha < (l-|y|)\sin\alpha \leq b\} \wedge y \in [-l,0[$

I	$-0.5\,(+b+b\cos\alpha+l\sin\alpha)$	$< x \leq$	$-0.5\,(+b-b\cos\alpha+l\sin\alpha)$
II	$-0.5\,(+b-b\cos\alpha+l\sin\alpha)$	$< x \leq$	$-0.5\,(+b+b\cos\alpha-l\sin\alpha)+y\sin\alpha$
III	$-0.5\,(+b+b\cos\alpha-l\sin\alpha)+y\sin\alpha$	$< x \leq$	$-0.5\,(-b+b\cos\alpha+l\sin\alpha)$
IV	$-0.5\,(-b+b\cos\alpha+l\sin\alpha)$	$< x \leq$	$+0.5\,(-b+b\cos\alpha+l\sin\alpha)+y\sin\alpha$
V	$+0.5\,(-b+b\cos\alpha+l\sin\alpha)+y\sin\alpha$	$< x \leq$	$+0.5\,(+b+b\cos\alpha-l\sin\alpha)$
VI	$+0.5\,(+b+b\cos\alpha-l\sin\alpha)$	$< x \leq$	$+0.5\,(+b-b\cos\alpha+l\sin\alpha)+y\sin\alpha$
VII	$+0.5\,(+b-b\cos\alpha+l\sin\alpha)+y\sin\alpha$	$< x \leq$	$+0.5\,(+b+b\cos\alpha+l\sin\alpha)+y\sin\alpha$

Case 5: $\{b < (l-|y|)\sin\alpha \leq b+b\cos\alpha\} \wedge y \in [0,l]$

I	$-0.5\,(+b+b\cos\alpha+l\sin\alpha)+y\sin\alpha$	$< x \leq$	$-0.5\,(+b-b\cos\alpha+l\sin\alpha)+y\sin\alpha$
II	$-0.5\,(+b-b\cos\alpha+l\sin\alpha)+y\sin\alpha$	$< x \leq$	$-0.5\,(-b+b\cos\alpha+l\sin\alpha)+y\sin\alpha$
III	$-0.5\,(-b+b\cos\alpha+l\sin\alpha)+y\sin\alpha$	$< x \leq$	$-0.5\,(+b+b\cos\alpha-l\sin\alpha)$
IV	$-0.5\,(+b+b\cos\alpha-l\sin\alpha)$	$< x \leq$	$+0.5\,(+b+b\cos\alpha-l\sin\alpha)+y\sin\alpha$
V	$+0.5\,(+b+b\cos\alpha-l\sin\alpha)+y\sin\alpha$	$< x \leq$	$+0.5\,(-b+b\cos\alpha+l\sin\alpha)$
VI	$+0.5\,(-b+b\cos\alpha+l\sin\alpha)$	$< x \leq$	$+0.5\,(+b-b\cos\alpha+l\sin\alpha)$
VII	$+0.5\,(+b-b\cos\alpha+l\sin\alpha)$	$< x \leq$	$+0.5\,(+b+b\cos\alpha+l\sin\alpha)$

Case 6: $\{b < (l-|y|)\sin\alpha \leq b+b\cos\alpha\} \wedge y \in [-l,0[$

I	$-0.5\,(+b+b\cos\alpha+l\sin\alpha)$	$< x \leq$	$-0.5\,(+b-b\cos\alpha+l\sin\alpha)$
II	$-0.5\,(+b-b\cos\alpha+l\sin\alpha)$	$< x \leq$	$-0.5\,(-b+b\cos\alpha+l\sin\alpha)$
III	$-0.5\,(-b+b\cos\alpha+l\sin\alpha)$	$< x \leq$	$-0.5\,(+b+b\cos\alpha-l\sin\alpha)+y\sin\alpha$
IV	$-0.5\,(+b+b\cos\alpha-l\sin\alpha)+y\sin\alpha$	$< x \leq$	$+0.5\,(+b+b\cos\alpha-l\sin\alpha)$
V	$+0.5\,(+b+b\cos\alpha-l\sin\alpha)$	$< x \leq$	$+0.5\,(-b+b\cos\alpha+l\sin\alpha)+y\sin\alpha$
VI	$+0.5\,(-b+b\cos\alpha+l\sin\alpha)+y\sin\alpha$	$< x \leq$	$+0.5\,(+b-b\cos\alpha+l\sin\alpha)+y\sin\alpha$
VII	$+0.5\,(+b-b\cos\alpha+l\sin\alpha)+y\sin\alpha$	$< x \leq$	$+0.5\,(+b+b\cos\alpha+l\sin\alpha)+y\sin\alpha$

Case 7: $\{b+b\cos\alpha \leq (l-|y|)\sin\alpha\} \wedge y \in [0,l]$

I	$-0.5\,(+b+b\cos\alpha+l\sin\alpha)+y\sin\alpha$	$< x \leq$	$-0.5\,(+b-b\cos\alpha+l\sin\alpha)+y\sin\alpha$
II	$-0.5\,(+b-b\cos\alpha+l\sin\alpha)+y\sin\alpha$	$< x \leq$	$-0.5\,(-b+b\cos\alpha+l\sin\alpha)+y\sin\alpha$
III	$-0.5\,(-b+b\cos\alpha+l\sin\alpha)+y\sin\alpha$	$< x \leq$	$-0.5\,(-b-b\cos\alpha+l\sin\alpha)+y\sin\alpha$
IV	$-0.5\,(-b-b\cos\alpha+l\sin\alpha)+y\sin\alpha$	$< x \leq$	$+0.5\,(-b-b\cos\alpha+l\sin\alpha)$
V	$+0.5\,(-b-b\cos\alpha+l\sin\alpha)$	$< x \leq$	$+0.5\,(-b+b\cos\alpha+l\sin\alpha)$
VI	$+0.5\,(-b+b\cos\alpha+l\sin\alpha)$	$< x \leq$	$+0.5\,(+b-b\cos\alpha+l\sin\alpha)$
VII	$+0.5\,(+b-b\cos\alpha+l\sin\alpha)$	$< x \leq$	$+0.5\,(+b+b\cos\alpha+l\sin\alpha)$

Case 8: $\{b + b\cos\alpha \leq (l - |y|)\sin\alpha\} \wedge y \in [-l, 0[$

I	$-0.5\,(+b + b\cos\alpha + l\sin\alpha)$	$< x \leq$	$-0.5\,(+b - b\cos\alpha + l\sin\alpha)$
II	$-0.5\,(+b - b\cos\alpha + l\sin\alpha)$	$< x \leq$	$-0.5\,(-b + b\cos\alpha + l\sin\alpha)$
III	$-0.5\,(-b + b\cos\alpha + l\sin\alpha)$	$< x \leq$	$-0.5\,(-b - b\cos\alpha + l\sin\alpha)$
IV	$-0.5\,(-b - b\cos\alpha + l\sin\alpha)$	$< x \leq$	$+0.5\,(-b - b\cos\alpha + l\sin\alpha) + y\sin\alpha$
V	$+0.5\,(-b - b\cos\alpha + l\sin\alpha) + y\sin\alpha$	$< x \leq$	$+0.5\,(-b + b\cos\alpha + l\sin\alpha) + y\sin\alpha$
VI	$+0.5\,(-b + b\cos\alpha + l\sin\alpha) + y\sin\alpha$	$< x \leq$	$+0.5\,(+b - b\cos\alpha + l\sin\alpha) + y\sin\alpha$
VII	$+0.5\,(+b - b\cos\alpha + l\sin\alpha) + y\sin\alpha$	$< x \leq$	$+0.5\,(+b + b\cos\alpha + l\sin\alpha) + y\sin\alpha$

area of the intersection for all cases described above
Following shortcuts are used to describe the intervals for case i:

$$\mathrm{I_{i,I}} = [a_{\mathrm{i,I}}, b_{\mathrm{i,I}}] \tag{A.50}$$
$$\mathrm{I_{i,II}} =]a_{\mathrm{i,II}}, b_{\mathrm{i,II}}] \tag{A.51}$$
$$\mathrm{I_{i,III}} =]a_{\mathrm{i,III}}, b_{\mathrm{i,III}}] \tag{A.52}$$
$$\mathrm{I_{i,IV}} =]a_{\mathrm{i,IV}}, b_{\mathrm{i,IV}}] \tag{A.53}$$
$$\mathrm{I_{i,V}} =]a_{\mathrm{i,V}}, b_{\mathrm{i,V}}] \tag{A.54}$$
$$\mathrm{I_{i,VI}} =]a_{\mathrm{i,VI}}, b_{\mathrm{i,VI}}] \tag{A.55}$$
$$\mathrm{I_{i,VII}} =]a_{\mathrm{i,VII}}, b_{\mathrm{i,VII}}] \tag{A.56}$$

The area of the intersection of the two slits for the different cases and intervals is then given by $A_{\mathrm{i,j}}$ for interval $\mathrm{I_{i,j}}$:
Case 1

$$A_{1,\mathrm{I}} = \frac{1}{\cos\alpha}\Big[0.5\,(x - a_{1,\mathrm{I}})^2\cot\alpha\Big] \tag{A.57}$$
$$A_{1,\mathrm{II}} = \frac{1}{\cos\alpha}\Big[0.5\,(a_{1,\mathrm{II}} - a_{1,\mathrm{I}})^2\cot\alpha + (x - a_{1,\mathrm{II}})\,(l - |y|)\Big] \tag{A.58}$$
$$A_{1,\mathrm{III}} = \frac{1}{\cos\alpha}\Big[0.5\,(a_{1,\mathrm{II}} - a_{1,\mathrm{I}})^2\cot\alpha + (a_{1,\mathrm{III}} - a_{1,\mathrm{II}})\,(l - |y|) + 0.5\,\left[(b_{1,\mathrm{VII}} - a_{1,\mathrm{VII}})^2 - (a_{1,\mathrm{V}} - x)^2\right]\cot\alpha\Big] \tag{A.59}$$
$$A_{1,\mathrm{IV}} = \frac{1}{\cos\alpha}\Big[0.5\,\left[(a_{1,\mathrm{II}} - a_{1,\mathrm{I}})^2 - (x - a_{1,\mathrm{IV}})^2\right]\cot\alpha + (a_{1,\mathrm{III}} - a_{1,\mathrm{II}})\,(l - |y|) + 0.5\,\left[(b_{1,\mathrm{VII}} - a_{1,\mathrm{VII}})^2 - (a_{1,\mathrm{V}} - x)^2\right]\cot\alpha\Big] \tag{A.60}$$
$$A_{1,\mathrm{V}} = \frac{1}{\cos\alpha}\Big[0.5\,\left[(a_{1,\mathrm{II}} - a_{1,\mathrm{I}})^2 - (x - a_{1,\mathrm{IV}})^2\right]\cot\alpha + (a_{1,\mathrm{III}} - a_{1,\mathrm{II}})\,(l - |y|) + 0.5\,(b_{1,\mathrm{VII}} - a_{1,\mathrm{VII}})^2\cot\alpha\Big] \tag{A.61}$$
$$A_{1,\mathrm{VI}} = \frac{1}{\cos\alpha}\Big[(a_{1,\mathrm{VII}} - x)\,(l - |y|) + 0.5\,(b_{1,\mathrm{VII}} - a_{1,\mathrm{VII}})^2\cot\alpha\Big] \tag{A.62}$$
$$A_{1,\mathrm{VII}} = \frac{1}{\cos\alpha}\Big[0.5\,(b_{1,\mathrm{VII}} - x)^2\cot\alpha\Big] \tag{A.63}$$

Case 2

$$A_{2,\mathrm{I}} = \frac{1}{\cos\alpha}\Big[\,0.5\,(x-a_{2,\mathrm{I}})^2\,\cot\alpha\,\Big] \tag{A.64}$$

$$\begin{aligned} A_{2,\mathrm{II}} = \frac{1}{\cos\alpha}\Big[\,&0.5\,(a_{2,\mathrm{II}}-a_{2,\mathrm{I}})^2\,\cot\alpha \\ &+(x-a_{2,\mathrm{II}})\,(l-|y|)\,\Big] \end{aligned} \tag{A.65}$$

$$\begin{aligned} A_{2,\mathrm{III}} = \frac{1}{\cos\alpha}\Big[\,&0.5\,(a_{2,\mathrm{II}}-a_{2,\mathrm{I}})^2\,\cot\alpha \\ &+(a_{2,\mathrm{III}}-a_{2,\mathrm{II}})\,(l-|y|) \\ &+0.5\,\left[(b_{2,\mathrm{VII}}-a_{2,\mathrm{VII}})^2-(a_{2,\mathrm{V}}-x)^2\right]\,\cot\alpha\,\Big] \end{aligned} \tag{A.66}$$

$$\begin{aligned} A_{2,\mathrm{IV}} = \frac{1}{\cos\alpha}\Big[\,&0.5\,\left[(a_{2,\mathrm{II}}-a_{2,\mathrm{I}})^2-(x-a_{2,\mathrm{IV}})^2\right]\,\cot\alpha \\ &+(a_{2,\mathrm{III}}-a_{2,\mathrm{II}})\,(l-|y|) \\ &+0.5\,\left[(b_{2,\mathrm{VII}}-a_{2,\mathrm{VII}})^2-(a_{1,\mathrm{V}}-x)^2\right]\,\cot\alpha\,\Big] \end{aligned} \tag{A.67}$$

$$\begin{aligned} A_{2,\mathrm{V}} = \frac{1}{\cos\alpha}\Big[\,&0.5\,\left[(a_{2,\mathrm{II}}-a_{2,\mathrm{I}})^2-(x-a_{2,\mathrm{IV}})^2\right]\,\cot\alpha \\ &+(a_{2,\mathrm{III}}-a_{2,\mathrm{II}})\,(l-|y|) \\ &+0.5\,(b_{2,\mathrm{VII}}-a_{2,\mathrm{VII}})^2\,\cot\alpha\,\Big] \end{aligned} \tag{A.68}$$

$$\begin{aligned} A_{2,\mathrm{VI}} = \frac{1}{\cos\alpha}\Big[\,&(a_{2,\mathrm{VII}}-x)\,(l-|y|) \\ &+0.5\,(b_{2,\mathrm{VII}}-a_{2,\mathrm{VII}})^2\,\cot\alpha\,\Big] \end{aligned} \tag{A.69}$$

$$A_{2,\mathrm{VII}} = \frac{1}{\cos\alpha}\Big[\,0.5\,(b_{2,\mathrm{VII}}-x)^2\,\cot\alpha\,\Big] \tag{A.70}$$

Case 3

$$A_{3,\mathrm{I}} = \frac{1}{\cos\alpha}\Big[\,0.5\,(x-a_{3,\mathrm{I}})^2\,\cot\alpha\,\Big] \tag{A.71}$$

$$\begin{aligned} A_{3,\mathrm{II}} = \frac{1}{\cos\alpha}\Big[\,&0.5\,(a_{3,\mathrm{II}}-a_{3,\mathrm{I}})^2\,\cot\alpha \\ &+(a_{3,\mathrm{II}}-a_{3,\mathrm{I}})\,\cot\alpha\,(x-a_{3,\mathrm{II}})\,\Big] \end{aligned} \tag{A.72}$$

$$\begin{aligned} A_{3,\mathrm{III}} = \frac{1}{\cos\alpha}\Big[\,&0.5\,(a_{3,\mathrm{II}}-a_{3,\mathrm{I}})^2\,\cot\alpha \\ &+(a_{3,\mathrm{II}}-a_{3,\mathrm{I}})\,\cot\alpha\,(a_{3,\mathrm{III}}-a_{3,\mathrm{II}}) \\ &+0.5\,\left[(b_{3,\mathrm{VII}}-a_{3,\mathrm{VII}})^2-(a_{3,\mathrm{V}}-x)^2\right]\,\cot\alpha\,\Big] \end{aligned} \tag{A.73}$$

$$\begin{aligned} A_{3,\mathrm{IV}} = \frac{1}{\cos\alpha}\Big[\,&0.5\,\left[(a_{3,\mathrm{II}}-a_{3,\mathrm{I}})^2-(x-a_{3,\mathrm{IV}})^2\right]\,\cot\alpha \\ &+(a_{3,\mathrm{II}}-a_{3,\mathrm{I}})\,\cot\alpha\,(a_{3,\mathrm{III}}-a_{3,\mathrm{II}}) \\ &+0.5\,\left[(b_{3,\mathrm{VII}}-a_{3,\mathrm{VII}})^2-(a_{3,\mathrm{V}}-x)^2\right]\,\cot\alpha\,\Big] \end{aligned} \tag{A.74}$$

$$\begin{aligned} A_{3,\mathrm{V}} = \frac{1}{\cos\alpha}\Big[\,&0.5\,\left[(a_{3,\mathrm{II}}-a_{3,\mathrm{I}})^2-(x-a_{3,\mathrm{IV}})^2\right]\,\cot\alpha \\ &+(a_{3,\mathrm{II}}-a_{3,\mathrm{I}})\,\cot\alpha\,(a_{3,\mathrm{III}}-a_{3,\mathrm{II}}) \\ &+0.5\,(b_{3,\mathrm{VII}}-a_{3,\mathrm{VII}})^2\,\cot\alpha\,\Big] \end{aligned} \tag{A.75}$$

$$\begin{aligned} A_{3,\mathrm{VI}} = \frac{1}{\cos\alpha}\Big[\,&(a_{3,\mathrm{II}}-a_{3,\mathrm{I}})\,\cot\alpha\,(a_{3,\mathrm{VII}}-x) \\ &+0.5\,(b_{3,\mathrm{VII}}-a_{3,\mathrm{VII}})^2\,\cot\alpha\,\Big] \end{aligned} \tag{A.76}$$

$$A_{3,\mathrm{VII}} = \frac{1}{\cos\alpha}\Big[\,0.5\,(b_{3,\mathrm{VII}}-x)^2\,\cot\alpha\,\Big] \tag{A.77}$$

Case 4

$$A_{4,\mathrm{I}} = \frac{1}{\cos\alpha}\Big[\,0.5\,(x-a_{4,\mathrm{I}})^2\,\cot\alpha\,\Big] \tag{A.78}$$

$$\begin{aligned} A_{4,\mathrm{II}} = \frac{1}{\cos\alpha}\Big[\,&0.5\,(a_{4,\mathrm{II}}-a_{4,\mathrm{I}})^2\,\cot\alpha \\ &+(a_{4,\mathrm{II}}-a_{4,\mathrm{I}})\,\cot\alpha\,(x-a_{4,\mathrm{II}})\,\Big] \end{aligned} \tag{A.79}$$

$$\begin{aligned} A_{4,\mathrm{III}} = \frac{1}{\cos\alpha}\Big[\,&0.5\,(a_{4,\mathrm{II}}-a_{4,\mathrm{I}})^2\,\cot\alpha \\ &+(a_{4,\mathrm{II}}-a_{4,\mathrm{I}})\,\cot\alpha\,(a_{4,\mathrm{III}}-a_{4,\mathrm{II}}) \\ &+0.5\,\left[(b_{4,\mathrm{VII}}-a_{4,\mathrm{VII}})^2-(a_{4,\mathrm{V}}-x)^2\right]\,\cot\alpha\,\Big] \end{aligned} \tag{A.80}$$

$$\begin{aligned} A_{4,\mathrm{IV}} = \frac{1}{\cos\alpha}\Big[\,&0.5\,\left[(a_{4,\mathrm{II}}-a_{4,\mathrm{I}})^2-(x-a_{4,\mathrm{IV}})^2\right]\,\cot\alpha \\ &+(a_{4,\mathrm{II}}-a_{4,\mathrm{I}})\,\cot\alpha\,(a_{4,\mathrm{III}}-a_{4,\mathrm{II}}) \\ &+0.5\,\left[(b_{4,\mathrm{VII}}-a_{4,\mathrm{VII}})^2-(a_{4,\mathrm{V}}-x)^2\right]\,\cot\alpha\,\Big] \end{aligned} \tag{A.81}$$

$$\begin{aligned} A_{4,\mathrm{V}} = \frac{1}{\cos\alpha}\Big[\,&0.5\,\left[(a_{4,\mathrm{II}}-a_{4,\mathrm{I}})^2-(x-a_{4,\mathrm{IV}})^2\right]\,\cot\alpha \\ &+(a_{4,\mathrm{II}}-a_{4,\mathrm{I}})\,\cot\alpha\,(a_{4,\mathrm{III}}-a_{4,\mathrm{II}}) \\ &+0.5\,(b_{4,\mathrm{VII}}-a_{4,\mathrm{VII}})^2\,\cot\alpha\,\Big] \end{aligned} \tag{A.82}$$

$$\begin{aligned} A_{4,\mathrm{VI}} = \frac{1}{\cos\alpha}\Big[\,&(a_{4,\mathrm{II}}-a_{4,\mathrm{I}})\,\cot\alpha\,(a_{4,\mathrm{VII}}-x) \\ &+0.5\,(b_{4,\mathrm{VII}}-a_{4,\mathrm{VII}})^2\,\cot\alpha\,\Big] \end{aligned} \tag{A.83}$$

$$A_{4,\mathrm{VII}} = \frac{1}{\cos\alpha}\Big[\,0.5\,(b_{4,\mathrm{VII}}-x)^2\,\cot\alpha\,\Big] \tag{A.84}$$

Case 5

$$A_{5,\mathrm{I}} = \frac{1}{\cos\alpha}\Big[\,0.5\,(x-a_{5,\mathrm{I}})^2\,\cot\alpha\,\Big] \tag{A.85}$$

$$\begin{aligned} A_{5,\mathrm{II}} = \frac{1}{\cos\alpha}\Big[\,&0.5\,(a_{5,\mathrm{II}}-a_{5,\mathrm{I}})^2\,\cot\alpha \\ &+(a_{5,\mathrm{II}}-a_{5,\mathrm{I}})\,\cot\alpha\,(x-a_{5,\mathrm{II}})\,\Big] \end{aligned} \tag{A.86}$$

$$\begin{aligned} A_{5,\mathrm{III}} = \frac{1}{\cos\alpha}\Big[\,&0.5\,\left[(a_{5,\mathrm{II}}-a_{5,\mathrm{I}})^2-(x-a_{5,\mathrm{III}})^2\right]\,\cot\alpha \\ &+(a_{5,\mathrm{II}}-a_{5,\mathrm{I}})\,\cot\alpha\,(x-a_{5,\mathrm{II}})\,\Big] \end{aligned} \tag{A.87}$$

$$\begin{aligned} A_{5,\mathrm{IV}} = \frac{1}{\cos\alpha}\Big[\,&0.5\,\left[(a_{5,\mathrm{II}}-a_{5,\mathrm{I}})^2-(x-a_{5,\mathrm{III}})^2\right]\,\cot\alpha \\ &+(a_{5,\mathrm{II}}-a_{5,\mathrm{I}})\,\cot\alpha\,(a_{5,\mathrm{IV}}-a_{5,\mathrm{II}}) \\ &+0.5\,\left[(b_{5,\mathrm{VII}}-a_{5,\mathrm{VII}})^2-(a_{5,\mathrm{VI}}-x)^2\right]\,\cot\alpha\,\Big] \end{aligned} \tag{A.88}$$

$$\begin{aligned} A_{5,\mathrm{V}} = \frac{1}{\cos\alpha}\Big[\,&(a_{5,\mathrm{II}}-a_{5,\mathrm{I}})\,\cot\alpha\,(a_{5,\mathrm{VII}}-x) \\ &+0.5\,\left[(b_{5,\mathrm{VII}}-a_{5,\mathrm{VII}})^2-(a_{5,\mathrm{VI}}-x)^2\right]\,\cot\alpha\,\Big] \end{aligned} \tag{A.89}$$

$$\begin{aligned} A_{5,\mathrm{VI}} = \frac{1}{\cos\alpha}\Big[\,&(a_{5,\mathrm{II}}-a_{5,\mathrm{I}})\,\cot\alpha\,(a_{5,\mathrm{VII}}-x) \\ &+0.5\,(b_{5,\mathrm{VII}}-a_{5,\mathrm{VII}})^2\,\cot\alpha\,\Big] \end{aligned} \tag{A.90}$$

$$A_{5,\mathrm{VII}} = \frac{1}{\cos\alpha}\Big[\,0.5\,(b_{5,\mathrm{VII}}-x)^2\,\cot\alpha\,\Big] \tag{A.91}$$

Case 6

$$A_{6,\mathrm{I}} = \frac{1}{\cos\alpha}\Big[0.5\,(x-a_{6,\mathrm{I}})^2\,\cot\alpha\Big] \tag{A.92}$$

$$A_{6,\mathrm{II}} = \frac{1}{\cos\alpha}\Big[0.5\,(a_{6,\mathrm{II}}-a_{6,\mathrm{I}})^2\,\cot\alpha + (a_{6,\mathrm{II}}-a_{6,\mathrm{I}})\,\cot\alpha\,(x-a_{6,\mathrm{II}})\Big] \tag{A.93}$$

$$A_{6,\mathrm{III}} = \frac{1}{\cos\alpha}\Big[0.5\,\left[(a_{6,\mathrm{II}}-a_{6,\mathrm{I}})^2-(x-a_{6,\mathrm{III}})^2\right]\cot\alpha + (a_{6,\mathrm{II}}-a_{6,\mathrm{I}})\,\cot\alpha\,(x-a_{6,\mathrm{II}})\Big] \tag{A.94}$$

$$A_{6,\mathrm{IV}} = \frac{1}{\cos\alpha}\Big[0.5\,\left[(a_{6,\mathrm{II}}-a_{6,\mathrm{I}})^2-(x-a_{6,\mathrm{III}})^2\right]\cot\alpha + (a_{6,\mathrm{II}}-a_{6,\mathrm{I}})\,\cot\alpha\,(a_{6,\mathrm{IV}}-a_{6,\mathrm{II}}) + 0.5\,\left[(b_{6,\mathrm{VII}}-a_{6,\mathrm{VII}})^2-(a_{6,\mathrm{VI}}-x)^2\right]\cot\alpha\Big] \tag{A.95}$$

$$A_{6,\mathrm{V}} = \frac{1}{\cos\alpha}\Big[(a_{6,\mathrm{II}}-a_{6,\mathrm{I}})\,\cot\alpha\,(a_{6,\mathrm{VII}}-x) + 0.5\,\left[(b_{6,\mathrm{VII}}-a_{6,\mathrm{VII}})^2-(a_{6,\mathrm{VI}}-x)^2\right]\cot\alpha\Big] \tag{A.96}$$

$$A_{6,\mathrm{VI}} = \frac{1}{\cos\alpha}\Big[(a_{6,\mathrm{II}}-a_{6,\mathrm{I}})\,\cot\alpha\,(a_{6,\mathrm{VII}}-x) + 0.5\,(b_{6,\mathrm{VII}}-a_{6,\mathrm{VII}})^2\,\cot\alpha\Big] \tag{A.97}$$

$$A_{6,\mathrm{VII}} = \frac{1}{\cos\alpha}\Big[0.5\,(b_{6,\mathrm{VII}}-x)^2\,\cot\alpha\Big] \tag{A.98}$$

Case 7

$$A_{7,\mathrm{I}} = \frac{1}{\cos\alpha}\Big[0.5\,(x-a_{7,\mathrm{I}})^2\,\cot\alpha\Big] \tag{A.99}$$

$$A_{7,\mathrm{II}} = \frac{1}{\cos\alpha}\Big[0.5\,(a_{7,\mathrm{II}}-a_{7,\mathrm{I}})^2\,\cot\alpha + (a_{7,\mathrm{II}}-a_{7,\mathrm{I}})\,\cot\alpha\,(x-a_{7,\mathrm{II}})\Big] \tag{A.100}$$

$$A_{7,\mathrm{III}} = \frac{1}{\cos\alpha}\Big[0.5\,\left[(a_{7,\mathrm{II}}-a_{7,\mathrm{I}})^2-(x-a_{7,\mathrm{III}})^2\right]\cot\alpha + (a_{7,\mathrm{II}}-a_{7,\mathrm{I}})\,\cot\alpha\,(x-a_{7,\mathrm{II}})\Big] \tag{A.101}$$

$$A_{7,\mathrm{IV}} = \frac{1}{\cos\alpha}\Big[(a_{7,\mathrm{II}}-a_{7,\mathrm{I}})\,\cot\alpha\,(a_{7,\mathrm{IV}}-a_{7,\mathrm{II}})\Big] \tag{A.102}$$

$$A_{7,\mathrm{V}} = \frac{1}{\cos\alpha}\Big[(a_{7,\mathrm{II}}-a_{7,\mathrm{I}})\,\cot\alpha\,(a_{7,\mathrm{VII}}-x) + 0.5\,\left[(b_{7,\mathrm{VII}}-a_{7,\mathrm{VII}})^2-(a_{7,\mathrm{VI}}-x)^2\right]\cot\alpha\Big] \tag{A.103}$$

$$A_{7,\mathrm{VI}} = \frac{1}{\cos\alpha}\Big[(a_{7,\mathrm{II}}-a_{7,\mathrm{I}})\,\cot\alpha\,(a_{7,\mathrm{VII}}-x) + 0.5\,(b_{7,\mathrm{VII}}-a_{7,\mathrm{VII}})^2\,\cot\alpha\Big] \tag{A.104}$$

$$A_{7,\mathrm{VII}} = \frac{1}{\cos\alpha}\Big[0.5\,(b_{7,\mathrm{VII}}-x)^2\,\cot\alpha\Big] \tag{A.105}$$

Case 8

$$A_{8,\mathrm{I}} = \frac{1}{\cos\alpha}\Big[\,0.5\,(x-a_{8,\mathrm{I}})^2\,\cot\alpha\,\Big] \tag{A.106}$$

$$A_{8,\mathrm{II}} = \frac{1}{\cos\alpha}\Big[\,0.5\,(a_{8,\mathrm{II}}-a_{8,\mathrm{I}})^2\,\cot\alpha + (a_{8,\mathrm{II}}-a_{8,\mathrm{I}})\,\cot\alpha\,(x-a_{8,\mathrm{II}})\,\Big] \tag{A.107}$$

$$A_{8,\mathrm{III}} = \frac{1}{\cos\alpha}\Big[\,0.5\,\left[(a_{8,\mathrm{II}}-a_{8,\mathrm{I}})^2-(x-a_{8,\mathrm{III}})^2\right]\,\cot\alpha + (a_{8,\mathrm{II}}-a_{8,\mathrm{I}})\,\cot\alpha\,(x-a_{8,\mathrm{II}})\,\Big] \tag{A.108}$$

$$A_{8,\mathrm{IV}} = \frac{1}{\cos\alpha}\Big[\,(a_{8,\mathrm{II}}-a_{8,\mathrm{I}})\,\cot\alpha\,(a_{8,\mathrm{IV}}-a_{8,\mathrm{II}})\,\Big] \tag{A.109}$$

$$A_{8,\mathrm{V}} = \frac{1}{\cos\alpha}\Big[\,(a_{8,\mathrm{II}}-a_{8,\mathrm{I}})\,\cot\alpha\,(a_{8,\mathrm{VII}}-x) + 0.5\,\left[(b_{8,\mathrm{VII}}-a_{8,\mathrm{VII}})^2-(a_{8,\mathrm{VI}}-x)^2\right]\,\cot\alpha\,\Big] \tag{A.110}$$

$$A_{8,\mathrm{VI}} = \frac{1}{\cos\alpha}\Big[\,(a_{8,\mathrm{II}}-a_{8,\mathrm{I}})\,\cot\alpha\,(a_{8,\mathrm{VII}}-x) + 0.5\,(b_{8,\mathrm{VII}}-a_{8,\mathrm{VII}})^2\,\cot\alpha\,\Big] \tag{A.111}$$

$$A_{8,\mathrm{VII}} = \frac{1}{\cos\alpha}\Big[\,0.5\,(b_{8,\mathrm{VII}}-x)^2\,\cot\alpha\,\Big] \tag{A.112}$$

The calculated line profiles for the center, $y = 0$, of the intensity distribution at the detector is shown in figure A.10. For the calculations it is assumed that:

- the distance between the source aperture and the sample aperture is the same, $L_\mathrm{C} = L_\mathrm{D}$,
- the source aperture has a width of 0.5 mm and a height of 55 mm, corresponding to the USANS II parameters,
- and the sample aperture is matched to the source aperture according to equation (2.45).

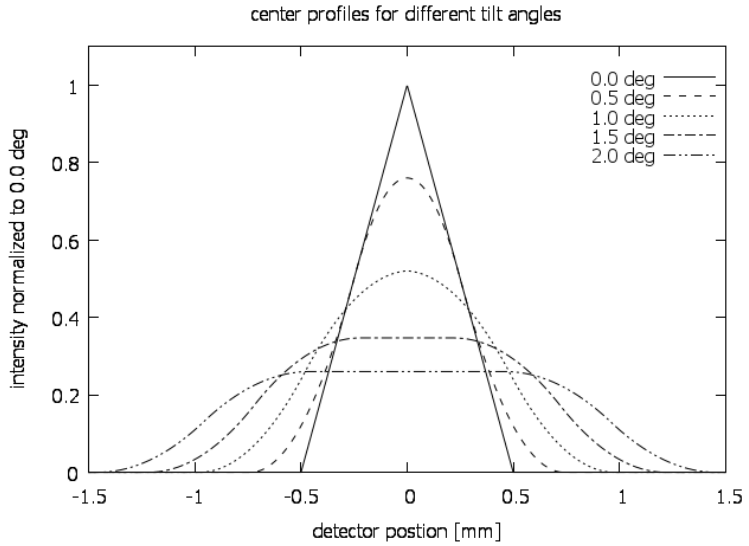

Fig. A.10: Tilting one of the apertures around the neutron beam axis causes a broadening of the center of the intensity profile at the detector. Profiles corresponding to two slit shaped apertures are shown for different tilt angles. The profiles are comparable to the profiles expected form a source aperture of a width of 0.5 mm and a height of 55 mm.

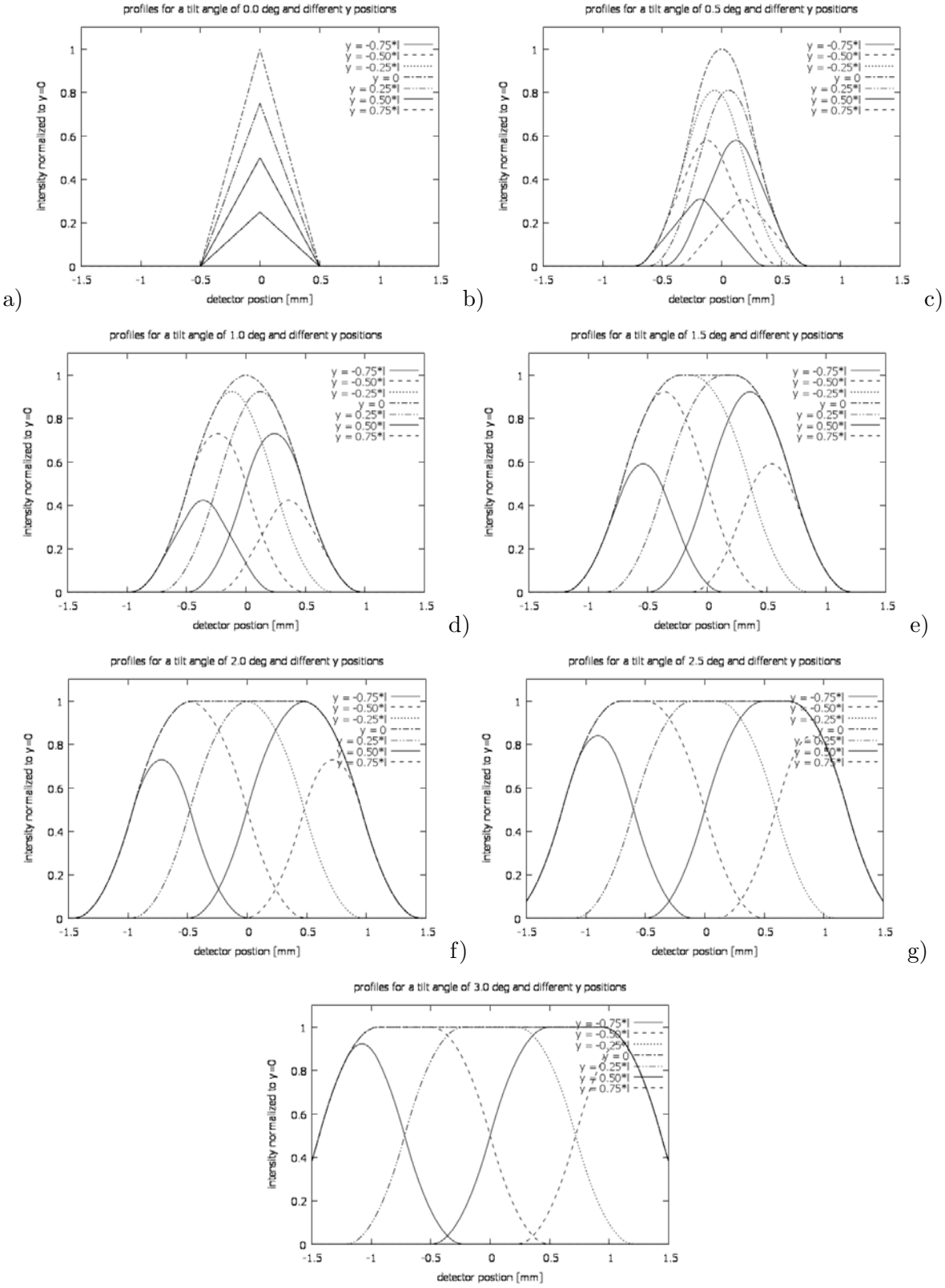

Fig. A.11: If the slits are tilted with respect to each other the line profiles along the x-direction differ depending on the y-position on the detector. Several line profiles for tilt angles of: a) 0.0°, b) 0.5°, c) 1.0°, d) 1.5°, e) 2.0°, f) 2.5°, g) 3.0°.

As the expected intensity profile at the detector can be gained by using a Fast Fourier Transformation (FFT) to calculate the correlation of the source aperture and the sample aperture it is possible to compare the results with the analytical approximation derived above. The intensity distributions at the detector using a FFT to evaluate the correlation of the source aperture and the sample aperture are in figure A.12 for different tilt angles of the sample aperture with respect to the source aperture. Lenses act like point-shaped apertures. Thus cylindrical lenses like the ones

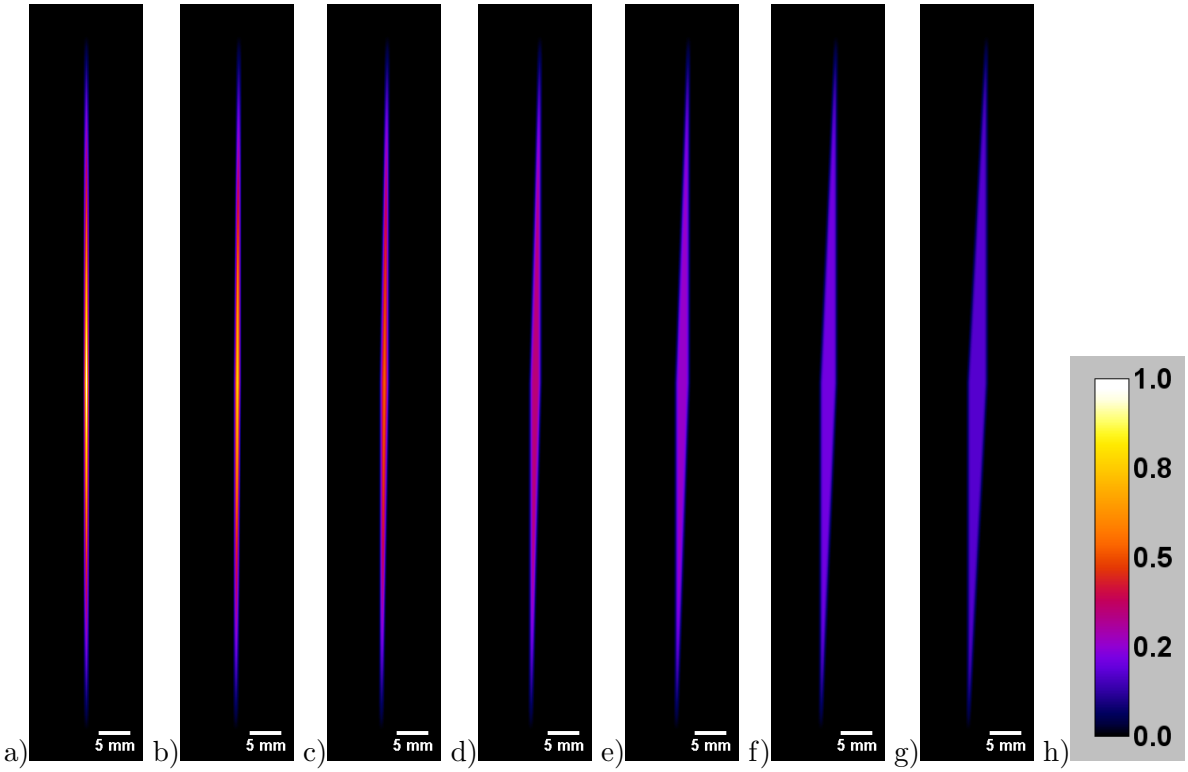

Fig. A.12: Intensity profiles at the detector plane resulting form a slit shaped source aperture of 55 mm in length and 0.5 mm in width, when the sample aperture is matched corresponding to the distances between the source aperture, the sample aperture and the detector. It is assumed that $L_C = L_D$. The intensity distributions are shown for different tilt angles of the sample aperture with respect to the source aperture: a) 0.0 °, b) 0.5 °,c) 1.0 °, d) 1.5 °, e) 2.0 °, f) 2.5 °, g) 3.0 °. The intensities are normalized to the maximum intensity at the center of the detector for a tilt angle of 0.0 ° between the apertures and color coded according to the calibration bar shown in h).

used for the USANS I and USANS II setups will not alter the shape of the line profiles when tilted around the neutron beam axis by a small angle. But similar shifts towards positive or negative directions are expected like the ones shown above for the profiles of tilted slit-shaped apertures.

A.11 Reduction of Beam Divergence

There are several components that may restrict the divergence of a neutron beam at a SANS/USANS instrument:

i) the entrance of the collimation, which is given by the cross section of the end of the coated neutron guide,

ii) the slits of the source aperture acting like a collimator,

iii) the velocity selector,

iv) the reflectivity of the coated neutron guide and

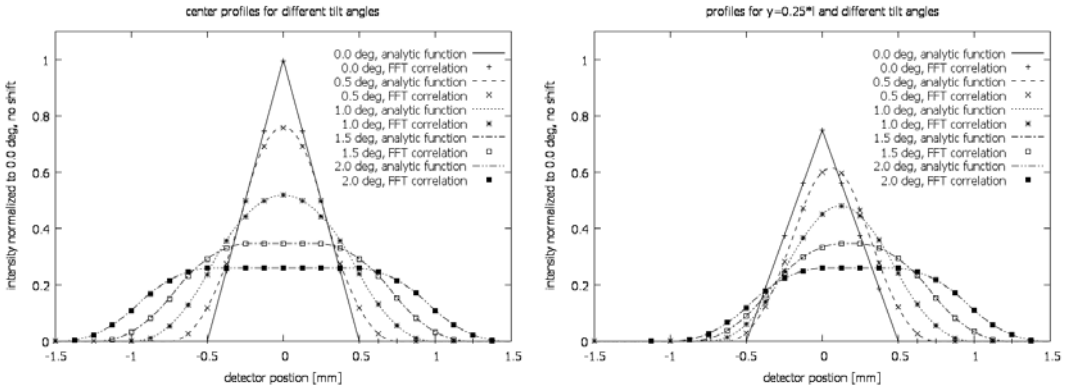

Fig. A.13: Comparison of the intensity profile for slit shaped apertures for the analytic function derived and the intensity distribution resulting from a correlation of the apertures calculated using a FFT. Here at the center of the detector and 25 % of the length of the slit above the center.

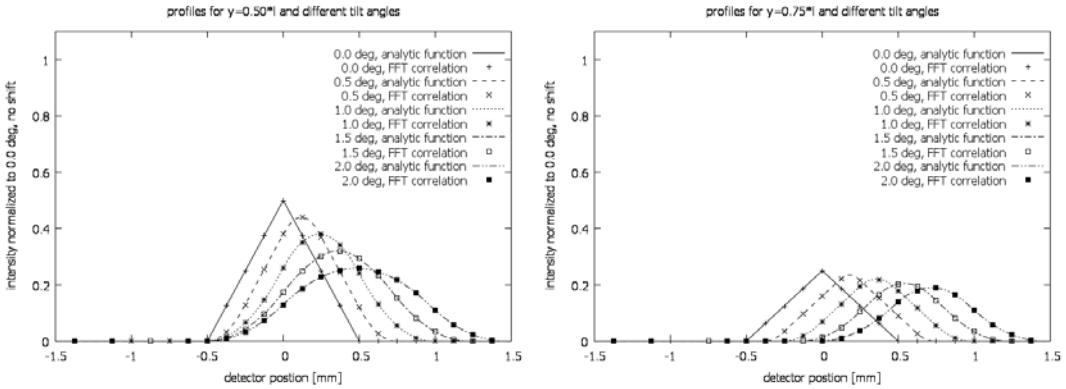

Fig. A.14: 50 % of the length of the slit above the center and 75 % of the length of the slit above the center.

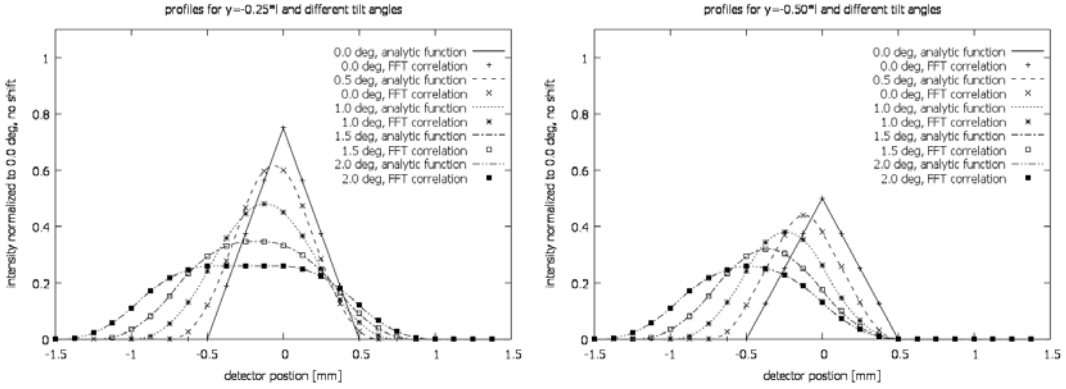

Fig. A.15: 25 % of the length of the slit below the center and 50 % of the length of the slit below the center.

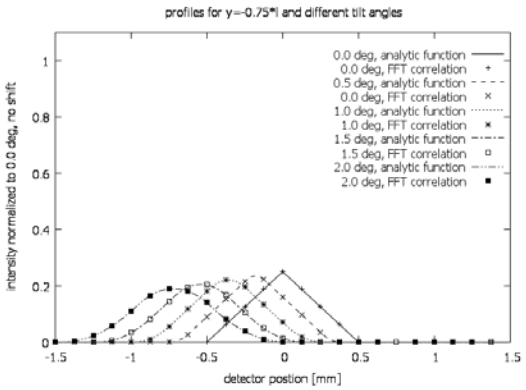

Fig. A.16: 75 % of the length of the slit below the center.

v) the reflectivity of the uncoated neutron guide in front of the source aperture.

In the following the transmitted divergence of the components listed above is calculated or estimated. Only the horizontal divergence of the neutron beam is of interest here, as the intensity distribution in vertical direction is not evaluated due to the slit geometry of the source aperture array and the sample aperture array.
The horizontal divergence is defined by the width of the coated neutron guide at the entrance of the collimation, 30 mm, and the length of the neutron path to reach the source aperture, 20000 mm. Thus the horizontal divergence is

$$\frac{30\,\mathrm{mm}}{20000\,\mathrm{mm}} = 1.5 \cdot 10^{-3} \mathrel{\widehat{=}} 0.086\,^\circ\,. \tag{A.113}$$

The slits of the source aperture have a width of 0.5 mm and length of 3.175 mm in beam direction [14]. Thus the slits accept a horizontal divergence of

$$\frac{0.5\,\mathrm{mm}}{3.175\,\mathrm{mm}} = 0.16 \mathrel{\widehat{=}} 8.9\,^\circ\,. \tag{A.114}$$

This is even much larger than the maximum beam divergence transmitted through the velocity selector of about 2 ° [68], [69].
If a reflectivity of $m = 2$ is assumed for the coated neutron guide in front of the selector, the beam divergence for a neutron wavelength of 9.6 Å is

$$0.1\,^\circ \cdot 2 \cdot 9.6 = 1.9\,^\circ \tag{A.115}$$

The uncoated glass guide inside the collimation has a reflectivity of $m = 0.65$ [70]. Therefore the accepted divergence of this guide at a wavelength of 9.6 Å is

$$0.1\,^\circ \cdot 0.65 \cdot 9.6 = 0.62\,^\circ\,. \tag{A.116}$$

A.12 USANS Software

A scattering signal along the y direction, the direction of the slits of the source aperture, can not be evaluated. Neutrons scattered in this direction alter the intensity profile measured along Q_y for $Q_\mathrm{x} = 0$. The standard method for the initial data reduction described in section 2.2.2 uses this signal to derive the transmission of the sample of the sample container. It is assumed that the shape of the intensity distribution of the transmitted signal $T(Q_\mathrm{x}, Q_\mathrm{y})$ is equal to the shape of the primary beam $I_0(Q_\mathrm{x}, Q_\mathrm{y})$ and diminished only by the transmission coefficient $\hat{T}_0$ (Eqn. (2.49)):

$$T(Q_\mathrm{x}, Q_\mathrm{y}) = I_0(Q_\mathrm{x}, Q_\mathrm{y}) \cdot \hat{T}_0\,. \tag{A.117}$$

If now neutrons scattered along the y-direction cause a change of the shape of the "transmitted" signal, it is not possible anymore to retrieve the correct transmission $\hat{T}_0$. The transmission correction for the evaluated data in x-direction would therefore be erroneous.

μSANS Ii is not possible to evaluate the USANS data with the standard SANS software. First of all the peaks of the primary intensity of the multiple USANS pattern can not be masked for evaluation by a single region like it is done for standard pinhole SANS software. Second a radial summation of the signal known from pinhole SANS is not possible owing to the slit geometry of the apertures and lenses applied for beam shaping. Third there is no beam stop to block the transmitted primary beam. This is necessary to measure the scattered intensity profile close to $Q = 0$. The intensity of the transmitted primary beam has to be subtracted from the measured "scattering" intensity.
There is a clear advantage due to the use of an integrating detector, as it allows for an evaluation of the scattering signal down to Q-values close to 0, which is a difference to an evaluation of data starting from a Q-value of a certain distance to $Q = 0$. Data reduction of the USANS data taken using a CCD detector is different to the methods applied for standard SANS data. Important points for USANS data reduction:

- The preliminary USANS setup only allows to evaluate scattering profiles in one dimension (i.e. x-direction). All signals are summed along the slit direction (i.e. y-direction).

- There is no beam stop to block neutrons at the center of each of the multiple peaks at the detector. The center each peak corresponds to $Q = 0$. Thus line profiles of scattered intensities may be extended down to "$Q = 0$", which is not possible for standard pinhole SANS setups. The neutron imaging detector operating in an integrating mode rather than a counting mode enables to do so, because there is no upper limit for the neutron flux to be detected.

- Transmission calculations of standard SANS data require an extra intensity profile of the sample taken without a beam stop. This is not necessary for the USANS setups using a CCD detector, because transmission values can be calculated from the intensity values at $Q = 0$ of images containing the scattered intensity data directly.

An ImageJ-Plugin[10] has been written to provide a quick and flexible way to evaluate the data. Due to the Plugin-concept all inbuilt function of ImageJ may be used inside and along with the evaluation software. The evaluation software is called **μSANS** as the evaluated Q-range in reciprocal space corresponds to structures of several micrometers in size in real space.
All steps during data reduction are kept as close as possible to the structure given in [11].
If it is appropriate, similarities to the data evaluation of neutron radiography are pointed out. The nomenclature of the acquired images listed in the following table [11, page 32]:

$I^{\mathrm{m}}_{\mathrm{S+SB}}$	measured scattered intensity of Sample and Sample Background
$I^{\mathrm{m}}_{\mathrm{SB}}$	measured scattered intensity of Sample Background
$I^{\mathrm{m}}_{\mathrm{Cd}} = I_{\mathrm{Cd}}$	background signal: electronic, ... (dark current image in neutron radiography)
$I^{\mathrm{m}}_{\mathrm{H_2O+ec}}$	measured intensity scattered by water standard inside container (glass cell)
$I^{\mathrm{m}}_{\mathrm{ec}}$	measured intensity scattered by empty container (empty glass cell)
I^{m}_{0}	measured intensity of primary beam (open beam image in neutron radiography
T_{S}	transmission of sample
T_{SB}	transmission of sample container

[10] ImageJ homepage `http://rsbweb.nih.gov/ij/`

A.12.1 Data Evaluation Step by Step

The single steps during the data reduction/evaluation with μSANS are described in this subsection; beginning with the selection of the different input files and ending with a line profile of the scattered intensities over Q.

Selection of Input Images During the first step of the data evaluation the acquired images have to be selected:

- **empty beam** I_0^{m}

  The first image the user is asked to select is an intensity distribution of the empty beam. It is the primary intensity without anything blocking or disturbing the neutron beam. In neutron radiography this would be called open beam image. Beside the image of the intensity scattered by the sample this is most important for the evaluation of the data. Thus μSANS will not continue, if no image is selected here.

- **sample + sample background** $I_{\mathrm{S+SB}}^{\mathrm{m}}$

  The user is asked to select an image of the measured intensity scattered by the sample ans sample background, i.e. the image taken while a sample inside a sample container was placed in the neutron beam. If no images is selected here, the Plugin is stopped.

- **sample background** $I_{\mathrm{SB}}^{\mathrm{m}}$

  The user is also asked to select an image of the measured intensity of the sample background, i.e. the image taken while an container was placed in the neutron beam. If no image is selected, the program assumes that there is no sample background and that the sample background intensity is equal to the intensity of the primary beam, $I_{\mathrm{SB}}^{\mathrm{m}} = I_0^{\mathrm{m}}$.

- **cadmium** $I_{\mathrm{Cd}}^{\mathrm{m}}$

  The user is asked to select an image of the measured intensity while a peace of cadmium or of comparable material is blocking the beam at the sample position. The image acquired that way is a measure for the hall background. In case of the CCD-detector it is mainly an offset signal of the readout electronics. It is called dark current image in neutron radiography. If no image is selected here, the hall background is set to 0 by the program: $I_{\mathrm{Cd}}^{\mathrm{m}} = 0$. It is advisable to select an image here especially if the input data was taken using a CCD detector. The inherent offset of the detector might otherwise spoil the calculation of transmission of sample and background completely, if it is treated as 0.

- **water** $I_{\mathrm{H_2O+ec}}^{\mathrm{m}}$

  An image containing the scattered intensity of a standard water sample can be selected here. It is used to yield an absolute calibration of the scattered intensities, as scattered intensity of the standard sample is supposed to be known exactly.
  As a correction factor is calculated form this image, μSANS will stop, if no image is selected here. In case data for absolute calibration are not available, μSANS should be run in "not calibrated" mode.

  This option is not activated up to now, because no images of a water sample have been acquired using the preliminary USANS setups, USANS I and USANS II.

- **empty cell/container** $I_{\mathrm{ec}}^{\mathrm{m}}$

  Please select an image of the scattered intensity, while an empty container comparable to the one used for the measurement with water is placed in the neutron beam. The background for water calibration is treated as 0, if no image is selected here: $I_{\mathrm{ec}}^{\mathrm{m}} = 0$.

  Again this option is not activated in the current version.

Determination of Maxima The slits of the multi apertures of the USANS setups, USANS I and USANS II are aligned along y-direction. Therefor an evaluation of scattered neutrons is reasonable in x-direction only. The Q-values for each pixel of the detector are determined by their distance to the center of the corresponding peak in x-direction. To be able to calculate this distance it is necessary to determine the position of the center of the primary peaks for each line of the acquired image. Including an option to select a Region Of Interest (ROI) is considered to offer the user a way to choose peaks definite for the evaluation.
The algorithm mapping the peak positions takes several steps to do so:

- It starts by generating a copy of the intensity profile of the empty beam.
- A despeckle filter[11] is used to get rid of some noisy pixels.
- Then a Gaussian blur is used to smoothen the peak profiles.
- A convolution of the image with the kernel (-1,0,1) results in a differentiation of each line in x-direction.
- The next step determines possible peak positions, which are given by a change of the sign of the derivative calculated in the previous step.
- If two of the peak positions determined are adjacent to each other, the one having the lower intensity is remove to avoid double peaks.
- Only peaks providing a reasonable statistics are used for the evaluation. Thus all peak positions are removed, which do exceed a certain intensity threshold.
- Then the total number of pixels labeled as a peak position is determined.
- Finally the mean distance between the maxima in x-direction is derived from the peak positions. This allows to fix the limit for the evaluated Q-range, which is half of the mean distance between the peaks.

Each peak position is equivalent to $Q = 0$ and used as a starting point for the single line profiles, which are extracted after the data reduction. The maximum length of an evaluated line profile is set to be half the mean distance between two peaks in x-direction. Thus it is possible to measure over a Q-range from $Q = 0$ up to $Q_{\max}$. This maximum value of the Q-range is

$$Q_{\max} = \underbrace{\frac{4\,\pi}{\lambda \cdot 2 \cdot L_2}}_{\Delta Q \text{ per pixel}} \cdot \frac{1}{2}\,(\text{"mean peak distance"}) \tag{A.118}$$

Q-mapping on CCD-Detector In order to get intensity distributions in Å^{-1} rather than pixels the CCD-detector has to be calibrated. With the known values for

- number of pixel of the detector
- field of view (FOV), the area on the scintillation screen viewed by the CCD camera
- distance between sample and detector/scintillation screen
- wavelength, which was set

it is possible to calculate a ΔQ corresponding to a single pixel on the detector. Starting from Bragg's law in Q-space

$$Q = \left|\vec{Q}\right| = 2 \cdot \left|\vec{k}\right| \cdot \sin(\theta) = \frac{4\,\pi}{\lambda}\,\sin(\theta)\,. \tag{A.119}$$

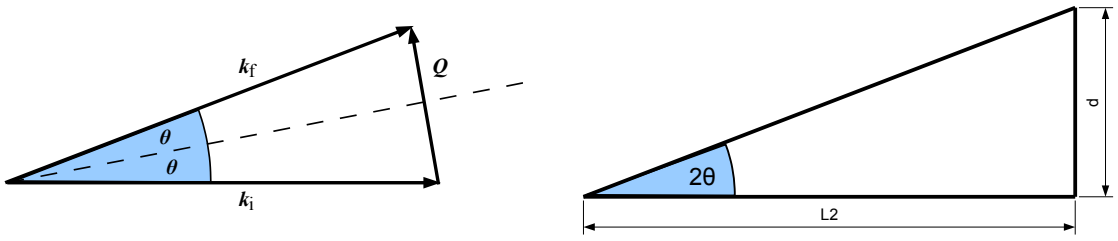

Fig. A.17: The scattering angle Θ is given by distance L_D between sample and detector and distance d on the detector measured from a peak position corresponding to $Q = 0$.

$\sin(\theta)$ can be replaced by distance d on the detector and distance L_D from sample to the detector.

$$\tan(2\,\theta) = \frac{d}{L_D} \quad \Longrightarrow \quad 2\,\theta \approx \frac{d}{L_D} \tag{A.120}$$

$$\sin(\theta) \quad \approx \quad \frac{d}{2\,L_D} \tag{A.121}$$

From (A.119) and (A.121) and the pixel size Δd given by the dimensions of the FOV of the detector divided by the corresponding number of pixels a ΔQ equivalent to a single detector pixel is calculated to

$$\Delta Q \;=\; \frac{2\,\pi}{\lambda \cdot L_D} \cdot \Delta d\,. \tag{A.122}$$

Then the Q-value of each position on the detector is derived from the number of pixels N_p this position is away from the center of the peak of the primary intensity profile it is associated to.

$$Q(N_p) \;=\; \Delta Q \cdot N_p \tag{A.123}$$

An alternative way is to use the real distance d on the detector to determine Q by

$$Q(d) \;=\; \frac{2\,\pi \cdot d}{\lambda \cdot L_D}\,. \tag{A.124}$$

A.12.2 Data Reduction

The basic data reduction of the USANS data is carried out in analogy to [11, page 32]. It is assumed that images have been acquired containing the following signals:

- I_0^m, the intensity profile of the incident neutrons at the detector corresponding to the superposition of the multiple neutron beams,
- I_{Cd}^m, the background signal including the hall background and electronic background,
- I_{SB}^m, the sample background, e.g. of the empty sample container, and
- I_{S+SB}^m, the intensity profile acquired while the sample is placed inside the neutron beam.

If an image of the sample background is not available, the intensity profile of the empty beam is used instead. The intensity I_S of the scattered neutron signal is calculated using equations (A.125) to (A.126) listed below. In contrast to the derivation in [11] terms representing the transmission signal of the incident neutrons are added. The measured intensity I_{SB}^m of neutrons scattered by the empty sample container or the solvent and the measured intensity I_{S+SB}^m of the sample inside the sample container or solvent are given by

$$I_{SB}^m \;=\; \hat{T}_{SB}\,I_{SB} + I_{Cd} + \hat{T}_{SB}\,I_0 \tag{A.125}$$

$$I_{S+SB}^m \;=\; \hat{T}_S\,\hat{T}_{SB}\,I_S + \hat{T}_S\,\hat{T}_{SB}\,I_{SB} + I_{Cd} + \hat{T}_S\,\hat{T}_{SB}\,I_0 \tag{A.126}$$

[11] standard despeckle filter of ImageJ

These equations are valid for all Q-values. From and (A.126) the intensity I_S scattered by the sample can easily be calculated, when solving equation (A.125) for $\hat{T}_\mathrm{SB}\, I_\mathrm{SB}$

$$\hat{T}_\mathrm{SB}\, I_\mathrm{SB} \;=\; I^\mathrm{m}_\mathrm{SB} - I_\mathrm{Cd} - \hat{T}_\mathrm{SB}\, I_0 \tag{A.127}$$

and inserting this into equation (A.126)

$$\begin{aligned} I^\mathrm{m}_\mathrm{S+SB} &= \hat{T}_\mathrm{S}\,\hat{T}_\mathrm{SB}\, I_\mathrm{S} + \hat{T}_\mathrm{S}\,\left(I^\mathrm{m}_\mathrm{SB} - I_\mathrm{Cd} - \hat{T}_\mathrm{SB}\, I_0\right) + I_\mathrm{Cd} + \hat{T}_\mathrm{S}\,\hat{T}_\mathrm{SB}\, I_0 \\ \Leftrightarrow I_\mathrm{S} &= \frac{I^\mathrm{m}_\mathrm{S+SB} - \hat{T}_\mathrm{S}\, I^\mathrm{m}_\mathrm{SB} + \hat{T}_\mathrm{S}\, I_\mathrm{Cd} - I_\mathrm{Cd}}{\hat{T}_\mathrm{S}\,\hat{T}_\mathrm{SB}} \\ &= \frac{I^\mathrm{m}_\mathrm{S+SB} - I_\mathrm{Cd}}{\hat{T}_\mathrm{S}\,\hat{T}_\mathrm{SB}} - \frac{I^\mathrm{m}_\mathrm{SB} - I_\mathrm{Cd}}{\hat{T}_\mathrm{SB}}\,. \end{aligned}$$

The transmission values $\hat{T}_\mathrm{S}$ of the sample and $\hat{T}_\mathrm{SB}$ of the sample container can be derived from the intensities measured at $Q = 0$. Here it it assumed that there is no overlap of the scattered intensity and the transmitted primary beam close to $Q = 0$. And for $Q = 0$ equations (A.125) and (A.126) can be simplified to

$$I^\mathrm{m}_\mathrm{SB}(Q=0) \;=\; I_\mathrm{Cd} + \hat{T}_\mathrm{SB}\, I_0(Q=0) \tag{A.128}$$

$$I^\mathrm{m}_\mathrm{S+SB}(Q=0) \;=\; I_\mathrm{Cd} + \hat{T}_\mathrm{S}\,\hat{T}_\mathrm{SB}\, I_0(Q=0)\,. \tag{A.129}$$

Using the correlations $I_\mathrm{Cd} \equiv I^\mathrm{m}_\mathrm{Cd}$ and $I_0 = I^\mathrm{m}_0 - I^\mathrm{m}_\mathrm{Cd}$ and solving for the transmission values gives

$$\hat{T}_\mathrm{S}\,\hat{T}_\mathrm{SB} \;=\; \frac{I^\mathrm{m}_\mathrm{S+SB}(Q=0) - I^\mathrm{m}_\mathrm{Cd}(Q=0)}{I_0(Q=0) - I^\mathrm{m}_\mathrm{Cd}(Q=0)} \tag{A.130}$$

$$\hat{T}_\mathrm{SB} \;=\; \frac{I^\mathrm{m}_\mathrm{SB}(Q=0) - I^\mathrm{m}_\mathrm{Cd}(Q=0)}{I_0(Q=0) - I^\mathrm{m}_\mathrm{Cd}(Q=0)} \tag{A.131}$$

If the sample shows a large scattering intensity in the Guinier range, this way to determine the transmission values is erroneous, because the scattered intensity alters the evaluated transmission value. In this case a different data reduction should be considered.

A.13 Transmission of Calibration Gratings

The fit functions $f'(x)$ and $g'(x)$ are defined in section 5.4.4. They are used to fit the primary multiple beam pattern and the intensity distribution at the detector composed of the transmitted primary intensity and the intensity scattered by the calibration gratings. The evaluated transmission values are listed in table A.5 to table A.7.

Transmission of the 4 μm phase grating for different peaks measured at 7.7 Å

amplitude	of primary intensity, $f(x)$ (exposure time 300 s)	of transmitted intensity, $g(x)$ (exposure time 300 s)	transmission
a_1	6800 ± 458	6093 ± 475	0.896 ± 0.092
a_2	17610 ± 464	16179 ± 409	0.918 ± 0.034
a_3	28660 ± 466	27867 ± 428	0.972 ± 0.022
a_4	39139 ± 469	38588 ± 374	0.986 ± 0.015
a_5	51729 ± 469	51102 ± 280	0.988 ± 0.010
a_6	58616 ± 469	57940 ± 291	0.988 ± 0.009
a_7	43547 ± 468	42799 ± 335	0.983 ± 0.013
a_8	34939 ± 468	33995 ± 355	0.973 ± 0.017
a_9	23148 ± 464	22812 ± 317	0.985 ± 0.024
a_{10}	13744 ± 460	13540 ± 322	0.985 ± 0.040
a_{11}	4424 ± 447	4476 ± 253	1.012 ± 0.117

Table A.5: The transmission values of the 4 μm grating are calculated from the amplitudes a_i of the primary intensity, $f'(x)$, and the transmitted intensity, $g'(x)$. The functions $f'(x)$ and $g'(x)$ are fitted to the measured line profiles.

Transmission of the 8.5 μm phase grating for different peaks measured at 9.5 Å

amplitude	of primary intensity, $f(x)$ (exposure time 50 s)	of transmitted intensity, $g(x)$ (exposure time 300 s)	transmission
a_1	1094 ± 91	3589 ± 234	0.547 ± 0.058
a_2	2865 ± 82	8827 ± 231	0.513 ± 0.020
a_3	4637 ± 80	14544 ± 248	0.523 ± 0.013
a_4	6694 ± 79	21331 ± 250	0.531 ± 0.009
a_5	9180 ± 79	29507 ± 263	0.536 ± 0.007
a_6	10787 ± 79	33859 ± 273	0.523 ± 0.006
a_7	8170 ± 79	25473 ± 276	0.520 ± 0.008
a_8	6453 ± 79	19509 ± 295	0.504 ± 0.010
a_9	4332 ± 79	12360 ± 319	0.476 ± 0.015
a_{10}	2433 ± 82	6356 ± 273	0.435 ± 0.024
a_{11}	660 ± 95	1905 ± 254	0.481 ± 0.094

Table A.6: The transmission values for the 8.5 μm grating are calculated from the amplitudes a_i of the primary intensity, $f'(x)$, and the transmitted intensity, $g'(x)$. The functions $f'(x)$ and $g'(x)$ are fitted to the measured line profiles.

Transmission of the 12 μm phase grating for different peaks measured at 9.5 Å

amplitude	of primary intensity, $f(x)$ (exposure time 50 s)	of transmitted intensity, $g(x)$ (exposure time 300 s)	transmission
a_1	1094 ± 91	3456 ± 223	0.527 ± 0.055
a_2	2865 ± 82	10293 ± 362	0.599 ± 0.027
a_3	4637 ± 80	16078 ± 225	0.578 ± 0.013
a_4	6694 ± 79	21781 ± 230	0.542 ± 0.009
a_5	9180 ± 79	28670 ± 220	0.521 ± 0.006
a_6	10787 ± 79	33656 ± 213	0.520 ± 0.005
a_7	8170 ± 79	25303 ± 208	0.516 ± 0.007
a_8	6453 ± 79	19680 ± 211	0.508 ± 0.008
a_9	4332 ± 79	13652 ± 206	0.525 ± 0.012
a_{10}	2433 ± 82	8068 ± 218	0.553 ± 0.024
a_{11}	660 ± 95	2948 ± 261	0.744 ± 0.126

Table A.7: The transmission values of the 12 μm grating are again calculated from the amplitudes a_i of the primary intensity, $f'(x)$, and the transmitted intensity, $g'(x)$. The functions $f'(x)$ and $g'(x)$ are fitted to the measured line profiles.

Bibliography

[1] Wikipedia. Intensified charge-coupled device, 2011. [online; last modified on 15 Dec 2011 at 09:05].

[2] J. Chadwick. Possible existence of a neutron. *Nature*, 192:312, 1932.

[3] A.A. Harms and D.R. Wyman. *Mathmatics and Physics of Neutron Radiography.* D. Reidel Publishing Company, P.O. Box 17, 3300 AA Dordrecht, Holland, 1986.

[4] F. Grünauer. *Design, optimization, and implementation of the new neutron radiography facility at FRM-II.* PhD thesis, Technische Universität München, 2005.

[5] K. Lorenz. *Implementation of neutron phase contrast imaging at FRM-II.* Dissertation, Technische Univeristät München, 2008.

[6] N. Kardjilov. *Further developments and applications of radiography and tomography with thermal and cold neutrons.* Dissertation, Technische Univeristät München, 2003.

[7] M. Schulz. *Radiography with Polarised Neutrons.* Dissertation, Technische Univeristät München, 2010.

[8] R. K. Hassanein. *Correction Methods fot the Quantitative Evaluation of Thermal Neutron Tomography.* PhD thesis, Swiss Federal Institute of Technology Zurich, 2006.

[9] A.S. Tremsin, N. Kardjilov, M. Dawson, M. Strobl, I. Manke, J.B. McPhate, J.V. Vallerga, O.H.W. Siegmund, and W.B. Feller. Scatter rejection in quantitative thermal and cold neutron imaging. *Nuclear Instruments and Methods in Physics Research Section A: Accelerators, Spectrometers, Detectors and Associated Equipment*, 651(1):145 – 148, 2011. ¡ce:title¿Proceeding of the Ninth World Conference on Neutron radiography (The Big-5 on Neutron Radiography)¡/ce:title¿.

[10] A.-J. Dianoux and G. Lander. Neutron data booklet. Philadelphia, USA, 2003. pdf download from www.ill.eu.

[11] P. Lindner and Th. Zemb, editors. *Neutron, X-ray and Light: Scattering Methods Applied to Soft Condensed Matter.* Elsevier Science B.V., Amsterdam, Netherlands, first edition edition, 2002.

[12] P. Lindner and Th. Zemb, editors. *Neutron, X-ray and Light Scattering: Introduction to an Invetigative Tool for Colloidal and Polymeric Systems.* North-Holland Elsevier Science Publisher B.V., Amsterdam, 1991.

[13] Institut Laue-Langevin. Instrument layout d11, 2012. [online; 27 September 2012].

[14] R. Gähler. State of usans test at d11. Talk, ILL, Grenoble, 2007.

[15] C. Erler. Usans-option for the d11 at the ill. report, Fachhochschule Jena, ILL Grenoble, 2007.

[16] C. Grünzweig, T. Hils, S. Mühlbauer, M. Ay, K. Lorenz, R. Georgii, R. Gähler, and P. Böni. Multiple small angle neutron scattering: A new two-dimensional ultrasmall angle neutron scattering technique. *Applied Physics Letters*, 91(20):203504, 2007.

[17] E. Hecht. *Optics*. Addison-Wesley Publishing Company, Inc., Reading, Massachusetts, second edition edition, 1987. world student series edition.

[18] V.F. Sears. *Neutron Optics*. Oxford University Press, 1989.

[19] P. Convert and J.B. Forsyth. *Position-Sensitive Detection of Thermal Neutrons*. Academic Press, London, 1983.

[20] G.C. Smith. Neutron imaging, radiography, and ct. *Encyclopedia of Imaging Science and Technology*, 2002.

[21] C.W.E. van Eijk. Neutron psds for the next generation of spallation neutron sources. *Nuclear Instruments and Methods in Physics Research Section A: Accelerators, Spectrometers, Detectors and Associated Equipment*, 477(1-3):383 – 390, 2002.

[22] M.M. Ter-Pogossian. *The Physical Aspects of Diagnostic Radiology*. Hoeber Medical Division, Harper & Row, Publishers, 49 East 33rd Street, New York, N.Y. 10016, 1967.

[23] C. Hesse. private communication, 2010.

[24] I.A. Cunningham, M.S. Westmore, and A. Fenster. A spatial-frequency dependent quantum accounting diagram and detective quantum efficiency model of signal and noise propagation in cascaded imaging systems. *Am. Assoc. Phys. Med.*, 21(3):417 – 427, 1994. Medical Physics.

[25] Wikipedia. Contrast, 2011. [online; last modified on 27 May 2011 at 12:00].

[26] P.C. Bunch, K.E. Huff, and R. Van Metter. Analysis of the detective quantum efficiency of a radiographic screen-film combination. *Journal of Optical Society of America*, 4(5):902–909, 1987.

[27] G. Zanella and R. Zannoni. The detective quantum efficiency of an imaging detector. *Nuclear Instruments and Methods in Physics Research A*, 359:474–477, 1995.

[28] Ju. N. Barmakov, E. P. Bogolubov, A. P. Koshelev, V. I. Mikerov, and V. I. Ryzhkov. Detection quantum efficiency and spatial resolution of neutron ccd-detectors. *Nuclear Instruments and Methods in Physics Research Section B: Beam Interactions with Materials and Atoms*, 213:241 – 245, 2004. 5th Topical Meeting on Industrial Radiation and Radioisotope Measurement Applications.

[29] L. Mandel. Image fluctuations in cascade intensifiers. *British Journal of Applied Physics*, 10(5):233–234, 1959.

[30] H.J. Zweig. Detective quantum efficiency of photodetectors with some amplification mechanisms. *Journal of optical society of America*, 55(5):525 – 528, 1965.

[31] M. Rabbani, R. Shaw, and R. Van Metter. Detective quantum efficiency of imaging systems with amplifying and scattering mechanisms. *J. Opt. Soc. Am. A*, 4(5):895–901, 1987.

[32] C. W. E. van Eijk. Neutron detection and neutron dosimetry. *Radiation Protection Dosimetry*, 110(1-4):5–13, 2004.

[33] V. Dangendorf. telephone conversation, 2008. in-motion unsharpness due to finite velocity of cold/thermal neutrons.

[34] N. Riehl. *Einführung in die Lumineszenz*. Verlag Karl Thiemig KG, München, 1971.

[35] Proxitronic Detector Systems (formerly Proxitronic Treo GmbH). *P43-PrCeF PHOSPHOR, GADOLINIUM OXYSULPHIDE:PRASEODYMIUM, CERIUM,FLUORINE*, 2008. data sheet.

[36] Proxitronic Detector Systems (formerly Proxitronic Treo GmbH). *P43-Tb PHOSPHOR, GADOLINIUM OXYSULPHIDE:TERBIUM*, 2008. data sheet.

[37] Martin Engelhardt. Imaging of dynamic processes with a timescale of microseconds at a thermal neutron beam. diploma thesis, Technische Universit"at M"unchen, 2004. Institute of Experimental Physics E21.

[38] J. Brunner. *Qantitativ time resolved neutron imaging methods at the high flux neutron source FRM-II.* Dissertation, Technische Universität München, 2005.

[39] M. Strobl, A. Hilger, M. Boin, N. Kardjilov, R. Wimpory, D. Clemens, M. Mühlbauer, B. Schillinger, T. Wilpert, C. Schulz, K. Rolfs, C.M. Davies, N. O'Dowd, P. Tiernan, and I. Manke. Time-of-flight neutron imaging at a continuous source: Proof of principle using a scintillator ccd imaging detector. *Nuclear Instruments and Methods in Physics Research Section A: Accelerators, Spectrometers, Detectors and Associated Equipment*, 651(1):149 – 155, 2011. ¡ce:title¿Proceeding of the Ninth World Conference on Neutron radiography (The Big-5 on Neutron Radiography)¡/ce:title¿.

[40] H. Li, B. Schillinger, E. Calzada, L. Yinong, and M. Muehlbauer. An adaptive algorithm for gamma spots removal in ccd-based neutron radiography and tomography. *Nuclear Instruments and Methods in Physics Research Section A: Accelerators, Spectrometers, Detectors and Associated Equipment*, 564(1):405 – 413, 2006.

[41] G.W. Fraser and J.F. Pearson. The direct detection of thermal neutrons by imaging microchannel-plate detectors. *Nuclear Instruments and Methods in Physics Research Section A: Accelerators, Spectrometers, Detectors and Associated Equipment*, 293(3):569 – 574, 1990.

[42] A.S. Tremsin, J.V. Vallgerga, J.B. McPhate, O.H.W. Siegmund, W.B. Feller, L. Crow, and R.G. Cooper. On the possibility to image thermal and cold neutron with sub-15 μm spatial resolution. *Nuclear Instruments and Methods in Physics Research A*, 592:374–384, 2008.

[43] A.S. Tremsin, W.B. Feller, and O.H.W. Siegmund. A new concept of thermal neutron counting with sub-microsecond timing resolution. *IEEE Transactions on Nuclear Science*, 55(3):1664–1669, 2008.

[44] A.S. Tremsin, W.B. Feller, and R.G. Downing. Efficiency optimization of microchannel plate (mcp) neutron imaging detectors. i. square channels with 10b doping. *Nuclear Instruments and Methods in Physics Research Section A: Accelerators, Spectrometers, Detectors and Associated Equipment*, 539(1-2):278 – 311, 2005.

[45] A.S. Tremsin, J.V. Vallerga, J.B. McPhate, O.H.W. Siegmund, J.S. Hull, W.B. Feller, L. Crow, and R.G. Cooper. High resolution neutron imaging at high counting rates with noiseless readout. In *Nuclear Science Symposium Conference Record, 2007. NSS '07. IEEE*, volume 1, pages 270–275, 2007.

[46] A.S. Tremsin, J.B. McPhate, J.V. Vallerga, O.H.W. Siegmund, W.B. Feller, L. Crow, and R.G. Cooper. High efficiency angular selective detection of thermal and cold neutrons. *SPIE Digital Library Proceedings*, 6945, 69451A, 2008.

[47] A.S. Tremsin, M.J. Mühlbauer, B. Schillinger, J.B. McPhate, J.V. Vallerga, O.H.W. Siegmund, and W.B. Feller. High resolution stroboscopic neutron radiography at the frm-ii antares facility. *Nuclear Science, IEEE Transactions on*, 57(5):2955 –2962, 2010.

[48] A.S. Tremsin. private communication, 2011.

[49] N. Takenaka, T. Kadowaki, Y. Kawabata, I.C. Lim, and C.M. Sim. Visualization of cavitation phenomena in a diesel engine fuel injection nozzle by neutron radiography. *Nuclear Instruments and Methods in Physics Research Section A*, 542:129 – 133, 2005.

[50] S. Som, S. K. Aggarwal, E. M. El-Hannouny, and D. E. Longman. Investigation of nozzle flow and cavitation characteristics in a diesel injector. *Journal of Engineering for Gas Turbines and Power*, 132(4):042802, 2010.

[51] A.S. Tremsin, J.B. McPhate, J.V. Vallerga, O.H.W. Siegmund, J.S. Hull, W.B. Feller, and E. Lehmann. High-resolution neutron radiography with microchannel plates: Proof-of-principle experiments at psi. *Nuclear Instruments and Methods in Physics Research Section A: Accelerators, Spectrometers, Detectors and Associated Equipment*, 605(1-2):103 – 106, 2009. ITMNR 08 - Proceedings of the sixth Topical Meeting on Neutron Radiography.

[52] A.S. Tremsin, J.B. McPhate, J.V. Vallerga, O.H.W. Siegmund, W.B. Feller, E. Lehmann, L.G. Butler, and M. Dawson. High-resolution neutron microtomography with noiseless neutron counting detector. *Nuclear Instruments and Methods in Physics Research Section A: Accelerators, Spectrometers, Detectors and Associated Equipment*, In Press, Corrected Proof:– , 2010.

[53] E.H. Lehmann, G. Frei, G. Kühne, and P. Boillat. The micro-setup for neutron imaging: A major step forward to improve the spatial resolution. *Nuclear Instruments and Methods in Physics Research A*, 576:389–396, 2007.

[54] F.J. Webb. The leakage of thermal neutrons through beryllium filters. *Nuclear Instruments and Methods*, 69(2):325 – 329, 1969.

[55] S. Pflaum. private converation, 2008. advice for operating injection setup.

[56] J. Wloka. private converation, 2008. operating parameters of injection nozzle.

[57] C. Grünzweig, G. Frei, E. Lehmann, G. Kühne, and C. David. Highly absorbing gadolinium test device to characterize the performance of neutron imaging detector systems. *Review of Scientific Instruments*, 78(5):053708, 2007.

[58] C. Grünzweig, F. Pfeiffer, O. Bunk, T. Donath, G. Kühne, G. Frei, M. Dierolf, and C. David. Design, fabrication, and characterization of diffraction gratings for neutron phase contrast imaging. *Review of Scientific Instruments*, 79(5):053703, 2008.

[59] M. Baron. *Messung von Quantenzuständen im Neutroneninterferometer*. PhD thesis, Technische Universität Wien, 2005.

[60] P. Boillat, G. Frei, E.H. Lehmann, G.G. Scherer, and A. Wokaun. Neutron imaging resolution improvements optimized for fuel cell applications. *Electrochemical and Solid-State Letters*, 13(3):B25–B27, 2010.

[61] K. Rossmann. Comparison of several methods for evaluating image quality of radiographic screen-film systems. *Am. J. Roentgenol.*, 97(3):772–775, 1966.

[62] M.J. Mühlbauer. *Bau eines Entwicklungssystems für Radiographie und Tomographie mit Neutronen - Building μTOS*. Diplomarbeit, Technische Univeristät München, 2005.

[63] Estman Kodak Company. *CCD Image Sensor Noise Sources*. Rochester, New York 14650-2010, revision 2 edition, 2003.

[64] H. Stöcker. *Taschenbuch der Physik*. Verlag Harri Deutsch, 2000.

[65] S. Pflaum. private converation, 2011. steel used for nozzle and nozzle needle, Shell V-oil 1404.

[66] Shell Deutschland Oil GmbH. *Shell V-Oil 1404 Einspritzpumpenprüföl nach DIN ISO 4113*. Hamburg, Germany, 2006.

[67] Wikipedia. Higher alkanes, 2011. [online; last modified on 31 October 2011 at 18:32].

[68] H. Friedrich, V. Wagner, and P. Wille. A high-performance neutron velocity selector. *Physica B: Condensed Matter*, 156-157:547 – 549, 1989.

[69] V. Wagner, H. Friedrich, and P. Wille. Performance of a high-tech neutron velocity selector. *Physica B: Condensed Matter*, 180-181(Part 2):938 – 940, 1992.

[70] K. Lieutenant, P. Lindner, and R. Gähler. A new design for the standard pinhole small-angle neutron scattering instrument D11. *Journal of Applied Crystallography*, 40(6):1056–1063, 2007.

Danksagung

In erster Linie gilt mein Dank Prof. Dr. Peter Böni für die Möglichkeit meine Arbeit am Lehrstuhl E21 durchzuführen. Die Diskussionen mit ihm als Betreuer der Arbeit haben mir immer wieder neuen Antrieb gegeben und mich motiviert Neues auszuprobieren.
An zweiter Stelle darf ich mich bei der wissenschaftlichen Leitung der Forschnungs-Neutronenquelle Heinz Maier-Leibnitz (FRM II), Prof. Dr. Winfried Petry und Dr. Jürgen Neuhaus, bedanken, dass sie mir Messzeit und Neutronen für meine Experimente zugänglich gemacht haben.
Dr. Burkhard Schillinger danke ich für die Betreuung am Instrument ANTARES, an dem ich einen Großteil der Zeit während meiner Promotion am FRM II verbracht habe. In diesem Zusammenhang möchte ich mich bei den Kollegen Dr. Johannes Brunner, Dr. Klaus Lorenz und Philipp Schmakat für die gute Zusammenarbeit bedanken. Dr. Michael Schulz soll an dieser Stelle gesondert erwähnt werden, da er nicht nur das Büro mit mir geteilt hat, sondern auch Teile der Arbeit Korrektur gelesen hat. Elbio Calzada gebührt mein Dank für all die großen und kleinen Konstruktionen, die während meiner Zeit in der Gruppe immer wieder nötig waren, und für seine Tipps, die mir die Arbeit mit CAD-Programmen erleichtert haben. Ebenfalls soll Dr. Thomas Bücherl als Verantwortlicher für die Schwesteranlage NECTAR an dieser Stelle für die gute Zusammenarbeit und seine Korrekturen gedankt werden. Dr. Florian Grünauer war für mich als ehemaliges Mitglied der ANTARES-Gruppe ebenfalls immer ein wichtiger Ansprechpartner. Über die Jahre ist er mir bei schon fast unzähligen Gesprächsabenden durch sein Interesse auf den verschiedensten Fachgebieten zu einem geschätzten und kompetenten Diskussionpartner geworden. Insbesonders hat er sich spontan dazu bereit erkärt, die Monte-Carlo-Simulation als Vergleich zu den gerechneten Radiographien für die Auswertung der Messungen an der Einspritzdüse zu erstellen.
Prof. Dr.-Ing. Wachtmeister vom Lehrstuhl für Verbrennungskraftmaschinen der TUM danke ich für die Unterstützung beim Aufbau für die dynamischen Neutronenradiographiemessungen. Sein Lehrstuhl hat die Einspritzdüsen und die Hochdruckpumpe für die durchgeführten Experimente zur Verfügung gestellt. Besonders sollen an dieser Stelle Dipl.-Ing. Johann Wloka und Dr.-Ing. Sebastian Pflaum erwähnt werden, die mir durch ihr Fachwissen als Berater zur Seite standen und somit zum Erfolg der Messungen beigetragen haben.
Dr. Anton S. Tremsin hat die Strahlzeit für die zeitaufgelösten Messungen an der Einspritzdüse begleitet, die mit seinem MCP-Detektor durchgeführt wurden. Hierdurch konnte ich von seiner jahrelangen Erfahrung, die er mit dem Detektorsystem gesammelt hat, profitieren. Es ist mir immer eine Freude mit ihm zusammenzuarbeiten, da er stets mit vollem Einsatz und überdurchschnittlichem Enthusiasmus an die Messungen heran geht.
Dr. Karl Zeitelhack vom Detektorlabor des FRM II danke ich für die DELCam-Kamerabox, die er als Basis für den hochauflösenden Detektoraufbau mit der intensivierten CCD-Kamera zur Verfügung gestellt hat.
Die Messungen zur Ultra-Kleinwinkel-Neutronenstreuung basieren auf Ideen und Überlegungen von Dr. Roland Gähler, ohne den diese Experimente sicher nicht stattgefunden hätten. Ich bin ihm daher zu besonderem Dank verpflichtet, da er mich eingeladen hat an den Experimenten mitzuwirken. Somit hatte ich die Gelegenheit erste Erfahrungen auf dem Gebiet der Ultra-Kleinwinkel-Neutronenstreuung zu sammeln, um schließlich die gemessenen Daten im Rahmen meiner Promotion zu nutzen. Die Messungen wurden am Instrument D11 am Institut Laue-Langevin in Grenoble zusammen mit den Instrumentverantwortlichen Dr. Peter Lindner und Dr. Ralf Schweins durchgeführt, und durch den Instrumenttechniker David Bowyer tatkräftig unterstützt. Dipl.-Ing. Chritoph Erler gilt in diesem Zusammenhang mein Dank für die umfangreichen Vorarbeiten, die er zusammen mit Dr. Roland Gähler geleistet hat, und seine Mithilfe bei der gemeinsamen Messzeit. Im Rahmen dieser Messzeit hat Herr Dr. Christian Grünzweig Gitter zur Verfügung gestellt, die für die Charakterisierung des Messaufbaus und die Kontrolle der Detektoreichung verwendet wurden, wofür ihm mein Dank gilt.
Wenn mehrere Leute an einem Projekt arbeiten, merkt man wie bei einem Getriebe sehr schnell,

wenn nicht alle Zahnräder richtig ineinander greifen. Manchmal kann das schlimmer sein als einfach nur mal stehen zu bleiben. Da freut man sich umso mehr, wenn z.B. die Zusammenarbeit zwischen den Werkstätten nicht nur auf dem FRM-Gelände sondern auch in der Physik oder dem Maschinenbau wie geschmiert funktioniert. In diesem Sinne möchte ich allen Werkstätten danken, da sie meist schneller waren als veranschlagt und auch nach Feierabend manchmal mit dem fehlenden Werkzeug aushelfen konnten und sei es, dass nur ein 17er-Schlüssel gefehlt hat. Namentlich kann ich hier stellvertretend für alle Mitarbeiter in den Werkstätten nur die Werkstattleiter aufführen, es sind dies Manfred Pfaller für die Zentralwerkstatt der Fakultät für Physik, Christian Herzog und Uwe Stiegel für die Werkstätten am FRM II, Herbert Größlhuber für die Werkstatt der Radiochemie München und Uli Ebner für das Technische Labor des Lehrstuhls für Medizintechnik.
Parallel zu meinen eigenen Arbeiten bot sich mir an der Anlage ANTARES die Möglichkeit auch an zahlreichen Messungen anderer Institute und Einrichtungen mitzuwirken. Hierdurch konnte ich einen Einblick in die jeweiligen Fachbereiche und Forschungsthemen gewinnen. Daher möchte ich mich bei folgenden Personen für die Zusammenarbeit im Rahmen der genannten Projekte bedanken: Dr. Andreas Joos von der Technischen Universität Hamburg-Harburg, Ansammlung von Feuchtigkeit in der Kabinenisolierung von Flugzeugen; Dipl.-Rest. Kathrin Adelfinger vom Lehrstuhl für Restaurierung, Kunsttechnologie und Konservierungswissenschaft der Technischen Universität München in Zussammenarbeit mit dem Staatlichen Museum für Völkerkunde München, Tanzmasken aus Guatemala für den baile de toritos; Dr. Gabriele Hörnig und Dipl.-Ing. Peter Völk vom Lehrstuhl für Analytische Chemie, Institut für Wasserchemie und chemische Balneologie der Technischen Universität München und dem Lehrstuhl für Verbrennungskraftmaschinen der Technischen Universität München; Russablagerungen in Abgaswärmetauschern; Dipl.-Ing. Johannes Bergmaier vom TU-fast racing team, Neutronentomographie eines Zylinderkopfes; Dipl.-Ing. Sophie Hippmann und Dr. Uwe Wasmuth vom Lehrstuhl für Umformtechnick und Gießereiwesen (UTG) der TUM, Arbeiten zum reverse engineering, Neutronentomographie am metallischen Klettverschluss Metaklett und Untersuchung unterschiedlicher Gussproben; Dipl.-Ing. Robert Metzke vom Lehrstuhl für Numerische Mechanik der TUM, Neutronentomographie einer Rattenlunge mit Ziel der Optimierung von Beatmungsgeräten in der Humanmedizin; PhD Yan Gao und PhD Job Rijssenbeek von GE Global Research, Arbeiten an ZEBRA-Batterien; Dr. Cornelia Kemp vom Deutschen Museum München, Neutronenradiographieaufnahmen von historischen Fotoobjektiven für die Ausstellung "Foto und Film"; Dr. Kai-Uwe Hess vom Department für Geo- und Umweltwissenschaften Sektion Mineralogie, Petrologie und Geochemie der Ludwig-Maximilian-Universität München, Neutronentomographie an Gesteinsproben; Dr. Giulia Festa von der Universitá degli Studi di Roma Tor Vergata, Dipartimento di Fisica, Neutronenradiographien an Reliefs der Paradiespforte des Baptisterium San Giovanni in Florenz erschaffen von Lorenzo Ghiberti; Dr. Emma Hammerlund vom Biologisk Institut der Syddansk Universitet, Studien zur Bildung von Fossilien; Dr. Dirk Visser von der Universität Delft und ISIS, Neutronentomographie der Duellpistolen von James Monroe und weiterer Bronze-Artefakte; Dr. Anatoliy Senyshyn und Prof. Dr. Helmut Ehrenberg, Arbeiten an Litium-Ionen-Zellen.
Gerade im Bereich der Untersuchung von Kunstobjekten hat sich ein besonders ausgeprägter Kontakt zum Lehrstuhl für Restaurierung der Technischen Universität München und der Archäologischen Staatssammlung München entwickelt. Wobei durch die enge Zusammenarbeit auch das Völkerkundemuseum und das Landesamt für Denkmalpflege in München Proben für Messungen aus ihrem Fundus an den FRM transferierten. Stellvertretend will ich nur einige Personen nennen, die diesen Institutionen angegliedert sind oder waren: Prof. Dr. habil. Rupert Gebhard, Dr. Brigitte Haas-Gebhard, Prof. Dipl.-Rest. Emmerling, Dipl.-Rest. Ina Meißner, Dipl.-Rest. Johanna Lang und Dipl.-Rest. Jens Wagner. In diesem Zusammenhang durfte ich gemeinsam mit Dr. Andras Kratzer vom Physik Department der TUM am Instrument ANTARES drei Schüler-Facharbeiten und eine Zulassungsarbeit für das Lehramtsstudium mit Schwerpunkt auf Untersuchungen an Kunstobjekten betreuen.
Ein Dankeschön geht auch an die Kollegen an der Nachbarinstrumente in der Experimentierhalle

Dr. Klaudia Hradil, Dr. Richard Mole, Dr. Thomas Keller, Dr. Michael Hofmann, Dr. Julia Repper, da sie auch zu später Stunde noch mit Ratschlägen, Werkzeug oder Material aushelfen konnten, wenn mal wieder etwas Unvorhergesehenes passiert ist. Die Gespräche bei den gemeinsamen Abendessen haben mir oft die Zeit bis zum nächsten Probenwechsel verkürzt.
Hier sollte auch die gesamte Positronentruppe genannt werden, die angeführt von Christoph Hugenschmidt oft über meinem Kopf für Unterhaltung sorgte und durch geschickte Schraubenschlüssel-Gravitations-Experimente auch schon mal für einen kompletten Stromausfall an der Radiographieanlage gesorgt hat.
Nicht zu vergessen Dr. Markus Hölzel, Dr. Anatoliy Senyshyn, Dr. Oleksandr Dolotko und Josef Pfanzelt bei denen ich sozusagen eine neue Wirkungsstätte am Instrument SPODI gefunden habe.
In diesem Zusammenhang möchte ich mich auch bei Prof. Dr. Helmut Ehrenberg und Prof. Dr. Hartmut Fueß für die Aufnahme in das Transferprojekt zur Untersuchung von Li-Ionen Batterien bedanken.
Für viele informative Gespräche möchte ich mich bei allen Teilnehmern der Kaffeerunde im Betriebsgebäude bedanken: Thomas Keller, Michael Schulz, Andreas Ofner, Christian Breunig, Johannes Brunner, Klaus Lorenz, Jörgen Franke, Adrian Rühm, Phillip Schmackat, Elbio Calzada, Franz Tralmer, Kathrin Buchner, ... Da es viele und wechselnde Teilnehmer waren, möge man es mir verzeihen, wenn ich einige vergessen haben sollte.
Einen ganz speziellen Dank gilt es auch Christian Hesse, Matthias Lettner, Simon Lud, Martin Mühlegger und Albert Schließer aus meiner Physiklerngruppe auszusprechen. Unsere wöchentlichen Treffen zum Mittagessen haben meinen Kontakt zum Unibetrieb aufrecht erhalten und damit zur Motivation beigetragen weiter an der Dissertation zu arbeiten. Hervorzuheben ist hier Christian Hesse, der bis zum Ende die Tradition des Freitagmittagsstammtisches unter nicht gerade geringen eigenem Aufwand aufrecht erhalten hat.
Zu guter Letzt möchte ich mich natürlich besonders bei meinen Eltern aber auch bei meinen Geschwistern und Verwandten für ihre Unterstützung bedanken. Ich darf wohl sagen, dass ich von ihnen und durch sie mehr gelernt habe als durch die Vorlesungen an der Universität. Vor allem konnte ich mich immer darauf verlassen, dass sie für mich da sind, wenn es drauf ankommt. Oft reichte allein diese Gewissheit aus um sich auch durch Rückschläge nicht so einfach unterkriegen zu lassen.

Nochmals allen ein großes und herzliches

Dankeschön!